CORA Cork Open Research Archive
Cartlann Taighde Oscailte Chorcaí

Title	Improved statistical quantitation of dynamic PET scans
Authors	Gu, Fengyun
Publication date	2023-03-15
Original Citation	Gu, F. 2023. Improved statistical quantitation of dynamic PET scans. PhD Thesis, University College Cork.
Type of publication	Doctoral thesis
Rights	© 2023, Fengyun Gu. - https://creativecommons.org/licenses/by-nc-nd/4.0/
Download date	2026-11-06 08:14:05
Item downloaded from	https://hdl.handle.net/10468/14486

UCC
University College Cork, Ireland
Coláiste na hOllscoile Corcaigh

Improved Statistical Quantitation of Dynamic PET Scans

Fengyun Gu

Thesis submitted for the degree of Doctor of Philosophy



NATIONAL UNIVERSITY OF IRELAND, CORK

DEPARTMENT OF STATISTICS

March 2023

Head of Department: Dr. Michael Cronin

Supervisors: Prof. Finbarr O'Sullivan
Dr. Jian Huang

Contents

List of Figures v
List of Tables xi
Acknowledgements xvi
Abstract xvii

1 Overview of Thesis **1**
1.1 Introduction 1
1.2 Main Contributions 2
1.3 Publications Related to Thesis 4
1.4 Thesis Structure 5

2 Background **6**
2.1 Medical Imaging 6
2.1.1 Computed Tomography 7
2.1.2 Magnetic Resonance Imaging 9
2.1.2.1 Structural MRI 9
2.1.2.2 Functional MRI - DSC/DCE 10
2.2 Positron Emission Tomography 11
2.2.1 Development of PET Scanners 11
2.2.2 Radiotracer 15
2.2.3 Scanning Procedure 16
2.2.3.1 The Physics of PET 17
2.2.3.2 Image Reconstruction 19
2.2.4 Structure of PET Data 24
2.2.5 Performance Evaluation 26
2.3 Quantitation of PET Imaging 29
2.3.1 Static and Dynamic PET Scans 30
2.3.2 The Basic Equation of Dynamic PET 32
2.3.2.1 Basics of Systems 33
2.3.2.2 Indicator-Dilution Method 34
2.3.2.3 ROI Versus Voxel-level Analysis 36
2.3.3 Arterial Input Function (AIF) 37
2.3.4 Kinetic Modeling 39
2.3.4.1 Compartmental Modeling 39
2.3.4.2 Spectral Analysis 41
2.3.4.3 Graphical Analysis: Patlak and Logan Plots . . 42
2.3.5 Current Status and Challenges in Whole-Body PET Imaging 44
2.3.5.1 Adaption of Traditional Approaches 46
2.3.5.2 The Promise of Novel Methodologies 47

3 Investigation of the Benefits of Combining Data in Multiple Injection PET Scans **49**
3.1 Introduction 50
3.2 Methodology 52

3.2.1 Voxel-level Kinetic Mapping by the NPRM Approach . . 54
3.2.1.1 Residue Decomposition and Mapping of Kinetics 56
3.2.1.2 Why is the NPRM Approach Reasonable? . . . 57
3.2.1.3 Local Error Characteristics of NPRM Mapping . 58
3.2.2 Multiple Injections and their Combined or Separated Analysis by NPRM 60
3.2.3 An Approximate Theoretical Analysis of Combined versus Separated Analysis 62
3.3 Illustration with a Flow-Metabolism Study in a Breast Cancer Patient 64
3.4 Numerical Experiments 66
3.4.1 Scanning Models 67
3.4.2 Source Patterns 68
3.4.3 Evaluation of Performance 70
3.5 Results 72
3.5.1 Sample Metabolic Parameters Estimates 72
3.5.2 MSE Performance Comparisons 73
3.5.2.1 H_2O-FDG Studies 73
3.5.2.2 Repeat H_2O Studies 74
3.6 Statistical Analysis of Simulation Results 75
3.6.1 MSE values scaled by Image Data Accuracy 76
3.6.2 Analysis of the Uptake MSE as a function of Dose 77
3.7 Discussion 79
3.7.1 The Choice of β 80
3.7.2 The Option of Weight 81
3.7.3 A Simplified Model 81

4 A Generalized Linear modeling approach to bootstrapping multi-frame PET image data 83
4.1 Introduction 84
4.1.1 General Bootstrap 84
4.1.2 Application of Bootstrap in PET 86
4.2 Methodology 88
4.2.1 Statistical Modeling of the Image-Domain Data 88
4.2.2 Bootstrapping Techniques 91
4.2.2.1 Projection-Domain Bootstrap: Non-parametric 91
4.2.2.2 Image-Domain Bootstrap: Model-based Approach 92
4.2.2.3 Approximate Image-Domain Bootstrap by Recycling 92
4.2.3 Specification of Unknowns in the Image-Domain Model 93
4.3 Illustrative Example 96
4.4 Numerical Studies 99
4.4.1 2-D Experiments 100
4.4.1.1 Bootstrapping Voxel-Level Summaries 102
4.4.1.2 Bootstrapping ROI Summaries 104
4.4.2 1-D Experiments 106

4.4.3 Statistical Interpretation of Simulation Data 110
4.5 Discussion 111

5 Bootstrap Averaging Enhances the Mean Square Error of Kinetic Maps Recovered from PET Data 114
5.1 Introduction 115
5.2 Methodology 117
5.2.1 Overview of Image-Domain Bootstrapping 117
5.2.2 Mapping Kinetics: NPRM and 2C Approaches 120
5.2.2.1 NPRM Mapping 121
5.2.2.2 2C Mapping 121
5.3 Illustrative Examples 122
5.4 Numerical Simulations 124
5.5 Results 127
5.6 Discussion 130

6 Discussion, Conclusions and Future Work 132
6.1 Discussion 132
6.1.1 Parametric imaging and associated uncertainty via the image-domain Bootstrap for a LAFOV PET FDG study . . 135
6.1.2 Adaption of NPRM for Digital Subtraction Angiography Imaging 136
6.1.3 Illustration of NPRM for the whole-body pregnant macaque PET imaging with multiple injections 137
6.1.4 Integration of Uncertainty Information of Biomarker to Clinical Decision Making 139
6.1.5 An Evaluation of the Benefits of Adaptive Bandwidth Scheme 141
6.2 Conclusions 143
6.3 Future Work 144
6.3.1 Enhancement of Total-Body PET Parametric Imaging . . 144
6.3.2 Towards Personalized Medicine 145
6.3.3 Generalization to other Medical Imaging Modalities . . . 145
6.3.4 Parallel speedup 145
6.3.5 Open-Source Tools 146

A List of Publications and Presentations by the Author A1
A.1 Peer Reviewed Journals A1
A.2 Conference Publications A3
A.3 Conference Presentations A4

B Details of Derivations B1
B.1 Radon and Fourier Transform B1
B.1.1 Line Integral B1
B.1.2 Radon Transform B2
B.1.3 Fourier Transform B3
B.1.4 Radon Transform with Fourier Transform B5
B.2 Derivation of Equation (2.14) B5

B.3 Solution of One Compartmental Model Ordinary Differential Equation (2.18) B6
B.4 Laplace's Transformation B6
B.4.1 Introduction to the Laplace Transform B6
B.4.2 The Inverse Laplace Transform B7
B.4.3 Solution of Initial Value Problems B8
B.5 Solution of Two Compartmental Model Ordinary Differential Equation (2.20) B9

Nomenclature **C1**

Bibliography **D1**

List of Figures

1.1 Overview of PET reconstruction and post-processing. 2

2.1 Reconstructions of data acquired by PET, MRI and CT of the same patient (Ehrhardt et al., 2014). 7
2.2 Simplified schematic of the computed tomography (CT) imaging process (Stiller, 2018). 8
2.3 The process of magnetic resonance imaging (MRI) signal acquisition to image display (Seeram, 2015). 10
2.4 New-generation long axial field of view (LAFOV) PET systems. A. uEXPLORER (United imaging Healthcare); B. Penn PET Explorer (University of Pennsylvania); C. Biography Vision Quadra (Siemens). 14
2.5 Glucose and FDG cellular uptake and metabolism (Trinder et al., 2020; Rudd et al., 2010). GLUT: glucose transporter. 16
2.6 Schematic of PET scanning process. 17
2.7 Principles of conventional and time of flight (TOF) PET scanners (Lecoq and Gundacker, 2021) and the relationship between the (x, y) coordinate system of the object and the (r, ϕ) coordinate system in which PET data are commonly stored (Cherry and Dahlbom, 2006). 18
2.8 Diagram of the filtered backprojection (FBP) reconstruction. . . 19
2.9 The general structure of iterative image reconstruction. 21
2.10 PET images generated on an early scanner (A) with FBP reconstruction (Mankoff et al., 2002), a recent scanner (B) with OSEM reconstruction (Kostakoglu et al., 2015) and a latest long axial field of view scanner - Siemens Quadra (C) with OSEM reconstruction (Sari et al., 2022) for breast cancer patients. Radiotracers are indicated on each row and columns correspond to transverse, coronal and sagittal views. 23
2.11 Physical (Hardware) Phantoms: Uniform (Mou, 2018), NEMA (Ulrich et al., 2018) and CTN (Viswanath, 2020). 26
2.12 Point-spread function (PSF) at 0 and 10cm from the field of view (Saha, 2015). 27
2.13 Numerical (Software) Phantoms: Uniform (Mou, 2018), VSK (Vardi, Shepp and Kaufman, 1985), Brain Phantom. 28
2.14 A schematic summary of major PET quantitation methods (Veronese et al., 2016). 29
2.15 Static (A) versus dynamic (B) PET imaging (Bertoldo, Rizzo and Veronese, 2014). 30
2.16 An example of dynamic whole-body PET data acquisition by a multi-pass multi-bed protocol using conventional scanners (Karakatsanis et al., 2013; Rahmim et al., 2019). 32
2.17 A general system diagram. 33

2.18 Definition of delta function and impulse response (Smith et al., 1997). 34
2.19 System is characterized by measuring the input and output. . . 35
2.20 Region of interest (ROI) and voxel-level analysis. 36
2.21 Markov chain model for tracer atom dynamics within the body (Huang and O'Sullivan, 2014). Graph representation (left); Transition matrix (right). 38
2.22 One (A) and two (B) compartmental models. Residue function with key physiological parameters (C) (Hawe, 2016). 39
2.23 Patlak and Logan plots. The figure shows an example of a Patlak plot (A) and an example of a Logan plot (B). The data show a linear trend after the equilibration time t^* and the slope corresponds to the estimated parameter of interest (K_i for the Patlak plot and V_D for the Logan plot) (Bertoldo, Rizzo and Veronese, 2014). 42
2.24 Fitting of one tissue (1C), two tissue irreversible (2Ci) and reversible (2Cr) compartmental models for multiple organs. x-axis: time in seconds; y-axis: activity. Raw dynamic data is shown in grey points. Blue, red and black lines represent 1C, 2Ci and 2Cr fitted curves (Wu, Gu, Wu, Zhou and Wang, 2022). 46
2.25 Delay time estimated from various compartmental models and schemes (Wu, Gu, Wu, Zhou and Wang, 2022). 47
2.26 standard (sPatlak) and generalized (gPatlak) Patlak plots for different organs. Grey points, blue and orange lines represent data, sPatlak and gPatlak fits, respectively. R squared is indicated on each plot (Gu et al., 2022). 48

3.1 Multi-Injection Dynamic PET Studies. A: Separate Analysis; B: Combined Analysis. 52
3.2 Non-parametric residue mapping (NPRM) process. 54
3.3 Estimates of flow, flux and mismatch in a H_2O-FDG breast cancer study from combined and separate analysis. Row A: Combined Analysis; Row B: Separate Analysis; Row C: ROI Analysis. . . . 65
3.4 Diagram of Simulation Process 67
3.5 Source distribution, $\lambda_{xt} = \sum_{k=1} \alpha_k(x)\mu_k(t)$ for 2D simulations. Row 1: α map and normalized time courses (μ) for H_2O and FDG. Row 2: True parametric images for flow, flux and mismatch. 69
3.6 1-D phantom (mixing coefficients - α_k's) and their projections for H_2O-FDG (a,b) and repeat H_2O studies (c,d). x-axis is location (1-128) and y-axis is coefficient. Different colors represent different ROIs. Values of the Kety model parameters $(K_1, K_1/k_2)$ used to create simulated time courses are given in the legends for (c) and (d). 70

3.7 Fitted time courses and real data for six kinds of tissues - spleen, tumor, myocardium, normal breast, liver and left ventricle (LV). Red and blue lines are fitted time courses for the H_2O and FDG studies, respectively. Black points are real data. x and y axis are time (minutes) after injection and activities (MBq/cc). 71
3.8 True time courses and simulated image data at middle dose and dose ratio for same six kinds of tissues. Red and blue lines are true time courses for H_2O and FDG studies in simulation, respectively. Grey points are simulated data. x and y axis are time (minutes) after injection and activities (MBq/cc). 71
3.9 Sample metabolic estimates (at a middle dose setting) based on the FBP and ML reconstruction. x-axis gives location (1-128); y-axis is values of metabolic parameters in 1-D simulations. See Figure 3.6 for location of different structures. Plots (1) and (2) show flow and flux in H_2O-FDG study; (3) and (4) show flow and blood volume (V_B) in the repeat 2 H_2O studies. 73
3.10 MSE of combined (solid) and separate (dashed) analysis as a function of dose and dose ratio in H_2O-FDG study. Different colors represent different dose ratios. 74
3.11 MSE of combined and separate analysis in multiple H_2O studies. 75
3.12 MSE values scaled by image data accuracy for combined (solid) and separate (dashed) analysis as a function of dose and dose ratio in H_2O-FDG study. 76
3.13 MSE values scaled by image data accuracy for combined (solid) and separate (dashed) analysis as a function of dose and number of studies in the repeat H_2O setting. 77
3.14 Estimated relation between MSE improvements and study dose. Calculation based on (3.25) with different colors corresponding to a range of possible γ_τ values. 78

4.1 Schematic of the bootstrap process 84
4.2 Schematic summary of the Model-Based Bootstrap Concept in a Simple Linear Regression Model. 85
4.3 Metabolic Images with image-domain bootstrap assessment of standard errors for Breast tumor FLT study. The mapped parameters are shown on row 1 – the location of tumor volume of interest (VOI) on the slice is indicated with an arrow. Columns correspond to different metabolic parameters (labeled in yellow) with color bars indicating units - see section 3.2.1.1 for definitions. Computed standard errors (SE) are on row 2. Row 3 shows histograms of the bootstrap sampling distributions of the 95'th percentile of the metabolic parameter in the normal [black] and tumor [red] VOIs. 97

4.4 Diagnostics associated with the Image-Domain Bootstrapping Model (4.5) for the FLT-Breast data. Six plots, labeled (i) to (vi), are shown: (i) raw sub-TACs (dots) and fitted models (lines) for the selected basis set - columns of X. (ii) Non-parametric residues corresponding to the fitted model. (iii) Boxplots by time-frame of standardized residuals from the unconstrained least squares fit, $r_{ij}/\hat{\sigma}_i\hat{\phi}_j\hat{h}_{ij}$. The simple, $\hat{\phi}_j^0$ in (4.7), and optimized, $\hat{\phi}_j$, standard deviations are shown as green and red dots. (iv) Boxplots of scaled residuals, $\hat{\epsilon}_{ij} = r_{ij}/\hat{\sigma}_i\hat{\phi}_j$, for each κ-bin (each containing roughly 10000 data points). $\hat{h}_l$-values are shown as red points; the red line is for comparison with unity (zero skewness of bin data). (v) Histogram of the overall distribution of the standardized residuals and its relation to a Gaussian fit (purple curve). Super-imposed are points showing quantiles of standardized residuals from different κ-bins (colored from red to dark blue according to bin order) versus corresponding quantiles of the Gaussian (right y-axis). The quantile pattern for the overall histogram and the Gaussian fit are shown with dashed black and purple lines. (vi) Directional auto-correlation patterns of the normalized residuals, $\hat{\eta}$, as a function of distance in millimeters. X-Y are transverse with Y perpendicular to the scanning bed; Z is the axial direction. 98

4.5 **A:** Source distribution, $\lambda_{xt} = \sum_{k=1} \alpha_k(x)\mu_k(t)$, for the 2-D simulation experiments. $\alpha_k(x)$ patterns and attenuation in (i), time-courses for each component, $\mu_k(t)$ (normalized), are in (ii). Flux parameters are in (iii). **B:** Dynamic image-domain source leads to a corresponding projection domain array. Simulated counts are reconstructed and computed metabolic images. Each replicate of the simulation has both non-parametric (projection-domain) and model-based (image-domain) bootstrapping. **C:** Voxel estimates of average standard deviations of flux are shown. The true values are estimated by direct replication, these values are compared to image and projection domain bootstraps for a single replicate. 101

4.6 Schematic of 2D ROI generation scheme. A total of 676 ROIs with different sizes (6, 20, 50 and 100 pixels) are defined for Breast. Grids of rectangular ROIs and their size are indicated. . 104

4.7 Estimates of average ROI standard deviations of flux. Colors correspond to different ROI sizes. 105

4.8 Standard deviations of ROI **maxima** (Row 1) and coefficients of variation (**CVs**) (Row 2) of flux (K_i) in breast study. The true values are estimated by direct replication, compared to image and projection domain bootstrap results. Different colors represent different ROI sizes. 106

4.9 Scaled spatial patterns (α_j) for source distribution ($\lambda_{xt} = \sum_{j=1}^{6} \alpha_j(x)\mu_j(t)$) in 1-D experiments (dotted lines); projection domain patterns ($K_\beta \alpha_j$) are also shown (solid lines). Source sub-TACs (μ_j) are in Figure 4.5 A(ii). Colors of α_j's here match the colors of corresponding sub-TACs in Figure 4.5 A(ii). The solid black line is the attenuation pattern. 108

5.1 Random forests improves prediction error by averaging predictions from multiple trees trained on different bootstrap samples of data. 117
5.2 Graphical representation of the generalized linear model (GLM) used to define the data generation process (DGP) for PET image-domain bootstrapping. 118
5.3 Raw and averaged-bootstrap (AB) parametric imaging: Rows 1&2 show the results from Brain tumor FDG study; 3&4 for the Breast cancer FLT study. Red arrows indicate tumors. Columns correspond to different metabolic parameters. 123
5.4 The performance of non-parametric approach (NP) and two compartmental modeling (2C). A&C - The percentage of unexplained weighted residual sum of squares (WRSS) using both methods in the brain tumor FDG and breast cancer FLT studies. B&D - The percent relative performance of 2C versus NP at different significance levels for these two studies. 124
5.5 Ground truth for Brain tumor FDG (Row 1) and Breast cancer FLT (Row 2) simulation studies. True α patterns in 1D (A&D) and 2D (B&E) simulations; C&F: scaled true time courses, x-axis is in minutes with indicated temporal sampling (grey ticks). The real data basis time courses are solid lines; dashed lines are corresponding one compartmental model fits. 125
5.6 Flowchart of simulation process. 126
5.7 1D and 2D simulation results with FBP and ML reconstructions in a simulation matched to FDG brain and FLT breast studies. The ground truth are (non-parametric) basis elements extracted from the real data. Kinetics are mapped by the NPRM process. Left (A&C) are for Brain; right (B&D) are for Breast. Top two rows: RMSE of raw (dashed) and averaged-bootstrap (solid) kinetic parameters as a function of dose - log-log scale. Bottom two rows: boxplots of relative performance of raw vs averaged-bootstrap kinetics by dose levels, y-axis is the percent improvement. 128

5.8 1D results with FBP and ML reconstructions in Brain FDG and Breast FLT simulations in which ground truth follows a compartmental form. Both 2C and NP mapping of kinetics are used. A&B: root mean square error (RMSE) of raw (dashed) and averaged-bootstrap (solid) kinetic parameters as a function of dose at log-log scale for the brain FDG and breast FLT studies; C&D: boxplots of relative performance values raw and averaged-bootstrap kinetics by dose levels, y-axis is the percent improvement. . . . 129

6.1 Averaged-bootstrap (AB) parametric imaging and associated standard error (SE) maps for selected slices (blue and red lines on top row). Columns correspond to different metabolic parameters. . 136
6.2 Sagittal views of parametric images of fast volume(V_F), slow flow and volume(K_S,V_S) from the suspected stroke patient study. Color bars are augmented to present the values of physiological parameters for all pixels. 137
6.3 CsA inhibition of P-gp acitivity (Top Row) and PET scanning protocol (Bottom Row). 138
6.4 Volume of distribution ratio mapping before and after CsA infusion for water (V_DW21) and verapamil (V_DV21). Columns correspond to different pregnant non-human primates. 138
6.5 Schematic of the framework to construct the biomarker mean and confidence interval for individual patients. 139
6.6 95% confidence interval (CI) of predicted probability to have pathological complete response for individual patients in the UW-FDG cohort. 141
6.7 Diagram of Evaluation Procedure. 142
6.8 FLT simulation results at different dose levels. **Left:** root mean square error (RMSE) of reconstructed image; **Right:** RMSEs of seven metabolic parameters. V_b - volume of blood; V_d - volume of distribution; K_1 – overall flow; K_d – flow of distribution; K_i – flux; MTT – mean transit time; Ext – extraction. Dashed and solid lines represent fixed and dynamic bandwidth schemes respectively. 142

B.1 Illustration of Radon transform, where x, y are axes; s is the shifting constant; ϕ is rotation angle; $f(x, y)$ is the intensity of object in (x, y); and $g(\phi, s)$ is the forward projection value after Radon transform. B2
B.2 Radon transform $\mathcal{R}$ and its inversion $\mathcal{R}^{-1}$ (Wieczorek, Vogel and Lasser, 2014). B3
B.3 Definitions of the forward and inverse Fourier transforms in four cases. B4

List of Tables

2.1 Overview on existing long axial field of view commercial and research systems (Nadig et al., 2021; Zhang et al., 2020; Viswanath, 2020; Sari et al., 2022). 15
2.2 The commonly used radiotracers and their targeted processes in PET. 16
2.3 Characteristics and Challenges/Opportunities of long axial field of view PET scanners. 44
2.4 Current status of quantitation of long axial field-of-view PET imaging. 45

3.1 Relative Performance (3.6) of NPRM and 2C kinetic mapping in a PET-FDG setting. Based on a 1-D simulation model with source sub-TACs in case I matched to real Breast Cancer data Figure 3.8 and to their best-fitting 1C model fit in case II. Data reconstruction by both direct (FBP) and iterative (ML) methods. 59
3.2 Impact of data-adaptive sub-TAC selection in NPRM on Kinetic Mapping errors. Statistical model: RMSE $_p^{unknown} \approx \beta_p$ RMSE $_p^{known}$. Results based on a 2D PET-FDG simulation with FBP reconstruction. Standard errors for estimates are the order of 0.01. . . . 59
3.3 Voxel-level errors in NPRM kinetics as a function of the local reconstruction ($\hat{\sigma}_i$) and modeling ($\hat{\sigma}_i^{\lambda}$) errors - $c.f.$ (3.7),(3.8). Results based on 1D- PET-FDG simulation. 61
3.4 Combined analysis improvements (3.22) by dose level/ratio for H_2O-FDG study. 74
3.5 Combined analysis improvements (3.22) in multiple H_2O studies at 7 dose levels. 75
3.6 Modeling Scaled MSE in the H_2O-FDG study - $c.f.$ (3.23). . . . 76
3.7 Modeling Scaled MSE in the repeat H_2O study, see (3.24). 77
3.8 MSE characteristics of reconstructed data in H_2O-FDG and H_2O studies (H_2O*) based on FBP and ML. Analysis is based on equation (3.25). 78
3.9 The rate of convergence - $\hat{\varphi}_1$ using different β in 1-D simulation. 81
3.10 MSE characteristics using different weights in 1D H_2O-FDG study. 81
3.11 Improvements (%) from constrained weighted least square with fixed weights at 7 dose levels and 7 dose ratios in 1D H_2O-FDG study using FBP reconstruction. 82

4.1 Reliability of Bootstrap Estimates of voxel Standard Deviations for mapped kinetics in **2-D** setting. Means and maxima of **voxel kinetic** estimates, averaged over replicates, are shown as $\bar{\mu}_\bullet$ and $\bar{\mu}_\vee$. Mean of voxel standard deviations, averaged over replicates ($\bar{\sigma}_\bullet$) its standard error ($\bar{SE}_\bullet$) and the overall RMSE values, see (4.12), are reported as a percentage of the maximum ($\bar{\mu}_\vee$). Estimates $(\hat{a}, \hat{b}, \hat{c})$ correspond to (4.11). 103

4.2 Reliability of Bootstrap Estimates of Standard Deviations for **ROI means** of mapped Kinetics in **2-D** setting. Note approximately 700 ROIs are considered , see Fig 4.6. Means and maxima of ROI-averaged kinetic parameters, averaged over replicates, are shown as $\bar{\mu}_\bullet$ and $\bar{\mu}_\vee$. Mean ROI standard deviation, averaged over replicates ($\bar{\sigma}_\bullet$), its standard error ($\bar{SE}_\bullet$) and the overall RMSE values, computed by ROI version of (4.12), are reported as a percentage of the maximum ($\bar{\mu}_\vee$). Estimates $(\hat{a}, \hat{b}, \hat{c})$ are based on the ROI version of (4.11). 105

4.3 Estimates of standard deviations for ROI **Maxima** and **CVs** of metabolic parameters in **2-D** Breast FLT studies. Note approximately 700 ROIs are considered in each case. Means and maxima of ROI maximum and CV kinetic parameters, averaged over replicates, are shown as $\bar{\mu}_\bullet$ and $\bar{\mu}_\vee$. Mean ROI standard deviation, averaged over replicates ($\bar{\sigma}_\bullet$), its standard error ($\bar{SE}_\bullet$) and the overall RMSE values, computed by ROI version of (4.12), are reported as a percentage of the maximum ($\bar{\mu}_\vee$). Estimates ($\hat{a}$ and $\hat{b}$) are based on the ROI version of (4.11). 107

4.4 Reliability of Bootstrap Estimates of **voxel** Standard Deviations for mapping Kinetics in **1-D** based on FBP and ML reconstructed data. Means and maxima of voxel kinetic estimates, averaged over replicates, are shown as $\bar{\mu}_\bullet$ and $\bar{\mu}_\vee$. Mean of voxel standard deviations, averaged over replicates ($\bar{\sigma}_\bullet$), its standard error ($\bar{SE}_\bullet$) and the overall RMSE values, see (4.12), are reported as a percentage of the maximum ($\bar{\mu}_\vee$). Estimates $(\hat{a}, \hat{b}, \hat{c})$ correspond to (4.11). 109

4.5 Analysis of Voxel-level Error Characteristics across all Simulations. The coefficients are for the models in (4.14) and (4.15). The R^2-values only reported for (4.15). Corresponding values for (4.14), are uniformly high (in excess of 90%). 110

5.1 Percent Improvement, based on (5.10), with the averaged-bootstrap for the NPRM-based simulation results in Figure 5.7. Means and standard errors (SE) are shown. 127

5.2 Percent Improvement, based on (5.10), with the averaged-bootstrap for the 2C-based simulation results in Figure 5.8. Means and standard errors (SE) are shown. 129

5.3 Percent improvements averaged over simulation dimension and reconstructions, with the averaged-bootstrap with NPRM in Phantom I (general ground truth) and both NPRM and 2C-mapping in Phantom II (2C ground truth) simulations. Means and standard errors (SE) are shown. 130
5.4 Sample single 3.2 GHz processor Computation Times (in minutes) for Image-Domain Bootstrapping 130

6.1 Univariate and multivariate logistic and Cox proportional hazard analyses of potential variables associated with pathological complete response and disease-free survival in the UW-FDG trial. 140
6.2 Reconstruction RMSEs from dynamic and fixed bandwidth schemes at low, middle and high doses. Part (a) and (b) are divided by the ground truth and multiplied by 100. 143
6.3 Metabolic mapping RMSEs from dynamic and fixed bandwidth schemes at low, middle and high doses. First row is the true parameters, averaged over voxels. Part (a) and (b) are divided by the first row and multiplied by 100. 143

B.1 A brief table of Laplace transforms B8

I, Fengyun Gu, certify that this thesis is my own work and has not been submitted for another degree at University College Cork or elsewhere. All joint contributions, external references and sources are clearly acknowledged and identified within the contents. I have read and understood the regulations of University College Cork concerning plagiarism and intellectual property.



Fengyun Gu

To my incredible phd journey

Acknowledgements

First and foremost, I would like to express my sincere gratitude to my supervisors Prof. Finbarr O'Sullivan and Dr. Jian Huang for their unwavering support throughout my PhD study at UCC. I would like to thank Finbarr for his marvelous supervision and an endless supply of fascinating projects along the way. His patience, enthusiasm and insight have made this an inspiring experience for me. I am very proud of, and grateful for, my time working with him. I would also like to thank Jian for taking me on the boat and being continued to have faith in me over the years. Appreciation is extended to his participation in guiding, constructive feedback and advice for this research.

I would like to thank my internal examiner, Dr. Eric Wolsztynski and external examiner, Prof. Arman Rahmim at the University of British Columbia for their insightful comments and suggestions. In addition, I want to give my deepest thanks to Prof. Xianbing Cao for encouraging me to pursue this PhD degree and supporting me since I was an undergraduate at Beijing Technology and Business University. I would also like to thank Dr. Michael Cronin for teaching me many interesting courses in Statistics and for his kind help during school time.

My PhD career would not have been so well-rounded without the support of our international collaborators in the USA, Sweden, Switzerland and China. Many thanks to Prof. David A Mankoff at the University of Pennsylvania and Dr. Mark Muzi at the University of Washington for the multi-center clinical datasets, to Dr. Tian Mou and Prof. Yudi Pawitan for inviting me to visit Karolinska Institute, to Prof. Kuangyu Shi and Prof. Axel Rominger at Bern University Hospital for generously sharing the valuable datasets on Siemens Biograph Vision Quadra, to Prof. Yun Zhou for providing me an opportunity to do the internship in United Imaging Healthcare and guiding my research about the uEXPLORER Total-Body PET studies.

I am appreciative of everyone in the diagnostic imaging group and lab 2.11 WGB for the friendly, enjoyable and unique PhD experience, in particular, thanks to Dr. Zhaoyan Xiu for useful discussions in the early years and Qi Wu, my reliable colleague and close ally for spending too much time with me on many parts of the work. Much appreciation also goes to my dear family and friends in China, who endured this long process with me, for always being there for me, hearing my stories, cheering me up and boosting my productivity.

I acknowledge the financial support from School of Mathematical Sciences, Science Foundation Ireland, National Cancer Institute USA, Swedish Cancer Foundation and IEEE Foundation. Last but not least, a special thanks is given to my home country for recognizing my PhD work even before this thesis is formally done. It means a lot to me.

Abstract

Positron emission tomography (PET) scanning is an important diagnostic imaging technique used in the management of cancer patients and in medical research. It plays a key role in a variety of tasks related to diagnosis, therapy planning, prognosis and treatment monitoring by injecting a radiotracer to characterize the specific biologic process (e.g., tumor metabolism, proliferation or blood flow). The standardized uptake value (SUV) obtained at a single time point is widely employed in clinical practice. However, well beyond this simple static uptake measure, more detailed metabolic information may be recovered from dynamic PET scanning with multiple time frames. Assuming a tracer's interaction with the tissue is linear and time-invariant, the tissue time course can be expressed as a convolution between arterial input function (AIF) and the tissue impulse response/residue function. Kinetic analysis is concerned with the estimation of residue and associated physiological parameters such as flow, flux and volume of distribution. Some traditional methods including Patlak and compartmental modeling are well-established with a given form of residue function (constant or mixture of exponentials), but they are not flexible to represent data in which in-vivo biochemistry is not clear, especially for the whole-body imaging on the long axial field of view (LAFOV) PET systems.

The main goals of this thesis are to develop novel statistical approaches for improving and evaluating parametric imaging extracted from dynamic PET scans. The non-parametric residue mapping (NPRM) procedure has been constructed by a fully automatic process incorporating data-adaptive segmentation, non-parametric residue analysis of segment data and voxel-level kinetic mapping scheme. Based on this approach, the benefits of pooling data in multiple injection PET scans are investigated. Spatial and temporal patterns of residuals recovered by model diagnostics exhibit a non-Gaussian structure, which defines a bootstrap data generation process (DGP) in the image domain. The proposed bootstrap method has been used to assess the uncertainty (standard errors) in kinetic information and more complex regional summaries. We also examine its potential to improve the mean square error (MSE) characteristics of kinetic maps generated from either compartmental modeling or NPRM approach by averaging results from individual bootstrap samples. Dynamic breast cancer studies on the early, recent and latest LAFOV PET scanners are presented to illustrate these techniques. The performance of above models and schemes has been evaluated in a series of one and two-dimensional numerical simulations. Both direct filtered backprojection (FBP) and iterative maximum likelihood (ML) reconstructions are considered.

The proposed NPRM approach has some important features like the flexibility for diverse tissue environments and consideration of delays for different parts, which make it promising to be applied to the emerging total-body PET imaging. The developed image-domain bootstrap provides a practical way to quantify the uncertainties of biomarkers. This mechanism has the potential to further support clinical decision-making and enhance personalized medicine.

Chapter 1

Overview of Thesis

1.1 Introduction

In recent years, positron emission tomography (PET) has a wide range of clinical and research applications in oncology, cardiology and neurology (Hoh, 2007). It is a unique imaging modality that enables the measurements of a diverse range of functional and biological processes (e.g. tumor metabolism, proliferation, blood flow and receptor binding), depending on the radiotracer used (Pantel et al., 2022). Since the 1950's, there have been great advances with PET including the introduction of time-of-flight technologies, optimized detectors, new tracers, iterative reconstruction algorithms and novel quantitative methods by a variety of scientists in physics, engineering, chemistry and statistics, however, some constraints such as the limited axial coverage and temporal resolution still exist (Katal et al., 2022). The new-generation long axial field of view (LAFOV) PET scanners (e.g., uEXPLORER (Badawi et al., 2019), PennPET Explorer (Pantel et al., 2020) and Siemens Quadra (Alberts et al., 2021)) have been developed to overcome these limitations in the past few years. Their long axial field of view and ultra-high sensitivity can be exploited in various different ways to provide better image quality, reduce scan time, lower the injected dose and develop new drugs (Nadig et al., 2021). Next to all the exciting opportunities that arise with LAFOV PET systems, there remain some challenges like the analysis of large-scale data to be faced.

A number of issues within PET image reconstruction and post-processing (Figure 1.1) can be considered as statistical problems (Hudson, 1995), for example, the reconstruction process is basically to solve an inverse problem and the de-

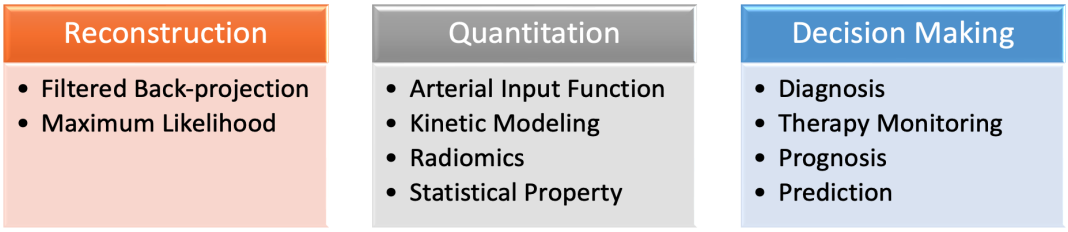


Figure 1.1: Overview of PET reconstruction and post-processing.

convolution model is also usually needed for kinetic analysis. PET imaging was brought to the attention of statistical community by the seminal work of Vardi, Sheep and Kaufman (Vardi, Shepp and Kaufman, 1985), who applied the maximum likelihood algorithm in the reconstruction procedure that leads to the current interest in the iterative method (Leahy and Qi, 2000). Similar to the PET reconstruction problem, there is a substantial role for innovation in the statistical methodology used in quantifying the dataset produced by dynamic PET scanning (Wang, Rahmim and Gunn, 2020), e.g. Markov chain for the extraction of input function (Huang and O'Sullivan, 2014), B-spline for the estimation of residue function (O'Sullivan et al., 2009; Chen, Goldsmith and Ogden, 2019) and Bootstrap for understanding the statistical property (Haynor and Woods, 1989; Dahlbom, 2001; Buvat, 2002; Ibaraki et al., 2014; O'Sullivan et al., 2021). The goal of improved individualized treatment also leads to an increasing need for prognostic or prediction biomarkers (Mankoff et al., 2019). These heavily rely on survival analysis (Laws et al., 2003; Dunnwald et al., 2008).

In this thesis, we provide a statistical perspective on dynamic PET reconstruction, quantitation and translation of the derived biomarkers to benefit clinical decisions. Our work mainly aims to generate more accurate parametric imaging and better understand their statistical characteristics. The end result would be more comprehensive information to clinicians for advancing diagnosis and therapy management in the era of precision medicine (Slart et al., 2021).

1.2 Main Contributions

The main contributions of this thesis are as follows:

- The feasibility of general quantitative methods including Patlak and compartmental modeling for total-body PET imaging is investigated and some

initial adaption schemes such as generalized Patlak analysis are suggested.

- Non-parametric Residue Mapping (NPRM) Technique
  - A non-parametric residue mapping procedure is proposed to generate parametric imaging and its performance is examined using different phantoms in which follow or not follow 2C assumptions.
  - The applicability of NPRM technique to dynamic PET scanning on the early, more recent and new-generation LAFOV PET scanners for breast cancer patients is assessed.
  - The benefits of pooling data from separate scans when mapping kinetics using NPRM approach in the multiple-injection PET scans are evaluated.
  - The generalization of NPRM to the preclinical whole-body animal study and other imaging modalities like digital subtraction angiography imaging.
- Image-Domain Bootstrap Technique
  - A novel image-domain bootstrap model without the reconstruction requirement is developed. This provides a practical mechanism to simulate 4D PET data efficiently.
  - The utilization of this procedure for evaluating uncertainties of kinetic mapping and regional summaries including maximum and coefficient of variation has been demonstrated.
  - The enhancement of mean square error characteristic of kinetic mapping by averaging results from image-domain bootstrap samples.
  - The integration of uncertainty information into clinical decision making procedure for individual patients.
- A dynamic bandwidth scheme applied in the reconstruction process is proposed to improve image quality and derived kinetic parameters.
- R programme to implement the above analysis has been developed.
- Several peer-reviewed journals and conference proceedings have been published and the ones relevant to this thesis are in section 1.3. The full publication and conference presentation list is in Appendix A.

1.3 Publications Related to Thesis

Related to Chapter 2

1. F Gu and Q Wu. "Quantitation of Dynamic Total-Body PET Imaging: Recent Developments and Future Perspectives". *European Journal of Nuclear Medicine and Molecular Imaging*, 2023. *Under Revision*.

Related to Chapter 3

2. F Gu, F O' Sullivan, M Muzi and D A Mankoff. "Quantitation of multiple injection dynamic PET scans: an investigation of the benefits of pooling data from separate scans when mapping kinetics". *Physics in Medicine & Biology*, 66(13), 2021.

Related to Chapter 4

3. F O' Sullivan, F Gu, Q Wu and L D O'Suilleabhain. "A Generalized Linear modeling approach to bootstrapping multi-frame PET image data". *Medical Image Analysis*, 72(102132), 2021.

4. F Gu, Q Wu and F O' Sullivan. "Image-domain bootstrapping of PET time-course data for assessment of uncertainty in complex regional summaries of mapped kinetics". *IEEE Nuclear Science Symposium and Medical Imaging (NSS& MIC) Records* 2021.

Related to Chapter 5

5. F Gu, F O' Sullivan and Q Wu. "Bootstrap averaging enhances the mean square error performance of kinetic maps recovered from PET data". *Under Review*.

Related to Chapter 6

6. F Gu, F O' Sullivan et al. "Evaluation of Blood Volume as a Prognostic Biomarker for Breast Cancer Patients and Associated Uncertainty via Image-Domain Bootstrapping". *Manuscript*.

7. F Gu and F O' Sullivan. "A simple adaptive bandwidth scheme that improves image quality and kinetic quantitation in dynamic PET scans". *Journal of Nuclear Medicine*, 62(Suppl. 1), p.1445, 2021.

8. F O' Sullivan, Q Wu, F Gu, K Shi, L O'Suilleabhain, S Xue and A Rominger. "Mapping FDG Tracer Kinetics and their Uncertainties via the Bootstrap using data from a Long-Axial FOV PET/CT Scanner". *Journal of Nuclear Medicine*, 63(Suppl. 2), p.3220, 2022.

1.4 Thesis Structure

This thesis is structured as follows:

Chapter 2 introduces general medical imaging tools, especially PET and its recent development in the ultra-high sensitivity and long axial field of view. Traditional methods of tracer kinetic analysis including compartmental modeling and Patlak analysis are reviewed and their limitations for whole-body PET imaging are also discussed. The chapter ends by identifying some areas where methodological developments are of interest.

Chapter 3 focuses on non-parametric residue mapping (NPRM) technique and its improvement relative to the two compartmental (2C) modeling is examined in different phantoms. The benefits of combined analysis using this approach for multi-tracer studies are evaluated. A combination of real data analysis, asymptotic theoretical calculation and numerical simulation, linked to flow-metabolism mismatch studies with ^{15}O-Water (H_2O) and ^{18}F-Fluorodeoxyglucose (FDG) for breast cancer patients, is presented in this chapter.

Chapter 4 develops an image-domain bootstrap model that gives the ability to efficiently simulate 4-D dynamic PET data. The utility of this approach to assess the uncertainty in kinetic information or complex regional summary is explored. Numerical experiments (using 1-D and 2-D models) are used to evaluate the accuracy of classic non-parametric projection-domain and novel image-domain bootstraps. These simulations are guided by experience with ^{18}F-Fluorothymidine (FLT) breast cancer study.

Chapter 5 considers the potential to improve the mean square error (MSE) of kinetic maps by averaging results from individual bootstrap samples. This scenario is motivated by the generalization of regression tree models by such an averaging process. A series of simulation studies are implemented to examine the performance of proposed scheme in both 2C and NPRM frameworks.

Chapter 6 summarizes the findings of the work and points to the possibility of these techniques for supporting clinical decision-making and other settings in which dynamic tracer imaging is used - either in clinical practice or research (including preclinical animal and whole-body human), also discusses the perspectives for future work.

Chapter 2

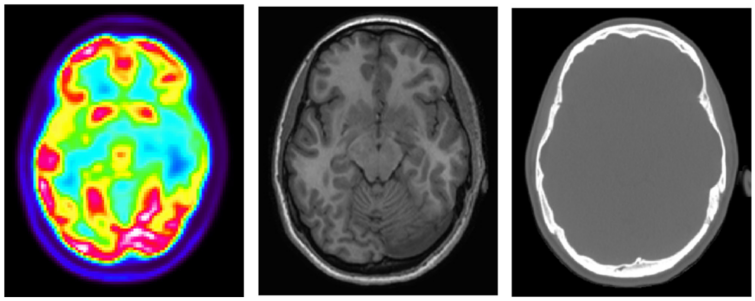
Background

2.1 Medical Imaging

Medical imaging has been a significant contributor over the process of modern medicine by offering anatomical and functional details of the human body for diverse diagnostic and therapeutic purposes. The true start of medical imaging, as we consider it today was in 1895 when Röntgen discovered the X-ray, a form of electromagnetic radiation (Röntgen, 1899). Since then, it has been an important tool in clinical practice. To create a radiograph, a patient is positioned between the X-ray source and detector so that the specific areas of the body can be imaged. Depending on the radiological density, each tissue absorbs different amounts of X-rays, then produces the "shadows" on the two-dimensional (2D) image. Dense materials such as bone appear whiter since they readily absorb X-rays. Conversely, X-rays travel more easily through fat, muscle and lungs, and thus, these structures are displayed in shades of gray. Due to its low cost and high efficiency, X-ray imaging has been extensively used in the detection of bone fractures, certain tumors as well as lung infections. But it still has some weaknesses such as limited image resolution, exposure to ionizing radiation and overlooked lesions in the overlapping part among tissues (Ou et al., 2021).

X-ray modalities can also be further extended to higher spatial or temporal dimensions. For example, computed tomography (CT) provides a more complete characterization of the human body through three-dimensional (3D) depictions and the temporal extension of 2D radiographs such as digital subtraction angiography (DSA) reveals functional information for a multiplicity of needs (e.g. vascular, cardiac and surgery) (Samei and Peck, 2019). In contrast to X-ray

imaging, nuclear medicine imaging modalities including planar, single-photon emission computed tomography (SPECT) and positron emission tomography (PET) are based on extracting energy (in the form of gamma rays) emitted from the body. Target-specific radioactive pharmaceuticals are injected into patients and imaged to reflect information about the physiological processes. Without the use of any (ionizing) radiation, magnetic resonance (MR) imaging harnesses the radio waves and magnetic properties of the human body to create detailed images of nearly every structure and organ, see the example in Figure 2.1 which shows PET, MR and CT images for the same patient. MR has become an exciting modality as it can achieve superior resolution, and is capable of yielding physiological information. As discussed above, modern imaging techniques using different types of energy sources (e.g., X-ray, gamma ray and radio waves) have various characteristics and applications, meeting specific requirements in different medical disciplines.



(a) PET (b) MRI (c) CT

Figure 2.1: Reconstructions of data acquired by PET, MRI and CT of the same patient (Ehrhardt et al., 2014).

Although PET is the focus of this thesis, it is not used in isolation. As PET images do not provide anatomical information, they are usually combined with co-registered anatomical data from other modalities, such as CT and MR. DSA and functional MR images (fMRI) have the similar data structure (e.g. temporal sequence) as dynamic PET and therefore the developed techniques in this thesis also have the potential to be adapted for these images. In this section, we give an introduction to the relevant medical imaging procedures including CT and MR. More details about PET will be presented in the next section.

2.1.1 Computed Tomography

The CT scanner was invented by Hounsfield (Hounsfield, 1973) and Cormack (Cormack, 1980). Both of them were jointly awarded the 1979 Nobel Prize.

CT uses X-ray to create valuable three-dimensional views of the organ/tissue of interest and eliminate the overlapping structures to make the anatomy more apparent (clear shape, size, density, and texture). Therefore, it is very remarkable to generate a dramatic increase in diagnostic information and preferred to conduct in several areas from emergency medicine to disease diagnosis such as liver, pancreatic and lung cancers (Seeram, 2015).

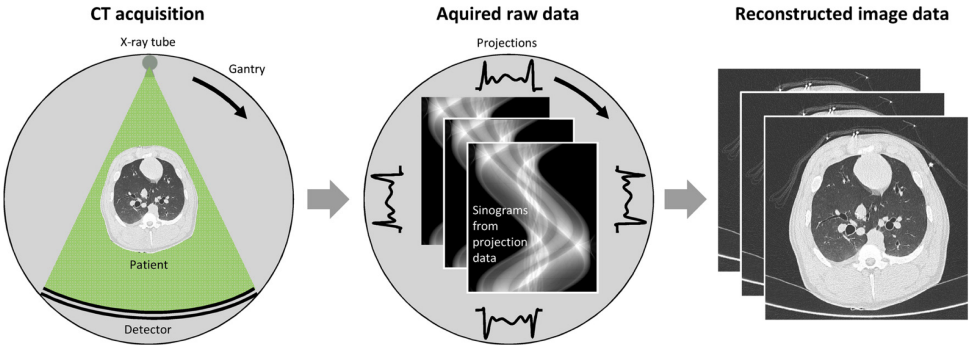


Figure 2.2: Simplified schematic of the computed tomography (CT) imaging process (Stiller, 2018).

To better understand the nature of CT, the scanning procedure is illustrated in Figure 2.2 and described as follows. X-rays are attenuated when they pass through tissues and anatomical structures in the body and subsequently measured by the detectors. The gantry of the CT scanner including the X-ray tube and detectors rotates around the patient during scanning so that attenuation profiles are acquired from different angles (views) making up the projection. By sorting projections, raw data (sinograms) can be derived, which is necessary for the reconstruction of transverse image by means of mathematical algorithms, e.g., filtered back projection (FBP) or maximum likelihood (ML) (Natterer, 2001). Finally, all images are combined with detailed cross sectional areas inside the body to present a 3D view with the overlying structures removed (Stiller, 2018).

In general, CT has the advantage of short study time with high quality images. However, it still has substantial limitations and drawbacks. For example, only anatomic information can be provided and it may be erroneous or incomplete to differentiate between pathologic and healthy tissues in some cases (e.g., small lesions) due to low inherent contrast (Davis et al., 1976). In clinical imaging, sometimes the (iodinated) contrast agents are administrated to address this issue, but they may cause kidney damage and trigger allergic reactions (Willemink et al., 2018). The exposure of patients to ionizing radiation is an-

other concern (Brenner and Hall, 2007; Fred, 2004). Some studies have found an increased risk of radiation-induced cancers in younger patients, particularly with serial examinations (Mehrotra, 2016; Zondervan et al., 2013). Although radiation doses can be reduced, it may lead to further problems such as image noise and artifacts. Thus, the appropriate and safe application of CT to obtain enough diagnostic information with the lowest possible dose of radiation is quite important (Kalra, Sodickson and Mayo-Smith, 2015).

2.1.2 Magnetic Resonance Imaging

Magnetic Resonance Imaging (MRI) (e.g., structural MRI and functional MRI) is a powerful modality that provides exquisite anatomical details or perfusion information without the exposure of patients to radiation during the examination. In this section, we give a brief overview of the history of MRI, and then discuss its specific physical principles and characteristics.

The observation of phenomenon of nuclear magnetic resonance (NMR) (Bloch, 1946; Purcell, Torrey and Pound, 1946) directly stimulated creation of the first biological MR images in 1973 (Lauterbur, 1973). By the 1980s, MRI became clinically prevalent, especially in the structural scanning of the brain. In early 1990, the discovery that changes in blood oxygenation could be measured using MRI ushered in a new era of functional studies (Ogawa et al., 1990). Since then, functional MRI (fMRI) has greatly progressed and recent advances in technologies are reviewed in (Bollmann and Barth, 2021).

2.1.2.1 Structural MRI

MRI relies on signals derived from water molecules, which comprise around 70% of the average human body. During the imaging procedure, the strong magnetic field created by the MRI scanner causes the hydrogen protons of water in the body to align in the same direction. Radio waves/frequency (RF) pulse towards specific spots are then sent from the MRI machine and move ("excite") these atoms out of the original position. When the RF pulse is turned off, the hydrogen protons slowly return ("relax") to their natural alignment within the magnetic field and release the energy absorbed from the RF pulses. The collected radio signals (high and low frequency) form a frequency domain space, called "K" space. Tissue can be characterized by different relaxation times – T1 and T2. T1 (longitudinal relaxation time) and T2 (transverse relaxation time) are the time constants that determine the rate at which excited protons

return to and reach equilibrium, respectively. T2* is "observed" transverse relaxation (T2*<T2<T1). The Fourier transform (FT) algorithm uses the data in K space to reconstruct magnetic resonance images and finally 3D visualization can be performed (Haidekker, 2013; Berger, 2002). These basic principles are depicted graphically in Figure 2.3.

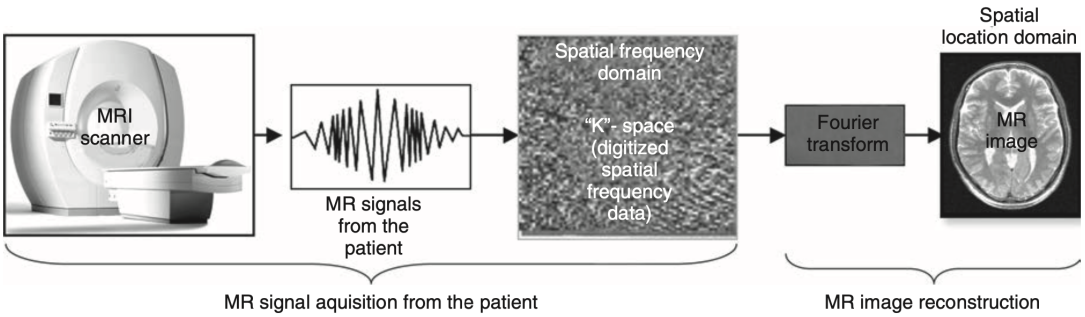


Figure 2.3: The process of magnetic resonance imaging (MRI) signal acquisition to image display (Seeram, 2015).

Due to the unique physics, MRI has been considered as a superior modality to other imaging techniques such as plain X-ray and CT and it is particularly useful for the detection of abnormalities in soft tissues (e.g.,ligaments and cartilage), organs (e.g., brain, heart and eyes) and blood vessels. More importantly, this scanning does not involve any kind of radiation, so it is safe for certain patients such as pregnant women or babies (Oldendorf, 1988). But MRI has the drawback of longer acquisition time, leading to high examination costs and reduced patient comfort (Neumayer et al., 2018).

2.1.2.2 Functional MRI - DSC/DCE

The changes to the magnitude and phase of the MR signal with time can be used to provide the physiological quantity of interest such as perfusion. Two techniques are generally used to measure perfusion using MRI: dynamic susceptibility contrast (DSC) and dynamic contrast enhanced (DCE) (Huettel et al., 2004). Both of them require intravenous bolus administration of gadolinium and will be briefly described below.

Dynamic Susceptibility Contrast MRI DSC MR perfusion imaging begins with the injection of a bolus of gadolinium-containing contrast and then rapid repeated imaging of the organ of interest is performed during the first pass.

These lead to a series of T2 or T2*-weighted MR images. After image acquisition, various parameters (e.g., blood volume, blood flow, mean transit time) can be extracted from the measured signal intensity time course (Jahng et al., 2014). As DSC imaging depends only on the first pass of the contrast agent, it is sometimes known as bolus tracking MRI and mostly used for brain (stroke/tumors) and heart (ischemia).

Dynamic Contrast Enhanced MRI Like DSC-MRI, DCE imaging also requires the administration of a gadolinium-based contrast agent. The repeated T1-weighted images over an approximately five to ten minute interval are acquired by exploiting the T1 shortening effects of gadolinium. The image data can be analyzed visually or semi-quantitatively. Physiological parameters such as transfer constant (K_{trans}) and fractional plasma volume (V_p) can also be obtained. This approach has mainly been applied in studies of the myocardium, brain and oncological research (Gordon et al., 2014).

2.2 Positron Emission Tomography

Positron emission tomography, also referred to as PET imaging or a PET scan, is a type of nuclear medicine technique that produces 3D images of the distribution of an administered radiopharmaceutical (radiotracer) within the body (Haidekker, 2013). Unlike other modalities, these images enable the evaluation of biological phenomena including glucose metabolism, cerebral blood flow and receptor sites in the brain, instead of showing anatomy and structure (Wacholtz, 2011). In this section, we will focus on the recent development, fundamental principles and performance characteristics of this fantastic technique.

2.2.1 Development of PET Scanners

The development of PET scanners spans over 70 years (1950 $\sim$ 2020s) and many outstanding physicists, chemists, biologists and mathematicians/statisticians made great contributions to the progression of this technology (Rich, 1997; Nutt, 2002; Wacholtz, 2011; Jones and Townsend, 2017; Vandenberghe, Moskal and Karp, 2020). Technical advances in various aspects are reviewed via the timeline from a historical perspective.

1950∼1960s: Pioneering Ideas for PET The ideas for PET could date back to the 1950s. Two initial reports of medical applications for the positron were published independently in 1951 (Wrenn Jr, Good and Handler, 1951; Sweet, 1951). Later on Brownell and Sweet created a precursor of PET scanner to record the annihilation for localizing brain tumors (Sweet, 1953). In the early 1960s, Kuhl and Edwards were the earliest pioneers to study the image reconstruction algorithms for single photon tomography (Kuhl and Edwards, 1963), but it was Chesler's filtered backprojection technique ultimately applied to the PET (Chesler, 1971, 1973; Chesler, Hoop and Brownell, 1973).

1970s: Beginning of Modern PET During this period, instrumentation and radiochemistry have been developed rapidly. In 1973, Phelps built the first PET tomography, known as positron emission transaxial tomography (PETT I) and later reduced the name to PET. However, this attempt is not successful mainly due to the limited sampling and lack of attenuation correction (Nutt, 2002). To address these physical issues and ensure image quality, Phelps, Ter-Pogossian and Hoffman et al. continued to create the PET II and clinically applicable PET III for animal and human studies at Washington University (Phelps et al., 1975; Ter-Pogossian et al., 1975; Phelps et al., 1976; Hoffman et al., 1976). The first published human images of blood blow oxygen and glucose metabolism and bone scans are generated from PET III, which consisted of 48 NaI (TI) detectors placed in a hexagonal array with eight detectors on a side and data were reconstructed using FBP algorithm (Phelps et al., 1976; Hoffman et al., 1976). Following the PET III development, the first commercial scanner - Emission Computed Axial Tomography (ECAT) was designed and delivered to University of California, Los Angeles (UCLA) in 1976.

Another development that contributed to the emergence of PET is the detector that determines sensitivity, image resolution etc. Cho et al. developed a system with a single ring of NaI (TI) detectors (Cho, Chan and Eriksson, 1976) and eventually expanded to multiple rings with more efficient crystal, bismuth germanium oxide (BGO) (Cho and Farukhi, 1977). The other development includes biosynthesis of the first fluorodeoxyglucose (FDG) by Wolf and Flowler's group (Ido et al., 1978) that laid the groundwork for more in-depth PET studies. The first PET imaging with FDG was performed and the cerebral glucose metabolic rate was subsequently measured by Phelps et al. (Phelps et al., 1979; Reivich et al., 1979).

1980∼1990s: Advancements in the Research and Clinical Sectors The progressions of PET in the research and clinical sectors have been associated with several aspects including further improved detectors, better image reconstruction algorithms and commercialization.

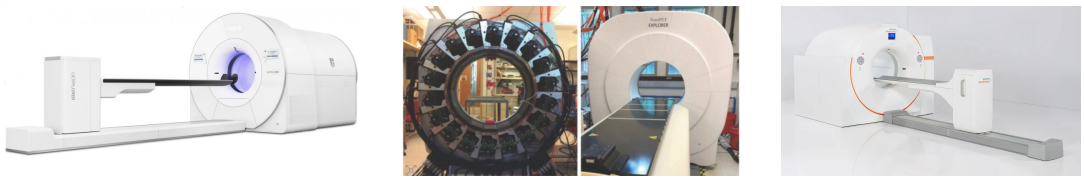
(i) The block detector concept pioneered by Casey and Nutt (Casey and Nutt, 1986) was composed of four photomultipliers coupled to a 2D array of crystal elements. This invention led to high resolution and efficient PET tomographs at a much-reduced cost (Nutt, 2002). Moreover, a new detector material - Lutetium Oxyorthosilicate (LSO) was discovered (Melcher and Schweitzer, 1992) and fabricated for PET by Cherry et al. of UCLA (Cherry et al., 1997). The performance of LSO results in a combination of speed and light output improvement of 37.5 over BGO (Nutt, 2002). The derivation of LSO incorporating a small percentage of yttrium - LYSO was also introduced which benefits the development of time-of-flight (TOF) PET imaging (Jones and Townsend, 2017).

(ii) The iterative reconstruction approach based on maximum likelihood was proposed by Dempster et al. (Dempster, Laird and Rubin, 1977) and subsequently applied to PET by Shepp et al. (Shepp and Vardi, 1982; Lange, Carson et al., 1984; Vardi, Shepp and Kaufman, 1985). Considering the computational efficiency, an accelerated version - ordered subset expectation maximization (OSEM) was developed by Hudson and Larkin (Hudson and Larkin, 1994) and made it a practical alternative to FBP algorithm. The OSEM technique provides the foundation for today's most popular reconstruction methods.

(iii) Two major imaging companies, i.e., General Electric (GE) and Siemens entered into PET industry in the late 1980s and served to validate this technology for clinical applications, no longer limited to research. Thus, the 1990s marked the start of PET as a clinical service (Nutt, 2002). In 1991, the first whole-body PET scan was obtained by a multi-bed protocol (Dahlbom et al., 1992) to detect primary and metastatic diseases simultaneously. The introduction of whole-body concept expands PET as a weapon against cancer and further stimulates researchers' interest in axial coverage extension (Jones and Townsend, 2017; Vandenberghe, Moskal and Karp, 2020).

2000s: PET/CT Scanner The PET/CT scanner, designed by Townsend and Nutt, was featured in Time as the medical invention of the year in 2000. Computer software was developed and applied to combine anatomic information from CT with functional imaging from PET into one efficient device. Thus, PET/CT scanner is able to produce superior fused images that are particularly helpful for early diagnosis, tumor detection, precise localization and assessment of patient response to therapy. Furthermore, fast and low noise attenuation correction from CT also speeds up PET scanning, which makes the examination more convenient and comfortable for patients (Wacholtz, 2011; Jones and Townsend, 2017).

2010∼2020s: Long Axial Field of View PET Scanner The conventional PET/CT systems generally have a short field of view (FOV) of about 15∼30cm and typically only a special organ (e.g., brain) is imaged. Whole-body scanning can also be implemented by adopting a multiple bed scenario, but it is very time-consuming. Recently, the new-generation PET scanners (see Figure 2.4) - the uEXPLORER (United Imaging Healthcare & UC Davis) (Badawi et al., 2019), the PennPET Explorer (University of Pennsylvania) (Karp et al., 2020) and the Biograph Vision Quadra (Siemens Healthineers) (Prenosil et al., 2022) have achieved long axial field of view (LAFOV) between 64 and 194cm. Their characteristics are summarized in Table 2.4.



A. uEXPLORER
United Imaging Healthcare

B. PennPET Explorer
University of Pennsylvania

C. Biograph Vision Quadra
Siemens

Figure 2.4: New-generation long axial field of view (LAFOV) PET systems. A. uEXPLORER (United imaging Healthcare)[1]; B. Penn PET Explorer (University of Pennsylvania)[2]; C. Biography Vision Quadra (Siemens)[3].

These state-of-the-art scanners show a tremendous increase in system sensitivity

[1]URL: https://usa.united-imaging.com/products/molecular-imaging/uexplorer/
[2]URL: https://www.med.upenn.edu/pennpetexplorer/
[3]URL: https://www.siemens-healthineers.com/molecular-imaging/pet-ct/biograph-vision-quadra

and allow the simultaneous imaging of all of the main organs in the body using the single-bed position, providing numerous opportunities to improve clinical workflow and patients' comfort (e.g., reduction of scanning time and administration of low-dose tracer) and also explore new applications (e.g., development of new tracers and drugs) (Jones and Townsend, 2017; Vandenberghe, Moskal and Karp, 2020; Pantel, Mankoff and Karp, 2022).

Table 2.1: Overview on existing long axial field of view commercial and research systems (Nadig et al., 2021; Zhang et al., 2020; Viswanath, 2020; Sari et al., 2022).

	uEXPLORER	**PennPET Explorer**	**Quadra**
Year developed	2019	2020	2020
Company/University	United Imaging Healthcare	University of Pennsylvania	Siemens Healthineers
First installed	Zhongshan Hospital	as above	Bern University Hospital
Purpose	Commercial	Research	Commercial
Scintillators	LYSO (18.1 mm)	LYSO (19 mm)	LSO (20 mm)
Axial field of view (cm)	194	64,140	106
Spatial resolution (mm)	2.9	4.0	3.4
Sensitivity (kcps/MBq)	174	55	174
Image matrix	192×192×672	144×144×160	440×440×645
Time frames	90∼ 200	70	62

2.2.2 Radiotracer

PET imaging usually requires the use of radiotracer/radiopharmaceutical, which is injected into the body, swallowed, or inhaled as a gas. The administrated tracer enables to target different cancer biomarkers (e.g., enzymes, receptors and transporters) or biological processes (e.g., energy metabolism and hypoxia) (Lau et al., 2020). Generally it is a molecule containing the natural substrate (e.g., glucose) that is labeled with a positron-emitting radioisotope. The commonly used radioisotopes include Fluorine-18 (^{18}F), Oxygen-15 (^{15}O), Carbon-11(^{11}C) and Nitrogen-13 (^{13}N) (Miller et al., 2008) and they can be transformed into many PET radiotracers, see the list in Table 2.2. Fluorine-18 labeled Fluorodeoxyglucose (^{18}F-FDG) provides, without question, the widest range of applications in oncology, neurology and cardiology (Wacholtz, 2011). The mechanism of uptake and metabolism of FDG will be introduced in detail as follows.

Fluorodeoxyglucose (FDG) Glucose ($C_6H_{12}O_6$) is an essential source of energy in all organisms. FDG ($C_6H_{11}{}^{18}FO_5$) is an analog of glucose where one hydroxyl group (an oxygen atom bonded to a hydrogen atom - OH) is replaced with an atom of ^{18}F (Kobayashi et al., 2012). Both glucose and FDG are transported into cells by glucose transporter (GLUT) membrane proteins

Table 2.2: The commonly used radiotracers and their targeted processes in PET.

Radioisotope	Half-life (min)	Radiotracer	Biological Process/Target
^{18}F	109.8	FDG	glucose metabolism
		FLT	cell proliferation
		PSMA	PSMA protein
^{15}O	2.04	H_2O	blood flow
^{11}C	20.4	Acetate	myocardial oxidative metabolism
		Verapamil	P-gp Activity
^{13}N	9.97	Ammonia	myocardial blood flow

FLT: fluorothymidine; PSMA: prostate-specific membrane antigen; P-gp: P-glycoprotein

and phosphorylated by hexokinase. Dephosphorylation may occur by glucose-6-phosphatase (G-6-phosphatase) in some cells. Phosphorylated glucose (G-6-phosphate) is available to be further metabolized by glycolysis, whereas FDG-6-phosphate cannot and is therefore considered as "metabolic trapping" (Rudd et al., 2010). The whole process is illustrated in Figure 2.5.

Understanding these biochemical pathways is critical for PET image interpretation. Typically, the active tumor has a higher rate of glycolysis, which is exhibited as the high phosphorylation of FDG, resulting in increased metabolic trapping and consequently signal enhancement on the PET images (Muzi et al., 2012). Thus, the FDG-PET scan is very useful for diagnosis, staging and recurrence detection of various cancers.

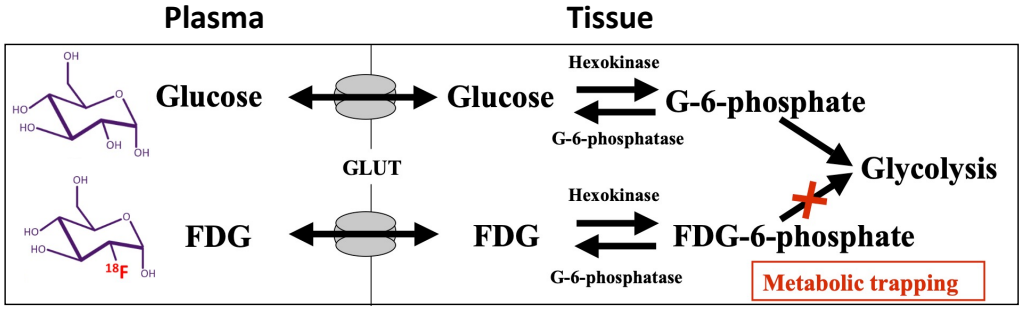


Figure 2.5: Glucose and FDG cellular uptake and metabolism (Trinder et al., 2020; Rudd et al., 2010). GLUT: glucose transporter.

2.2.3 Scanning Procedure

Figure 2.6 shows an overview of the PET scanning procedure involving the positron emission, detection of gamma rays, the form of projection view and ultimately image reconstruction. We begin with PET physics and review reconstruction algorithms in this section.

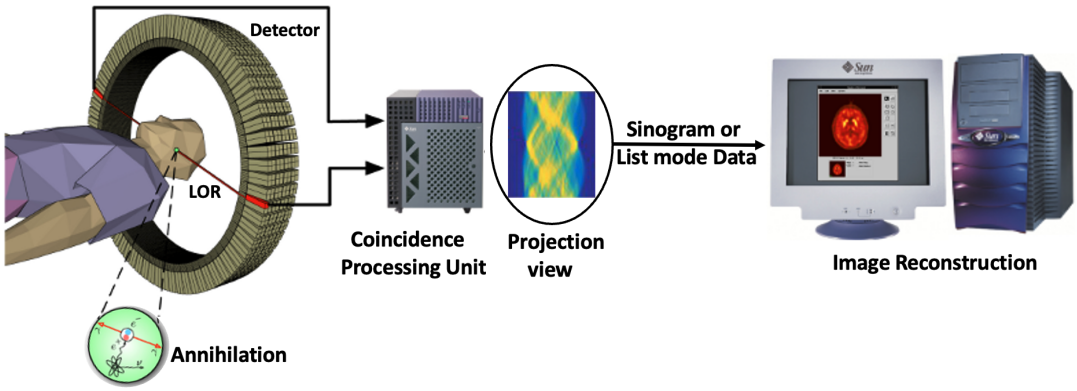


Figure 2.6: Schematic of PET scanning process.[4]

2.2.3.1 The Physics of PET

During the PET scanning, the patient is positioned on a flat bed and surrounded by detectors once the radiotracer is administered. After a certain amount of time, the radioactive tracer arrives at the targeted tissues/organs. Since the radioisotopes in the tracer are not stable, they may decay through positron emission. Essentially, *radioactive decay* is a proton (p) in the nucleus of the atom converted into a neutron (n), a positron (e^+) and an undetectable neutrino (v) with release of energy. The generated positrons then travel to annihilate with a nearby electron (e^-) and produce two high energy (511 KeV) photons in the form of gamma rays (γ) moving away from each other in opposite directions (approximately 180 degrees). A coincidence event is registered if an *annihilation* occurred somewhere along the line of response (LOR) are detected within a fixed time window (e.g., 6∼12 ns) (Fahey, 2002; Schmitz et al., 2005; Zaidi, 2006).

Raw data, which consists of the recorded events, are acquired directly into a *sinogram* in a 2-D matrix. Each row represents parallel line integrals or a projection of the activity at a particular angle ϕ and each column represents the radial offset (r) from the center of the scanner (Cherry and Dahlbom, 2006). As indicated in Figure 2.7, their relationship with the original coordinates (x, y) is given by:

$$r = xcos\phi + ysin\phi \tag{2.1}$$

[4]URL: https://en.wikipedia.org/wiki/Positron_emission_tomography#/media/File:PET-schema.png

For each coincidence event detection, the corresponding pixel (r, ϕ) in the sinogram is determined, and a count is added to the pixel. Thus, the total counts in each pixel represent the number of coincidence events detected during the counting time along an LOR. Each sinogram represents the data for a slice across all angles and a series of projection views can be generated from sinograms from multiple slices. The data can be written in either frame mode or list mode in the sorting hardware. In the frame mode, the events are integrated over a time interval that must be defined prior to data acquisition. Conversely, the list mode data are binned into specific time intervals after the completion of study, which is advantageous for dynamic scans. While the frame mode is routinely used, the list mode is being more widely used for the newer PET scanners now (Saha, 2015).

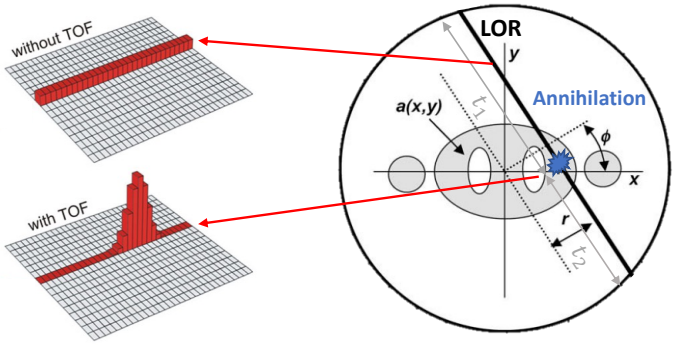


Figure 2.7: Principles of conventional and time of flight (TOF) PET scanners (Lecoq and Gundacker, 2021) and the relationship between the (x, y) coordinate system of the object and the (r, ϕ) coordinate system in which PET data are commonly stored (Cherry and Dahlbom, 2006).

However, this data acquisition process is not perfect and many factors need to be corrected. For example, attenuation of annihilation photons occurs due to absorption and scatter may cause uneven distribution of counts over different organs or tissues, therefore, attenuation correction must be applied before image reconstruction. Another issue is, not only true coincidences, some background events (e.g., scattered, randoms and multiples) that not arise from the same annihilation event or lie on the same line can also be detected. These backgrounds need to be removed or minimized. The recent development of scintillators (i.e. LYSO) and detector electronics with improved time resolution and stability has made it possible to apply the time-of-flight (TOF) technique to the conventional PET, which leads to the increased sensitivity and signal-to-noise ratio. The concept of TOF-PET scanner is illustrated in Figure 2.7. The

location of an annihilation pair is determined by the detection of the time-of-flight difference ($\Delta t = t_1 - t_2$) between the two photons. Therefore, the distribution of annihilation positions is not uniform (Vandenberghe et al., 2016; Jiang, Chalich and Deen, 2019).

2.2.3.2 Image Reconstruction

After the acquisition of PET projection data, the distribution of the administrated radiotracer is reconstructed through mathematical algorithms. The reconstruction process involves the solution of an inverse problem with the Radon-type transform. Over the past four decades, many efforts have been devoted to the development of PET image reconstruction methods, either analytic or iterative. The analytic approach typically yields explicit formulas for the reconstruction problem and produces a practical solution to compute, such as the standard filtered backprojection (FBP) based on least squares. Iterative reconstruction has no implicit equation and uses the maximum likelihood estimation to find the more accurate image. This section provides a basic introduction to both methods.

Filtered Backprojection (FBP) Filtered Backprojection method assumes that the PET data is noise-free and attempts to reconstruct images from the known projections by the inverse Radon transform (Chesler, 1973). The basic flowchart for FBP reconstruction is presented in Figure 2.8.

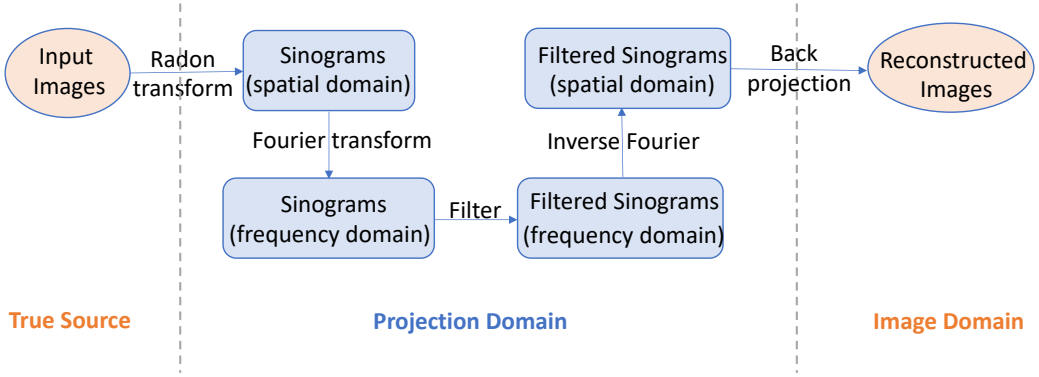


Figure 2.8: Diagram of the filtered backprojection (FBP) reconstruction.

The imaging process (forward projection) is formulated simply as:

$$\boldsymbol{p} = \mathcal{R}\boldsymbol{f} \tag{2.2}$$

If $\boldsymbol{f}$ is a discrete representation of the continuous 2D or 3D object, then its Radon transform ($\mathcal{R}$) represents the projection data ($\boldsymbol{p}$).

As in (2.3), the implementation of FBP involves serval steps: (i) convert projection data from the spatial domain to the frequency domain by *Fourier transform* ($\mathcal{F}$); (ii) apply a filter ($\boldsymbol{H}$) in the frequency domain; (iii) take inverse Fourier transform ($\mathcal{F}^{-1}$) of filtered frequency projection; (iv) backproject the filtered projection by inverse Radon transform ($\mathcal{R}^{-1}$) to reconstruct images ($\hat{\boldsymbol{f}}$) (O'Sullivan, 1995; Wernick and Aarsvold, 2004; Cherry and Dahlbom, 2006; Tong, Alessio and Kinahan, 2010; Saha, 2015). For more mathematical descriptions of Random and Fourier transform, see Appendix B.1.

$$\boldsymbol{P} = \mathcal{F}\boldsymbol{p}, \quad \boldsymbol{P'} = \boldsymbol{H}\boldsymbol{P}, \quad \boldsymbol{p'} = \mathcal{F}^{-1}\boldsymbol{P'}, \quad \hat{\boldsymbol{f}} = \mathcal{R}^{-1}\boldsymbol{p'} \tag{2.3}$$

where $\boldsymbol{P}$ is the Fourier transform of $\boldsymbol{p}$ and similarly $\boldsymbol{p}$ is the inverse Fourier transform of $\boldsymbol{P}$.

A number of Fourier filters have been designed and used in the frequency domain to improve image quality. In practice, the typical projection view tends to have high amplitudes at low frequencies and low amplitudes at high frequencies. Filter plays a role to attenuate or remove high frequencies and enhance the signal-to-noise, however, it is also at the expense of degrading image resolution. Ramp filter is a commonly used "high-pass" filter, but it usually amplifies the noise associated with high frequencies. To eliminate the high-frequency noise, some "low-pass" filters such as Hanning, Hamming and Shepp-Logan filters have been developed (Cherry and Dahlbom, 2006; Saha, 2015). If images still appear noisy after reconstruction, they may be further smoothed using the spatial filters (e.g., Gaussian and non local mean) in the image domain (Schmitz et al., 2005; Dutta, Leahy and Li, 2013; Arabi and Zaidi, 2021).

The main advantage of FBP is its computational efficiency, but the reconstruction accuracy is limited by several aspects. First, this method does not apply positive constraints leading to negative artifacts. Second, FBP model (2.2) cannot describe the real data precisely and many physical factors such as intercrystal scatter, positron range and noncollinearity are ignored (Cherry and Dahlbom, 2006; Tong, Alessio and Kinahan, 2010).

Iterative Reconstruction The alternative approach to image reconstruction is the use of iterative techniques, which determine the "best" estimate of im-

ages based on the measured projections. Rather than assuming a Radon form (2.2), a more complex model encompassing underlying physics and data noise is employed and given by (2.4),

$$\boldsymbol{p} = \boldsymbol{M}\boldsymbol{f}, \quad \boldsymbol{M} = \boldsymbol{M}_{sensitivity}\boldsymbol{M}_{blur}\boldsymbol{M}_{attenuation}\boldsymbol{M}_{geometry}\boldsymbol{M}_{positron} \tag{2.4}$$

where the matrix $\boldsymbol{M}$ contains a few components of the imaging process such as sensitivity, detector blurring, attenuation, geometric factor and positron range.

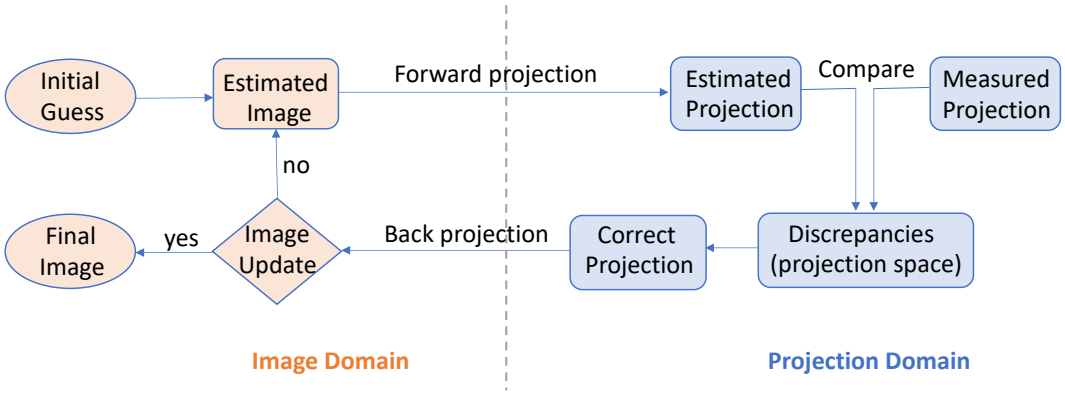


Figure 2.9: The general structure of iterative image reconstruction.

The basic idea behind iterative reconstruction algorithms is summarized in Figure 2.9. It begins with an initial guess made of the image distribution (e.g., a uniform grayscale image), then the estimated projection is calculated by forward projecting the initial image. Based on the discrepancies between estimated and measured projections, a correction is applied to the current projection. All corrected projections are backprojected to update image, which is used as the estimated image for the next iteration. This "forward project, compare, backproject, adjust" process would be repeated until the image reaches a certain criterion (Saha, 2015; Tong, Alessio and Kinahan, 2010). There are two key parts for all iterative approaches, (i) the definition of the optimization criterion, which is represented as an objective or cost function; (ii) the numerical algorithm to determine how to update image (Cherry and Dahlbom, 2006). Historically, many efforts have concentrated on these two parts developing iterative techniques (Iriarte et al., 2016) and the most widely used approaches are based on maximum likelihood (ML) methods (Rockmore and Macovski, 1976).

The expectation-maximization (EM) algorithm is commonly used to find the maximum likelihood estimate (MLE) (Dempster, Laird and Rubin, 1977) under

a Possion data model. This approach considers the statistical noise and assures non-negative by implicitly treating the projection data as a Poisson distribution. Subsequently, the maximum likelihood expectation maximization (ML-EM) method, adopting ML as the optimization criterion and using the EM algorithm to update image, is introduced to PET reconstruction by Shepp et al. (Shepp and Vardi, 1982; Lange, Carson et al., 1984; Vardi, Shepp and Kaufman, 1985). The ML-EM algorithm has a simple form consistent with the general structure of iterative approaches (Figure 2.9). Suppose $\hat{f}_j^{(n+1)}$ is the image estimate for voxel j at iteration n, it can be written as:

$$\hat{f}_j^{(n+1)} = \frac{\hat{f}_j^{(n)}}{\sum_{i'} M_{i'j}} \sum_i M_{ij} \frac{p_i}{\sum_k M_{ik} \hat{f}_k^{(n)}} \tag{2.5}$$

In this case, the multiplicative update by the ratio of measured over estimated projections guarantees non-negative values and predictable convergence behavior. While ML-EM has many attractive properties, this algorithm still has some shortcomings. The main limitation is the lengthy computation time. Due to the slow convergence, one solution may require 30 to 50 iterations where each iteration involving forward and back projection steps takes approximately double time as long as FBP reconstruction. Thus, the required time is indeed considerable and hampers its application in clinical use. Another drawback is the ML criterion may generate noisy reconstructed images and often some post-processing smoothing is applied to reduce overall noise levels (Wernick and Aarsvold, 2004; Zaidi, 2006).

To address the issue of slow convergence, an ordered subset expectation maximization (OSEM) technique has been proposed by Hudson and Larkin (Hudson and Larkin, 1994) to accelerate ML-EM and become the most widely used iterative reconstruction method as a practical alternative to FBP algorithm. The OSEM method is a simple modification of the ML-EM algorithm (2.5) and the update equation is reformulated as (2.6) to increase the magnitude of change at each iteration.

$$\hat{f}_j^{(n,b)} = \frac{\hat{f}_j^{(n,b-1)}}{\sum_{i' \in S_b} M_{i'j}} \sum_{i \in S_b} M_{ij} \frac{p_i}{\sum_k M_{ik} \hat{f}_k^{(n,b-1)}} \tag{2.6}$$

This approach partitions the full set of projections into B mutually exclusive subsets and uses only one subset (S_b) for each update, termed as one *subiteration* (b). The processing time for one iteration, which passes through all of the

subset data, is roughly equivalent to that of one iteration of ML-EM. A greater number of updates in each iteration, leads to significant acceleration, usually on the order of the number of subsets. OSEM algorithm has similar characteristics as ML-EM, but with substantial speed improvement. It is also important to note that OSEM does not have a general proof of convergence and image noise is increased with the number of subsets. So an appropriate partition is required and 8∼10 subsets are possible with little increase in noise (Leahy and Qi, 2000; Wernick and Aarsvold, 2004).

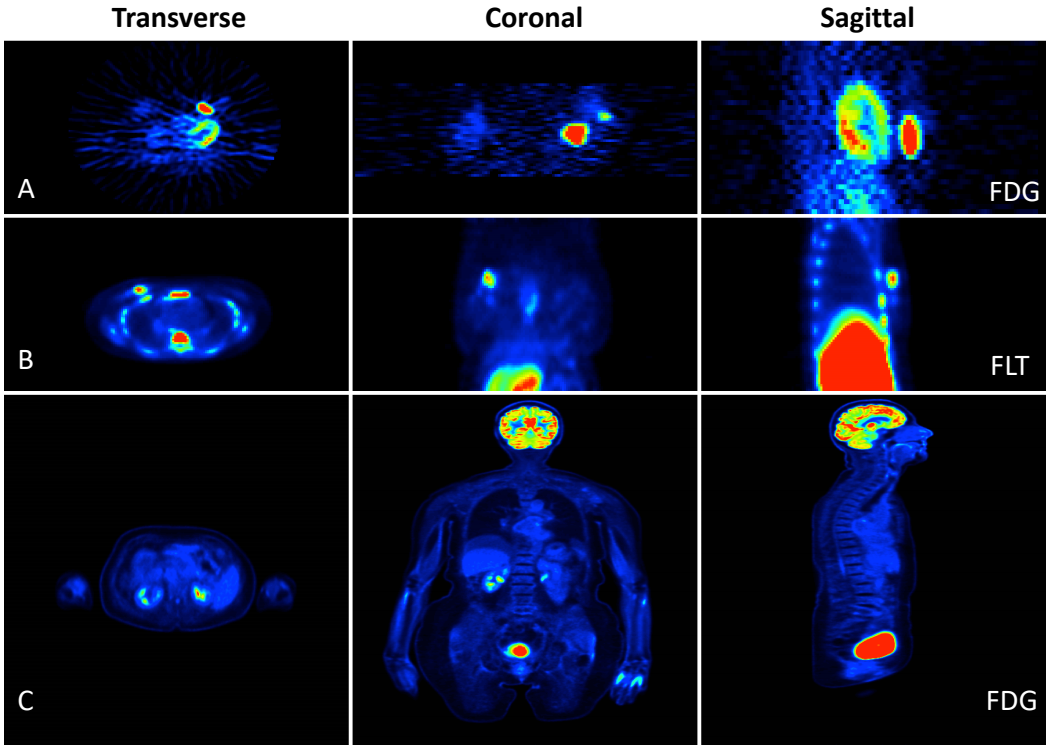


Figure 2.10: PET images generated on an early scanner (A) with FBP reconstruction (Mankoff et al., 2002), a recent scanner (B) with OSEM reconstruction (Kostakoglu et al., 2015) and a latest long axial field of view scanner - Siemens Quadra (C) with OSEM reconstruction (Sari et al., 2022) for breast cancer patients. Radiotracers are indicated on each row and columns correspond to transverse, coronal and sagittal views[5].

The principal trade-off between FBP and iterative reconstructions is accuracy versus computation efficiency. Iterative algorithms tend to produce better signal-to-noise images and greatly reduce streak artifacts that are commonly produced

[5]A and B: data shared by Prof. David A Mankoff at Univeristy of Pennsylvania and Dr. Mark Muzi at University of Washington; C: data shared by Prof. Kuangyu Shi and Prof. Axel Rominger at Bern Univeristy Hospital. Details can be had from Prof. Finbarr O'Sullivan at University College Cork.

in FBP reconstruction. Owing to improvements in computer power and development of acceleration techniques, iterative reconstructions are in widespread clinical use now (Wernick and Aarsvold, 2004; Zaidi, 2006). A visual comparison of FBP and OSEM reconstructed images from different PET scanners (i.e, the early, recent and latest generation) for breast patients is presented in Figure 2.10. The FBP image shows apparent artifacts and appears overall noisier than the OSEM images. The long axial field of view PET image exhibits excellent spatial resolution and remarkably improved image quality for multiple organs/tissues.

2.2.4 Structure of PET Data

A better understanding of PET data structures and characteristics in the projection and image domain may benefit the further development of reconstruction algorithms and post-processing techniques. In this section, we start with the Poisson nature of emission process and then discuss the image noise characteristics.

The Poisson Nature of Emission Process As mentioned in section 2.2.3.1, the raw data in the projection-domain is generated by detecting two photons being emitted from an annihilation. This procedure is, essentially, a counting process where the location and time of detected annihilation are recorded. There are a large number of annihilations and they follow the Poisson distribution, however, only a small proportion of these are actually detected by the PET scanner. Considering the detected annihilation to be a success and assuming the emission process is independent, the number of observed events also follows a Poisson distribution based on the thinning (splitting) theory. In dynamic PET studies, raw data from distinct time frame is deemed to have the Poisson statistics (Haynor and Woods, 1989; Carson et al., 1993; Hawe, 2016; Mou, 2018). Although the emission process possesses Poisson nature, the noise in PET projection may not the case. Many noise sources other than Poisson statistics, e.g., attenuation, scatter, and randoms may introduce additional deviations. Some noise models have been developed to characterize the pseudo-Poisson nature of raw measurements (Rowe and Dai, 1992; Maitra and O'Sullivan, 1997; Sitek and Celler, 2015).

Correction for Decay and Duration Different facilities may employ specific scanning protocols with various starting time points (e.g., from the tracer in-

jection time or after a time period) and durations (a few seconds or minutes). Thus, the decay and duration are usually corrected prior to any other calculation with the sinogram or (dynamic) image (Zaidi, 2006; Hawe et al., 2012; Hawe, 2016).

The atoms of a radioactive sample decay randomly and the average decay of the atoms is generally focused (Saha, 2015). The decay rate (dN/dt) is proportional to the number of radioactive atoms (N), thus the decay equation is expressed as

$$-\frac{dN}{dt} = \lambda N \tag{2.7}$$

where λ is the decay constant and depends on the particular radioactive nuclide and decay mechanism involved. Let $A = \lambda N$, integrating (2.7) gives the activity at time t (A_t):

$$A_t = A_0 e^{-\lambda t} \tag{2.8}$$

If the activity at time $t = 0$ (A_0) is known, we can calculate the activity at any time by (2.8).

The half-life ($t_{1/2}$) of a radionuclide is defined as the time required to reduce the initial activity to one-half, which is unique for every radionuclide and related to the decay constant as follows:

$$\lambda = \frac{ln2}{t_{1/2}} \tag{2.9}$$

Suppose y_t is the raw count over a time-bin with duration Δ_t, the corresponding activity value corrected by decay and duration is given by

$$z_t = y_t \frac{e^{\lambda t}}{\Delta_t} c \equiv y_t f_t c \tag{2.10}$$

where c is a scale factor taking account of attenuation, calibration etc.

Image Noise Characteristic Knowledge of the statistical properties of reconstructed images is essential for data analysis schemes. In particular, the accurate noise measures can be incorporated into the weighting factors for tracer kinetic modeling in dynamic PET studies (Carson et al., 1993; Yaqub et al., 2006; Thiele and Buchert, 2008; Huang et al., 2018; Cavalcanti et al., 2019). The noise characteristic of PET images reconstructed using FBP algorithm has been studied extensively and Gaussian noise model is often applied (Pajevic et al., 1998). However, image reconstructed by the widely used iterative EM algorithm reveals non-Gaussian character in nature due to the positive constraints. Some

studies have demonstrated that the noise in iterative reconstructions could be characterized by the log-normal (Barrett, Wilson and Tsui, 1994; Li, 2011) or Gamma distribution (Teymurazyan et al., 2013; Mou, Huang and O'Sullivan, 2017).

2.2.5 Performance Evaluation

The performance of PET scanners, image reconstruction algorithms and quantitative methodologies can be evaluated by quality management system or computer simulation.

Quality Assurance Routine quality assurance (QA) is necessary for optimal clinical performance which starts after installation of the imaging equipment and continues on a periodic basis (e.g., monthly) throughout its life time (Busemann Sokole et al., 2010). Physical (Hardware) phantoms are indispensable tools for assessing image quality or characterizing imaging systems in the QA procedure and have some advantages as the data are acquired with an actual scanner (Morgan, 2012). They are usually designed as simplified structures (e.g., a particular organ or tissue) and injected with a specific radiotracer. Three typical phantoms (uniform, NEMA and CTN) (Ulrich et al., 2018) are presented in Figure 2.11 and introduced briefly as follows. For more information, you can access SNMMI's Phantom Analysis Toolkit (PAT): https://www.snmmi.org/PAT.

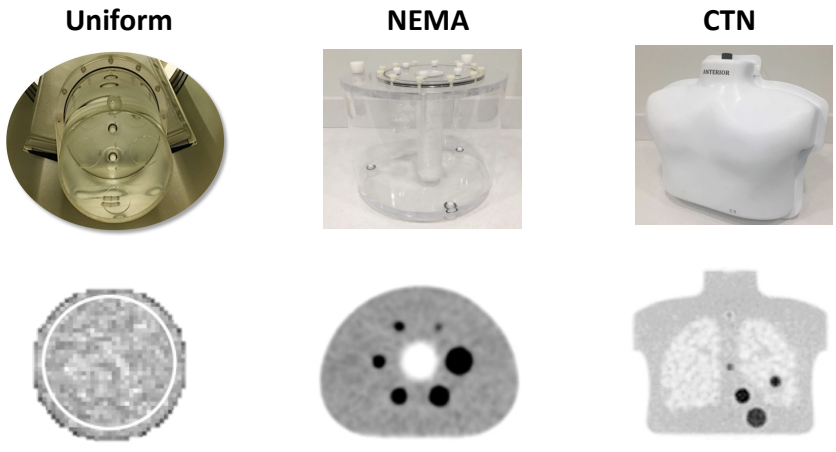


Figure 2.11: Physical (Hardware) Phantoms: Uniform (Mou, 2018), NEMA (Ulrich et al., 2018) and CTN (Viswanath, 2020).

(i) Uniform phantom is a standard cylinder container filled with well-mixed radioactive fluid.

(ii) NEMA phantom with six spheres is used to mimic human body and tumors. It was first published in 1994 by National Electrical Manufacturers Association (NEAM) and the current version is NEMA NU 2-2018 standard.

(iii) CTN phantom is a simple anthropomorphic chest phantom, which is published by the Clinical Trials Network (CTN) of Society of Nuclear Medicine and Molecular Imaging (SNMMI).

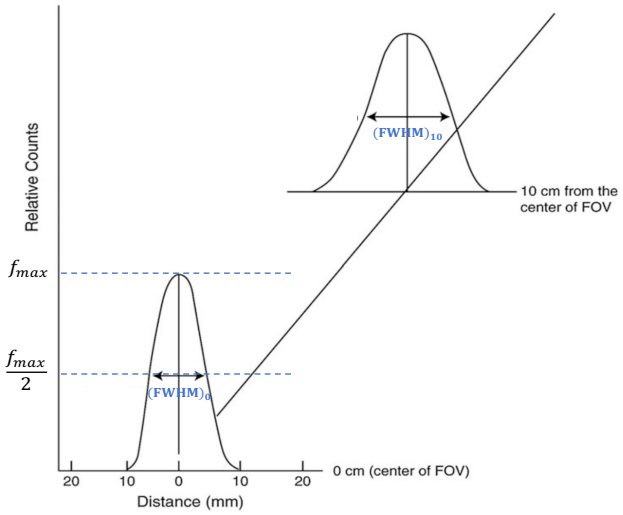


Figure 2.12: Point-spread function (PSF) at 0 and 10cm from the field of view (Saha, 2015).

The measurement of performance parameters includes sensitivity, scatter fraction, noise-equivalent count rate (NECR), spatial resolution, correction accuracy etc. Some important physical parameters (Saha, 2015) are described.

(i) Sensitivity is a measure of the counting efficiency of a PET scanner and expressed as the number of counts per unit time detected by the device for each unit of activity present in a source.

(ii) Image noise is the random variation in pixel counts across the image and given by $(1/\sqrt{N}) \times 100$, where N is the count in the pixel.

(iii) Point-spread function (PSF) describes the response of an imaging system to a point source or object and varies throughout the field of view (FOV), see Figure 2.12.

(iv) Full width at half maximum (FWHM) is determined from the width at half of the peak of each PSF.

(v) Spatial resolution is determined by the FWHM of PSF obtained from the measurement of activity distribution.

Computer Simulation Computer simulation has been a commonly used numerical technique for scanner design, protocol optimization, image reconstruction and quantification assessment in the PET field. The simulator is an efficient tool that can be used to mimic the real physical process and generate data in a controllable manner. The digital images of the phantom - numerical (software/mathematical) phantoms modeling different organs/tissues of the body, e.g., VSK phantom made up of several ellipses as a simplified imitation of the brain (Vardi, Shepp and Kaufman, 1985), are usually needed (Zaidi, 2006) as the known source (ground truth). Figure 2.13 shows three numerical phantoms involving the uniform and VSK phantom, also one slice of the real brain image as the phantom. Some progress has been made towards implementation of the computer simulation, for example, the publicly available code - GATE for Monte Carlo simulations (Jan et al., 2004; Buvat and Lazaro, 2006; Sarrut et al., 2021) and many "home-made" ("in house") codes (O'Sullivan, 1995; Huang et al., 2020; Gu et al., 2021; O'Sullivan et al., 2021) to simulate PET scanning.

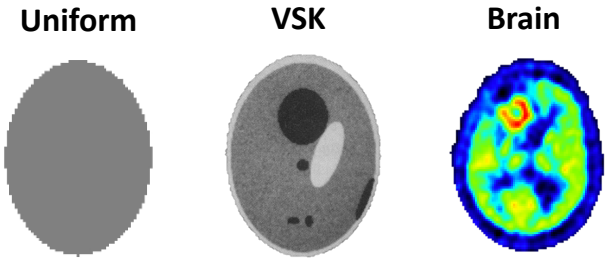


Figure 2.13: Numerical (Software) Phantoms: Uniform (Mou, 2018), VSK (Vardi, Shepp and Kaufman, 1985), Brain Phantom[6].

There are several considerable advantages of the numerical technique. One is the no need for the expensive manufacturing and testing of equipment. Also, it allows to add studied parameters that are not measurable in practice and turn off certain effects, which make it so powerful compared with real measurements. But it still has some limitations, the major one is the accuracy of the results depends on the applied computer model. Therefore, developing a simulation procedure to include all the possible factors in real situations is particularly important (Wernick and Aarsvold, 2004).

[6]Contributed by Qi Wu, Statistics, University College Cork

2.3 Quantitation of PET Imaging

PET images are normally assessed visually or using simple indices in daily clinical practice. Although these are sufficient for many diagnostic applications, the quantitation potential of PET can be further exploited in more avenues for clinical diagnosis, response assessment and therapy management (Tomasi, Turkheimer and Aboagye, 2012). Quantitation is not a single-step procedure and involves several issues such as input function and tracer kinetic modeling. Some standard methodologies have been well-developed for semi-quantitative or quantitative PET scanning, but they differ in terms of application assumptions and produced information (Bertoldo, Rizzo and Veronese, 2014) as summarized in Figure 2.14. In this section, we provide an overview of these approaches and also discuss the potential challenges and promise of novel methodologies in the emerging whole-body PET imaging (Zhang et al., 2020; Viswanath et al., 2021; Sari et al., 2022) from a statistical perspective.

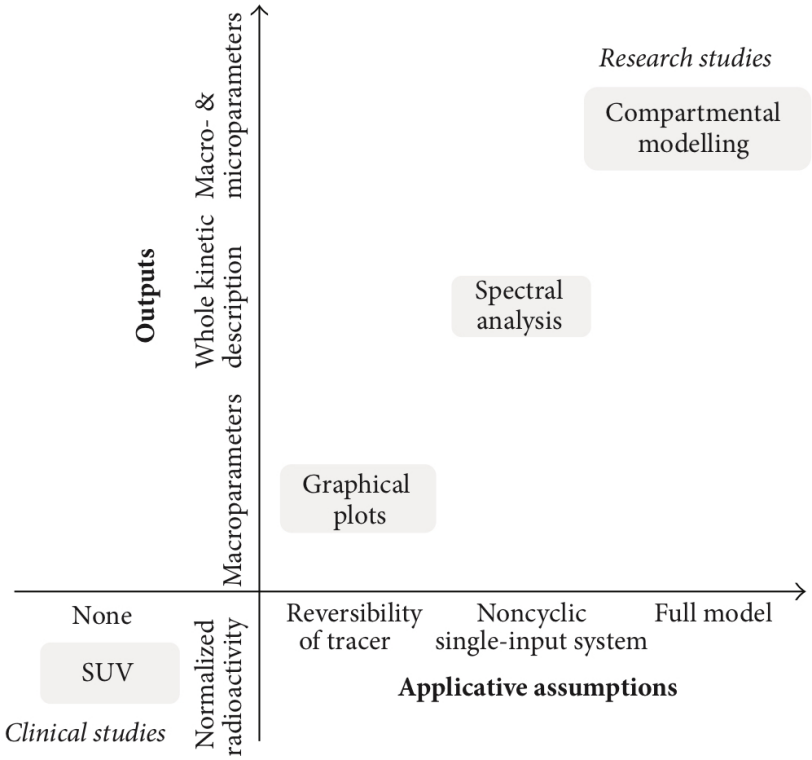


Figure 2.14: A schematic summary of major PET quantitation methods (Veronese et al., 2016).

2.3.1 Static and Dynamic PET Scans

There are two classic experimental frameworks for PET scanning as shown in Figure 2.15. The static scan is made by a single-frame acquisition at a given time after the tracer administration, which is generally used in clinical practice due to its feasibility such as reasonable costs and high patient throughput (Veronese et al., 2016). In this setting, PET quantitation is routinely performed by using standardized uptake value (SUV) - a semi-quantitative index, see below.

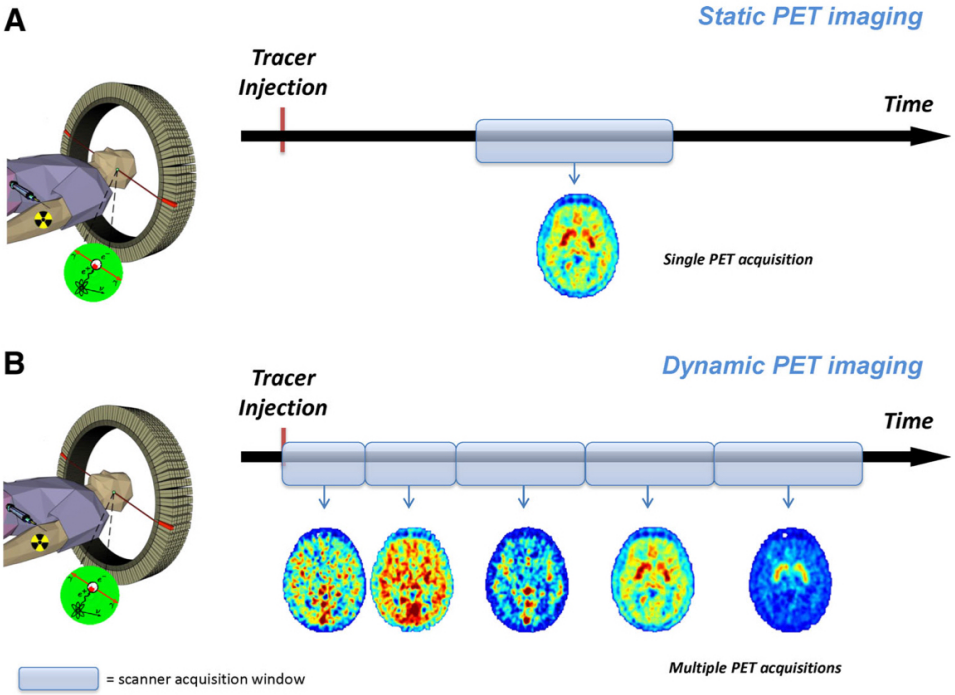


Figure 2.15: Static (A) versus dynamic (B) PET imaging (Bertoldo, Rizzo and Veronese, 2014).

Semi-quantitative index: SUV The application of SUV in PET dates back to 1985 (Kubota et al., 1985) and now it has been the most widely used index for the analysis not only of ^{18}F-FDG but also of most tracers in oncology. SUV is simply computed as the radiotracer concentration in a region or voxel of interest normalized by the injected dose and a normalization factor (NF) based on the subject's anthropometric characteristics.

$$SUV = \frac{ratiotracer \quad concentration}{injected \quad dose/NF} \tag{2.11}$$

where the radiotracer concentration (e.g. kBq/ml) indicates the concentration measured with PET over a short interval (usually from 5 to 15 mins) after a pre-

defined time has been allowed to elapse following tracer administration (e.g. 45 or 60 mins) (Bertoldo, Rizzo and Veronese, 2014). The injected dose (e.g. MBq) is the total administered dose and the most common NFs are body weight (in kg) and body surface area (in m^2)(Kim et al., 1994).

The simplicity and versatility of the SUV make it suitable for various types of cancer including lung (Hickeson et al., 2002), breast (Ulaner et al., 2013) and ovarian (Rockall et al., 2014). However, this metric can be affected by a number of factors such as respiratory motion, partial volume effect and reconstruction method. Also, it is only possible to quantify the tracer uptake, not reflect any physiological or pharmacological process, which poses quantitative limitations for the assessment of some cases such as three-vessel disease (Lammertsma, 2019). In view of these considerations, SUV can be regarded as a semi-quantitative surrogate index of tumor metabolism (Zaidi and Karakatsanis, 2017).

Differently from the static scans, the activity of the tracer is measured at multiple time frames starting from the time of injection in dynamic PET scans, resulting in 4D (3D in space and 1D in time) datasets. It is often coupled with blood sampling and mainly used in the research setting. Such dynamic scans give the possibility to characterize more detailed kinetics in the tissue. Due to the limitation of axial field of view (15$\sim$30 cm), generally only a single organ like the brain is covered in the imaging. Traditionally, whole-body and dynamic PET images are mutually exclusive. Recent advancements in PET technology and scanning protocol have made dynamic total/whole-body PET imaging possible[7].

Multi-bed dynamic whole-body PET imaging On the conventional PET scanners, the dynamic whole-body (DWB) imaging can be generated by performing a multi-bed multi-pass framework proposed by Karakatsanis and Rahmim et. al (Karakatsanis et al., 2013; Rahmim et al., 2019). The data acquisition scheme is illustrated in Figure 2.16 and has been implemented on commercial scanners (Dias et al., 2022; Yao et al., 2021). But DWB images still have some pitfalls including patient motion, low temporal resolution and missing early-phase data, which limit its wide use.

[7]In this thesis, total-body PET imaging exclusively refers to studies using the uEXPLORER scanner. whole-body PET imaging includes single or multiple-bed studies covering the most of main organs and preclinical animal studies.

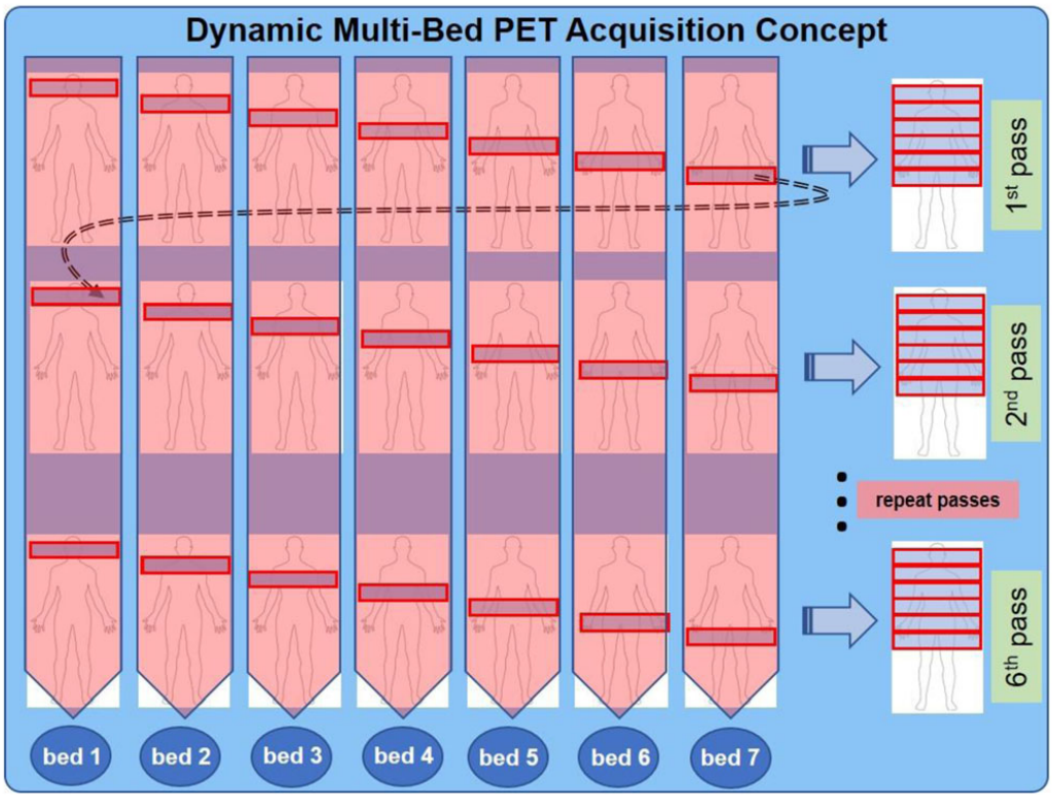


Figure 2.16: An example of dynamic whole-body PET data acquisition by a multi-pass multi-bed protocol using conventional scanners (Karakatsanis et al., 2013; Rahmim et al., 2019).

Single-bed dynamic whole-body PET imaging The advent of new-generation PET scanners with LAFOV ($> 1m$) and enhanced sensitivity, e.g., uEXPLORER (Badawi et al., 2019), PennPET Explorer (Pantel et al., 2020) and Siemens Quadra (Alberts et al., 2021), enables simultaneous dynamic imaging of multiple organs using single-bed position. The analysis of such large-scale datasets also presents many challenges such as the selection of image-derived input function and organ-specific kinetics, see section 2.3.5.

2.3.2 The Basic Equation of Dynamic PET

Understanding the targeted biochemical pathway is critical for the interpretation of dynamic PET imaging data. In this section, we begin with a simple system and then introduce the indicator dilution method (Meier and Zierler, 1954) for measuring the properties (e.g blood flow and volume) of biological systems.

2.3.2.1 Basics of Systems

A system can be considered as some part of the physical world that interacts with its environment, which is any process that produces an output signal (y) in response to an input signal (x) as shown in Figure 2.17. $H = H[\cdot]$ denotes the system, so the output can be expressed as:

$$y(t) = H[x(t)] \tag{2.12}$$

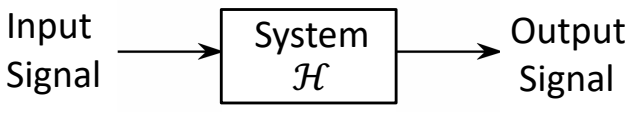


Figure 2.17: A general system diagram.

Two particularly useful properties are linearity and time-invariance, which we describe next. Although real systems are rarely exactly linear or time-invariant, results for the idealized assumptions still provide useful models for understanding more complex systems[8].

Linearity[8] A system is linear if adding or scaling inputs to the system simply results in adding or scaling the corresponding outputs. More precisely, a system H is linear if the following two conditions are satisfied:

1. $H[ax(t)] = aH[x(t)]$ for all constants a and input signals $x(t)$
2. $H[x_1(t) + x_2(t)] = H[x_1(t)] + H[x_2(t)]$ for all input signals $x_1(t)$, $x_2(t)$.

Time-Invariance[8] Time-invariance means that whatever behavior a system has, if the inputs were delayed by some amount of time, then the behavior of the system would be unchanged other than just being delayed by that same amount of time. More precisely, H is time-invariant if

$$H[x(t - t_0)] = y(t - t_0) \tag{2.13}$$

for all times t_0 and input signals $x(t)$.

Linear time-invariant (LTI) system We now focus on the class of linear time-invariant systems (also known as LTI systems) with two properties (i.e, lin-

[8]URL: https://www.princeton.edu/~cuff/ele201/kulkarni_text/systems.pdf

earity and time-invariance). Here we consider the case of discrete-to-discrete systems (Figure 2.18), see (Barrett and Myers, 2013) for more situations, e.g, continuous-to-discrete systems. Suppose we apply the discrete-time delta function/unit impulse (a value of one, while all other samples have a value of zero) as the input to the system, that is $x[n] = \delta[n]$. The output will be some signal which we will denote as $h[n]$, so that $h[n] = H[\delta[n]]$. It is also the impulse response of this system because the input is a delta function (impulse).

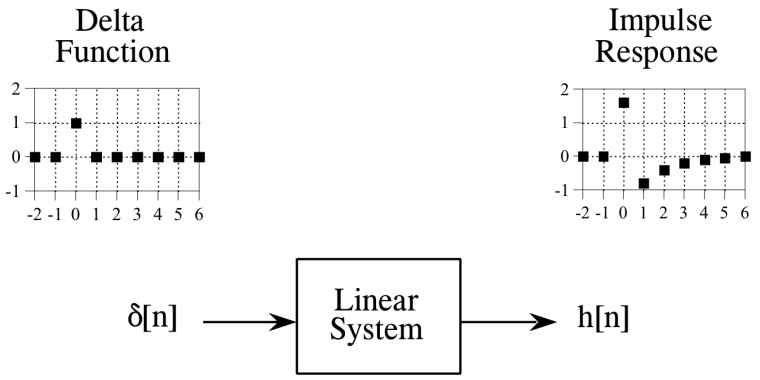


Figure 2.18: Definition of delta function and impulse response (Smith et al., 1997).

Assume the input signal $x[n] = \sum_{i=-\infty}^{\infty} x[i]\delta[n-i]$, then we can have

$$y[n] = \sum_{i=-\infty}^{\infty} x[i]h[n-i] \equiv (x \otimes h)[n] \tag{2.14}$$

The detailed derivation is in Appendix B.2. Hence, we can say the output (y) of an LTI system is simply the input (x) convolved ($\otimes$) with the impulse response (h).

2.3.2.2 Indicator-Dilution Method

Indicator-dilution method is introduced by Stewart (Stewart, 1897) and developed for the measurement of cardiac output by Hamilton et.al (Hamilton et al., 1932). It was also Swewart (Stewart, 1921) who first used the technique to measure the volume of blood in the heart and lungs, and again it was Hamilton et. al who developed and emphasized the use of mean circulation time to determine the volume of a vascular bed (Hamilton et al., 1932). The interpretation of dynamic PET data can also be approached using this theory built on the seminal work of Meier and Zierler (Meier and Zierler, 1954). Assuming the radiotracer's interaction with tissue is substantially linear and time-invariant,

the vascular network can be regarded as an LTI system with an arterial input as shown in Figure 2.19. Hence, the measured tissue time course can be expressed as a convolution between the arterial input function (AIF) and the so-called tissue residue or impulse response function as in (2.15).

$$C_T(t) = \int_0^t R(t-s)C_p(s)ds \equiv R(t) \otimes C_p(t) \tag{2.15}$$

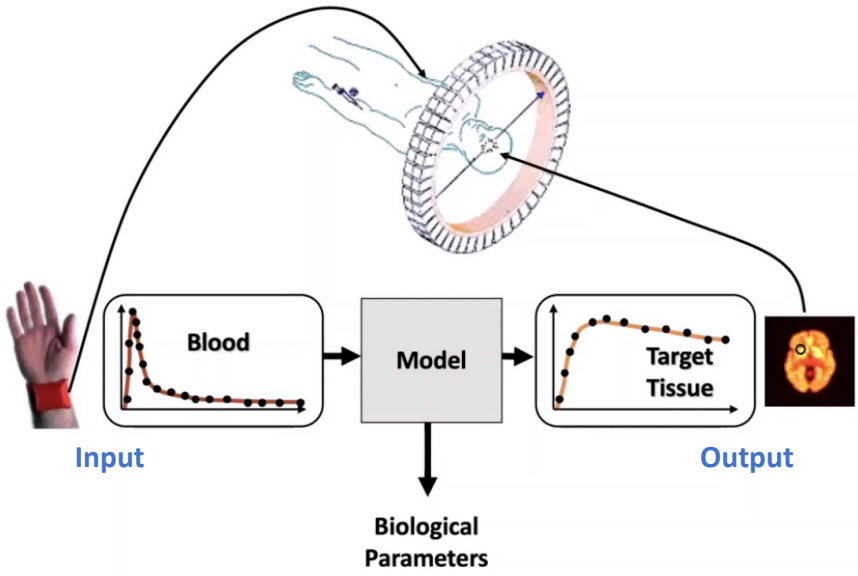


Figure 2.19: System is characterized by measuring the input and output[9].

Where C_T is the tissue activity per unit volume (KBq/cm^3), C_p is the AIF which is activity per milliliter (mL) of blood. The impulse response R is a necessarily monotone decreasing function and several kinetic models are generally used to estimate this function, see section 2.3.4. Many biologically important parameters such as transport and metabolic flux (K_i) can be extracted from the estimated impulse response.

When the model is applied to PET time-course data, there is typically an adjustment for the fractional blood volume (V_B), this gives rise to a model representation of the tissue time-course as

$$C_T(t) = V_B C_p(t) + (1 - V_B) \int_0^t R(t-s)C_p(s)ds \tag{2.16}$$

The site to recover AIF (radial artery, left ventricle or descending aorta) may be

[9] 2021 IEEE NSS&MIC Short Course by Prof. Roger Gunn at Imperial College London.

remote from the tissue, so a delay term (Δ) can be included as well to represent tracer activity in arterial blood. It has been found particularly necessary to describe the whole-body kinetics (Wang, Nardo, Jones, Cherry and Badawi, 2021), see detailed discussion in section 2.3.5. Hence, the basic equation of dynamic PET data finally becomes (2.17).

$$C_T(t) = V_B C_p(t-\Delta) + (1-V_B)\int_0^t R(t-s)C_p(s-\Delta)ds \tag{2.17}$$

2.3.2.3 ROI Versus Voxel-level Analysis

In quantitative PET data analysis, computation of the physiological parameters (e.g. K_i) can be performed either at the region or voxel level (Figure 2.20). Due to the average of the voxel information in a region of interest (ROI), the noise can be reduced dramatically. ROI analysis leads to more robust results, especially in the case of dynamic PET studies, but also introduces some biases when defining ROIs from summed or anatomic images (Bertoldo, Rizzo and Veronese, 2014). An alternate approach to regional estimates is performing analysis at the voxel level and parametric images are generated. They can reveal the heterogeneity of tumors and have the potential for improved lesion detection and response assessment (Muzi et al., 2012). In this procedure, many issues need to be considered carefully such as the selection of appropriate kinetic models and noise suppression (Wang, Nardo, Jones, Cherry and Badawi, 2021). Whether working at ROI or voxel level, there are several confounding effects that may limit the reliability of parameter estimates including patient's movement, partial volume (Erlandsson et al., 2012) and spillover activity.

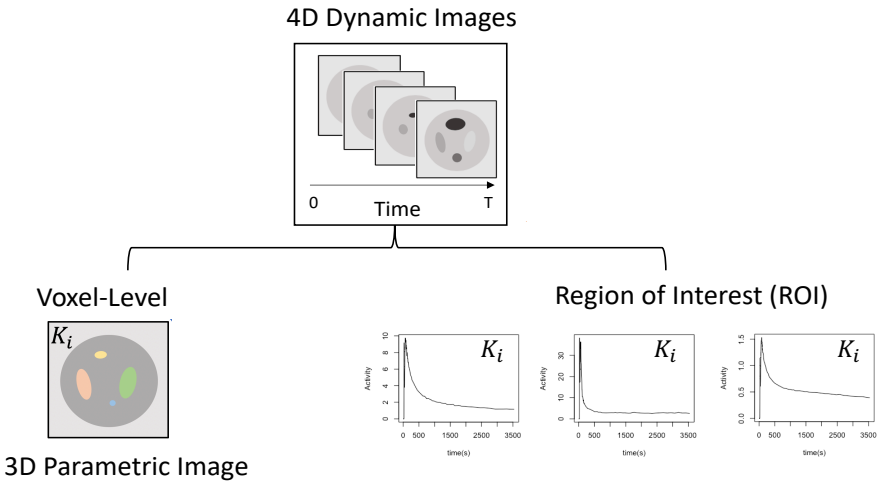


Figure 2.20: Region of interest (ROI) and voxel-level analysis.

2.3.3 Arterial Input Function (AIF)

For standard PET quantitation, the knowledge of the tracer arterial plasma concentration is required as an arterial input function (AIF). The input function can be derived either from (i) arterial blood samples, (ii) time course of ROI drawn on the PET image, or (iii) based on the population. Here we provide a brief review of these commonly used and model-based approaches together with their performance characterizations.

Blood Sampling Arterial blood sampling during dynamic acquisition has been considered as the gold standard for input function measurements (Graham and Lewellen, 1993). However, this is an invasive procedure and cannot be recommended for routine clinical purposes since it implies discomfort for the patient (insertion of arterial lines and increased radiation) and additional costs for the analysis of numerous blood samples (extraction of metabolites and plasma radioactivity from the whole-blood) (Feng, Chen and Wen, 2020). Hence, some non-invasive techniques (based on image/population/mathematical model) have been developed as follows.

Image-derived input function (IDIF) Many efforts have been made to derive input function information from a region drawn at a blood pool (left ventricle, aorta or other big blood vessels) on the PET dynamic images as it obviates the need for blood sampling. Unfortunately, only the whole blood activity concentration can be derived and the time course may be inaccurate and noisy for images with low spatial and temporal resolution. It is impossible to obtain plasma concentrations or parent fractions in plasma. Interesting results are obtained only with PET tracers that do not produce any metabolites, such as ^{18}F-FDG (Bertoldo, Rizzo and Veronese, 2014).

Population-based input function (PBIF) Assuming individuals have the same tracer injection protocol and similar physiological characteristics in a cohort, the population-based input function is generally obtained by averaging and scaling this set of input functions using arterial catheterization invasively (Takikawa et al., 1993). Such a method is probably the most interesting approach for use in clinical practice with many radiotracers, but currently it has been validated almost exclusively for ^{18}F-FDG (Vriens et al., 2009), whereas few attempts have been made with other tracers (Zanotti-Fregonara et al., 2012).

Model-based input function (MBIF) Model-based descriptions of the arterial samples are introduced to obtain continuous and noise-free input functions. The most common models are Feng's model (Feng, Huang and Wang, 1993) and its variation, i.e. tri-exponential model (Parsey et al., 2000), but they both cannot describe the complex behavior of the AIF and account for different injection protocols properly (Tonietto et al., 2015). Some approaches are developed to overcome these limitations. A novel Markov chain model for the representation of the whole-body tracer circulation (Figure 2.21) is proposed to estimate the AIF (Huang and O'Sullivan, 2014). This approach has great potential to be applied to the emerging whole-body PET imaging (Zhang et al., 2020; Viswanath et al., 2021; Sari et al., 2022). Recently, a population-based projection model (PBPM) has been developed which combines population profiling (as in a PBIF approach) with individual arterial input data modeling (as in an IDIF approach). The model incorporates knowledge of injection duration into the fit, allowing for varying injection protocols (Xiu et al., 2022).

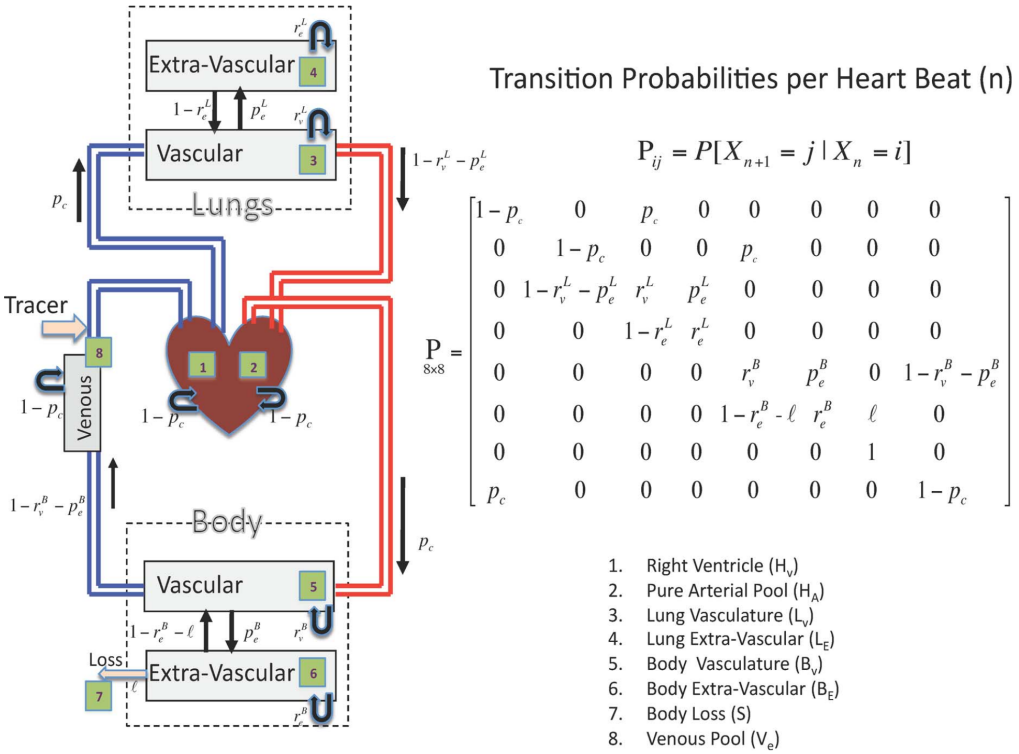


Figure 2.21: Markov chain model for tracer atom dynamics within the body (Huang and O'Sullivan, 2014). Graph representation (left); Transition matrix (right).

2.3.4 Kinetic Modeling

This section will offer an overview of the advantages and limitations of the different kinetic models available for PET quantification in order to allow the most appropriate solutions to be chosen for any given needs.

2.3.4.1 Compartmental Modeling

Compartmental modeling forms the basis for tracer kinetics of dynamic PET data. There are two most important models used to derive physiological information in absolute measurement units. One tissue compartmental (1C) model (Figure 2.22A) with two rate constants (K_1 in ml/min/cm^3 and k_2 in min^{-1}) was developed by Kety (Kety and Schmidt, 1948) for quantitative assessment of blood flow (perfusion). Two tissue reversible compartmental (2Cr) model with four rate constants (K_1 in ml/min/cm^3, k_2, k_3 and k_4 in min^{-1}) as shown in Figure 2.22B is mainly used for quantifying receptor ligand binding studies (Mintun et al., 1984). While k_4 equals to 0 (irreversible), it becomes the most famous Sokolov-Huang model (2Ci) (Sokoloff et al., 1977; Phelps et al., 1979; Huang et al., 1980) generally employed for the quantitation of metabolic rate for glucose. C_1 and C_2 are tissue compartments and C_p represents the plasma compartment. More generalized compartmental models and detailed underlying biochemical mechanisms, see (Gunn, Gunn and Cunningham, 2001). These models are described by a system of first-order time-dependent differential equations, which can be solved by a numerical procedure known as non-linear least squares (NLLS) in order to appropriately estimate the residue function (Figure 2.22C) and associated physiological parameters such as flow (K), metabolic flux (K_i) and volume of distribution (V_D). More details are presented as follows.

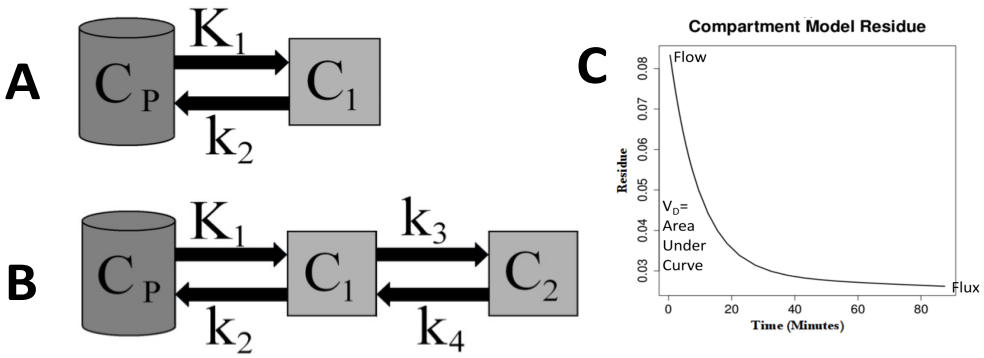


Figure 2.22: One (A) and two (B) compartmental models. Residue function with key physiological parameters (C) (Hawe, 2016).

One Tissue Compartmental (1C) Model One tissue compartmental model is given by a differential equation and solved by the method of integrating factor (2.18). Detailed derivations are in Appendix B.3.

$$\frac{dC_1(t)}{dt} = K_1 C_p(t) - k_2 C_1(t) \Rightarrow C_1(t) = \int_0^t K_1 e^{-k_2(t-s)} C_p(s) ds \tag{2.18}$$

Related to the simple basic equation (2.15), the resiude function can be obtained as

$$R(t) = K_1 e^{-k_2 t} \tag{2.19}$$

Hence, the parameter of interest - blood flow (perfusion) $= R(0) = K_1$.

Two Tissue Compartmental (2C) Model Similar to the 1C model, two tissue compartmental model is represented by a coupled system of differential equations as (2.20) and can be solved by the Laplace transform, see Appendix B.4 and its inversion (Trench, 2013). Full details of solutions can be found in Appendix B.5 and the final result is shown in (2.21). Again recall the fundamental equation (2.15), residue can be expressed as a mixture of exponentials (2.22).

$$\begin{cases} \frac{dC_p}{dt} = k_2 C_1(t) - K_1 C_p(t) \\ \frac{dC_1}{dt} = K_1 C_p(t) - (k_2 + k_3) C_1(t) + k_4 C_2(t) \\ \frac{dC_2}{dt} = k_3 C_1(t) - k_4 C_2(t) \end{cases} \tag{2.20}$$

$$C_T(t) = C_1(t) + C_2(t) = K_1(\pi_1 e^{-\theta_1 t} + \pi_2 e^{-\theta_2 t}) \otimes C_p(t) \tag{2.21}$$

where

$$\begin{cases} \pi_1 = \frac{k_4 - \theta_1 + k_3}{\theta_2 - \theta_1}, \pi_2 = \frac{\theta_2 - k_4 - k_3}{\theta_2 - \theta_1}; \pi_1 + \pi_2 = 1 \\ \theta_1 = \frac{k_2 + k_3 + k_4 - \sqrt{(k_2+k_3+k_4)^2 - 4k_2k_4}}{2}, \theta_2 = \frac{k_2 + k_3 + k_4 + \sqrt{(k_2+k_3+k_4)^2 - 4k_2k_4}}{2}; \theta_1\theta_2 = k_2k_4 \end{cases}$$

$$R(t) = K_1(\pi_1 e^{-\theta_1 t} + \pi_2 e^{-\theta_2 t}) \tag{2.22}$$

For the irreversible 2C model ($k_4 = 0$), the key parameter metabolic flux is focused, which is $K_i = \lim_{t\to\infty} R(t) = \frac{K_1 k_3}{k_2 + k_3}$. The distribution of volume is usually calculated for the reversible tracers, that is $V_D = \int_0^\infty R(t)dt = K_1(\frac{k_4 + k_3}{k_2 k_4})$.

The advantages of compartmental modeling are the reliability and independency on the scanning time. But its application is not practical in clinical practice as it requires complex acquisition protocol (full dynamic scanning - over one hour and arterial blood sampling). Also when dealing with very noisy data (e.g voxel-level analysis), this method has several pitfalls including convergence issues, high computational time and sensitivity to initial estimates due to the nature of NLLS (Bertoldo, Rizzo and Veronese, 2014). For the compartmental modeling to be feasible, some assumptions need to be satisfied. Hence, we must justify each case carefully for the use of compartmental modeling.

Justification Assumptions for the compartmental modeling include homogeneity of each compartment, instant mixing within compartments and following the law of mass action (Hawe, 2016). The selection of these models (1C, 2Ci, 2Cr) also depends on the PET radiotracer and the aim of study, even the organ/tissue of interest. For example, 1C is generally adopted for ^{15}O-H_2O and 2Cr for ^{11}C-raclopride. The irreversible model is usually employed for the most commonly applicable PET radiotracer ^{18}F-FDG in the brain or breast studies, but its uptake into the liver exhibits reversible kinetics (Keramida et al., 2014).

2.3.4.2 Spectral Analysis

The residue function in the compartmental model was demonstrated to be the mixture of exponentials (one or two) in the previous section. It may not have sufficient degrees of freedom to capture full variability in PET data. Spectral Analysis (SA) proposed by Cunningham and Jones in 1993 (Cunningham and Jones, 1993) assumes the residue to be the sum of $M+1$ exponential terms (2.23).

$$R(t) = \sum_{j=0}^{M} \alpha_j e^{-\beta_j t}, \alpha_j \geq 0, \beta_j \geq 0, \beta_0 = 0 \tag{2.23}$$

C_T is expressed as

$$\begin{aligned} C_T(t) &= \sum_{j=0}^{M} \alpha_j e^{-\beta_j t} \otimes C_p(t) \\ &= \sum_{j=0}^{M} \alpha_j C_p(t) \otimes e^{-\beta_j t} \\ &= \sum_{j=0}^{M} \alpha_j g_j(t) \end{aligned}$$

$g_j(t)$ are known since a grid of eigenvalues β_j is defined, whereas the amplitudes α_j are estimated by NLLS algorithm. The model structure (reversibility or irreversibility, number of compartments) are derived from α_j, also called spectrum. The information of macroparameters, such as K_1, K_i and V_D is also obtained (Tomasi, Turkheimer and Aboagye, 2012).

$$K_1 = \sum_{j=0}^{M} \alpha_j, K_i = \lim_{t\to\infty} R(t) = \lim_{t\to\infty} \sum_{j=0}^{M} \left[\alpha_j e^{-\beta_j t}\right] = \alpha_0, V_D = \int_0^{\infty} R\,(t)\,dt = \sum_{j=1}^{M} \frac{\alpha_j}{\beta_j}$$

The main strength of spectral analysis is its flexibility which can be applied to reversible or irreversible kinetics, single or multiple compartmental models, and homogeneous as well as heterogeneous systems. This characteristic makes this method adaptable to various tracers and physiological systems without any prior assumptions (Veronese et al., 2016). But it is sensitive to the data noise, for this reason, several strategies have been proposed such as rank-shaping spectral analysis (RSSA) (Turkheimer et al., 2003) and spectral analysis with iterative filter (SAIF) (Veronese et al., 2010).

2.3.4.3 Graphical Analysis: Patlak and Logan Plots

Two main graphical methods - the Patlak (Patlak, Blasberg and Fenstermacher, 1983) and the Logan plot (Logan et al., 1990) are applied to irreversible and reversible tracers, respectively. They can estimate the specific physiological parameters (Figure 2.23) by appropriately transforming the equations of compartmental modeling.

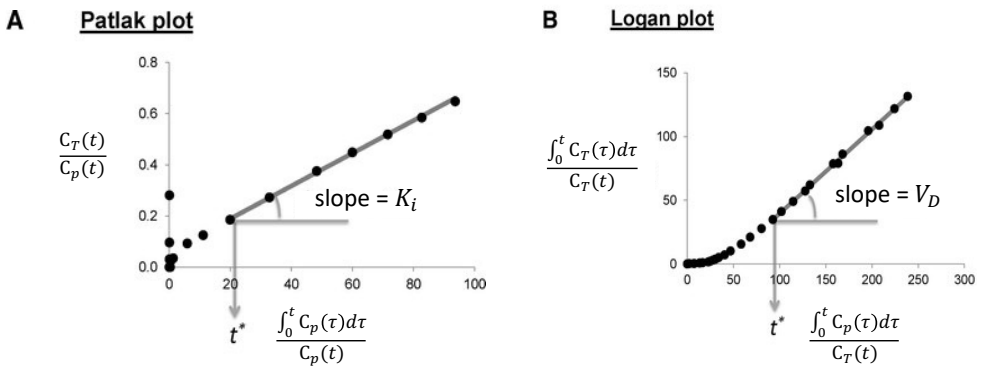


Figure 2.23: Patlak and Logan plots. The figure shows an example of a Patlak plot (A) and an example of a Logan plot (B). The data show a linear trend after the equilibration time t^* and the slope corresponds to the estimated parameter of interest (K_i for the Patlak plot and V_D for the Logan plot) (Bertoldo, Rizzo and Veronese, 2014).

Patlak plot As the most popular graphical method, Patlak model has been widely applied to dynamic PET imaging due to its simplicity and robustness (Patlak, Blasberg and Fenstermacher, 1983). It is assumed that: (i) the underlying tracer kinetics such as ^{18}F-FDG follow two-tissue irreversible compartmental model; (ii) it is valid after the time that steady state conditions between reversible tissue and plasma compartments are reached. If these assumptions are all satisfied, K_i can be estimated easily as the slope of Patlak plot after the equilibrium time (t^*) using linear regression. The Patlak plot (Figure 2.23A) is given by the expression as below:

$$\frac{C_T(t)}{C_p(t)} = K_i \frac{\int_0^t C_p(\tau)d\tau}{C_p(t)} + constant, \quad t > t^* \tag{2.24}$$

K_i can be computed using a non-iterative strategy - ordinary least square (OLS). The method requires dynamic scanning, but only a few late frames, starting 15–30 min after injection (the typical range of values of t^*). Due to the nature of linearity, it should be much faster and less sensitive to noise than NLLS and it is therefore appropriate for applications at the voxel level (Tomasi, Turkheimer and Aboagye, 2012). On the other hand, it must be noted that the choice of t^* is very critical and final estimates would be affected (Choi et al., 1991). Only a reduced set of parameters (K_i) can be obtained and this approach does not provide any insight regarding the complete profile of tracer kinetics.

Logan plot Logan plot (Figure 2.23B) is developed for the quantitation of reversible tracers and allows the estimation of V_D from the slope of data transformation (Logan et al., 1990) in (2.25).

$$\frac{\int_0^t C_T(\tau)d\tau}{C_T(t)} = V_D \frac{\int_0^t C_p(\tau)d\tau}{C_T(t)} + constant, \quad t > t^* \tag{2.25}$$

The choice of t^* is also critical for the Logan plot. Different from the Patlak analysis, Logan estimates are affected by the noise. As a result, V_D tends to be underestimated when data is noisy. Several procedures have been proposed to reduce this bias including smoothing data, different estimators or rearrangement of the Logan equation (Bertoldo, Rizzo and Veronese, 2014).

2.3.5 Current Status and Challenges in Whole-Body PET Imaging

The recent development of new-generation PET scanners, e.g., uEXPLORER (Badawi et al., 2019), PennPET Explorer (Pantel et al., 2020) and Siemens Quadra (Alberts et al., 2021) enables to simultaneously image the entire human body or main organs. Given the ultra-high sensitivity (10 $\sim$ 40 fold), extended field of view (1 $\sim$ 2m) and enhanced temporal resolution (60 $\sim$ 200 time frames), the potential clinical applications for these innovative technologies have been fully discussed in several review papers (Nadig et al., 2021; Slart et al., 2021; Katal et al., 2022). In this section, we focus on the quantitation of dynamic whole-body PET imaging, particularly the generation of parametric images.

Table 2.3: Characteristics and Challenges/Opportunities of long axial field of view PET scanners.

Characteristics	**Challenges/Opportunities**
Multiple organs/tissues	• Organ-specific kinetics
	• Large blood pool
	• Heterogeneity
	• Delay
Higher temporal resolution	• Capture faster kinetics
Higher spatial resolution	• High signal-to-noise
Huge data set	• Extensive computation

As summarized in Table 2.3, these unique characteristics create a series of new challenges and opportunities for improved quantitative accuracy. Details are presented as follows:

(i) Improved image-derived input function. IDIF can be measured from multiple blood pools (e.g., heart ventricle, aorta, artery) due to the long axial field of view and higher temporal resolution (1$\sim$2s per frame) allows better temporal sampling of the input function (Viswanath et al., 2021).

(ii) Organ-dependent time delay correction. The arrival time of tracer to different organs is significantly varied, which has been an important factor for accurate whole-body kinetics (Feng et al., 2019, 2021). The correction is generally accomplished by the inclusion of delays in the modeling procedure as (2.17).

(iii) Organ-specific kinetics. Each organ has its own physiological mechanism and some organs such as the liver, kidney and bladder even exhibit more complex kinetics. Hence a single kinetic model may not be feasible for multiple organs and appropriate model selection is necessary (Wang, Nardo, Jones, Cherry and Badawi, 2021; Wang, Li, Cherry and Wang, 2021; Wu, Gu, Wu, Zhou and Wang, 2022).

(iv) Capture fast kinetics. The high temporal sampling imaging provides an opportunity for better investigation of fast kinetics such as the blood volume (V_b) or blood flow (perfusion) , which are potentially impactful cancer biomarkers for the prediction of response or survival (Meikle et al., 2021), see example in section 6.1.4.

(v) High quality dynamic PET images. The enhanced sensitivity enables the generation of high signal-to-noise (SNR) image, which is greatly beneficial to the quantitation of dynamic imaging at the voxel level, e.g., noise reduction and accuracy increase of parametric imaging.

(vi) Huge data set. It is challenging to store and process such enormous and complex datasets, which may be addressed by some automation forms using artificial intelligence or more comprehensive approaches (e.g. segmentation) (Slart et al., 2021).

Table 2.4: Current status of quantitation of long axial field-of-view PET imaging.

	Application	Adaption
IDIF	✓	
PBIF	✓	
MBIF		
Compartmental Modeling	✓	Delay Effect (Feng et al., 2021)
		Model Selection (Wang, Nardo, Jones, Cherry and Badawi, 2021)
Spectral Analysis		
Patlak Analysis	✓	Direct Patlak (Sari et al., 2022)
		Generalized Patlak (Gu et al., 2022)
		Adaptive t* (Wu, Gu, Gu, Xu, Zhou and Shi, 2022)
Other Methods	✓	NPRM (O'Sullivan et al., 2022)
		Deep Learning (Huang et al., 2022)

Until now, there is limited research on the work of quantitation of dynamic whole-body PET images and an overview is provided in Table 2.4. Most of them refer to the direct application of traditional approaches (Zhang et al., 2020; Liu et al., 2021; Wu, Feng, Zhao, Xu, Fu, Huang, Meng, Li, Shao and Wang, 2022; Viswanath et al., 2021; Sari et al., 2022). Several adaptions have

been proposed to address the possible issues discussed above and some novel methodological developments that are likely to have a significant impact.

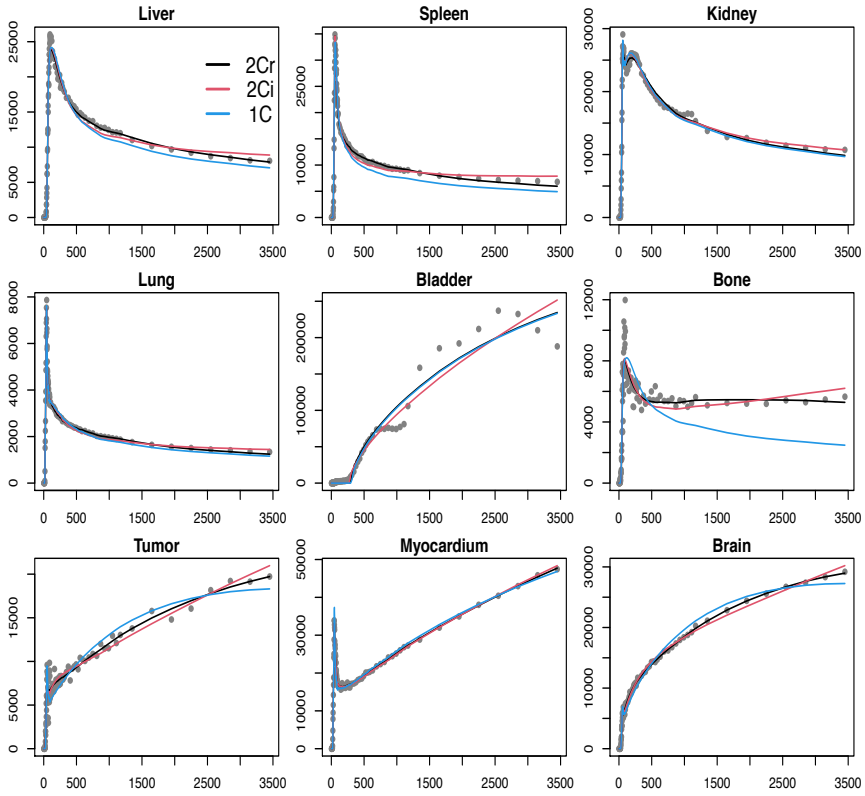


Figure 2.24: Fitting of one tissue (1C), two tissue irreversible (2Ci) and reversible (2Cr) compartmental models for multiple organs. x-axis: time in seconds; y-axis: activity. Raw dynamic data is shown in grey points. Blue, red and black lines represent 1C, 2Ci and 2Cr fitted curves (Wu, Gu, Wu, Zhou and Wang, 2022).

2.3.5.1 Adaption of Traditional Approaches

Compartmental Modeling The effects of delay of the input function were studied using 1C modeling and early kinetics (first 5 mins) of a total-body FDG PET scan by Feng et al (Feng et al., 2019, 2021). Subsequently, Wang et al further demonstrated that both the time delay estimation (full dynamic acquisition) and model selection (0C, 1C and 2Ci) are necessary for accurate parametric imaging (Wang, Nardo, Jones, Cherry and Badawi, 2021). Recently, a more comprehensive assessment of two delay scheme estimations using only early time frames or full data and various compartmental models (1C,2Ci and 2Cr) has been implemented for diverse tissues (Wu, Gu, Wu, Zhou and Wang, 2022). As in Figure 2.24 and 2.25, results show that (i) 2Cr has the advantages

for liver, spleen, lung, bone, tumor and brain and 2Ci fits best for the kidney; (ii) the feasibility of the compartmental models for the bladder is questionable; (iii) the delay estimation scheme using 1C with early time frames data is very efficient.

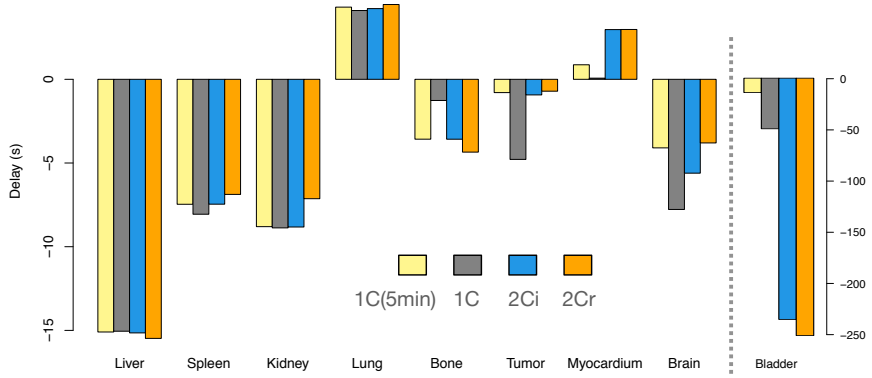


Figure 2.25: Delay time estimated from various compartmental models and schemes (Wu, Gu, Wu, Zhou and Wang, 2022).

Patlak Analysis As introduced in section 2.3.4.3, Patlak analysis depends on some assumptions and unsatisfied ones may introduce additional errors in estimated flux (K_i), such as the improper t^*. When adopting Patlak method for dynamic total-body PET imaging, the single t^* may not be appropriate for diverse tissues. Hence an adaptive t^* scheme is proposed to improve the accuracy of kinetic parameters like K_i (Wu, Gu, Gu, Xu, Zhou and Shi, 2022). The feasibility of standard and generalized Patlak models (Patlak and Blasberg, 1985; Karakatsanis et al., 2015) is also assessed for multiple organs, especially for certain tissues like the liver where ^{18}F-FDG may exhibit mild positive uptake reversibility and bladder associated with the complex tracer excretion process (Gu et al., 2022). Results show that standard Patlak is applicable to most of the organs except the bladder and generalized Patlak can bring some benefits for liver, kidney and lung, especially bladder (Figure 2.26).

2.3.5.2 The Promise of Novel Methodologies

Many multivariate statistical methods including factor analysis (FA) (Ahn et al., 2000), singular value decomposition (SVD) (Zanderigo, Parsey and Ogden, 2015), principal component analysis (PCA) (Pedersen et al., 1994; Razifar, 2005), cluster analysis (Wong et al., 2002) and mixture analysis (O'Sullivan, 1993) have been applied to the analysis of dynamic PET images, which enable to identify organs and structures with different kinetic patterns in a dy-

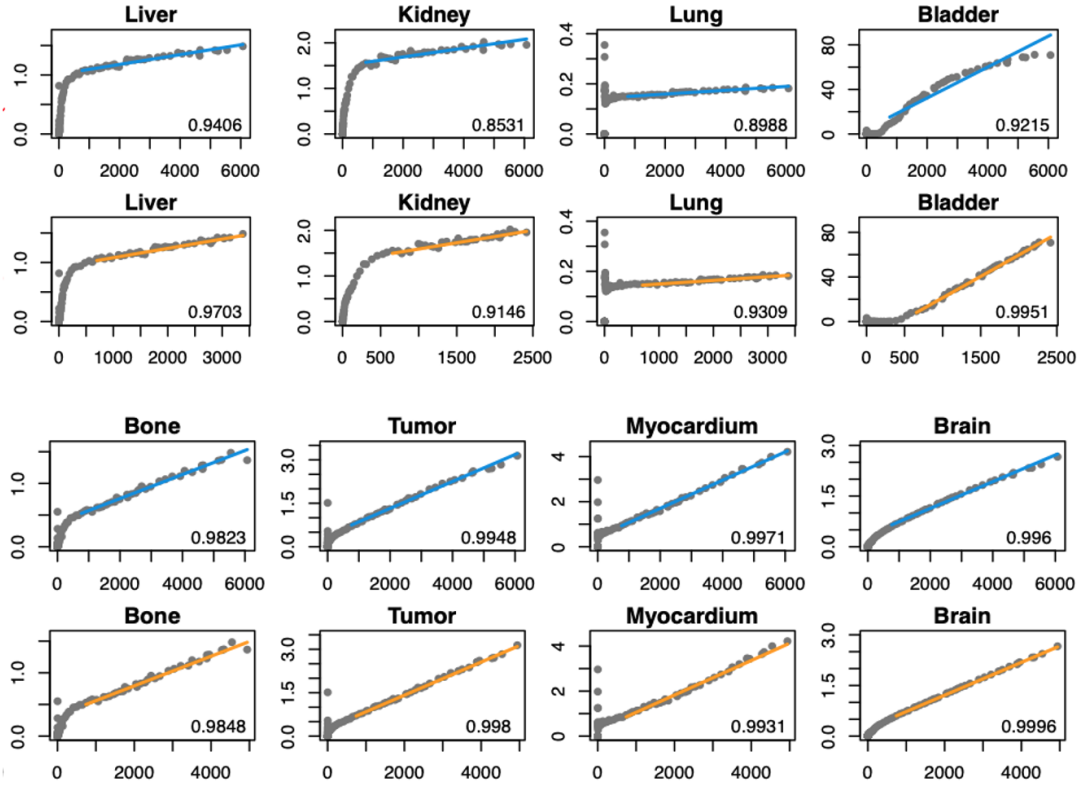


Figure 2.26: standard (sPatlak) and generalized (gPatlak) Patlak plots for different organs. Grey points, blue and orange lines represent data, sPatlak and gPatlak fits, respectively. R squared is indicated on each plot (Gu et al., 2022).

namic sequence. These approaches would be particularly efficient to handle the complexities in dynamic whole-body image datasets. To better characterize the underlying kinetics, some non-parametric methodologies (e.g. B-spline and piecewise linear constant) have been employed (O'Sullivan et al., 2009; Hawe et al., 2012; Chen, Goldsmith and Ogden, 2019). They are more flexible to describe the various kinetics in multiple organs as no parametric restrictions are placed. Furthermore, deep learning is also an appealing tool for the improvement of quantitative accuracy (Wang, Li, Cherry and Wang, 2021; Huang et al., 2022).

Chapter 3

Investigation of the Benefits of Combining Data in Multiple Injection PET Scans

Abstract

Multiple injection dynamic positron emission tomography (PET) scanning is used in the clinical management of certain groups of patients and in medical research. The analysis of these studies can be approached in two ways: (i) separate analysis of data from individual tracer injections, or (ii), concatenate/pool data from separate injections and carry out a combined analysis. The simplicity of separate analysis has some practical appeal but may not be statistically efficient. We use a linear model framework associated with a kinetic mapping scheme to develop a simplified theoretical understanding of separate and combined analysis. The theoretical framework is explored numerically using both 1-D and 2-D simulation models. These studies are motivated by the breast cancer flow-metabolism mismatch studies involving ^{15}O-Water (H_2O) and ^{18}F-Fluorodeoxyglucose (FDG) and repeat ^{15}O-H_2O injections used in brain activation investigations. Numerical results are found to be substantially in line with the simple theoretical analysis: mean square error (MSE) characteristics of alternative methods are well described by factors involving the local voxel-level resolution of the imaging data, the relative activities of the individual scans and the number of separate injections involved. While voxel-level resolution has dependence on scan dose, after adjustment for this effect, the impact of a combined analysis is understood in simple terms associated

with the linear model used for kinetic mapping. This is true for both data reconstructed by direct filtered backprojection (FBP) or iterative maximum likelihood (ML). The proposed analysis has potential to be applied to the emerging long axial field-of-view PET scanners.

3.1 Introduction

Positron emission tomography (PET) scanning is an important diagnostic imaging technique used in the management of patients with cancer and other diseases, as well as in medical research. In clinical settings, PET is typically used to create a single 3-D *static* image of the distribution of the tracer atoms in the field of view in a time-frame of interest, after the tracer has been administered. But PET can also be used to obtain a temporal sequence of scans after radiotracer injection. Such *dynamic* PET scans give the possibility to analyze the transport and retention of tracer in order to recover more detailed metabolic information (Cunningham and Jones, 1993; O'Sullivan, 1993). Most dynamic PET studies involve the use of a single radiotracer, such as ^{15}O-Water (H_2O) for blood flow (Herscovitch, Markham and Raichle, 1983), ^{18}F-Fluorodeoxyglucose (FDG) for glucose metabolism (Phelps et al., 1979) or ^{11}C-verapamil for P-glycoprotein (P-gp) activity (Deo et al., 2014). Studies in which multiple radiotracers are used in the same subject in the same imaging session have the potential to provide more comprehensive profiles of tissue function (Eary et al., 2011; Kadrmas, Rust and Hoffman, 2013), *in-vivo*. Examples include: repeat ^{15}O-H_2O imaging for brain activation studies (Beason-Held et al., 1999), ^{15}O-H_2O and ^{18}F-FDG for breast cancer (Mankoff et al., 2002), ^{13}N-NH3 and ^{18}F-FDG for myocardial viability (Yamagishi et al., 1999; Dilsizian et al., 2013), ^{15}O-H_2O and ^{11}C-Verapamil for assessment of multi-drug resistance (Eyal et al., 2009).

While data from multiple radiotracer scans could be assembled *post-hoc* from separate imaging sessions, acquiring the data in a single imaging session has several advantages. (i) It can reduce issues of anatomic co-registration. This is important for comparing the facets of biology related to multiple tracers, especially for targets that may move between studies, for example, breast (Fowler et al., 2016) and ovarian (Makvandi et al., 2018) cancers comparing FDG PET/CT staging studies to therapeutic biomarkers. No doubt longer separation of injections can lead to more patient motions. (ii) It can reduce potential variation in the physiologic state of the subject from one session to the next (Huang et al., 1982). This is especially true for metabolic studies using H_2O

and FDG or Glutamine and FDG (Zhou et al., 2017). (iii) Tracer parameter estimation for multi-tracers may provide more reliable kinetic analysis due to common dependence of parameters: tracer delivery on flow or tracer clearance on plasma volume and hydration, etc.

With the development of new PET scanners such as Penn Explorer (Karp et al., 2020), uEXPLORER (Badawi et al., 2019) and Siemens Biograph Vision Quadra (Alberts et al., 2021), the longer field of view, increased temporal and spatial resolution, with lower dose are possible. These new scanners offer new opportunities for multi-tracer studies like the dual-tracer imaging with two 18F-labeled tracers using PennPET Explorer (Viswanath et al., 2021; Viswanath, 2020) where combined data with conjoint modeling can help make more robust the comparison of regional differences in the relationship between the biologic parameters measures (Paquette et al., 2020; Mankoff et al., 2019).

Multi-tracer studies bring a range of significant challenges (Krohn et al., 2007), data analysis being one. There are many situations in which the analysis of multi-tracer dynamic studies *must* consider the full temporal time-course of data, see for example, (Spence et al., 1998; Rust and Kadrmas, 2005; Zhang, Morey and Kadrmas, 2016). However, whenever the temporal separation between different tracer injections is much longer than the radiotracer half-life or there is a simple mechanism to correct for spillover (Huang et al., 1982; Koeppe et al., 1998, 2001; Black, McJames and Kadrmas, 2009; El Fakhri et al., 2013), analysis can be approached in one of two ways: (i) studies can be processed separately to recover kinetic information corresponding to individual tracers (Figure 3.1A), or (ii), studies can be concatenated temporally and a combined analysis (Figure 3.1B) of the resulting data carried out.

This chapter develops a simplified theoretical framework for understanding the relative performance of separate and combined analysis of multi-tracer PET studies. The approach is based on a type of linear modeling framework for mapping kinetics (O'Sullivan, 1993; O'Sullivan et al., 2014) - details in section 3.2. The theoretical analysis suggests that after controlling for voxel-level imaging accuracy (resolution), the relative performance of separate and combine kinetic mapping can be understood in simplified terms. A series of numerical experiments, motivated by flow-metabolism mismatch and repeat brain activation studies, are used to directly assess mean square error (MSE) characteristics of combined and separate analysis techniques. These studies consider both filtered backprojection (FBP) and maximum likelihood (ML) reconstructed data

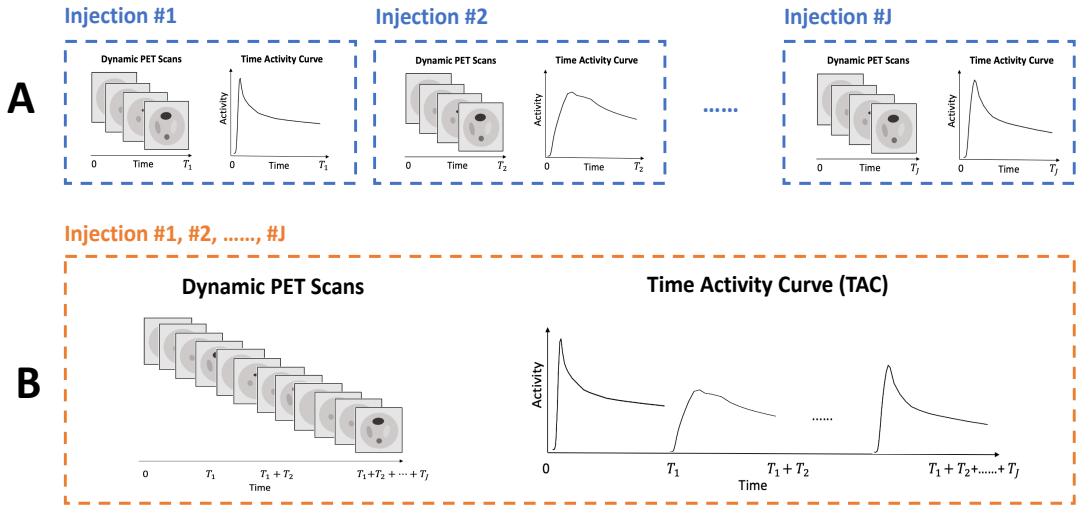


Figure 3.1: Multi-Injection Dynamic PET Studies. A: Separate Analysis; B: Combined Analysis.

as well as a number of important factors including, overall dose, the relative dose of individual tracers and the number of injections involved. Data from numerical experiments are subjected to careful statistical analysis. This helps to clarify the main findings. In flow-metabolism studies, combined analysis improves MSE performance by between 8% and 30%, depending on the reconstruction method used. In the repeat injection studies, MSE improvements increase linearly with the number of injections involved. This is in line with the proposed theory.

The outline of the chapter is as follows: The kinetic mapping approach and the associated analysis of the impact of data combination are developed in section 3.2. An illustrative practical example from a flow-metabolism mismatch study in a breast cancer patient is given in section 3.3. Section 3.4 describes a series of numerical studies based on 1-D and 2-D scanning models. Results are presented in section 3.5. Section 3.6 presents a detailed statistical analysis of simulation results. Further investigations and adaptions are discussed in section 3.7.

3.2 Methodology

The focus is on dynamic PET studies in which it can be assumed that the tracer's interaction with tissue is substantially linear and time-invariant. This assumption is valid for a large class of tracers used in PET, particularly in a cancer setting. The interpretation of time-course data from dynamic studies can be

approached using classical indicator dilution theory (Meier and Zierler, 1954). This theory expresses the measured time-course as a convolution between the arterial input function (AIF) and the so-called tissue residue or impulse response function. The tissue residue is a necessarily monotone decreasing function. Widely used compartmental models (Kety and Schmidt, 1948; Phelps et al., 1979), typically approximate the residue as a positive linear combination of 1 or 2 mono-exponential functions. The spectral method (Cunningham and Jones, 1993) generalizes this to allow the positive combination of potentially many mono-exponentials. In statistical terms, the residue may be viewed as a life-table for tracer atoms introduced to the tissue at time zero via the arterial supply - indeed this is a key part of (Meier and Zierler, 1954). As life-tables can be represented in terms of the underlying distribution (density/histogram) of travel times associated with the physiologic/metabolic journey of individual tracer atoms in the tissue, any residue modeling assumption carries with it a specification for the distribution of such travel times within the volume of tissue being analyzed (O'Sullivan et al., 2009). Compartmental and spectral approximation requires that travel-time densities be spiked at time zero and be monotone decreasing. However, strict monotonicity of travel-time densities may not always be reasonable (Li, Yipintsoi and Bassingthwaighte, 1997). One might imagine this may only be practically important in studies with high-frequency temporal sampling - perhaps only in the context of the emerging PET scanning technologies (Badawi et al., 2019; Karp et al., 2020). However (O'Sullivan et al., 2009) used circa-1996 PET scanner data involving relatively crude temporal sampling to demonstrate significant statistical deficiencies in the ability of the standard 2-compartmental model to correctly represent the regional cerebral time-course of PET-FDG data in highly homogeneous brain regions of normal subjects. The anomaly was identified by considering a more flexible non-parametric analysis of the residue function, with suitable cross-validation adjustment for potential overfitting relative to the 2-compartmental model. In light of this finding, we have been motivated to employ a non-parametric representation of the tissue residue, particularly when analyzing PET time-course data corresponding to large and potentially heterogeneous regions of interest. The concept has been incorporated into a non-parametric residue mapping (NPRM) methodology that we have found useful for parametric imaging of dynamic data from PET imaging of cancer (O'Sullivan, 1993; O'Sullivan et al., 2014). Figure 3.2 shows a schematic. Before we consider the topic of combined analysis of multiple-injection studies, we elaborate on

important details of the NPRM approach. Theoretical points are illustrated numerically in the context of kinetic mapping PET-FDG data.

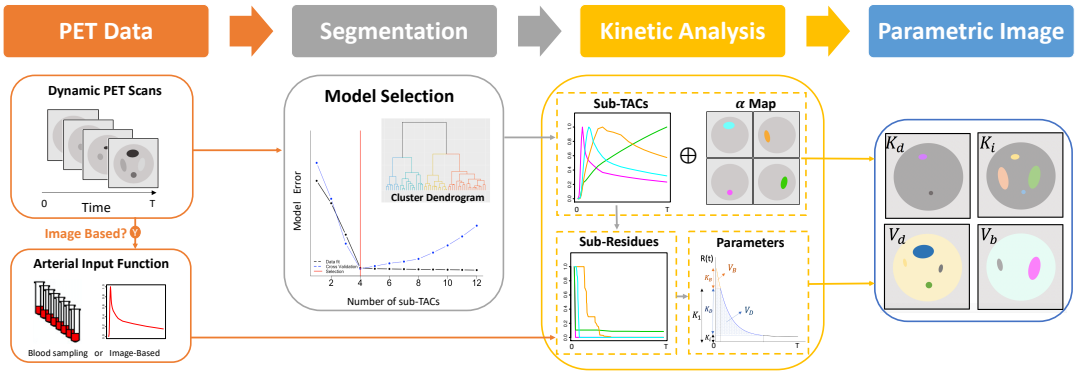


Figure 3.2: Non-parametric residue mapping (NPRM) process.

3.2.1 Voxel-level Kinetic Mapping by the NPRM Approach

There is extensive literature on techniques for mapping kinetics from dynamic PET data - see (Wang, Rahmim and Gunn, 2020) for a recent review including many references. A broad family of techniques, including (Cunningham and Jones, 1993; O'Sullivan, 1993), involves voxel-level representation of the tissue residue as a (positive) linear combination of suitable basis functions. Mono-exponential basis residues are used in (Cunningham and Jones, 1993); more elaborate basis elements, incorporating potentially complex blood-tissue exchange models are proposed in (O'Sullivan, 1993). NPRM technique is a variation on the latter approach in which basis elements (known as sub-TACs) are represented in terms of flexible model-free residues. A full account of the method with several cancer imaging applications is provided in (O'Sullivan et al., 2014). In the current implementation of NPRM, sub-TACs are constructed by a **2-step** data-adaptive process. We elaborate on these steps and indicate how derived kinetic are mapped.

Step 1 applies a standard recursive hierarchical clustering scheme to partition the image volume into a set of S segments or clusters, with the property that the time course data for voxels in the same segment are each approximately proportional to the mean time-course for that segment. Typically the number of segments needed for this is on the order of 100-200. The mean PET-measured time-course data for segments ($\bar{z}_s$) together with their standard deviations ($\bar{\sigma}_s$) are used to produce a reduced data set $\mathcal{D}_S = \{(\bar{z}_{sl}, \bar{\sigma}_{sl}), s = 1, 2, ..., S, l =$

$1, 2, ..., N_T\}$. Here N_T is the number of time-frame of PET data acquisition. Next, the mean time-course data for each segment is modeled to create an associated set of modeled elements $\mathcal{M} = \{\hat{\mu}_s, s = 1, 2..., S\}$. In the case of a single-injection, a generic time-course ($\bar{z}$) in $\mathcal{D}_S$ is modeled ($\hat{\mu}$) by one of: (a) a scaled (venous) injection-site signal (C_{IV}), (b) a non-parametric residue function (R), or (c), a scaled non-parametric distribution function (F) representing the total number of tracer atoms no longer in blood-tissue exchange as a function of time. The first case is applied for the data in the areas between injection site and the corresponding pathway to the left ventricle where arterial pattern is irrelevant. The last case is to accommodate data in which the bladder is in the field of view. Thus

$$\hat{\mu}_l = \hat{A} \cdot C_{IV}(t_l - \hat{\Delta}) \;\; ; \;\; \hat{\mu}_l = \hat{R} \star C_p[t_l - \hat{\Delta}] \;\; ; \;\; \hat{\mu}_l = \hat{F} \star C_p[t_l - \hat{\Delta}] \qquad (3.1)$$

for $l = 1, 2, ..., N_T$. Here $\hat{A}$ is a scale constant and C_p is the time-course of the tracer in the arterial blood (AIF). $\hat{\Delta}$ is an optimized delay factor. $\hat{R}$ and $\hat{F}$ are non-parametrically specified as piece-wise linear functions and estimated using constrained weighted least squares with weights $1/\bar{\sigma}_l^2$. It is important to appreciate that, apart from Δ, all unknowns in (3.1) are linear, so the computation of the optimal fit, for any fixed Δ, is evaluated by quadratic programming (QP). A grid search is used to determine the optimal delay. Choices other than the residue case are only selected if they significantly improve on the residue fit. Modeled elements are supplemented to include time-courses corresponding to the AIF and a further time-course corresponding to the integral of the AIF - the AIF exactly models a spike residue; the integral of the AIF corresponds to a constant residue. In deference to (Patlak and Blasberg, 1985), the latter component is referred to as the Patlak-element. With multiple injections an elaboration of (3.1) is used - details of this are indicated below.

Step 2 of the basis selection procedure takes the full collection of modeled time-course patterns and applies a cross-validation guided backwards elimination procedure to identify a subset of these with the property that positive linear combinations of these patterns adequately fit the reduced dataset $\mathcal{D}_S$. This leads to a final set of basis elements given by a $N_T \times K$ matrix $X = \{\hat{\mu}_1, ..., \hat{\mu}_K\}$. These basis elements ($\hat{\mu}$) are referred to as *sub-TACs* and K is their total number. Given the manner in which the segmentation process is implemented, voxel-level time-course data (z_i) can be expected to be well-approximated by a positive linear combination of sub-TACs. NPRM fits voxel-level data by the

linear model and approximates the voxel-level residue using the components that correspond to a residue process (3.1)

$$z_{il} \approx \sum_{k=1}^{K} \hat{\alpha}_{ik}\hat{\mu}_{lk} = X\hat{\alpha}_i \quad \rightarrow \quad \hat{R}(t, x_i) = \sum_{k \in K_r} \hat{\alpha}_{ik}\hat{R}_k(t) \tag{3.2}$$

where $\hat{R}(t\cdot, x_i)$ is the residue for the i'th voxel. Here K_r is the indices of the subset of sub-TACs that are specified by a residue in (3.1). QP is used to evaluate $\hat{\alpha}_i$.

3.2.1.1 Residue Decomposition and Mapping of Kinetics

Suppose a generic residue function R can be measured over a time interval $[0, T_E]$ - the PET scanning time-frame. Let T_B for $0 < T_B < T_E$ represent a realistic upper-bound for the large-vessel travel-time of tracer atoms - a T_B value of 15 seconds seems physiologically reasonable, for most PET tracers, including FDG and H_2O. Following (O'Sullivan et al., 2014), the residue can be written as a sum of vascular, in-distribution and extracted elements

$$R(t) = R_B(t) + R_D(t) + R_E(t) \tag{3.3}$$

where $R_E(t) = R(T_E)$ for $t \in [0, T_E]$; $R_B(t) = R(t) - R(T_B)$ for $t \in [0, T_B]$ and $R_B(t) = 0$ for $t > T_B$; $R_D(t) = R(t) - R_B(t) - R_E(t)$. Four useful summaries are

$$V_B = \int_0^{T_B} R_B(t)dt \;\; ; \;\; V_D = \int_0^{T_E} R_D(t)dt \;\; ; \;\; K_D = R_D(0) \;\; ; \;\; K_i = R_E(0) \tag{3.4}$$

These assess, large vessel and small vessel distribution volumes (V_B, V_D), non-large vessel flow (K_D) and retention or apparent flux (K_i) at the end of scanning period. Note, that all of these quantities are linear functions of the residue. Tracer extraction is measured as K_i/K_1 where $K_1 = K_D + K_i$ represents the overall flow. By the central volume theorem (Meier and Zierler, 1954), mean transit time (MTT) of non-extracted tracer is measured by a ratio of volume to flow. The measure may be adjusted to account for an overall delay (Δ) in the arrival of tracer atoms to the tissue region. This gives MTT $= V_D/K_D + \Delta$.

In the NPRM procedure voxel-level kinetic parameters are based on the estimated residue in (3.2). This leads to mapped values for $(V_B, V_D, K_D, K_i, K_i/K_1)$. For MTT, we use $\frac{V_D}{K_D} + \bar{\Delta}$ where $\bar{\Delta}$ is the flow-weighted average of the delays $(\hat{\Delta}_k)$ associated with residue components at the voxel being mapped, $i.e.$ at

voxel i, $\bar{\Delta} = \frac{\sum_{k\in K_r} \hat{\alpha}_{ik} K_{Dk} \hat{\Delta}_k}{\sum_{k\in K_r} \hat{\alpha}_{ik} K_{Dk}}$ with K_{Dk} the flow for $\hat{R}_k$. Note (V_B, V_D, K_D, K_i) are linear and $(\text{MTT}, K_i/K_1)$ are (smooth) non-linear functions of α-coefficients in (3.2).

3.2.1.2 Why is the NPRM Approach Reasonable?

The NPRM approach has three important features: (i) In diverse tissue environments the formal theoretical support for compartmental models may be limited (even from an in-vitro stand-point), especially with more novel PET tracers. In this context a non-parametric approach has improved flexibility to adapt to the true (unknown) kinetics. (ii) NPRM can accommodate significant variations in the arrival of tracer to different parts of the field of view. This is accomplished by the inclusion of delays in the modeling of sub-TACs. (iii) NPRM gives an ability to adjust for potential artifacts associated with the bladder or the injection site within the scanner field of view. This is not important in the data presented in this chapter but has relevance in abdominal scanning and in cases where there may be enhanced temporal scanning resolution.

An alternative non-parametric approach, based on a truncated singular value decomposition (SVD), has been used to map perfusion parameters with MR and CT data (Østergaard et al., 1996; Konstas et al., 2009). Unlike the method used here, the SVD approach does not constrain the target residue to be either positive or monotone decreasing. Also, it does not have a mechanism to address heterogeneity voxel-level data or indeed to accommodate artefacts associated with the retention of tracer in the bladder or signals associated with a venous injection site in the field of view. Further examination would be helpful in getting a detailed clarification of the performance of the truncated SVD approach relative to the NPRM technique. NPRM mapping would also seem to have potential for application to perfusion imaging with MR and CT. In addition, the approach may also have a role in quantitative analysis of digital subtraction angiography imaging (DSA) data (Liang et al., 2019).

A small 1-D PET-FDG numerical simulation study comparing NPRM with classic voxel-by-voxel compartmental analysis (Kety and Schmidt, 1948; Phelps et al., 1979) is implemented. Details of the scanning model and source distribution are as specified in section 3.4. The source distribution is specified as a linear combination of specified sub-TACs (μ_k) - like (3.2). In one case (I), source sub-TACs correspond to non-parametric residues derived from regional analysis of breast cancer imaging data; in the second case (II) source sub-TACs are replaced

by the best fitting one-compartment (1C) model (Kety and Schmidt, 1948) to the real data. The table reports the relative root mean square error (RMSE) performance of mapping the six summary kinetic parameters described above, when voxel-level residues are estimated using either the NPRM technique or by application of a 2-compartment (2C) model (Phelps et al., 1979) that includes adjustment for the fractional blood volume and tracer delay (O'Sullivan et al., 2009). The model function (η) is:

$$\eta(t|\beta) = f_b C_p(t-\Delta) + \int_0^t (A_1 e^{-\lambda_1(t-s)} + A_2 e^{-\lambda_2(t-s)}) C_p(s-\Delta) ds \qquad (3.5)$$

where C_p is the AIF and f_b accounts for the contribution from the vasculature. The unknown parameters are $\beta = (\Delta, f_b, A_1, A_2, \lambda_1, \lambda_2)$ - Δ is unconstrained but the other components of β are constrained to be positive.

For computational reasons, associated with the 2C model fitting, RMSE values are based on $N_R = 50$ replicate simulations at each dose. Relative RMSE values, $\hat{e}_{ipd}$ in (3.6), are consistent across $N_d = 5$ dose levels (d) and N voxels (i). Average values and standard errors are summarized for each of the six parameters (p) - $(V_B, V_D, K_D, K_i, MTT, K_i/K_1)$.

$$\hat{e}_p = \frac{1}{NN_d} \sum_{i,d} \hat{e}_{ipd} \quad ; \quad p = 1, 2..., 6 \quad \text{where} \quad \hat{e}_{ipd} = \text{RMSE}^{2C}_{ipd} / \text{RMSE}^{NPRM}_{ipd} \qquad (3.6)$$

Table 3.1 presents the comparisons between the NPRM and 2C methods when the source sub-TACs are generated by a compartmental form (case II) and also when the sub-TACs follow a non-parametric form (case I). Results show substantially enhanced performance of NPRM when the source is not compartmental and a more similar performance when the source is compartmental. Remarkably however, perhaps due to spatial mixing associated with data reconstruction, the 2C method does not perform as well for the V_B and V_D parameters. Indeed NPRM is seen to be strongly competitive with the 2C mapping scheme when the underlying source is specified in terms of a compartment model structure. At its worst, in the case of K_i/K_1, the relative RMSE efficiency of NPRM mapping is 84%. This result is quite typical.

3.2.1.3 Local Error Characteristics of NPRM Mapping

Although the voxel-level model in (3.2) used by NPRM has a linear form, the sub-TACs involved, $X = \{\hat{\mu}_1, ..., \hat{\mu}_K\}$, are derived by a complex data-adaptive

Table 3.1: Relative Performance (3.6) of NPRM and 2C kinetic mapping in a PET-FDG setting. Based on a 1-D simulation model with source sub-TACs in case I matched to real Breast Cancer data Figure 3.8 and to their best-fitting 1C model fit in case II. Data reconstruction by both direct (FBP) and iterative (ML) methods.

Parameters (p)		V_B	V_D	K_D	K_i	MTT	K_i/K_1
I	FBP	1.64 ± 0.02	1.45 ± 0.03	1.13 ± 0.02	1.06 ± 0.01	1.60 ± 0.03	1.60 ± 0.05
	ML	1.78 ± 0.02	1.43 ± 0.03	1.19 ± 0.02	1.05 ± 0.01	1.51 ± 0.03	1.65 ± 0.05
II	FBP	1.32 ± 0.01	1.36 ± 0.02	0.92 ± 0.02	0.97 ± 0.01	0.97 ± 0.01	0.84 ± 0.02
	ML	1.38 ± 0.02	1.31 ± 0.02	0.97 ± 0.03	0.96 ± 0.01	0.94 ± 0.01	0.85 ± 0.02

process. Hence the overall error in voxel-level kinetics is a function of the uncertainties in the estimation of α-coefficients *and* the uncertainties in the construction of sub-TACs. Intuitively, because the sub-TACs are constructed by modeling average time-course data for segments, one might expect that the uncertainties associated with the sub-TACs have a minor impact on the error on NPRM voxel-level kinetics. In order to justify this intuition, we report on another simulation. Here we used a standard 2D PET-FDG simulation in which voxel-level kinetics were assessed using both known and unknown data-estimated sub-TACs. The 2-D context is used as the segmentation process with 2-D data gives rise to more realistic subsets of data defining each sub-TAC. The scanning model and source structure are as described in section 3.4. The statistical relation between the RMSE (averaged across voxels) using known and unknown sub-TACs are shown in Table 3.2. This study only considered a single (realistic) dose and was restricted to a modest number of replications ($N_R = 50$) - standard errors of simulation estimated quantities of interest do not suggest we need any more. The results show that kinetic mapping errors are substantially the same regardless of whether or not sub-TACs are known. Thus when analyzing voxel-level NPRM kinetic mapping errors, it seems sufficient to focus on error associated with determination of voxel-level α-coefficients conditional on known model sub-TACs. We will adopt this approach in our analysis of the impact of data combination.

Table 3.2: Impact of data-adaptive sub-TAC selection in NPRM on Kinetic Mapping errors. Statistical model: RMSE $_p^{unknown} \approx \beta_p$ RMSE $_p^{known}$. Results based on a 2D PET-FDG simulation with FBP reconstruction. Standard errors for estimates are the order of 0.01.

Parameters (p)	V_B	V_D	K_D	K_i	MTT	K_i/K_1
β	0.99	0.97	0.82	1.01	0.92	1.03
R^2	0.99	0.97	0.93	0.97	0.90	0.94

We now focus on what controls NPRM kinetic mapping error. A simplistic linear model analysis (Seber, 2009) of the NPRM model (3.2) would suggest that the RMSE of the kinetic summaries should substantially scale with the level of uncertainty in the reconstructed data. Thus for a given voxel (i) the error in an estimate of kinetic variable, $\hat{\theta}_{ip}$, denoted RMSE_{ip}^{NPRM} should have a strong relation to the corresponding root-mean-square deviation between the reconstructed time-course data (z_{il}) and the true voxel-level time course (λ_{il}) - $\text{RMSE}_i^z = \sqrt{\frac{1}{N_T}\sum_{j=1}^{N_T}[z_{il}-\lambda_{il}]^2} \equiv \hat{\sigma}_i$. We examined this numerically using the simulation data used to produce Table 3.1. The statistical analysis, which incorporated data from a range of dose settings, finds

$$\log(RMSE_{ip}/\theta_{ip}) \approx \alpha_p + \beta_p \log(\hat{\sigma}_i/\theta_{ip}) \tag{3.7}$$

well-describes the relation between voxel-level errors in kinetics and the local reconstruction accuracy of the input data ($\hat{\sigma}_i$). Model R^2-values and β-coefficients are given in Table 3.3. Note that (3.7) suggests formal mean square error convergence of the NPRM procedure - as the reconstruction error diminishes so too does the error in determination of kinetics. The rate of convergence, measured by the β_p coefficient, is seen to be close to 1 and suggests that standard parametric inference asymptotics apply to this situation (Van der Vaart, 2000). A similarly strong relation is found between the modeling error associated with the linear model (3.2), $\text{RMSE}_i^{\hat{\lambda}} = \sqrt{\frac{1}{N_T}\sum_{j=1}^{N_T}[\hat{\lambda}_{il}-\lambda_{il}]^2} \equiv \hat{\sigma}_i^{\lambda}$, and the RMSE of the kinetic summaries, $i.e.$

$$\log(RMSE_{ip}/\theta_{ip}) \approx \alpha'_p + \beta'_p \log(\hat{\sigma}_i^{\lambda}/\theta_{ip}) \tag{3.8}$$

In simulations this is important as it allows us to use modeling error as a surrogate metric for the analysis of errors in individual kinetic variables.

3.2.2 Multiple Injections and their Combined or Separated Analysis by NPRM

With multiple injections the model in (3.1) is elaborated to account for the effect of individual injections and the separate delay factors that may be associated with measurement of the tracer AIFs. This gives

$$\hat{\mu}_k = \sum_{j=1}^{J} \hat{A}_j \cdot C_{IV}^{(j)}(t_k - \hat{\Delta}_j) \;\; ; \;\; \hat{\mu}_k = \sum_{j=1}^{J} \hat{R}_j \star C_p^{(j)}[t_k - \hat{\Delta}_j] \;\; ; \;\; \hat{\mu}_k = \sum_{j=1}^{J} \hat{F}_j \star C_p^{(j)}[t_k - \hat{\Delta}_j] \tag{3.9}$$

Table 3.3: Voxel-level errors in NPRM kinetics as a function of the local reconstruction ($\hat{\sigma}_i$) and modeling ($\hat{\sigma}_i^{\lambda}$) errors - $c.f.$ (3.7),(3.8). Results based on 1D-PET-FDG simulation.

	Parameters (p)	V_B	V_D	K_D	K_i	MTT	K_i/K_1
FBP	β	0.82	1.03	0.82	0.95	0.99	0.97
	R^2	0.96	0.93	0.88	0.99	0.99	0.97
ML	β	0.78	1.02	0.88	0.97	0.99	0.98
	R^2	0.78	0.88	0.87	0.98	0.98	0.96
FBP	β'	0.86	1.03	0.88	0.97	0.99	0.99
	R^2	0.98	0.92	0.92	0.99	0.98	0.96
ML	β'	0.77	1.01	0.89	0.98	0.99	0.99
	R^2	0.83	0.88	0.88	0.98	0.98	0.96

Here the index j relates to individual injections. As with (3.1), the residue and outflow functions can either be modeled using suitable parametric forms (Kadrmas and Hoffman, 2013; O'Sullivan, 1993; Spence et al., 1998) or with non-parametric formulations as used by (Lan, Muzi and O'Sullivan, 2019). Note the non-parametric approach leads to an optimization problem, in which only the delay factors Δ_j enter in a non-linear fashion. This simplifies computation. Our interest is in the case where it is possible to consider the separate analysis of kinetics of individual injections. In this setting, because there is negligible temporal overlap (spillover) between the separate injections, modeling of sub-TACs in the NPRM voxel model can be accomplished by separate application of the simple form in (3.1). Regardless of whether there is overlap or not, voxel-level kinetic parameters, say $\{\theta_p, p = 1, 2, ...P\}$, are expressed as simple functions of the α-coefficients in (3.2). Thus $\hat{\theta}_{ip} = g_p(\hat{\alpha}_i)$ where g_p is a (smooth) function defined using the estimated residue functions and delay factors for separate injections.

If data are combined, coefficients are obtained based on the full time-course for the measured data and the sub-TACs. Separate analysis recovers kinetics based on the shorter sub-TAC time-course corresponding to individual injections. Now suppose we are interested in a kinetic summary variable corresponding to the j'th tracer injection - say $\theta = g(\alpha)$. The separate analysis estimate, $\hat{\theta}^j = g(\hat{\alpha}^j)$, is based on fitting (3.2) using only the j-injection time-course; the combined estimate, $\hat{\theta}^C = g(\hat{\alpha}^C)$, is based on fitting the full time-course data. Thus at the i'th voxel we would map the kinetic parameter associated with g using one of

$$\hat{\theta}_i^j = g(\hat{\alpha}_i^j) \text{ or } \hat{\theta}_i^C = g(\hat{\alpha}_i^C) \tag{3.10}$$

Intuitively, we expect that the combined data estimator will be preferred but it is helpful to have a quantitative appreciation of the factors that might be important. The results reported in the chapter address this issue via numerical simulation. Before that, we present a simplified theoretical analysis that may give some intuition.

3.2.3 An Approximate Theoretical Analysis of Combined versus Separated Analysis

Table 3.3 suggests that regular parametric statistical inference theory associated with Gaussian approximation applies to the NPRM model coefficient estimates and the derived kinetic variables. In light of this it seems reasonable to use Gaussian approximation to develop insight into the potential benefits of combined versus separate analysis for multi-injection studies. By Gaussian approximation we get the following.

Result 3.2.1. *If the conditions for Gaussian approximation hold, the combined analysis estimator always has lower variance than the separate injection estimator. For a given kinetic parameter (θ), the ratio of the MSE of the combined analysis estimate, based on J injections, to the MSE of the separate analysis estimate, using only study j, is given by the formula*

$$\frac{MSE(\hat{\theta}^C)}{MSE(\hat{\theta}^j)} = \frac{\sigma_j^{-2}}{\sigma_1^{-2} + \sigma_2^{-2} + ... + \sigma_J^{-2}} \tag{3.11}$$

where σ_j^2 is the variance of the kinetic parameter based on data from injection j.

The theoretical justification for this result is provided below. In replicate studies, individual scan variances (σ_j) are identical so the MSE ratio is $1/J$, $i.e.$ the percent improvement in MSE with the combined analysis is proportional to $(J-1)$. While the combined analysis will always produce better estimates, the amount of improvement will depend on the reliability of the other scans involved. (3.8) indicates that the reliability of kinetics for individual scans kinetics is a function of the associated source model error. We would anticipate that the study dose and relative sharpness of the AIF, which impact voxel-level model error, would play a role. Numerical studies will explore this in some detail.

Derivation of Formula in (3.11) Gaussian approximation of estimates of α-coefficients means that as any voxel we can assume

$$\hat{\alpha}^j \sim N(\alpha, \Sigma_j) \tag{3.12}$$

where Σ_j is a covariance matrix associated with the weighted least squares estimation process. Within the Gaussian framework $\hat{\alpha}^j$ is a sufficient statistic, $i.e.$ it captures the full information about α based on the j'th can data. As a result the optimal (maximum-likelihood) combined estimator of α is a matrix-weighted average of the individual scan estimators, $i.e.$

$$\hat{\alpha}^C = \left[\sum_{j^*} \Sigma_{j^*}^{-1}\right]^{-1} \left[\sum_{j} \Sigma_j^{-1}\hat{\alpha}^j\right] \quad ; \quad \hat{\alpha}^C \sim N(\alpha, \Sigma_C) \tag{3.13}$$

where $\Sigma_C = \left[\Sigma_1^{-1} + ... + \Sigma_J^{-1}\right]^{-1}$. We can write Σ_C as $\Sigma_j^{1/2}\left[I + B_j\right]^{-1}\Sigma_j^{1/2}$. where

$$B_j = \sum_{j^* \neq j} \Sigma_j^{1/2}\Sigma_{j^*}^{-1}\Sigma_j^{1/2} \tag{3.14}$$

Clearly B_j is symmetric and positive definite. Thus if λ_j is the smallest eigenvalue of B_j, then for any vector v, we have

$$v'[I + B_j]^{-1}v \leq [1 + \lambda_j]^{-1}v'v \tag{3.15}$$

Since $\lambda_j \geq 0$, it follows that for any parameter (θ) defined by a linear combination $\theta = \xi'\alpha$

$$\frac{E[\hat{\theta}^j - \theta]^2}{E[\hat{\theta}^C - \theta]^2} = \frac{Var(\hat{\theta}^j)}{Var(\hat{\theta}^C)} \geq [1 + \lambda_j] \geq 1 \tag{3.16}$$

$i.e.$ the combined estimator will always have a smaller MSE than the single scan estimate.

More generally suppose that Gaussian approximation applies directly to the kinetic parameter, $\theta = g(\alpha)$. This might follow by first-order Taylor series expansion of $g(\hat{\alpha})$ about α (Van der Vaart, 2000). With this we would have

$$\hat{\theta}^j \sim N(\theta, \sigma_j^2) \quad where \;\; \sigma_j^2 = v'\Sigma_j v \tag{3.17}$$

and v is the gradient of g evaluated at α. As in (3.12), $\hat{\theta}^j$ is now (to within the approximation) sufficient for estimation of θ based on the information acquired in the j'th scan. The optimal combined scan estimator is a weighted average of

these estimates

$$\hat{\theta}_C = \frac{\sigma_1^{-2}\hat{\theta}_1 + \sigma_2^{-2}\hat{\theta}_2 + ... + \sigma_J^{-2}\hat{\theta}_J}{\sigma_1^{-2} + \sigma_2^{-2} + ... + \sigma_J^{-2}} \tag{3.18}$$

Thus $\theta^C \sim N(\theta, \sigma_C^2)$ with $\sigma_C^2 = \frac{1}{\sigma_1^{-2}+\sigma_2^{-2}+...+\sigma_J^{-2}}$. The result in (3.11) follows from this.

3.3 Illustration with a Flow-Metabolism Study in a Breast Cancer Patient

The data come from a study conducted on a breast cancer patient prior to surgical resection and prior to scheduled neoadjuvant chemotherapy. PET scanning involved dynamic imaging with ^{15}O-H_2O and ^{18}F-FDG in the same session. ^{15}O-H_2O is a tracer used to measure blood flow and perfusion - the gold-standard technique for *in-vivo* measurement of such information. ^{18}F-FDG is the most widely used clinical PET tracer. FDG measures information about tissue glucose utilization. It is a key marker used in the diagnosis and clinical management of several cancers. Details of PET dynamic imaging protocols for H_2O-FDG scanning in breast cancer and reports on the prognostic utility of the derived information are given in the earlier reports - see (Mankoff et al., 2002, 2003; Dunnwald et al., 2008, 2011). For the data we present here, 1302 MBq of ^{15}O H_2O in a 1-4 mL volume was injected as a bolus and 318 MBq of ^{18}F-FDG in 7-10 mL volume was injected over 2 minutes with a constant infusion pump. Data were acquired on a GE-Advance scanner using a plane-by-plane FBP reconstruction algorithm with corrections for attenuation, scatter, deadtime and random events. The 4-D PET data set consists of an imaging volume with $N = 128 \times 128 \times 35$ voxels and $T = 82$ (57 for H_2O and 25 for FDG) time frames of acquisition. Dynamic ^{15}O-H_2O images were collected for 8.75 min according to the following acquisition sequence (number of time frames and their durations): 1×1 min (pre-injection), 15×2 s, 15×5 s, 12×10 s, 8×15 s and 6×20 s. The FDG injection and dynamic imaging followed H_2O. The FDG acquisitions were conducted over 61 minutes according to the sequence: 1×1 min (pre-injection), 4×20 s, 4×40 s, 4×1 min, 4×3 min and 8×5 min.

The data were analyzed using the NPRM technique described in section 3.2. Arterial input functions used were recovered from the left-ventricle (LV) of the heart using the technique reported in (O'Sullivan et al., 2017). Kinetics were mapped using both separate and combined analysis of the H_2O and FDG data.

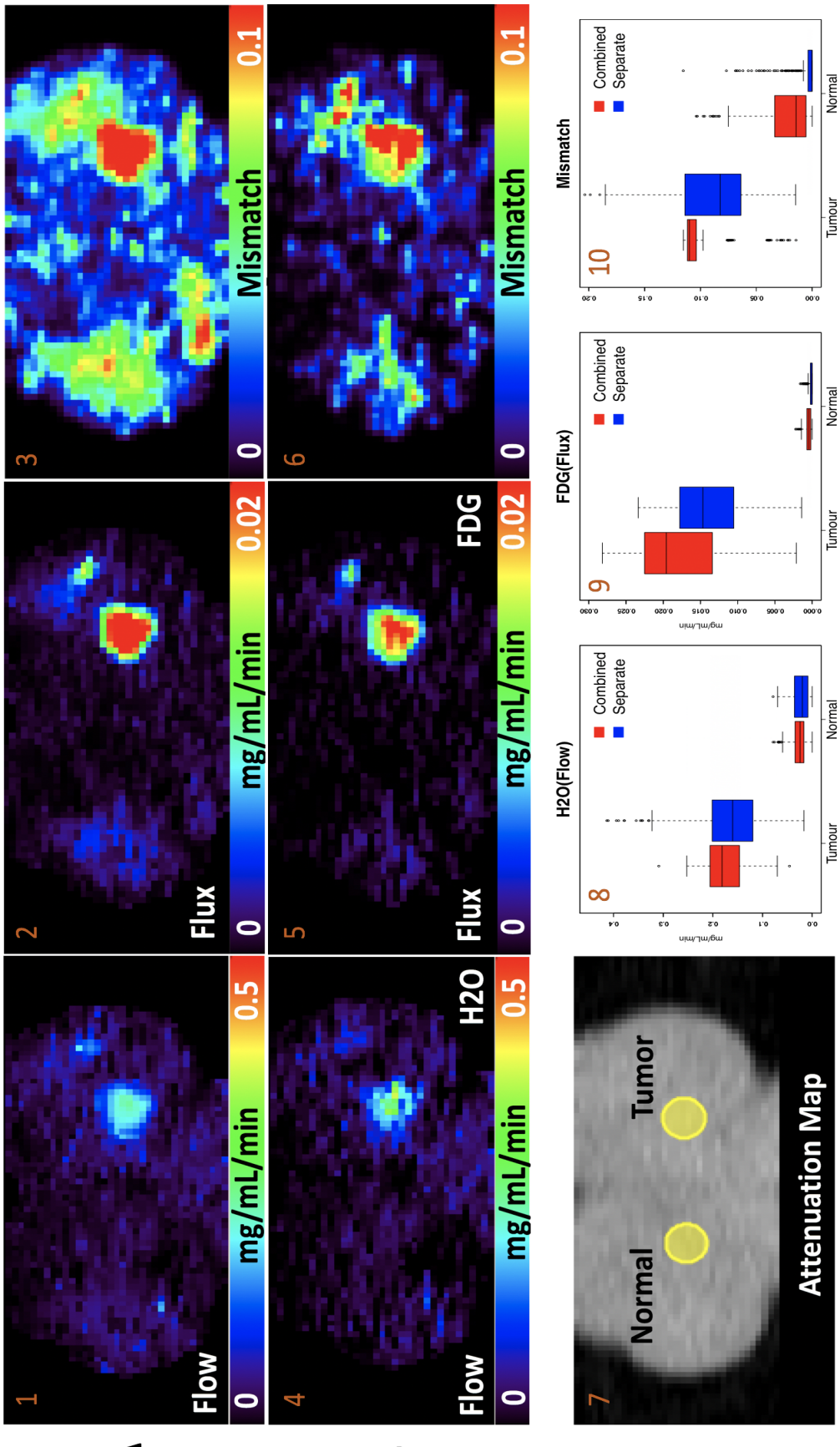


Figure 3.3: Estimates of flow, flux and mismatch in a H_2O-FDG breast cancer study from combined and separate analysis. Row A: Combined Analysis; Row B: Separate Analysis; Row C: ROI Analysis.

This analysis provides voxel-level mapping of H_2O blood flow (K_1^O, mg/mL/min), FDG metabolic rate or flux (K_i^F,mg/mL/min) and metabolism-flow mismatch ratio (K_i^F/K_1^O) for separate or combined analysis approaches. Results are presented in Figure 3.3. Coronal planes of metabolic parameters demonstrate increased flow and metabolism in the tumor. The flow-metabolism mismatch is also seen to be highly elevated in the tumor region - an elevated mismatch has been shown to be associated with poor response to chemo-therapy and early cancer relapse (Mankoff et al., 2002). In qualitative terms the flow and mismatch maps recovered by separate analysis appear more noisy, the flux maps are not much different. To explore these differences more carefully, two regions-of-interests (ROIs) - normal breast (335 voxels) and tumor (322 voxels) are extracted, as shown in Figure 3.3. The distribution of metabolic parameters in these two ROIs is presented in boxplots in Figure 3.3.

We can see the flow distributions in tumor and normal breast are more variable for the separate analysis, the standard deviations (SD) of flow from combined and separate analysis in 2 ROIs are 0.04 and 0.07 (tumor), 0.014 and 0.018 (normal breast) respectively. The additional variability is on the order of 75% and 28.6% in tumor and normal breast. For flux, the standard deviations with the two approaches are 0.006 and 0.005 (tumor), 0.0004 and 0.0003 (normal breast). These differences are small. The variability of mismatch from separate analysis is much bigger than the combined analysis in the tumor region - the situation is somewhat reversed in the normal region but this could also be due to an underestimation of the normal tissue flow in the separate analysis. In light of these results, we are motivated to develop a better understanding of the relative statistical behavior of combined and separate analysis of this and similarly structured multiple injection studies.

3.4 Numerical Experiments

We conducted two sets of experiments, one related to the H_2O-FDG study in section 3.3 and a second one relating to repeat H_2O activation studies. A schematic for the structure of the simulation process is provided in Figure 3.4. Below we provide details of the setup of the 1-D and 2-D simulation models used, the specification for the source distributions in the two examples and, finally, the procedure used to compare the performance of the combined and separate analysis techniques. FBP and ML reconstructions are both considered in 1D simulation studies, but for computational efficiency we restrict the H_2O-FDG

setup to only FBP reconstruction in the 2-D case.

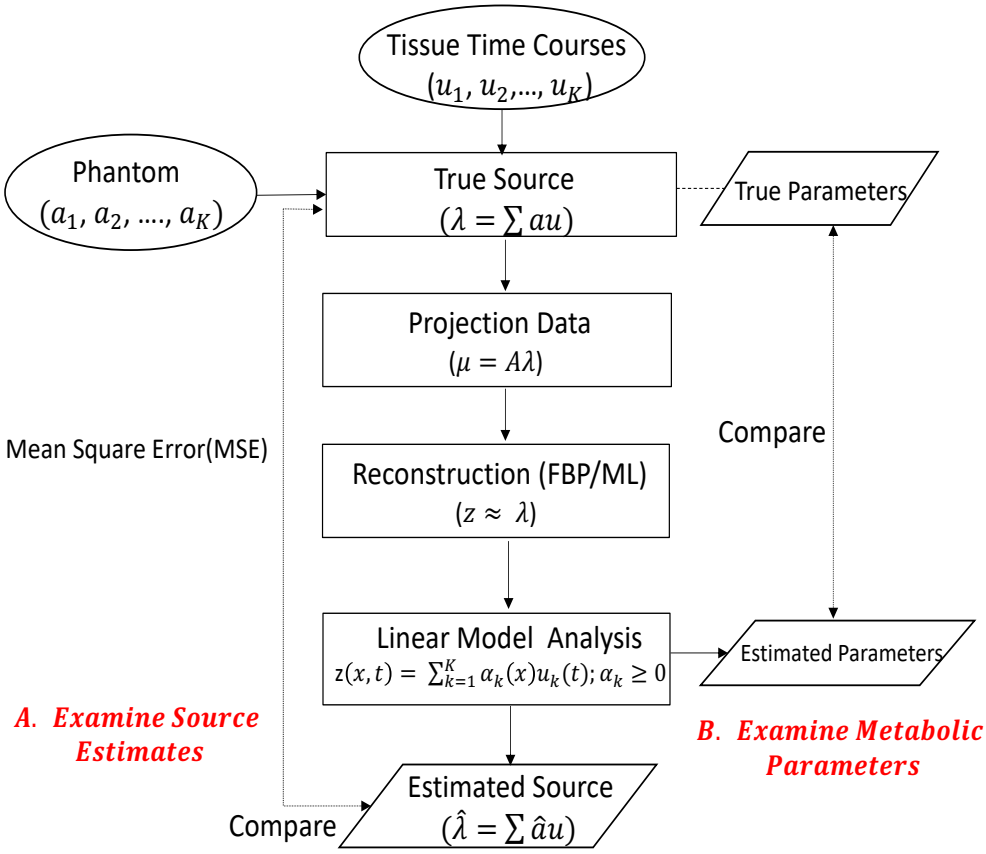


Figure 3.4: Diagram of Simulation Process

3.4.1 Scanning Models

In the 2-D case a standard PET scanning model involving Poisson sampling of a discretized (attenuated) parallel-beam Radon transform of the source is used (Kak, Slaney and Wang, 2002; Natterer, 2001). The imaging domain is the unit square, discretized to an array of dimension 128×128, and the projection domain is the region $[-\sqrt{2}, \sqrt{2}] \times [0, \pi]$, discretized to a 183×181 sinogram array of distances and angles. For computational reasons numerical experiments in 2-D only consider direct FBP reconstruction. In 1-D a less familiar Poisson deconvolution model is employed. The model is used because the computational efficiencies enable us to carry out a sufficient number of replicate studies using both direct and iteratively reconstructed data. Full details of the model are given in (O'Sullivan and Roy Choudhury, 2001). The observed data over a given time-frame is a realization from a projected and scaled source. The projection process is given by the product of a fixed attenuation profile ($a > 0$) and

the discrete convolution between the scaled source and a kernel κ^β ($\beta > 0$). The kernel acts to smooth the source - its discrete Fourier transform is given by

$$\kappa_\nu^\beta = |\nu|^{-\beta} \quad \text{for} \quad \nu = \pm 1, \pm 2 ... N/2 \; .$$

If y is a realization from the projected and scaled source then the direct reconstruction of y is simply obtained

$$z^* = \frac{1}{\tau} \mathcal{F}^{-1} \{ |\nu|^\beta \widehat{(y/a)}_\nu \}$$

where $\widehat{(y/a)}$ is the discrete Fourier transform of the attenuation corrected count data, $\mathcal{F}^{-1}$ represents the inverse transform and τ is the expected total counts (dose) used for scaling. Smoothing is achieved by convolving the raw reconstruction z^* with a discrete Gaussian kernel. The smoothed reconstruction is an analogue of an FBP reconstruction used in PET. ML reconstructions are readily obtained in this setting. Standard iteratively re-weighted least squares (IRLS) (with positivity constraints) apply. The convolution structure allows such iterates to be easily evaluated. Similar to FBP, the raw ML estimator can be smoothed to obtain an analogue of the expectation–maximization (EM) reconstruction methods used in PET. The simple convolution model captures the essential estimation complexity of PET. This is because the reconstruction filter acts like a fractional derivative. By choice of β, it is possible to adapt the model so that the behavior of the reconstruction MSE as a function of count rate, is matched to 2-D PET. Experimentation presented in section 3.7 with the breast FDG data in section 3.3 found that a value of $\beta = 1.35$ in the 1-D scanning model worked well. This is the setting we use in the studies reported here.

3.4.2 Source Patterns

The true (target) source is expressed as a linear model with K components.

$$\lambda(x,t) = \alpha_1(x)\mu_1(t) + \alpha_2(x)\mu_2(t) + ... + \alpha_K(x)\mu_K(t) \tag{3.19}$$

In the 2-D case we only consider the H_2O-FDG studies. The configuration is matched to the real data presented in section 3.3 - see Figure 3.5. Spatial patterns correspond to a central slice through the tumor region; the temporal patterns including the AIF come from the full data set.

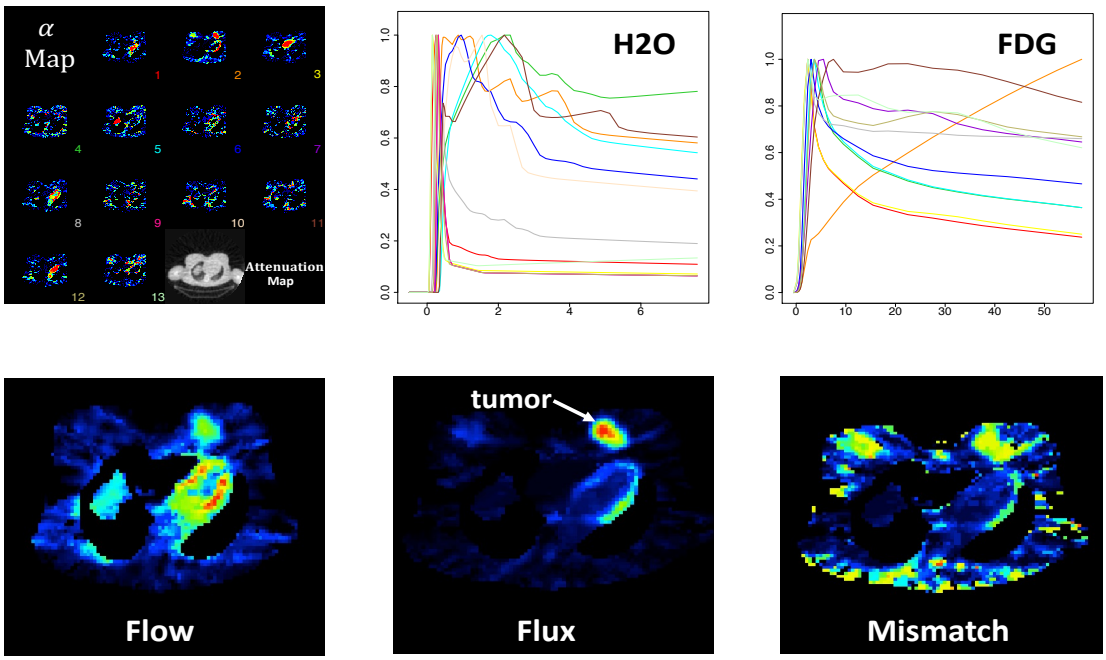


Figure 3.5: Source distribution, $\lambda_{xt} = \sum_{k=1} \alpha_k(x)\mu_k(t)$ for 2D simulations. Row 1: α map and normalized time courses (μ) for H_2O and FDG. Row 2: True parametric images for flow, flux and mismatch.

The source specification is more abstract in the 1-D case. Figure 3.6 shows the spatial pattern of the α-coefficients and how they are transformed into the measurement domain. This aspect is the same for H_2O-FDG and the repeat H_2O studies. The shape of the AIFs for H_2O and FDG match those in the breast cancer data. The time-course patterns for the H_2O-FDG are also adapted from the breast cancer analysis; in the repeat H_2O studies, a 1-compartmental Kety-Schmidt (Kety and Schmidt, 1948) model is used to create patterns relating to regions in a normal brain - parameters are given in Figure 3.6. Figure 3.7 shows observed time course patterns for H_2O and FDG from six ROIs in the breast data, together with the fit corresponding to the analysis in section 3.3. The time courses fitted by NPRM are used. The simulation uses a range of seven dose levels τ. The range is adapted to produce data with a voxel-level noise pattern matched to real data. For the H_2O-FDG studies, the relative dose of the H_2O and FDG injections are also varied. A range of seven dose-ratio settings from $16:1$ to $64:1$ are examined. The middle dose ratio corresponds to the data in section 3.3. Simulated data, at the middle dose and dose ratio for the H_2O-FDG studies, are in Figure 3.8. The simulation noise level is a reasonable match to that seen in the real data. The repeat H_2O study is calibrated in the same way, but not presented. In repeat H_2O studies we consider situations in

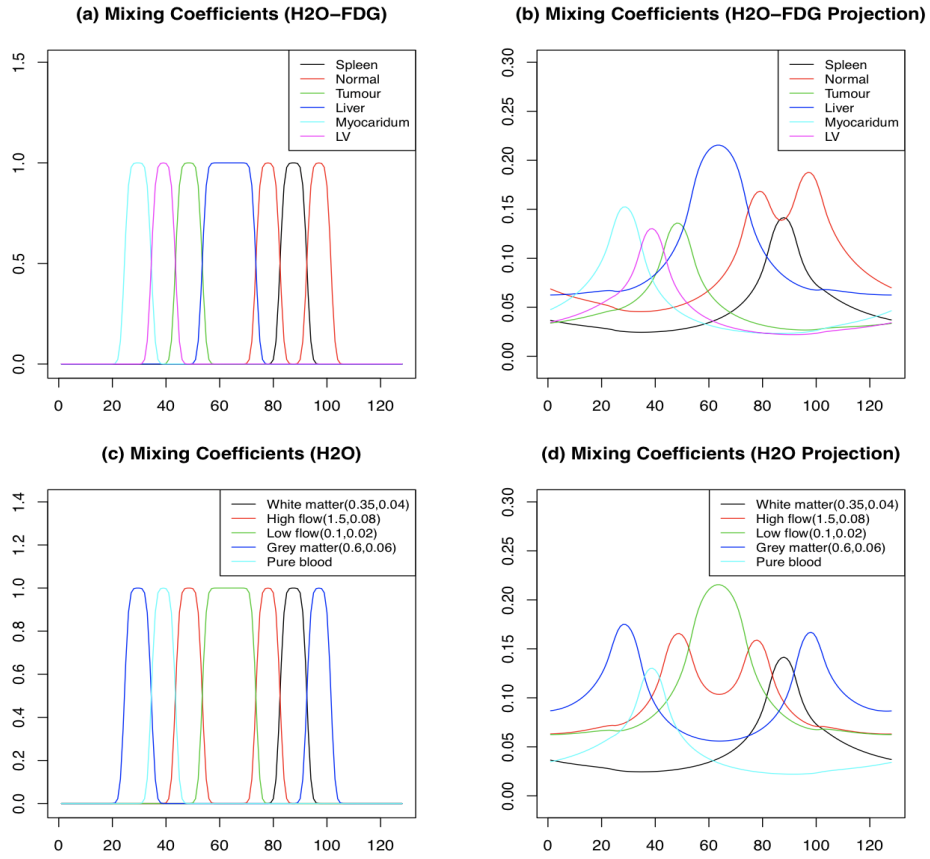


Figure 3.6: 1-D phantom (mixing coefficients - α_k's) and their projections for H_2O-FDG (a,b) and repeat H_2O studies (c,d). x-axis is location (1-128) and y-axis is coefficient. Different colors represent different ROIs. Values of the Kety model parameters $(K_1, K_1/k_2)$ used to create simulated time courses are given in the legends for (c) and (d).

which there are 2, 4, 6 and 8 separate H_2O injections. In 1-D studies with FBP and ML reconstructed data are reported. All studies, both for the H_2O-FDG and repeat H_2O, are replicated 500 times for each dose and in the H_2O-FDG case for each dose-ratio setting.

3.4.3 Evaluation of Performance

Our studies use the model MSE characteristics of the estimated source, as a surrogate for understanding the MSE characteristics of estimates of the mapped kinetics. The motivation for this comes from Table 3.3 which showed a setting where MSE characteristics of mapped kinetics are proportional to the MSE reliability of the underlying source estimate. As indicated in Figure 3.1 the overall scan period, T, is made up of a set of J non-overlapping time intervals corresponding to the scanning periods for the separate tracer injections under

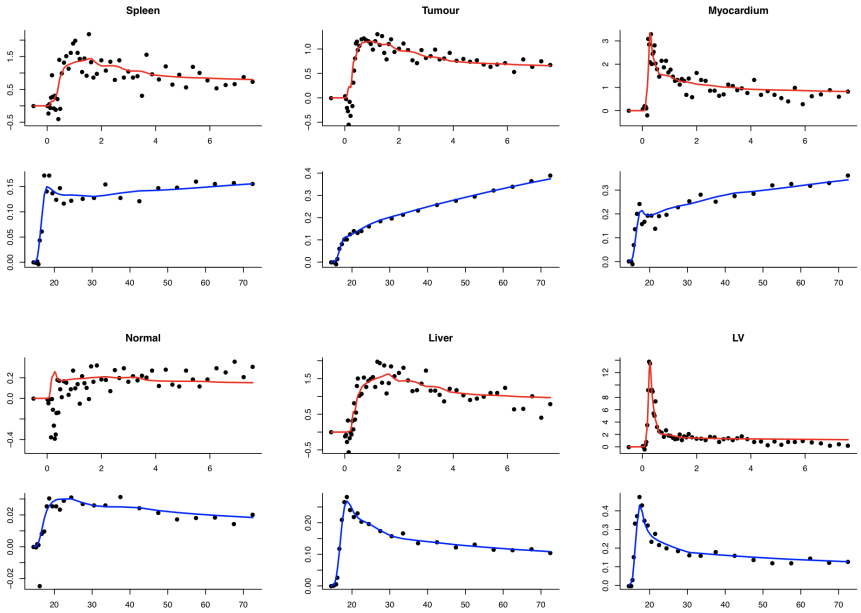


Figure 3.7: Fitted time courses and real data for six kinds of tissues - spleen, tumor, myocardium, normal breast, liver and left ventricle (LV). Red and blue lines are fitted time courses for the H_2O and FDG studies, respectively. Black points are real data. x and y axis are time (minutes) after injection and activities (MBq/cc).

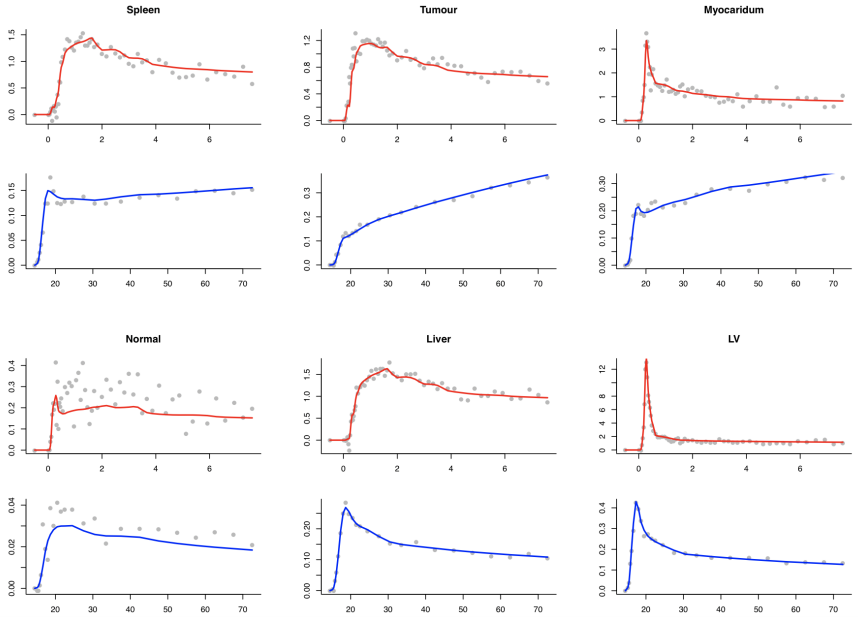


Figure 3.8: True time courses and simulated image data at middle dose and dose ratio for same six kinds of tissues. Red and blue lines are true time courses for H_2O and FDG studies in simulation, respectively. Grey points are simulated data. x and y axis are time (minutes) after injection and activities (MBq/cc).

consideration, $T = T_1 \cup T_2 \cdots \cup T_J$. If $\hat{\alpha}^C$ is the combined estimate coefficient, the corresponding estimated source is $\hat{\lambda}^C(x,t) = \sum_{k=1}^K \hat{\alpha}_k^C(x)\mu_k(t)$ and the squared error assessment is

$$Se(\hat{\lambda}^C, \lambda) = \int_{\Omega_x} \sum_j \frac{1}{D_j \bar{\lambda}_j^2} \int_{T_j} [\hat{\lambda}^C(x,t) - \lambda(x,t)]^2 dt dx \tag{3.20}$$

where D_j and $\bar{\lambda}_j$ are the durations and maximum intensities for the j'th scan. Integrals are evaluated by simple discretization. For the separate scan case, the estimate of the source for the j'th time-interval is based on the corresponding coefficients ($\hat{\alpha}^j$) - *i.e.* $\hat{\lambda}^S(x,t) = \sum_{k=1}^K \hat{\alpha}_k^j(x)\mu_k(t)$ for $t \in T_j$. In this way an overall assessment for the separate scan analysis is obtained as $Se(\hat{\lambda}^S, \lambda)$. With simulated data, we evaluate the error of combined and separated scan estimators for study replicates and by averaging an MSE assessment for the source error is obtained. This gives

$$MSE^C = E(Se(\hat{\lambda}^C, \lambda) \quad \text{and} \quad MSE^S = E(Se(\hat{\lambda}^S, \lambda) \tag{3.21}$$

Relative percent improvement is assessed by

$$\%\text{Improvement} = \frac{MSE^S - MSE^C}{MSE^C} \times 100\% = (\frac{MSE^S}{MSE^C} - 1) \times 100\% \tag{3.22}$$

3.5 Results

We begin by presenting some sample results for the H_2O-FDG and repeat H_2O studies. This is followed by detailed MSE comparisons, including some associated plots.

3.5.1 Sample Metabolic Parameters Estimates

In the breast cancer study, H_2O and FDG are used to measure blood flow and glucose metabolism, respectively. Metabolic parameter comparisons for a single replicate at the middle dose and dose-ratio are presented in Figure 3.9. True parameters are represented by black lines. Estimated parameters from combined and separate analysis are shown using dashed red and blue lines separately. We can see metabolic estimates from combined analysis are closer to the true parameters and show more advantages in H_2O study. Metabolism estimated from these two approaches are both close to the true values in FDG study and differ-

ence can be negligible. The quantitation of H_2O can get more benefits from the combined analysis and these results are also consistent with findings from the real dataset in section 3.3. Similarly, we also show one sample metabolic parameters - flow and blood volume (V_B) at the middle dose in a repeat H_2O study (H_2O^*) in Figure 3.9. The combined analysis is seen to achieve improvements in both situations.

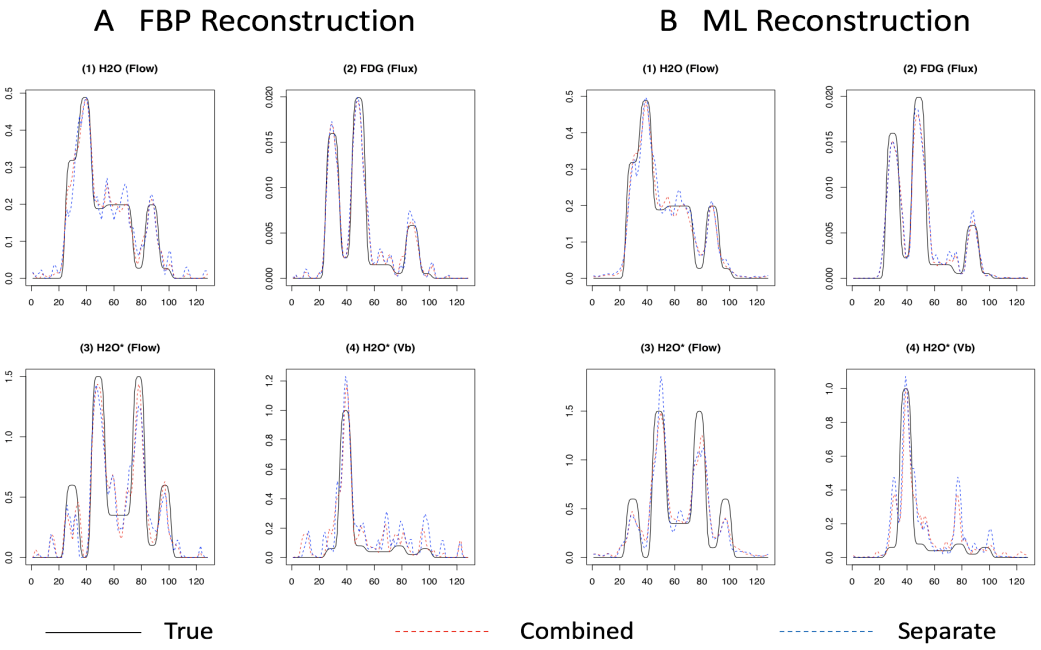


Figure 3.9: Sample metabolic estimates (at a middle dose setting) based on the FBP and ML reconstruction. x-axis gives location (1-128); y-axis is values of metabolic parameters in 1-D simulations. See Figure 3.6 for location of different structures. Plots (1) and (2) show flow and flux in H_2O-FDG study; (3) and (4) show flow and blood volume (V_B) in the repeat 2 H_2O studies.

3.5.2 MSE Performance Comparisons

3.5.2.1 H_2O-FDG Studies

The MSE in (3.21) as the function of the dose and dose ratio from combined and separated approach in 1-D and 2-D simulations are presented in Table 3.4. Figure 3.10 presents the information graphically. MSEs from combined and separated analysis decrease with the dose and increase with relative dose ratio. In 1-D simulation studies, the improvements are 20.85% and 11.65% from FBP and ML reconstruction at the reference dose and middle dose-ratio level - matched to the real dataset and improvement is smaller based on the ML reconstructed data. Benefits by combined approach in 2-D simulation with FBP reconstruction is similar to 1D FBP performance.

Table 3.4: Combined analysis improvements (3.22) by dose level/ratio for H_2O-FDG study.

	Dose / Dose Ratio	0.3	0.5	0.7	1	1.5	2.2	3.2
(a) FBP (1D)	16 : 1	16.97	17.12	17.37	18.01	18.71	19.25	19.79
	20 : 1	17.67	17.60	18.55	19.13	19.38	20.10	19.70
	25 : 1	18.13	18.05	18.94	19.09	19.95	20.85	21.17
	32 : 1	20.10	19.78	19.47	20.85	21.35	21.38	22.34
	40 : 1	20.91	20.80	21.16	22.20	22.79	23.44	23.75
	51 : 1	23.06	23.11	23.94	24.30	25.23	25.27	26.07
	64 : 1	25.08	25.93	26.57	27.22	27.26	27.99	28.86
(b) ML (1D)	16 : 1	8.23	8.91	9.19	10.44	10.77	12.34	12.97
	20 : 1	8.39	8.74	9.40	10.81	11.29	12.80	13.38
	25 : 1	8.55	9.08	9.55	10.45	11.84	13.27	14.81
	32 : 1	8.87	10.18	10.38	11.65	11.64	13.76	14.88
	40 : 1	8.98	10.75	10.81	12.11	12.33	13.92	15.65
	51 : 1	10.55	11.42	11.60	12.76	13.92	15.50	16.05
	64 : 1	10.71	12.35	12.69	13.61	15.06	16.70	17.23
(c) FBP (2D)	16 : 1	12.98	13.80	13.73	13.30	12.82	14.21	14.17
	20 : 1	13.83	13.26	12.75	14.02	13.82	13.28	13.08
	25 : 1	14.93	16.23	15.38	15.19	14.89	16.78	14.30
	32 : 1	16.75	15.74	17.37	16.60	16.31	15.65	15.26
	40 : 1	16.21	17.72	16.19	17.85	17.87	17.82	17.10
	51 : 1	17.39	19.27	18.33	20.74	19.71	19.29	18.93
	64 : 1	23.42	21.59	21.16	19.95	22.55	21.33	21.08

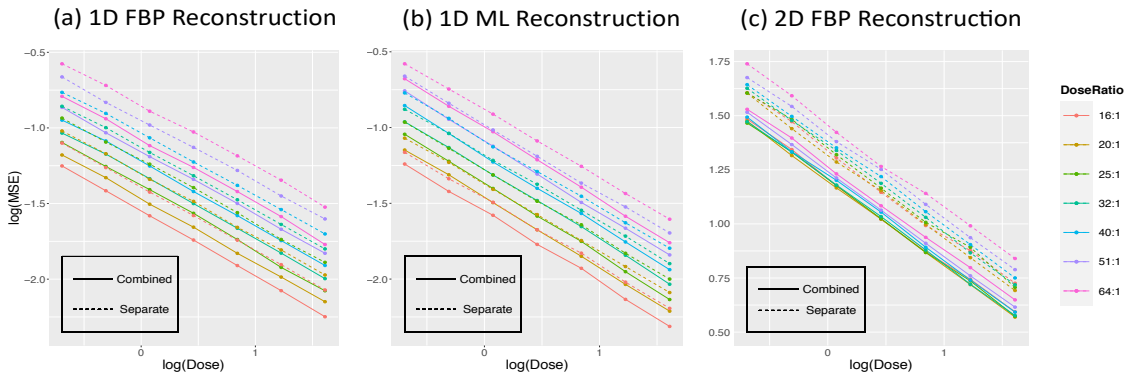


Figure 3.10: MSE of combined (solid) and separate (dashed) analysis as a function of dose and dose ratio in H_2O-FDG study. Different colors represent different dose ratios.

3.5.2.2 Repeat H_2O Studies

The quantitative improvements for different numbers of injections at seven dose levels from two reconstruction algorithms are presented in Table 3.5. We can

see, the number of injections has a strong effect. See also Figure 3.11. These results show lower doses and more injections have higher MSEs. Dramatically smaller improvements are seen with ML. This may be because the bandwidth of smoothing process used in reconstruction is adapted based on the total update scan so there is a more limited impact on individual time frames; the ML procedure constrains the reconstruction to be positive and in doing so implicity smooths the voxel-level time-course data.

Table 3.5: Combined analysis improvements (3.22) in multiple H_2O studies at 7 dose levels.

	Dose / No.Studies	0.3	0.5	0.7	1	1.5	2.2	3.2
(a) FBP	2	45.69	46.76	46.67	46.54	48.39	48.49	49.48
	4	125.91	129.36	133.47	136.76	133.89	140.95	137.81
	6	208.94	211.81	214.03	219.74	222.75	226.32	225.94
	8	284.02	283.77	297.29	293.94	304.76	306.66	314.65
(b) ML	2	9.51	10.17	11.21	12.14	13.66	15.19	17.15
	4	18.31	20.55	23.44	26.02	28.72	31.48	35.92
	6	23.67	26.53	29.95	33.94	37.92	42.47	48.95
	8	27.86	31.05	35.06	39.93	45.60	51.66	58.28

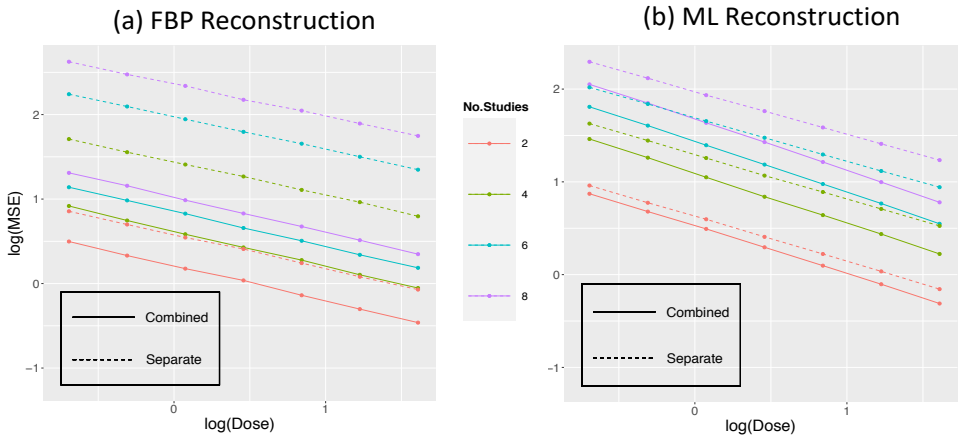


Figure 3.11: MSE of combined and separate analysis in multiple H_2O studies.

3.6 Statistical Analysis of Simulation Results

The highly structured nature of the MSE patterns in Figure 3.10 and 3.11, invites a more refined interpretation.

3.6.1 MSE values scaled by Image Data Accuracy

The overall accuracy of the input data is assessed by $\hat{\sigma}_z^2 = \frac{1}{N}\sum_i \hat{\sigma}_i^2$ - where $\hat{\sigma}_i$ was introduced in (3.7). While we can scale MSE values by this, a simpler (and statistically equivalent) procedure is to scale by the voxel-by-voxel error in the total-uptake reconstruction. We label this $\hat{\sigma}_{z\bullet}^2$. For the H_2O-FDG study, the scaled values are in Figure 3.12.

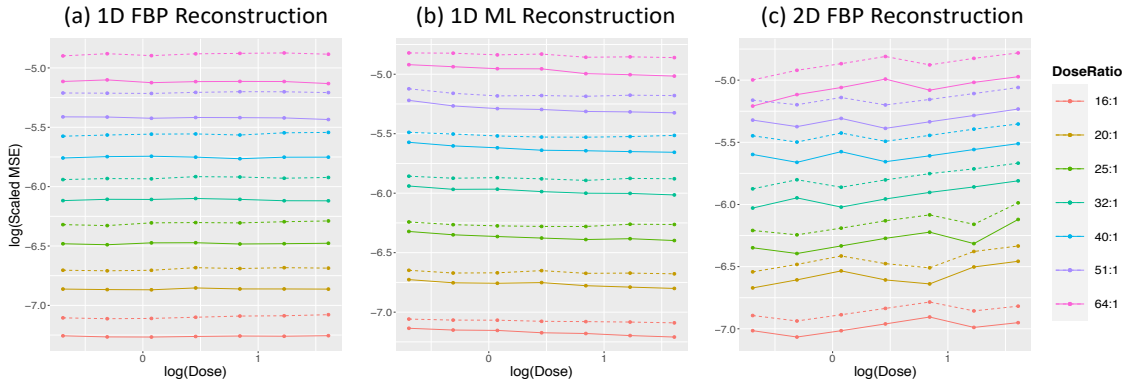


Figure 3.12: MSE values scaled by image data accuracy for combined (solid) and separate (dashed) analysis as a function of dose and dose ratio in H_2O-FDG study.

These data are well described by the model

$$log(MSE/\hat{\sigma}_{z\bullet}^2) \sim a_0 + a_1 I + a_2 DR \tag{3.23}$$

where I is the method indicator for combined or separate analysis and DR is the dose ratio. Table 3.6 reports estimates values for these coefficients. Note $\hat{a_1}$ corresponds to about 21% ($e^{0.19}-1$) and 12% ($e^{0.11}-1$) improvements at middle dose-ratio with the FBP and ML reconstruction in 1-D simulation studies. The results from 2D simulation have the similar performance.

Table 3.6: Modeling Scaled MSE in the H_2O-FDG study - $c.f.$ (3.23).

	$\hat{a_0}$	$\hat{a_1}$	$\hat{a_3}$
FBP(1D)	-6.29 ± 0.03	0.19 ± 0.04	1.40 ± 0.04
ML(1D)	-6.17 ± 0.03	0.11 ± 0.04	1.43 ± 0.04
FBP(2D)	-6.10 ± 0.03	0.15 ± 0.04	1.26 ± 0.04

A similar analysis of the scaled MSE data from the repeat H_2O study, leads to a

model with an interaction term:

$$log(MSE/\hat{\sigma}^2_{z\bullet}) \sim \beta_0 + \beta_1 I + \beta_2 No.Studies + \beta_3 (I \times No.Studies) \quad (3.24)$$

The scaled MSE values are in Figure 3.13 with the model results in Table 3.7. The improvements of combined analysis in the repeat H_2O studies with two injections are 55% and 15% for the FBP and ML reconstructed data, respectively. The impact of dose, although significant, is not substantial in comparison to the overall impact of dose on MSE.

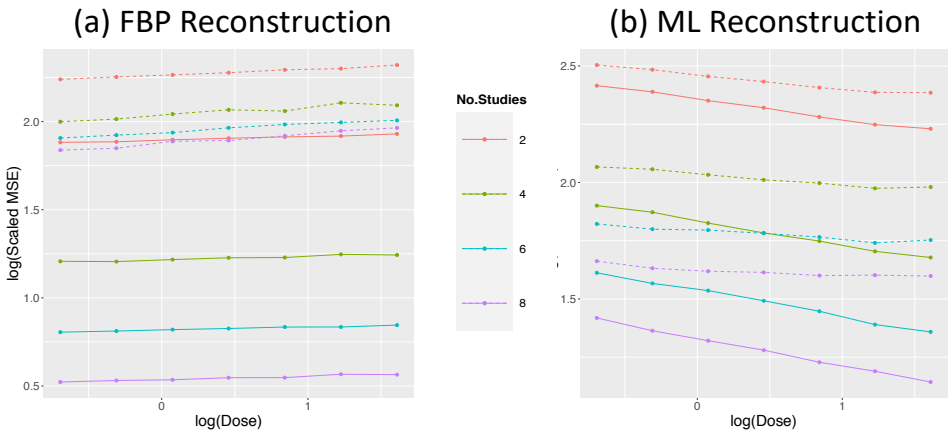


Figure 3.13: MSE values scaled by image data accuracy for combined (solid) and separate (dashed) analysis as a function of dose and number of studies in the repeat H_2O setting.

Table 3.7: Modeling Scaled MSE in the repeat H_2O study, see (3.24).

	$\hat{\beta}_0$	$\hat{\beta}_1$	$\hat{\beta}_2$	$\hat{\beta}_3$
FBP	1.80 ± 0.03	0.44 ± 0.04	-0.45 ± 0.01	0.32 ± 0.02
ML	2.23 ± 0.03	0.14 ± 0.04	-0.34 ± 0.02	0.07 ± 0.02

3.6.2 Analysis of the Uptake MSE as a function of Dose

Analysis of MSE of total uptake from FBP and ML reconstruction as a function of dose gives a 2-factor statistical model:

$$log(\hat{\sigma}^2_{z\bullet}) \sim \gamma_0 - \gamma_\tau log(\tau) + \gamma_M M \quad (3.25)$$

where τ is dose level, M is dose ratio (DR) for H_2O-FDG study and number of injections for repeat H_2O studies, respectively. The estimated coefficients $\hat{\gamma}_0$, $\hat{\gamma}_\tau$ and $\hat{\gamma}_M$ are shown in Table 3.8. We can see $\hat{\gamma}_\tau$ is similar in different studies and reconstruction methods. The intercept - $\hat{\gamma}_0$ in FBP is always bigger than

ML, which means uptake based on ML has smaller errors. Table 3.8 shows that the main effect of dose is described by $\tau^{-.42}$ - this is consistent with previous asymptotic analyses of ML and FBP in PET, e.g. (O'Sullivan, 1995). The fact that the rate of convergence is so similar between the 1-D and 2-D simulation models is a good indicator that the 1-D PET framework captures the estimation complexity of 2-D PET.

Table 3.8: MSE characteristics of reconstructed data in H_2O-FDG and H_2O studies (H_2O^*) based on FBP and ML. Analysis is based on equation (3.25).

		$\hat{\gamma}_0$	$\hat{\gamma}_\tau$	$\hat{\gamma}_M$
FBP(1D)	H_2O	2.91 ± 0.01	$\mathbf{0.42} \pm 0.01$	-0.20 ± 0.01
	FDG	4.41 ± 0.02	$\mathbf{0.42} \pm 0.03$	-1.41 ± 0.04
	H_2O-FDG	4.75 ± 0.02	$\mathbf{0.42} \pm 0.03$	-1.10 ± 0.04
	H_2O^*	-1.71 ± 0.05	$\mathbf{0.44} \pm 0.04$	0.71 ± 0.03
ML(1D)	H_2O	2.78 ± 0.01	$\mathbf{0.42} \pm 0.01$	-0.16 ± 0.01
	FDG	4.30 ± 0.02	$\mathbf{0.43} \pm 0.03$	-1.40 ± 0.04
	H_2O-FDG	4.65 ± 0.02	$\mathbf{0.43} \pm 0.03$	-1.06 ± 0.04
	H_2O^*	-1.85 ± 0.05	$\mathbf{0.43} \pm 0.04$	0.72 ± 0.03
FBP(2D)	H_2O	-2.21 ± 0.01	$\mathbf{0.44} \pm 0.01$	0.03 ± 0.02
	FDG	-2.15 ± 0.01	$\mathbf{0.37} \pm 0.01$	-0.03 ± 0.01
	H_2O-FDG	-2.33 ± 0.01	$\mathbf{0.42} \pm 0.01$	-0.05 ± 0.02

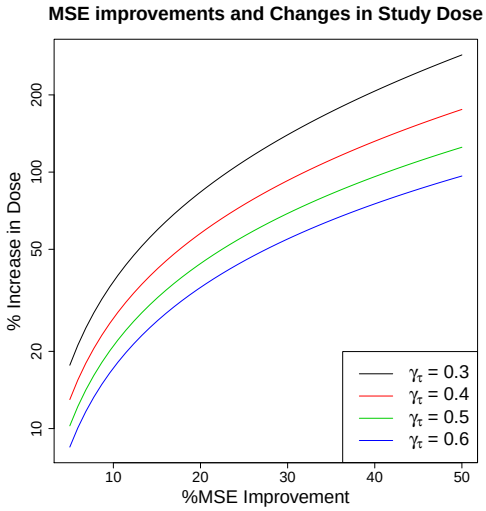


Figure 3.14: Estimated relation between MSE improvements and study dose. Calculation based on (3.25) with different colors corresponding to a range of possible γ_τ values.

The rate of convergence analysis allows us to develop a relation between percent improvements obtained by combined data analysis and the equivalent pre-

cent increase in dose that would be needed to ensure that the separate data matched the benefits of combined analysis. Figure 3.14 presents this equivalence. In light of Table 3.8, which gives a dose rate coefficient on the order of 0.42 for ML and FBP, a 10% improvement in MSE obtained by combined data analysis would require a 25% increase in dose if separate data analysis methods were used.

3.7 Discussion

We have presented a combination of theoretical intuition, real data and numerical simulation to examine the benefits of combined NPRM analysis of multiple injection studies in PET. This work has been fully motivated by practical imaging protocols. The results demonstrate that there are clear gains in MSE performance by a combined analysis approach. With H_2O-FDG studies the MSE improvement is around 21% on the same order of the regional variance comparisons found in section 3.3. For the repeat H_2O studies, improvements increase in accordance with the factor $(J-1)$ indicated by the theory in section 3.2. In general improvements are seen to be a function of intra-injection dose-ratio but are substantially independent of dose for FBP reconstructed data. In the ML case, the impact of dose is apparent with combined analysis leading to greater improvements at higher doses. Even though the theoretical analysis looks at the asymptotic situation in which variance is the main contributor to the error, the predictions from that theory provide good guidance on the nature of benefits that would be associated with combined analysis.

Our work has exclusively focused on parameter mean square error performance (MSE and RMSE). In kinetic mapping, the average accuracy of estimation of the target parameters, measured by the RMSE, is a natural metric and is used extensively in quantifying estimation error in many settings. Nevertheless, a number of other metrics could also be of interest. Data-fit or predictive error, with suitable adjustment for model flexibility, might also be considered. In addition, criteria based on parameters defined by functions of the kinetics variables associated with individual tracers would also be of interest. MSE improvements associated with combined analysis of ML-reconstructed data are smaller than those achieved with FBP-reconstructed data. This phenomenon may well have to do with the implicit regularization that ML achieves in low-count frames. Our studies used a common bandwidth for all injections. While this gives some assurance that the resolution of each scan is the same for FBP; it is not clear,

given the implicit regularisation achieved by imposition of positivity, if this is necessarily the case for ML. The effect is probably most significant in the repeat studies with many injections. In this setting the total uptake bandwidth selection will lead to very noisy individual scans. The bandwidth selection process ensures voxel-level FBP time-course data are inherently noisier than in ML so the analysis of kinetics for FBP data can end up being worse than the same analysis of ML. The issue is apparent in Table 3.5. An obvious way to address this issue could be to select bandwidths for individual injections separately. This may allow the noise characteristics of FBP to be more comparable to ML (O'Sullivan, 1995; O'Sullivan and Roy Choudhury, 2001). The issue merits further investigation - (Gu and O'Sullivan, 2021) reports on some initial work in this direction.

For computational reasons we made extensive use of a 1-D scanning model in this work. This allowed comprehensive evaluation of estimators with iteratively reconstructed ML data over a range of count rates and many replicates. While FBP is used very little in practice, we included it in simulations. The relation between 1-D and 2-D FBP results might be used as a vehicle to understand how combined analysis methods of 1-D ML data might perform in a 2-D or 3-D setting. The justification of some experiment details, see section 3.7.1, 3.7.2 and 3.7.3. Our simulations here demonstrate that combined analysis will significantly improve the accuracy of NPRM kinetic mapping in multiple injection studies. It will be important to see how these results translate into 3-D and especially for the next generation total-body PET scanners (Badawi et al., 2019; Karp et al., 2020). In this context the emerging techniques for efficient bootstrapping of 3-D multi-frame PET studies (Kucharczak et al., 2018; Gu, Wu, O'Sullivan, Huang, Muzi and Mankoff, 2019; Huang et al., 2020; O'Sullivan et al., 2021) may facilitate a more direct practical assessment of the benefits of combined analysis in a given patient, without the need for highly sophisticated step-by-step representations of the scanner emission measurements and reconstruction processes.

3.7.1 The Choice of β

As introduced in section 3.4.1, the parameter β controls the degree of difficulty problem and a larger β makes the inversion of A in Figure 3.4 more unstable (O'Sullivan, Pawitan and Haynor, 1993). An appropriate value of β needs to be matched with the difficulty in the realistic situation. 2D simulation is based on

the real dataset, the value of $\hat{\varphi}_1$ is 0.39. So we test several β in 1D simulation and results are shown in Table 3.9. The MSE would decrease more quickly with the increase of dose (τ) when β is smaller. 1D and 2D are similar when β equals 1.35.

Table 3.9: The rate of convergence - $\hat{\varphi}_1$ using different β in 1-D simulation.

$$log(MSE) \sim \varphi_0 - \varphi_1 * \tau + \varphi_2 * DR$$

β	0.75	1	1.25	1.35	1.5
$\hat{\varphi}_1$	0.53	0.47	0.42	0.41	0.36

3.7.2 The Option of Weight

When applying constrained weighted least square, there are some options of weights. Optimal weight is the reciprocal of true distribution and fixed for each replicate. We can also use the weights depending on image data z, which is dynamic for each replicate. Dynamic weight is used in our simulation above, which is more general as the true distribution is usually not available. We also test the fixed weights in 1D simulation using FBP reconstruction and just repeat 100 times for each dose and dose-ratio level based on the computational consideration. The results are shown in Table 3.10, we can see there is little difference between results with fixed and dynamic weights. The improvements are also presented in Table 3.11, which is also similar to Table 3.4(a).

Table 3.10: MSE characteristics using different weights in 1D H_2O-FDG study.

$$log(MSE) \sim \varphi_0 - \varphi_1 * \tau + \varphi_2 * DR$$

Weights	Methods	$\hat{\varphi}_0$	$\hat{\varphi}_1$	$\hat{\varphi}_2$
(a) Fixed	Combined	-1.54 ± 0.005	0.42 ± 0.006	0.31 ± 0.010
	Separate	-1.36 ± 0.005	0.41 ± 0.006	0.35 ± 0.009
(b) Dynamic	Combined	-1.53 ± 0.005	0.42 ± 0.007	0.31 ± 0.010
	Separate	-1.35 ± 0.005	0.41 ± 0.006	0.35 ± 0.010

3.7.3 A Simplified Model

We consider a simplified analysis of this setup theoretically. As the PET measurements using FBP reconstruction follow a Gaussian distribution (Teymurazyan et al., 2013), we can add Gaussian noise to the true distribution directly. A reasonable statistical model is:

$$z_x(t) = \lambda_x(t) + \phi w_x(t)^{-1/2} e_x(t) = \alpha_x \mu(t) + \phi w_x(t)^{-1/2} e_x(t) \tag{3.26}$$

Table 3.11: Improvements (%) from constrained weighted least square with fixed weights at 7 dose levels and 7 dose ratios in 1D H_2O-FDG study using FBP reconstruction.

DR \ Dose	0.3	0.5	0.7	1	1.5	2.2	3.2
16 : 1	17.46	16.85	17.87	17.97	19.06	18.83	19.30
20 : 1	17.65	18.03	17.39	18.84	19.59	19.96	20.26
25 : 1	18.26	18.19	18.68	18.90	19.95	21.22	19.66
32 : 1	18.51	20.12	19.18	19.78	21.56	22.39	23.38
40 : 1	21.11	19.99	22.69	21.69	22.68	23.66	23.01
51 : 1	23.01	23.95	21.95	24.23	24.08	25.66	25.08
64 : 1	23.99	26.24	26.76	27.10	28.42	27.98	28.45

where $w_x(t) = 1/\lambda_x(t)$, $e \sim N(0,1)$ and ϕ is a scale factor.

The standard approach to estimation is weighted least square. Considering the positive constraints of mixing coefficients, we apply constrained WLS here. The true mixing coefficients and time courses at the middle dose and dose-ratio in 1-D simulation in section 3.4.2 are used and the Gaussian noise is added by the random generator *rnorm* in R. There are no projection and reconstruction requirements using this simplified model. MSE is calculated and the improvement of combined analysis is around 22%. This result is similar to the middle dose and dose-ratio in 1-D simulation.

Chapter 4

A Generalized Linear modeling approach to bootstrapping multi-frame PET image data

Abstract

Imaging biomarkers extracted from diagnostic PET imaging scans are increasingly used in clinical decisions about the treatment of individual cancer patients. In this setting, measurements of uncertainty in the biomarker information presented for an individual patient may have an important role. Raw PET data can be viewed as a sample from an inhomogeneous Poisson process so there is the possibility to directly apply bootstrapping to raw projection-domain list-mode data. Unfortunately this is computationally impractical, particularly if data reconstruction is iterative or the acquisition protocol is dynamic. We develop a flexible statistical linear model analysis to be used with multi-frame PET image data to create valid bootstrap samples. The technique is illustrated using data from dynamic PET studies with fluoro-thymidine (FLT) in breast cancer patients. As is often the case with dynamic PET studies, data have been archived without raw list-mode information. Using the bootstrapping technique maps of kinetic parameters and associated uncertainties are obtained. The quantitative performance of this approach for the evaluation of kinetics and more complex imaging biomarkers - regional maximum and regional coefficient of variation is assessed. A series of numerical simulations matched to the dynamic PET imaging study with FLT in a breast cancer patient are carried out. A large (>650) collection of regions of interest (ROIs) with varying

size and location are considered. True target values of uncertainty are evaluated by study replication. Both the non-parametric projection-domain and the proposed image-domain bootstraps are evaluated. The results find that the accuracy of the image-domain assessment of uncertainty is very acceptable - within 10% of the accuracy of the non-parametric bootstrap approach. Analysis of results points to a close relation between relative uncertainty in voxel-level kinetic parameters and local reconstruction error. This is consistent with statistical theory.

4.1 Introduction

4.1.1 General Bootstrap

Bootstrap is a general statistical technique that was introduced in 1979 by Efron (Efron, 1979), with further developments in (Efron, 1981*a*,*b*, 1982; Efron and Tibshirani, 1986, 1994; Chernick, 2011). This is a data-based simulation method for statistical inference and the use of the term bootstrap derives from the phrase *to pull oneself up by one's bootstrap*. It can be used to evaluate the sampling distribution of a statistic and obtain bias and variance characteristics of a computed summary statistic, and also to formally access associated hypotheses that might be of interest. The flowchart of bootstrap procedure is presented in Figure 4.1. Two schemes are commonly used to generate bootstrap samples.

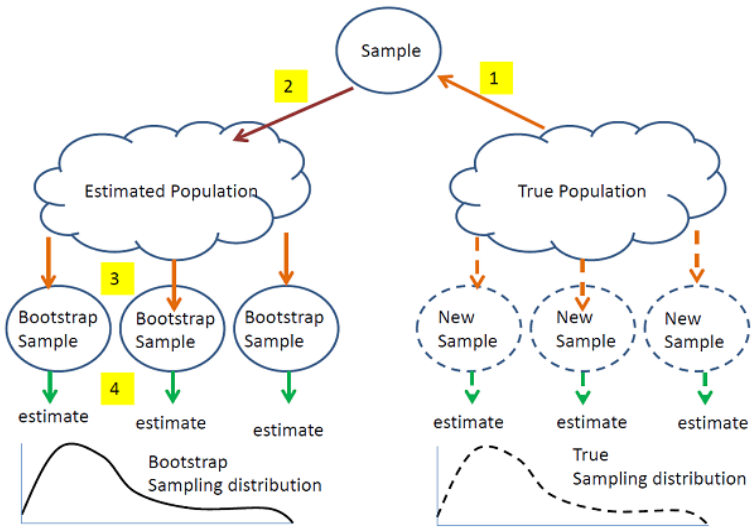


Figure 4.1: Schematic of the bootstrap process [1].

[1] URL: https://online.stat.psu.edu/stat555/node/119/

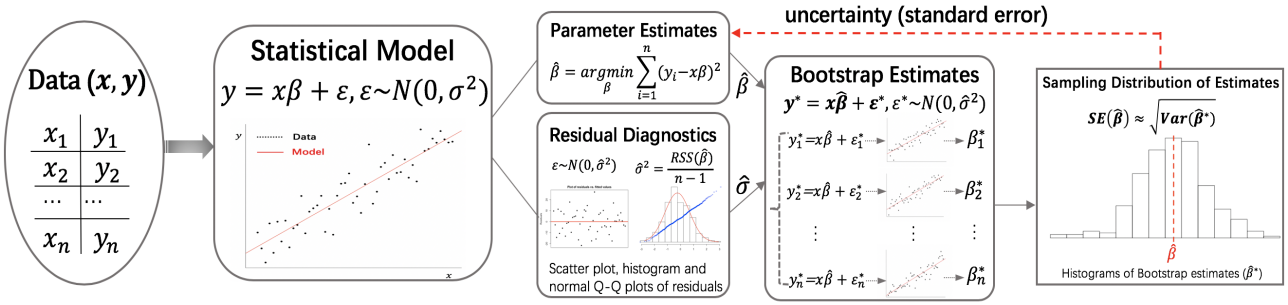


Figure 4.2: Schematic summary of the Model-Based Bootstrap Concept in a Simple Linear Regression Model.

Non-Parametric Bootstrap by Resampling Suppose that $x = (x_1, x_2..., x_n)$ is an observed random sample and θ is the parameter of interest. The non-parametric bootstrap procedure is as below (Rizzo, 2019).

1. For each bootstrap replicate, indexed $b = 1, ..., B$
   (a) Generate sample $x^{*(b)} = x_1^*, x_2^*, ...x_n^*$ by sampling with replacement from the observed sample $x_1, x_2..., x_n$.
   (b) Compute the b^{th} replicate $\hat{\theta}^{(b)}$ from b^{th} bootstrap sample.
2. The bootstrap estimate of $F_{\hat{\theta}}(\cdot)$ is the empirical distribution of the replicates $\hat{\theta}^{(1)}, \hat{\theta}^{(2)}, ...\hat{\theta}^{(B)}$.

Parametric (Model-Based) Bootstrap[2] Parametric bootstrapping assumes that the data comes from a known distribution with unknown parameters. We can estimate the parameters from the data that we have and use the estimated distributions to simulate the samples.

To have a better understanding of parametric bootstrap in further analysis, we simplify it in a linear model setting (Gu, Wu, O'Sullivan, Huang, Muzi and Mankoff, 2019). The process is summarized in Figure 4.2. We assume there is a linear relationship between the predictor variable x and response variable y. ε is a sequence of independent identically distributed (iid) random variables following a normal distribution with zero mean and standard deviation σ.

$$y = x\beta + \varepsilon, \ \varepsilon \sim N(0, \sigma^2) \tag{4.1}$$

[2]Fengyun Gu and Qi Wu contributed equally to this section and Figure 4.2.

The model fitting provides an estimation of β ($\hat{\beta}$) and residuals (r) as below:

$$\begin{cases} \hat{\beta} = \underset{\beta}{argmin} \sum_{i=1}^{n} (y_i - x\beta)^2 \\ r = y - x\hat{\beta} \end{cases}$$

A normal model can be used to fit the residual sum of squares (RSS) and estimate the noise variance σ^2.

$$\hat{\sigma}^2 = \frac{RSS(\hat{\beta})}{n-1}$$

If the linear model is appropriate, we can simulate data y based on the model fitting and diagnostics:

$$y^* = x\hat{\beta} + \varepsilon^*, \ \varepsilon^* \sim N(0, \hat{\sigma}^2) \tag{4.2}$$

The sampling distribution of bootstrap estimates can be obtained from linear model fitting of y^* and x. The variation of these estimates can be used to approximate the standard error/uncertainty of original estimate $\hat{\beta}$.

$$SE(\hat{\beta}) \approx \sqrt{Var(\hat{\beta}^*)} \tag{4.3}$$

4.1.2 Application of Bootstrap in PET

As the role of quantitative PET in clinical decision making evolves, it is likely that there will be an increasing interest in the availability of practical methods for evaluating uncertainty associated with the results reported for an individual patient. There is already a significant literature on variance assessment for PET. Much of this work has concentrated on the development of analytic approaches based on the linear approximations to the reconstruction process – see, for example, (Alpert et al., 1982; Barrett, Wilson and Tsui, 1994; Carson et al., 1993; Huesman, 1977; Ibaraki et al., 2014; Maitra and O'Sullivan, 1998; Qi and Leahy, 2000; Tanaka and Murayama, 1982; Wang and Gindi, 1997). The potential of applying Efron's statistical bootstrap (Efron and Tibshirani, 1994) in this setting was described by (Haynor and Woods, 1989). There have been a number of contributions - see, for example, (Buvat, 2002; Dahlbom, 2001; Lartizien, Aubin and Buvat, 2010; Ibaraki et al., 2014; Kucharczak et al., 2018) - that have attempted to implement variations on this approach. The attraction of the non-parametric bootstrap is that it does not involve detailed analytic assumptions which may be difficult to justify in a real patient study. So far,

bootstrapping methods for PET image data have concentrated on re-sampling in the raw measurement domain. We refer to such *list-mode* or *sinogram* sampling techniques as projection-domain methods.

(Huang et al., 2020) used a combination of physical phantom and numerical simulations to develop an image-domain bootstrapping strategy for PET data. The approach is based on a sub-ordinate Gaussian structure, a particular type of Gaussian copula form (Joe, 2014), with the ability to capture the Poisson-like nature of voxel-level measurements as well as relevant spatial and temporal covariances. In the context of standard clinical PET-FDG studies, involving imaging over a relatively short duration time frame between 45 and 60 minutes after tracer injection, (Huang et al., 2020) proposed sub-dividing frame data in order to obtain the near-replicate information needed to estimate unknown parameters in a proposed image-domain simulation model. This technique was illustrated using data from a clinical PET-FDG lung cancer study.

Our work here develops a more flexible procedure for image-domain bootstrapping. This new approach is applicable in situations where there may be a complex temporal structure in the measured PET data — a near-constant temporal structure is intrinsic to the method used in (Huang et al., 2020). In addition the latter work relied on a parametric Gamma-model form to represent the marginal distributions of voxel-level data and a parametric spatial auto-regressive (SAR) form to represent covariance patterns. The method here uses the empirical distribution of re-scaled data and a non-parametric approach for analysis of the spatial correlation structure. The purpose of this report is to describe the modeling techniques involved in a novel image-domain bootstrapping method and to numerically demonstrate its performance relative to the standard projection-domain bootstrapping technique. Similar to (Huang et al., 2020) the proposed approach is only applicable to situations where the PET data have a temporal extent — $e.g.$ dynamic PET studies. In this setting suitable modeling of the dynamic data enables us to identify an associated set of residuals that can be manipulated to construct a viable model-based image-domain bootstrapping procedure.

The technical framework for the methodology is set out in section 4.2 with the illustrative example presented in section 4.3. The example comes from a dynamic study with ^{18}F-labeled Fluorothymidine (FLT) on a PET scanner using iterative maximum likelihood (ML) reconstruction for the breast-cancer patient. A kinetic mapping technique is applied to the bootstrap-simulated

datasets in order to produce parametric images of metabolism and associated voxel-by-voxel standard errors. Section 4.4 presents numerical simulation studies, matched to the real data. These studies explore performance of the novel model-based bootstrapping technique relative to the projection-domain list-mode bootstrapping approach. In addition we examine if performance is impacted by the nature of the data reconstruction process used. The results are very promising, demonstrating that the efficient model-based image-domain bootstrapping substantially matches performance of the projection-domain approach, regardless of what data reconstructed scheme is used. The chapter concludes with some discussion in section 4.5.

4.2 Methodology

The input data for the approach is a 4-D dynamic PET dataset represented by an $N \times T$ array, $\{z_{ij};\ i = 1, .., N, j = 1, ..., T\}$. Here N represents the number of voxels in the field of view and T is the number of time-frames in the PET acquisition. z_{ij} is the reconstructed PET-measured tracer concentration value at the 3-D voxel co-ordinate, x_i, at a time t_j corresponding to the mid-point of the j'th time-frame of scanning. We begin by providing a formal mathematical description of the model, highlighting the various unknowns that must be estimated before it can be used for bootstrapping.

4.2.1 Statistical Modeling of the Image-Domain Data

Let the true mean and variance of the PET measurement z_{ij} be denoted μ_{ij} and σ^2_{ij}, respectively. The proposed approximation of measurements has the structure of a general linear model in which the error process, while allowed to be non-Gaussian and non-stationary, is linked to a sub-ordinate Gaussian process. The starting point for the specification is a set of data-dependent basis vectors, denoted $X = \{\mu_k, k = 1, 2, ..., K\}$, that have the ability to approximate local mean values, μ_{ij}. The method used to identify X is described in section 4.2.3 below. The statistical model for z_{ij} is expressed as a sum of systematic and random terms. The basic version is given by

$$\begin{aligned} z_{ij} &= \mu_{ij} + \sigma_{ij}\epsilon_{ij} \ ;\ \epsilon_{ij} = Q(\eta_{ij}) \ \text{ with } \ \eta_{ij} \sim N(0,1) \\ \mu_{ij} &= x'_j\alpha_i \ ;\ \sigma_{ij} = \sigma_i\phi_j \ ;\ \sum_{j=1}^{T} \phi_j^2 = T \end{aligned} \tag{4.4}$$

Here x_j is the j'th row of X and α_i is a vector of unknown coefficients. Note that the systematic part of z_{ij}, here μ_{ij}, is approximated by a linear form. The model is referred to as a *generalized linear model* because errors are allowed to be non-Gaussian and the scale factors, σ_{ij}, are not assumed constant (Seber, 2015). In (4.4), σ_{ij} is a product of spatial (σ_i) and temporal (ϕ_j) factors. The constraint on ϕ is required for identifiability. A key part of (4.4) is that the error term ϵ_{ij} is related to a sub-ordinate Gaussian variable, η_{ij}, by a (unknown) Q-transform. In statistical parlance, the inverse of Q defines the normal-quantile plot for the collection of measurement errors (Team et al., 2013). We assume Q is strictly monotone and, for identifiability, scaled so that $var(\epsilon_{ij}) = 1$. Monotonicity of Q is a requirement for the distribution of the measurement errors to be well-defined; it does not restrict the flexibility of the model to adapt to arbitrary distributional forms for the error. Strict monotonicity implies that the quantile mapping is invertible. If the model errors have a continuous distribution - a very plausible approximation for PET and many other types of medical imaging data - then Q must be strictly monotone. The sub-ordinate Gaussian η-process, $\eta = \{\eta_{ij}, i = 1, 2, ..., N, j = 1, 2, ..., T\}$, is assumed to have independent temporal components, matching the formal Poisson structure of PET (Vardi, Shepp and Kaufman, 1985), and a common stationary spatial auto-correlation, consistent with physical phantom measurements and simulations, see, for example, (Huang et al., 2020). Note that the concept using of a simple sub-ordinate stationary process, like η here, to describe dependency in multivariate data is well established. (Joe, 2014) provides a treatment of many instances in which has proved useful in applied statistical work.

While the model in (4.4) can capture non-stationarity (in mean and variance) and rather general correlation patterns, it has limited ability to adapt to the local skewness of PET data. Such skewness is particularly important for iteratively reconstructed PET data. Thus a more elaborate form of the model is needed for our proposed image-domain bootstrapping procedure. (Scheuermann et al., 2013; Mou, Huang and O'Sullivan, 2017) used Gamma-distributions to model the local skewness of iteratively reconstructed PET measurements of scanned physical phantoms. In a Gamma-distribution, the ratio of the mean to the standard deviation is the square-root of the shape parameter. This quantity is inversely proportional to the skewness of the distribution. As the shape parameter increases, skewness diminishes and the Gamma-distribution formally converges to a Gaussian form. Using the fit of the basic model in (4.4) to define $\tilde{\mu}_{ij}$, $\tilde{\sigma}_i$ and $\tilde{\phi}_j$, we let $\kappa_{ij} = \frac{\tilde{\mu}_{ij}}{\tilde{\sigma}_i \tilde{\phi}_j}$. The refined statistical modeling approach uses κ_{ij} as

a surrogate variable for representing deviations from the product form of the variance and the assumed distributional structure. This leads to the generalized linear model

$$\begin{aligned} z_{ij} &= \mu_{ij} + \sigma_{ij}\epsilon_{ij} \;\; ; \;\; \epsilon_{ij} = Q(\eta_{ij}|\kappa_{ij}) \;\; , \;\; \eta_{ij} \sim N(0,1) \\ \mu_{ij} &= x_j'\alpha_i \;\; ; \;\; \sigma_{ij} = \sigma_i\phi_j \; ; \; \sum_{j=1}^{T} \phi_j^2 = T \end{aligned} \tag{4.5}$$

where $Q(\cdot|\kappa)$ is strictly monotone for each fixed κ-value and is assumed to be slowly varying as a function of κ. For identifiability, a scaling constraint involving Q is also required. For this with $h^2(\kappa) = var(Q(\eta|\kappa))$, we require $\sum_{ij} h^2(\kappa_{ij}) = NT$. Obviously, model (4.5) reduces to model (4.4), when the transform Q does not vary with κ. If $Q(\cdot|\kappa)$ corresponded to a scaled Gamma distribution then, based on (Mou, Huang and O'Sullivan, 2017), κ would increase with dose or sensitivity. And with increasing κ, Q becomes linear. Indeed model (4.5) will converge to model (4.4), with $Q \equiv 1$, as these factors increase. This is in line with the results reported by (Mou, Huang and O'Sullivan, 2017). Thus the structure in (4.5) gives the ability to adapt to distributions that vary from being highly skewed to ones that are substantially Gaussian. In light of this the model gives the ability to accommodate both the skewed nature of iteratively reconstructed (ML) PET data and the Gaussian nature of analytically reconstructed (FBP) PET scans (Scheuermann et al., 2013; Mou, Huang and O'Sullivan, 2017). Regardless of Q, the variance structure specified in the model ensures that with particular choices for σ, ϕ and h, the specification in (4.5) accommodates the situation where variance is directly proportional to the mean - similar to what (Huesman, 1977) proposed for PET ROI data. For this, let $h(\kappa)^2$ be proportional to $|\kappa|$, $\phi_j = \tilde{\phi}_j$ and choose σ_i proportional to $\tilde{\sigma}_i$. In this situation the model in (4.5) could also be viewed within the Gaussian copula framework used by (Lennon and Yuan, 2019) to model time-series of count data.

Since the temporal components of the sub-ordinate Gaussian are assumed independent with a common stationary spatial structure, the covariance of η can be written in the form of a tensor product, $\Sigma_N \otimes I_T$, where Σ_N is a $N \times N$ matrix representing the spatial correlation pattern and I_T is an T-dimensional identity matrix. Spatial stationarity implies that the covariance can be diagonalized using the Fourier transform (Brockwell and Davis, 1991), *i.e.* $\Sigma_N = \mathcal{F}_N^t \Lambda_N \mathcal{F}_N$ where $\mathcal{F}_N$ is the matrix mapping an N-vector to its 3-D sine and cosine Fourier

coefficients. The action of $\mathcal{F}_N$ is of course computed using the standard 3D fast Fourier transform (FFT). The matrix Λ_N is diagonal with elements, $\lambda = \{\lambda_i, i = 1, ..., N\}$. λ, which will need to be estimated, has elements corresponding to the discretely sampled 3-D spectral density or power spectrum of η (Brockwell and Davis, 1991). While η has a stationary spatial structure, the measurement error in either (4.4) or (4.5) is neither first nor second order stationary in a spatial sense.

It is important to appreciate that even though the model specification in (4.5) has substantial flexibility it should only be viewed only as a device for obtaining reasonable inferences - here the computation of approximate variances of imaging biomarkers. The general context of modeling in science is worth keeping in mind - approximate models, such as (4.5), may not be correct to arbitrary precision but in a practical environment they are still often very useful (Box, 1976). Before providing details of how the various unknowns in (4.5) are specified, we describe bootstrapping procedures for PET based on our model and also based on a non-parametric model-free approach.

4.2.2 Bootstrapping Techniques

We consider two possibilities for creating bootstrap samples for PET data: a well-established Projection-Domain approach and a novel Image-Domain approach developed here. The Image-Domain method uses equations (4.4) and (4.5); the Projection-Domain is based on the raw count data before it has been reconstructed. It is helpful to record the steps involved in bootstrap simulation by these techniques. This is provided below. We also describe a simple recycling scheme that would be important where it is not practical to retain a large number bootstrap replications.

4.2.2.1 Projection-Domain Bootstrap: Non-parametric

This approach involves random sampling (with replacement) from the number (N_e) of detected events. If events are binned into count arrays, this is equivalent to drawing a random sample from a multinomial distribution with N_e trials and probabilities proportional to the observed counts in binned array. Each simulated count array is processed to produce a bootstrap reconstruction, z^*. Repeating the process N_B times leads to a projection-domain bootstrap sample, $\mathcal{B}_P = \{z^b, b = 1, 2, ..., N_B\}$. If raw data are binned count arrays before reconstruction, there would also be the possibility to sample bootstrap counts

using an inhomogeneous Poisson process with mean values proportional to the observed array counts. While this ensures that the simulated data is fully Poisson and more variable than the multinomial, because such sampling would not correspond to *list-mode* re-sampling, we do not use it here. Note that as the count-rate increases, there will be little percentage difference between counts produced by either sampling method.

4.2.2.2 Image-Domain Bootstrap: Model-based Approach

Let $\hat{X}$, $\hat{\alpha}$, $\hat{\sigma}$, $\hat{\phi}$, $\hat{\kappa}$, $\hat{Q}$ and $\hat{\lambda}$ be the estimated values of the various unknowns in (4.5). Bootstrap simulated data, z^*_{ij}, are generated by first creating an array $\xi^* = \{\xi^*_{ij}, i = 1, ..., N, j = 1, 2.., T\}$ with elements corresponding to a random sample of size NT from a standard Gaussian distribution with mean zero and unit variance. With $\mathcal{F}_N$ representing the normalized 3-D mixed sine and cosine transform (computed by the standard 3-D FFT) and $\hat{\sigma}_{ij} = \hat{\sigma}_i\hat{\phi}_j$, the simulated data are

$$z^*_{ij} = \hat{x}'_j\hat{\alpha}_i + \hat{\sigma}_{ij}\hat{Q}(\eta^*_{ij}|\hat{\kappa}_{ij}) \quad \text{where} \quad \eta^*_{\cdot j} = \mathcal{F}^t_N(\hat{\lambda}^{1/2}\xi^*_{\cdot j}) \tag{4.6}$$

where $\xi^*_{\cdot j}$ and $\eta^*_{\cdot j}$ are the j'th columns of the $N \times T$-dimensional arrays corresponding to ξ^* and η^*. Repeating the process N_B times gives an image-domain bootstrap sample, $\mathcal{B}_I = \{z^b, b = 1, 2, ..., N_B\}$ where z^b is the b'th realization of z^* in equation (4.6).

4.2.2.3 Approximate Image-Domain Bootstrap by Recycling

In practical clinical settings, data retention protocols can mean that raw list-mode data are not routinely archived especially for dynamic studies. In such environments it is also unlikely that there would be willingness to retain extensive bootstrap datasets. Hence a simplified alternative to the full image-domain bootstrap is of interest. The proposal here is to retain a set of fitted model α-coefficients for a small number of image-domain bootstrap samples ($N^*_B \ll N_B$) and to base further bootstrap inferences on that dataset - $\mathcal{B}^*_I = \{\alpha^b, b = 1, 2, ..., N^*_B\}$. To justify this, it is important that the coefficients retained are sufficient for the proposed inferences and also that the size of N^*_B is adequate. Under either of the models in (4.4,4.5), any target parameter, θ, associated with the measurable tracer concentration signal ($\mu_{i\cdot} \approx x'\alpha_i$) is readily expressed in terms of the associated model coefficient - *i.e.* $\theta_i = f(\mu_{i\cdot}) = f(x'\alpha_i) \equiv g(\alpha_i)$. Recall that a basic property of maximum likelihood is that if $\hat{\alpha}_i$ is an optimal estimator of α_i then $\hat{\theta}_i = g(\hat{\alpha}_i)$ is optimal for

θ_i, $c.f.$ (Rao, 1973). Thus if the errors in (4.4) are Gaussian and a corresponding weighted least squares procedure is used for estimation of coefficients, the α-coefficient data can be expected to be sufficient in a statistical sense.

We propose a novel *recycling* procedure to help enhance the value of the retained limited data $\mathcal{B}_I^*$. In the approach samples are generated by sampling from $\mathcal{B}_I^*$ a set of say $\tilde{N}_B$ values at each voxel and then, by application of a spatial filtering process, create a recycled bootstrap dataset $\tilde{\mathcal{B}}_I^* = \{\tilde{z}^b, b = 1, 2, ..., \tilde{N}_B\}$ where $\tilde{z}_{ij}^b = x_j' \tilde{\alpha}_i^b$. Importantly, the recycled $\tilde{\mathcal{B}}_I^*$ data is only created at the time that inferences are being considered – so there is no need to retain extensive bootstrap samples. More details are reported in (O'Sullivan et al., 2021).

4.2.3 Specification of Unknowns in the Image-Domain Model

Here, we give a summary of the specification of parameters in the proposed model and the full estimation procedure, see (O'Sullivan et al., 2021). As indicated earlier, the model in (4.5) has a number of unknowns all of which need to be defined before image-domain bootstrapping is possible. We begin by describing how the basis set, X, is specified and after that consider the other elements.

The goal in basis selection is to choose a configuration that is physiologically interpretable and has the ability to approximate the measured time-course data at all voxels in the volume. Detail of the basis selection scheme is described in section 3.2.1 and substantially follows (O'Sullivan, 1993; O'Sullivan et al., 2014; Gu et al., 2021). The process is implemented in two steps. The first step applies recursive hierarchical clustering to partition the data into a large set of clusters, $\{C_l, l = 1, 2, ...L\}$, with the property that the data in each cluster has a similar shape pattern: $i.e.$ if $i \in C_l$ then for a suitable constant a_i, $z_{ij} \approx a_i \mu_{jl}$ where $\tilde{\mu}_{jl} = \frac{1}{|C_l|} \sum_{i \in C_l} z_{ij}$ for $j = 1, 2, ..., T$ is the mean time-course for the l'th cluster. Step 2 takes the collection of mean time-course patterns associated with each of these clusters as an initial set of basis elements $X_L = \{\tilde{\mu}_1, ..., \tilde{\mu}_L\}$ and applies a cross-validation guided backwards elimination procedure to construct a final subset $X_K = \{\mu_1, ..., \mu_K\} \equiv \hat{X}$ with the property that voxel-level data can be adequately represented by a non-negative linear combination of the columns of $\hat{X}$. In the case that well-sampled time-course of PET-measured data is acquired and we have access to the time-course of the tracer in the arterial blood, the second step is modified by replacing each of the cluster mean time-courses by a modeled time-course. A non-parametric residue modeling process in section

3.2.1 is used for that. Modeling helps to ensure that the final set basis vectors satisfy physiological constraints linked to the basic principles of blood-tissue exchange (Meier and Zierler, 1954).

Specification of the Unknowns, apart from X

With X fixed, an unconstrained weighted least squares procedure, with a simple fixed temporal weighting scheme, is used for estimation of α_i's in (4.4). The simple weighting scheme and associated ϕ-values are

$$w_j^0 = e^{-t_j\zeta} dt_j/\bar{\mu}_j^* \quad , \quad \phi_j^0 \propto 1/\sqrt{w_j^0} \quad \text{for} \quad j = 1, 2, .., T \tag{4.7}$$

Here $\bar{\mu}_j^* = \max(\bar{\mu}_j, m)$ where $\bar{\mu}_j$ is average of the reconstructed concentration values over the j'th time-frame and m is taken to be a fraction (0.1) of the maximum of these $\bar{\mu}_j$ values. The duration of the scan time-frame is dt_j and $e^{-t_j\zeta}$, with ζ the decay constant for the radio-tracer isotope, is the standard tracer decay factor. While the estimates of α_i based on these simple weights may not be optimal, under general conditions weighted least squares estimates are unbiased and also consistent, as the scale of the error diminishes (Seber, 2015).

Residuals from the least squares fit are used to estimate the other unknowns in (4.5). The motivation for this comes from

$$\begin{aligned} r_{ij} &\equiv z_{ij} - x_j'\hat{\alpha}_i \approx z_{ij} - x_j'\alpha_i = \sigma_{ij}\epsilon_{ij} \equiv \sigma_i\phi_j\epsilon_{ij} \\ \text{so } r_{ij} &\approx \sigma_i\phi_j h_{ij} e_{ij} \quad \text{with} \quad h_{ij}^2 = Var(\epsilon_{ij}) \end{aligned} \tag{4.8}$$

and $e_{ij} = \epsilon_{ij}/h_{ij}$ has mean zero and unit variance. From (4.8), natural conditional estimates of ϕ and σ are

$$\hat{\phi}_j^2 = \frac{1}{N}\sum_{i=1}^{N} w_{ij}(\sigma, h) r_{ij}^2 \quad \text{and} \quad \hat{\sigma}_i^2 = \frac{1}{T}\sum_{j=1}^{T} w_{ij}(\phi, h) r_{ij}^2 \tag{4.9}$$

where $w_{ij}(\sigma, h) = \sigma_i^{-2} h_{ij}^{-2}$ and $w_{ij}(\phi, h) = \phi_j^{-2} h_{ij}^{-2}$. $\hat{\phi}_j^2$ values are scaled so that $\sum_j \hat{\phi}_j^2 = T$. For any specified h, (4.9) can be iterated, starting with σ constant, to obtain converged values $\tilde{\phi}(h)$ and $\tilde{\sigma}(h)$. These are maximum likelihood estimates when e_{ij} is standard Gaussian. With $h_{ij} = 1$, the converged values in (4.9), denoted $\tilde{\phi}$ and $\tilde{\sigma}$, are used as estimates of ϕ and σ in model (4.4). This is important for specification of κ. The set of $\hat{\kappa}$-values are defined by $\hat{\kappa}_{ij} = \frac{\hat{z}_{ij}}{\tilde{\sigma}_i\tilde{\phi}_j}$ where $\hat{z}_{ij} = x_j'\hat{\alpha}_i$.

For estimation of Q, we restrict to piecewise constant approximation as a function of the κ variable. With $\kappa_{(0)} = -\infty$ and $\kappa_{(l)}$ the $\frac{l}{L} \times 100\%$'th percentile of the $\hat{\kappa}_{ij}$ values, let I_l be the interval $(\kappa_{(l-1)}, \kappa_{(l)}]$, for $l = 1, 2, ..., L$. Piecewise constant approximation means $Q(\cdot|\hat{\kappa}) = \hat{Q}(\cdot|l)$ for $\hat{\kappa} \in I_l$. Our experience is that Q is a smooth function of $\hat{\kappa}$ so that a modest value for L (in the 50 to 100 range) seems to be quite adequate. As Q is piecewise constant, its variance is also piecewise constant - $Var(Q(\eta|\hat{\kappa})) = h(\hat{\kappa})^2 = h_l^2$ for $\hat{\kappa} \in I_l$. This implies $h_{ij} = h_l$ for $\hat{\kappa}_{ij} \in I_l$. Similar to (4.9), a conditional estimate of h_l given σ and ϕ is

$$\hat{h}_l^2 = \frac{1}{|I_l|} \sum_{\hat{\kappa}_{ij} \in I_l} w_{ij}(\sigma, \phi) r_{ij}^2 \quad \text{with} \quad w_{ij}(\sigma, \phi) = \sigma_i^{-2} \phi_j^{-2} \tag{4.10}$$

normalized so that $\sum_l \hat{h}_l^2 = L$. Combining (4.9) and (4.10), provides an iteration for joint estimation of σ, ϕ and h. This defines $\hat{\sigma}$ and $\hat{\phi}$. The converged $\hat{\sigma}$ values are inflated by multiplication by $\frac{T}{T-K}$ where K is the number of columns of X. This is to ensure there is adjustment for the bias arising from fitting the α-coefficients at each voxel. Such adjustments are standard in most parametric model fitting settings - see (Kutner et al., 2013; Seber, 2015) for its use in linear regression.

The converged values of $\hat{\sigma}$ and $\hat{\phi}$ are used to compute scaled residuals $\hat{\epsilon}_{ij} = r_{ij}/\hat{\sigma}_i\hat{\phi}_j$. The empirical distribution of these scaled residuals, $E_l = \{\hat{\epsilon}_{ij} \ ; \ \hat{\kappa}_{ij} \in I_l\}$, is used to evaluate $\hat{Q}(\cdot|l)$. Here we match order statistics of E_l to the corresponding quantiles of a standard normal distribution - $\mathcal{N}_l = \{\hat{\eta}_{ij} \ ; \ \hat{\kappa}_{ij} \in I_l\}$. This is simply the standard normal quantile-quantile plot procedure – $c.f.$ (Team et al., 2013). The inverse map allows arbitrary quantiles of the standard normal to be mapped to quantiles of E_l.

For estimation of λ, the full set of normalized residuals, $\hat{\eta}$, are mapped to the imaging domain and using the 3-D FFT their 3-D periodogram is evaluated for each time-frame. Averaging these periodograms over time-frames, with weights $\hat{\phi}_j^{-2}$, produces the final estimate of the required power spectrum, $\hat{\lambda}$. Using the Weiner-Khinchine theorem (Brockwell and Davis, 1991), the inverse 3-D FFT of the power spectrum provides the corresponding of the 3-D spatial autocorrelation function $\hat{\rho}$. This completes the specification of all unknowns in the image-domain bootstrapping model. Before investigating the reliability of the bootstrapping method, we first present some illustrations of the technique with real data. Model diagnostics are an essential part of any statistical modeling process, particularly if model-based bootstrapping is of interest. This aspect is

highlighted in the illustrative examples.

4.3 Illustrative Example

Cellular DNA is replicated during cell division so that its concentration in rapidly proliferating tumor tissues can be expected to be higher than in normal tissue. PET FLT imaging has the potential to provide an approximate measure of DNA concentration and for this reason FLT imaging may be helpful for diagnosis and treatment planning with certain cancers. Our data is from a multicenter American College of Radiology Imaging Network clinical imaging trial (ACRIN 6688) which conducted dynamic PET-FLT imaging of breast tumor before and during neo-adjuvant chemotherapy. The goal was to see if PET-FLT imaging could give an early indication of the tumor response – trial results are reported in (Kostakoglu et al., 2015). The ACRIN data are part of an anonymized cancer imaging archive developed and maintained by the National Cancer Institute (https://www.cancerimagingarchive.net). The data considered here are from a patient studied at baseline (before chemotherapy). The study was conducted on a 74-plane scanner using a 3-D acquisition process and ML reconstruction. The 4-D PET data set consists of an imaging volume with $N = 168 \times 168 \times 74$ voxels ($2.97 \times 2.97 \times 2.01mm^3$) and $T = 45$ time-frames of acquisition over one hour. The time-frame binning sequence was: 16(5 sec), 7(10 sec), 5(30 sec), 5(1 min), 5(3 min) and 7(5 min). Note that more than half of the temporal sampling is focused on the first 2.5 minutes of the 1-hour acquisition. This is in part because the kinetics of FLT (a small molecule) are faster than those of FDG. The left-ventricle of the heart was used to directly recover a blood time-course, which after approximate adjustment for metabolites provided an arterial input function, C_p, used for kinetic analysis.

Data were processed using NPRM as described in section 3.2.1. $N_B = 500$ image-domain bootstrap replicates were used for evaluation of sampling variation in computed metabolic images. Metabolic images and associated bootstrap estimates of their voxel-level standard errors are in Figure 4.3. Metabolic images shown are for a transverse slice through the tumor region (indicated by an arrow on the flux image). Volume of distribution(V_d), flow(K_d) and flux (K_i) show significant enhancement in the tumor region. In a compartmental modeling framework, all three parameters have been suggested as appropriate ways to quantify FLT time-course data (Kostakoglu et al., 2015). Standard errors again demonstrate a pseudo-Poisson characteristic — variability is higher

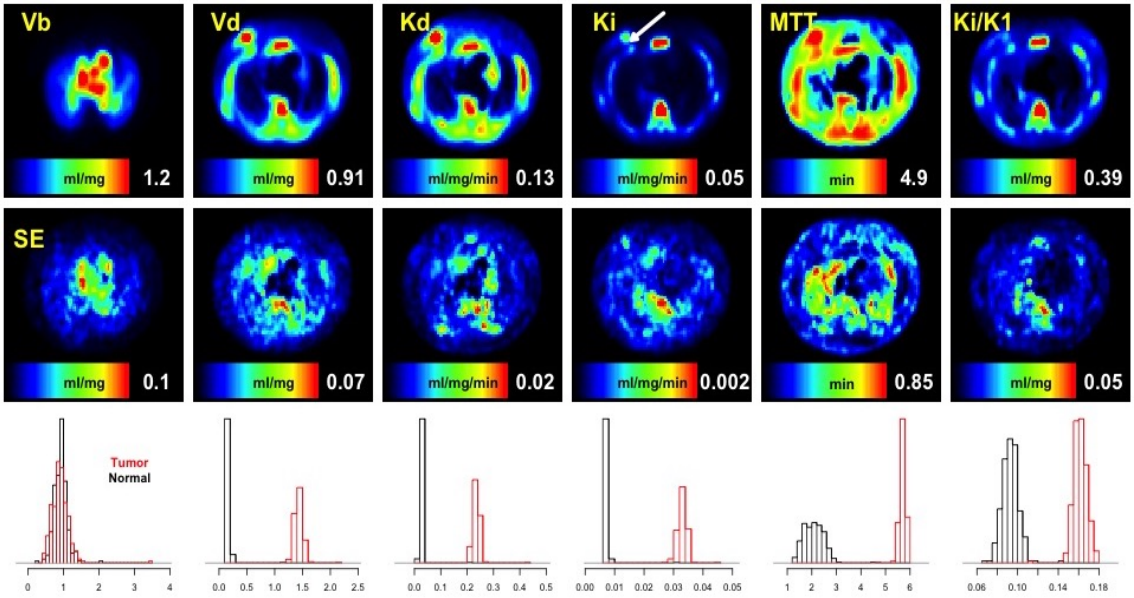


Figure 4.3: Metabolic Images with image-domain bootstrap assessment of standard errors for Breast tumor FLT study. The mapped parameters are shown on row 1 – the location of tumor volume of interest (VOI) on the slice is indicated with an arrow. Columns correspond to different metabolic parameters (labeled in yellow) with color bars indicating units - see section 3.2.1.1 for definitions. Computed standard errors (SE) are on row 2. Row 3 shows histograms of the bootstrap sampling distributions of the 95'th percentile of the metabolic parameter in the normal [black] and tumor [red] VOIs[3].

in regions with higher values. The typical percent error, measured by the standard deviation relative to metabolic parameter value, is on the order of 10-20% for most of the metabolic variables displayed. It is again notable that the mean transit time (MTT) and extraction (K_i/K_1) appear quite stable as is the associated uncertainty measure. Volumes of interest (VOIs) for tumor and contralateral normal breast were also accessed. The tumor region had 1280 voxels extending over 16 slices (3.2cm in axial extent); the normal VOI is not quite as large - 1054 voxels - but with a very similar shape. The bootstrap estimated histograms of the sampling distribution of the 95'th percentile of the metabolic parameters in the VOIs are shown in Figure 4.3. Differences between tumor and normal VOIs are quite dramatic for all parameters, except for the vascular blood volume measure (V_b). These differences are highly significant when formally assessed via the bootstrap information.

[3]Contributed by Prof. Finbarr O'Sullivan.

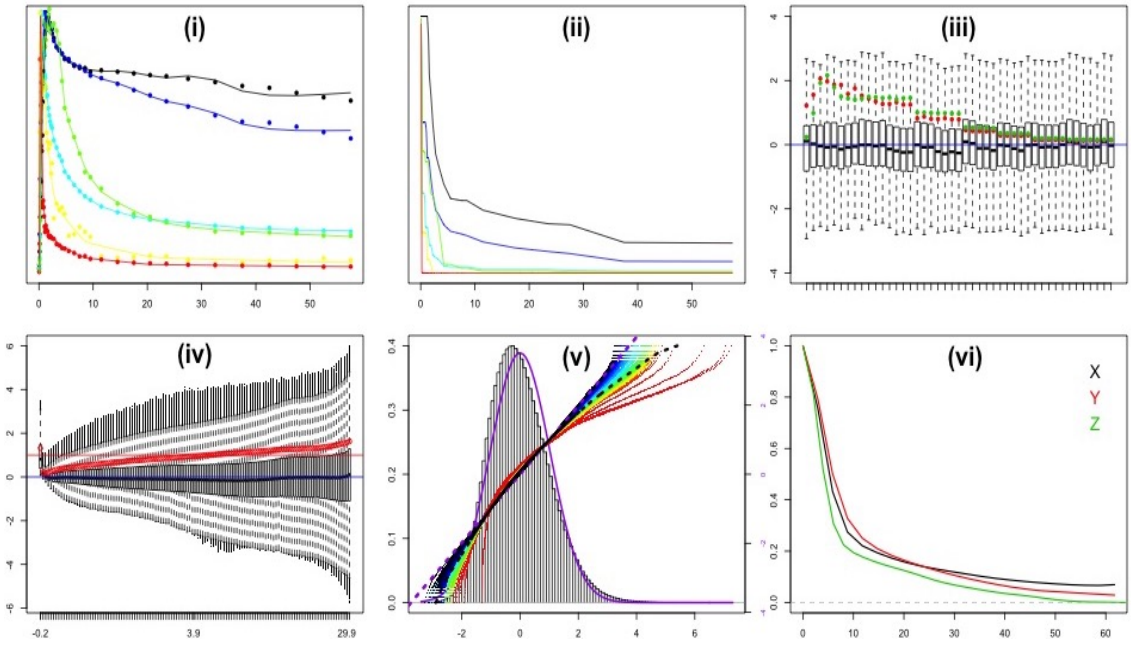


Figure 4.4: Diagnostics associated with the Image-Domain Bootstrapping Model (4.5) for the FLT-Breast data. Six plots, labeled (i) to (vi), are shown: (i) raw sub-TACs (dots) and fitted models (lines) for the selected basis set - columns of X. (ii) Non-parametric residues corresponding to the fitted model. (iii) Boxplots by time-frame of standardized residuals from the unconstrained least squares fit, $r_{ij}/\hat{\sigma}_i\hat{\phi}_j\hat{h}_{ij}$. The simple, $\hat{\phi}_j^0$ in (4.7), and optimized, $\hat{\phi}_j$, standard deviations are shown as green and red dots. (iv) Boxplots of scaled residuals, $\hat{\epsilon}_{ij} = r_{ij}/\hat{\sigma}_i\hat{\phi}_j$, for each κ-bin (each containing roughly 10000 data points). $\hat{h}_l$-values are shown as red points; the red line is for comparison with unity (zero skewness of bin data). (v) Histogram of the overall distribution of the standardized residuals and its relation to a Gaussian fit (purple curve). Super-imposed are points showing quantiles of standardized residuals from different κ-bins (colored from red to dark blue according to bin order) versus corresponding quantiles of the Gaussian (right y-axis). The quantile pattern for the overall histogram and the Gaussian fit are shown with dashed black and purple lines. (vi) Directional auto-correlation patterns of the normalized residuals, $\hat{\eta}$, as a function of distance in millimeters. X-Y are transverse with Y perpendicular to the scanning bed; Z is the axial direction[4].

Residual diagnostics for the analysis are shown in Figure 4.4. Eight vectors are identified by basis selection procedure. The cluster mean data defining the

[4]Contributed by Prof. Finbarr O'Sullivan.

six non-AIF and Patlak basis vectors and their corresponding non-parametric residue model fits are again shown in Figure 4.4(i) and (ii). Temporal boxplots of the fully standardized residuals are shown in Figure 4.4(iii). The optimized and initial temporal scaling factors, $\hat{\phi}_j$ and ϕ_j^0 match each-other quite closely, apart from first few time-frames. Boxplots of residuals scaled by temporal ($\hat{\phi}_j$) and spatial ($\hat{\sigma}_i$) factors and binned by values of $\hat{\kappa}_{ij}$ ($= \hat{z}_{ij}/\tilde{\sigma}_i\tilde{\phi}_j$) are in Figure 4.4(iv). Apart from the very first bin, the distributions show variation increasing with increasing values of $\hat{\kappa}$ - this is confirmed by $\hat{h}$ which is substantially linear as a function of the quantiles of $\hat{\kappa}$. The distribution of the standardized residuals, $(z_{ij} - \hat{\mu}_{ij})/\hat{\sigma}_{ij}$, show a marked skewness. The pattern deviates substantially from the Gaussian – Figure 4.4(v). Detailed evaluation of the distributions across κ-bins shows that as κ-increases, there is increasing conformity to the Gaussian. As discussed in section 4.2, in a Gamma distribution κ is proportional to the shape parameter and as that parameter increases the Gamma distribution formally converges to a Gaussian. Thus the data are in line with (Mou, Huang and O'Sullivan, 2017) who showed that a Gamma-form was a good approximation for ML-reconstructed data. The directional spatial auto-correlation patterns of the scaled residuals are given in Figure 4.4(vi).

4.4 Numerical Studies

The purpose here is to evaluate the performance of the novel image-domain bootstrapping technique for PET and make comparisons with the more computationally intensive, but fully non-parametric, projection-domain approach. Assessment of variance estimators is somewhat complicated because we do not have an analytic formula for the true target variance. Hence a number of replicate simulations (N_S) are needed to evaluate the true target variance with reasonable accuracy. Bootstrapping techniques involve simulation and the number of such simulations (N_B) also needs to be considered. Apart from the computation, in practice the storage requirements associated with retention of bootstrap samples may also be a factor. We will report studies in which both modest and large numbers of bootstraps are examined.

In mathematical terms, PET has the structure of a linear inverse problem. The raw list mode data is a realization of an inhomogeneous Poisson process in which the rate is linearly related to the target source. Our studies use a simplified representation of PET scanning. This enables us to conduct a more detailed set of studies. We assume that critical performance differences between

image-domain and projection domain bootstrapping methods for real PET scanners should be apparent in a simplified simulation setting, provided of course that the mathematical complexity of the simplification is substantially similar to PET. We report on experiments with 2-D and 1-D PET scanning models. The 2-D studies are focused on analytic (FBP) reconstruction only, but iterative ML and analytic reconstruction are considered in the 1-D case. Dynamic aspects of both 1-D and 2-D studies are based on results obtained for the FLT breast cancer data presented in section 4.3.

4.4.1 2-D Experiments

The overall study structure is outlined in Figure 4.5. The 2-D setup focuses on central slice containing the tumor. The dynamic source for the selected slice, Figure 4.5A, corresponds to the models fitted in NPRM mapping of kinetics. Temporal sampling and tissue attenuation are also matched to the real data. The scanning model is same as in section 3.4.1. It involves Poisson sampling of a discretized (attenuated) parallel-beam Radon transform of the source (Kak, Slaney and Wang, 2002; Natterer, 2001). The imaging domain is the unit square, discretized to an array of dimension 128×128, and the projection domain is the region $[-\sqrt{2}, \sqrt{2}] \times [0, \pi]$, discretized to a 183×181 sinogram array of distances and angles. Note the π-periodicity of the parallel beam Radon transform restricts the angular extent of the projection domain. As shown in Figure 4.5B, the discretized dynamic source is projected to produce the corresponding dynamic sinogram array of suitably attenuated rates. The scale of the rate array is adjusted by a factor corresponding to study dose, τ_R. This dose is specified so that the voxel-level noise in the reconstructed data matches the apparent voxel-level noise level of the real data. Independent Poisson count simulation from each element of the scaled sinogram array yields the synthetic projection-domain data (y). Each frame of the sinogram data is reconstructed analytically using a standard filtered backpojection (FBP) procedure with the raw ramp-filter result smoothed by convolution with a Gaussian resolution filter. The resolution filter bandwidth is required to be common across all time frames and by grid-search its value is selected in order to minimize the average squared error difference between the estimated and true activity summed over frames. This choice of bandwidth is to ensure that the uptake image is objectively adapted to the study dose (O'Sullivan, 1995). Simulated data are processed using the NPRM procedure in section 3.2.1, to produce a set of metabolic maps. In addition data sets for the projection-domain (non-parametric), the image-domain

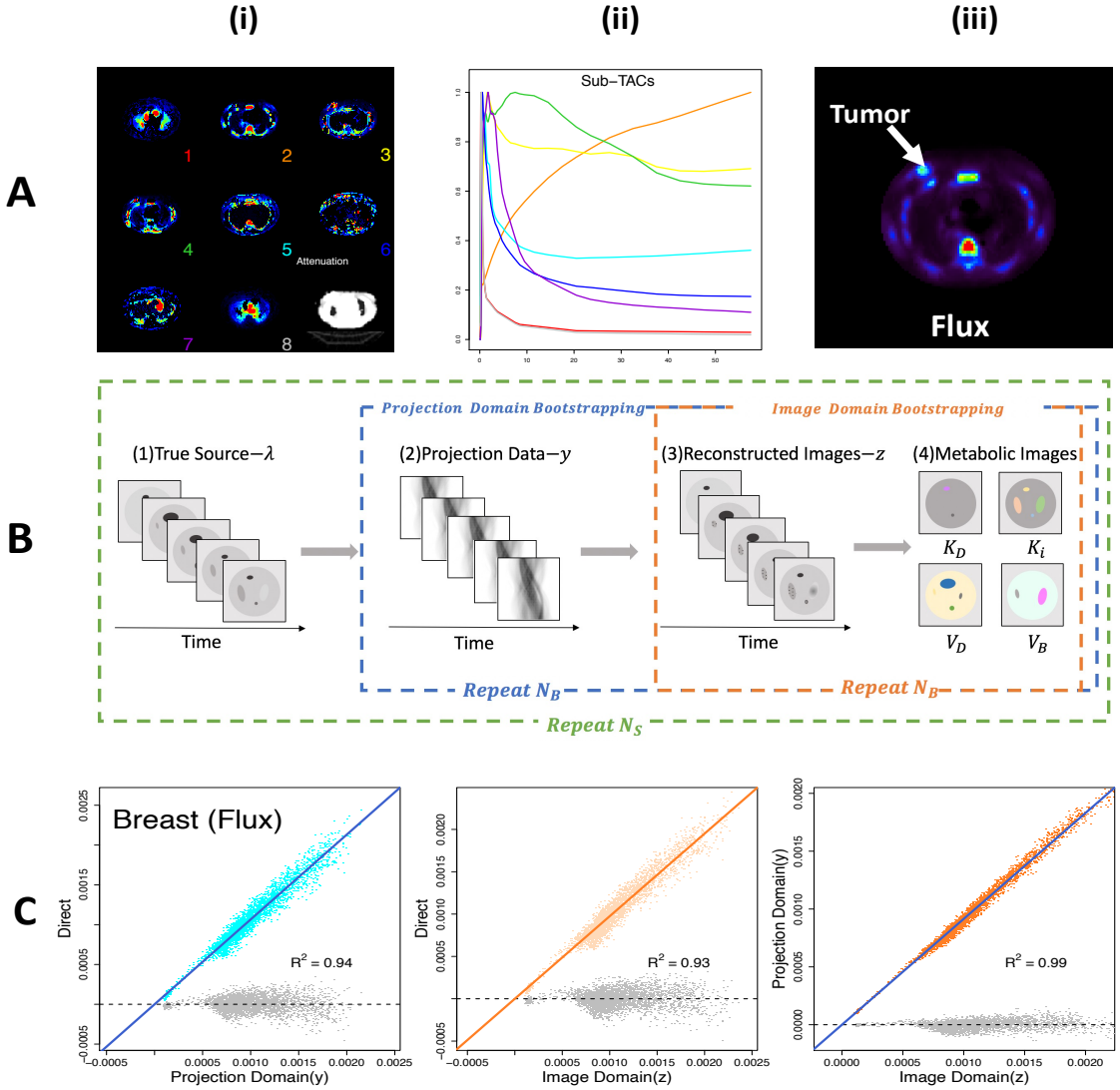


Figure 4.5: **A:** Source distribution, $\lambda_{xt} = \sum_{k=1} \alpha_k(x)\mu_k(t)$, for the 2-D simulation experiments. $\alpha_k(x)$ patterns and attenuation in (i), time-courses for each component, $\mu_k(t)$ (normalized), are in (ii). Flux parameters are in (iii). **B:** Dynamic image-domain source leads to a corresponding projection domain array. Simulated counts are reconstructed and computed metabolic images. Each replicate of the simulation has both non-parametric (projection-domain) and model-based (image-domain) bootstrapping. **C:** Voxel estimates of average standard deviations of flux are shown. The true values are estimated by direct replication, these values are compared to image and projection domain bootstraps for a single replicate.

and the approximate image-domain bootstraps are acquired. $N_B = 25$ bootstrap samples are used for the projection and image-domain bootstraps; a set of, $N_B^* = 10$, samples were used with the approximate image-domain method, with $\tilde{N}_B = 200$ samples used in recyclying - see Section 4.2.2.3. Note these

numbers of bootstrap samples would be viewed as quite small relative to what might be used in standard statistical application (Efron and Tibshirani, 1994), however, they are likely to be realistic for practical use in most clinical imaging settings. The bootstrap datasets were used to evaluate a set of voxel-by-voxel standard deviations in estimated metabolic parameters. These values are compared to the true values estimated by direct replication. This is indicated in part C of Figure 4.5.

4.4.1.1 Bootstrapping Voxel-Level Summaries

Quantitative comparisons between the estimated and true standard deviations were assessed on a voxel-by-voxel basis using a simple linear regression analysis and also in terms of an overall root mean square error (RMSE) measure. Regression analysis considered the relation between the true standard deviation, estimated by replication, with the corresponding values evaluated by the bootstrap methods. These regression analysis models are expressed as

$$\sigma_{ip} \approx a_p \, \sigma_{ip}^{y} \quad ; \quad \sigma_{ip} \approx b_p \, \sigma_{ip}^{z} \quad ; \quad \sigma_{ip} \approx c_p \, \sigma_{ip}^{z*} \tag{4.11}$$

for $i = 1, 2, ..., N$. Here σ_{ip} is the true standard deviation of the p'th metabolic parameter estimate for the i'th voxel; $\sigma_{ip}^{y}, \sigma_{ip}^{z}$ and $\sigma_{ip}^{z^*}$, are the values for the projection-domain, image-domain and recycled image-domain bootstraps. In all cases, the simple linear regression analysis models are found to very well describe the relation between the true and bootstrap estimated standard deviation. The model R^2 exceeds 0.9 for all metabolic parameters and for FLT simulation – values for flux (K_i) are shown in Figure 4.5C.

The regression parameters, (a, b, c), in (4.11) summarize the average bias in the bootstrap estimate. If the regression parameter is close to unity it indicates that the bootstrap estimated standard deviations are well aligned with the true; a value less/greater than unity, indicates over/under-estimation of standard deviation by the bootstrapping method. Table 4.1 reports the values of these regression coefficients estimated from the simulation data. There is little indication of significant bias with any of the bootstrapping methods - the non-parametric projection domain approach generally tends to under-estimate the true standard deviation by an average of 9-10% in FLT setting. In contrast the image-domain procedures tend to over-estimate the standard-deviation, typically by around 1-3%. RMSE evaluates the mean square deviation between the estimated and true standard deviation at each voxel, with these values then

averaged over all voxels. If $\hat{\sigma}_{ips}$ is the standard deviation in the p'th metabolic parameter estimate at voxel i for the s'th replicate data for the bootstrap estimate, the RMSE is given by

$$\text{RMSE}^{\hat{\sigma}}_{p\bullet} = \sqrt{\frac{1}{NN_S}\sum_{i=1}^{N}\sum_{s=1}^{N_S}[\hat{\sigma}_{ips} - \sigma_{ip}]^2} \tag{4.12}$$

The RMSE values for projection-domain and image-domain methods are denoted $\text{RMSE}^{y}_{p\bullet}$, $\text{RMSE}^{z}_{p\bullet}$ and $\text{RMSE}^{z*}_{p\bullet}$. These values are reported in percentage terms in Table 4.1. There is little difference between the alternative bootstraps procedures with the image-domain technique out-performing the projection-domain method for some parameters (MTT and K_i/K_1) but not for other parameters (V_b, V_d, K_d and K_i). RMSE values for the approximate image-domain bootstrap are consistently the largest. However it needs to be appreciated that, in light of the typical standard error of the true standard deviation, the significance of any of these differences is small. Standard errors are reported as $\bar{\text{SE}}_{p\bullet}$ in Table 4.1. Note that the corresponding standard errors for averaged bootstrap estimates of standard deviations are very similar - these are not reported in the table. Further 2D studies with higher are lower count rates were also conducted and gave results very much in line with those reported in Table 4.1.

Table 4.1: Reliability of Bootstrap Estimates of voxel Standard Deviations for mapped kinetics in **2-D** setting. Means and maxima of **voxel kinetic** estimates, averaged over replicates, are shown as $\bar{\mu}_\bullet$ and $\bar{\mu}_\vee$. Mean of voxel standard deviations, averaged over replicates ($\bar{\sigma}_\bullet$) its standard error ($\bar{SE}_\bullet$) and the overall RMSE values, see (4.12), are reported as a percentage of the maximum ($\bar{\mu}_\vee$). Estimates ($\hat{a}, \hat{b}, \hat{c}$) correspond to (4.11).

Parameters	V_b	V_d	K_d	K_i	MTT	K_i/K_1
Mean ($\bar{\mu}_\bullet$)	0.22	0.23	0.04	0.01	4.58	0.12
Max ($\bar{\mu}_\vee$)	1.96	1.54	0.19	0.07	8.36	0.59
$\bar{\sigma}_\bullet$	2.61	3.81	11.14	1.52	22.73	12.52
$\bar{SE}_\bullet$	0.19	0.26	0.87	0.10	1.38	1.00
$\hat{a}$	1.04	1.08	1.12	1.07	1.20	1.18
$\hat{b}$	0.90	0.98	1.00	0.98	1.14	1.08
$\hat{c}$	0.91	0.99	1.03	0.99	1.16	1.11
$\text{RMSE}^{y}_{\bullet}$	0.69	1.00	4.14	0.35	8.43	5.13
$\text{RMSE}^{z}_{\bullet}$	0.91	1.11	4.35	0.40	8.04	5.09
$\text{RMSE}^{z*}_{\bullet}$	1.08	1.35	5.08	0.50	9.40	5.88

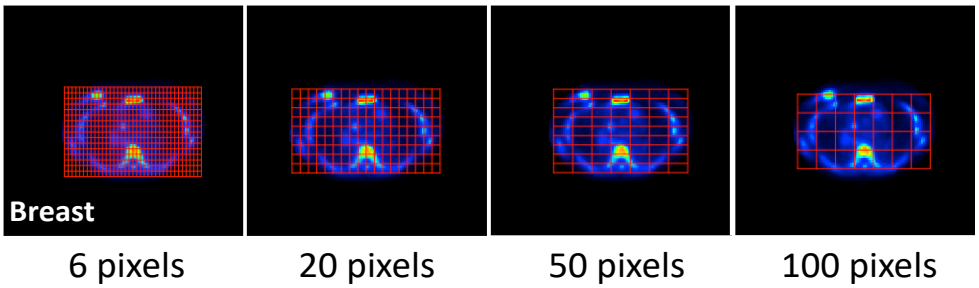


Figure 4.6: Schematic of 2D ROI generation scheme. A total of 676 ROIs with different sizes (6, 20, 50 and 100 pixels) are defined for Breast. Grids of rectangular ROIs and their size are indicated.

4.4.1.2 Bootstrapping ROI Summaries

For this analysis a nested sequence of grids were used to construct a range of ROIs with different sizes (6, 20, 50 and 100 pixels) and tissue heterogeneity characteristics. Figure 4.6 gives a schematic of the ROI generation scheme.

ROI averages Comparison between bootstrap estimates of standard deviations of ROI averages of flux (K_i) is shown in Figure 4.7. There is no indication that the alignment of the bootstrap estimates with the true standard deviations varies by ROI size. Detailed assessments of the reliability of the bootstrap estimates is provided in Table 4.2. These are based on an ROI version of (4.11) and (4.12) - $i.e.$ the voxel indicator (i) is replaced by an indicator of the ROI.

Similar to the voxel case, bootstrap estimates perform very well. There is no evidence that these results are substantially impacted by the size-distribution or positioning of ROIs. The non-parametric and image-domain method (with $N_B = 25$ replicates) have very similar RMSE reliabilities. Both bootstraps tend to under-estimate the true ROI mean standard deviation. However, the amount of bias is small - on the order of 10-14% across the different kinetic parameters. Recycling is found to lead to more unreliable values - largely due to a greater systematic over-estimation of the true ROI standard deviation - on the order of 20% for most parameters. But the overall indication from the 2-D experiments is that image-domain bootstrapping scheme is very well aligned with the non-parametric projection domain approach and provides a viable mechanism for assessments of uncertainties at both the voxel and ROI level.

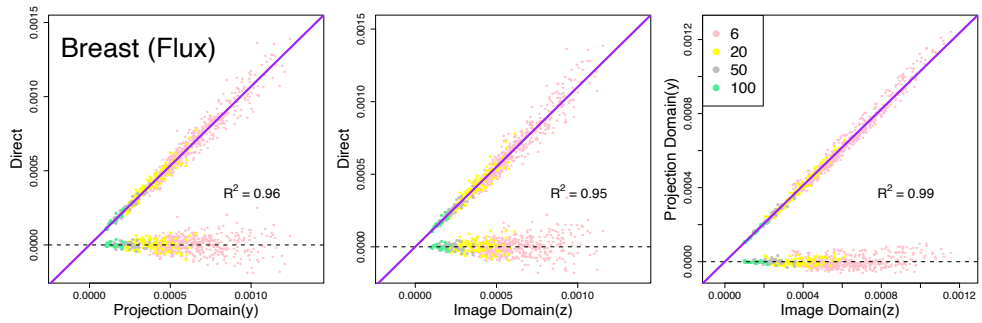


Figure 4.7: Estimates of average ROI standard deviations of flux. Colors correspond to different ROI sizes.

Table 4.2: Reliability of Bootstrap Estimates of Standard Deviations for **ROI means** of mapped Kinetics in **2-D** setting. Note approximately 700 ROIs are considered , see Fig 4.6. Means and maxima of ROI-averaged kinetic parameters, averaged over replicates, are shown as $\bar{\mu}_\bullet$ and $\bar{\mu}_\vee$. Mean ROI standard deviation, averaged over replicates ($\bar{\sigma}_\bullet$), its standard error ($\bar{SE}_\bullet$) and the overall RMSE values, computed by ROI version of (4.12), are reported as a percentage of the maximum ($\bar{\mu}_\vee$). Estimates ($\hat{a}, \hat{b}, \hat{c}$) are based on the ROI version of (4.11).

Parameters	V_b	V_d	K_d	K_i	MTT	K_i/K_1
Mean ($\bar{\mu}_\bullet$)	0.27	0.26	0.04	0.01	4.24	0.14
Max ($\bar{\mu}_\vee$)	1.63	1.30	0.17	0.07	8.04	0.52
$\bar{\sigma}_\bullet$	1.82	2.54	7.00	0.85	11.58	7.24
$\bar{SE}_\bullet$	0.12	0.17	0.50	0.06	0.76	0.52
$\hat{a}$	1.27	1.18	1.23	1.10	1.24	1.23
$\hat{b}$	1.04	1.08	1.11	1.07	1.20	1.16
$\hat{c}$	0.71	0.63	0.58	0.57	0.87	0.55
$\text{RMSE}^y_\bullet$	0.38	0.54	1.92	0.17	3.36	2.27
$\text{RMSE}^z_\bullet$	0.54	0.64	2.23	0.19	3.51	2.44
$\text{RMSE}^{z*}_\bullet$	1.22	2.04	6.83	0.85	7.35	8.08

ROI Maxima and CVs Two complex statistic summaries of kinetic parameters in ROI - maximum and the coefficient of variation (CV) defined as standard deviation divided by the mean are also calculated and their uncertainties are assessed by the direct replication, projection and image-domain bootstrapping. Quantitative comparisons between the estimated and true standard deviations of the biomarkers of interest were assessed on different ROIs using a simple linear regression analysis (4.11) and also in terms of an overall root mean square error (RMSE) measure (4.12) .

The relationship between bootstrap estimates of standard deviations of ROI maxima and CVs of flux (K_i) are shown in Figure 4.8. The standard errors estimated by the projection and image domain bootstrapping are highly consistent and regression parameters, (a, b) in (4.11) and RMSE in (4.12) for maxima and

CVs in ROIs are presented in Table 4.3. For all kinetic parameters, results based on image-domain bootstrapping are highly in line with the classic approach.

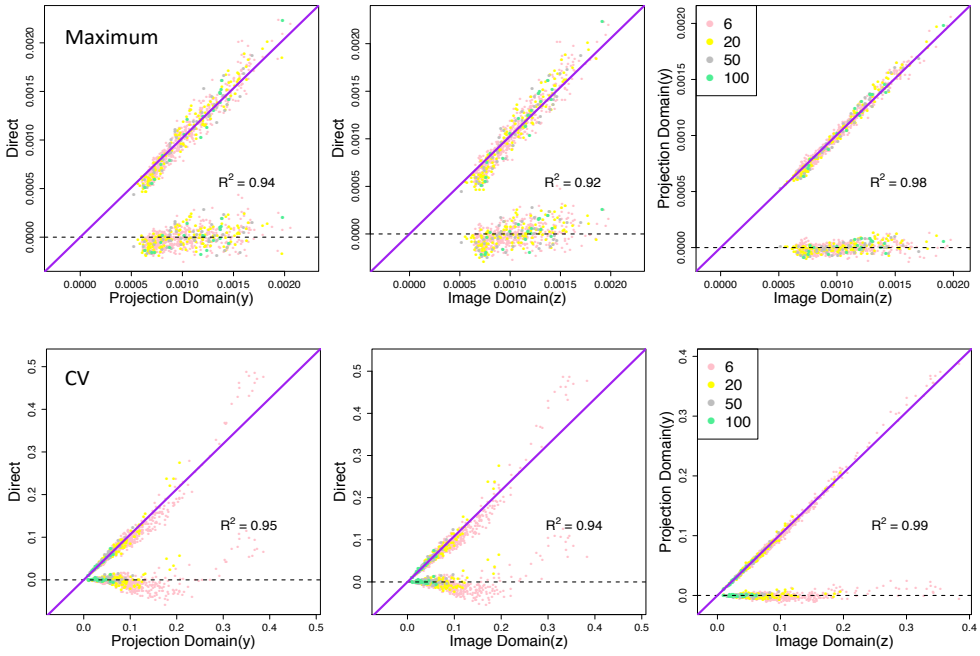


Figure 4.8: Standard deviations of ROI **maxima** (Row 1) and coefficients of variation (**CVs**) (Row 2) of flux (K_i) in breast study. The true values are estimated by direct replication, compared to image and projection domain bootstrap results. Different colors represent different ROI sizes.

4.4.2 1-D Experiments

These studies have a similar temporal structure to the 2-D simulations but a more simplified 1-dimensional Poisson deconvolution scanning model from (O'Sullivan and Roy Choudhury, 2001) is used. The simplified structure is same as section 3.4.1 and allows a detailed investigation of bootstrapping when the input data used for kinetic analysis has been reconstructed by methods analogous to the direct FBP and iterative maximum likelihood (ML) procedures used in PET. The scanning model is defined as follows: we observe a discretized Poisson process whose intensity is of the form $\gamma_{xt} = a_x[\mathcal{R}\lambda]_{xt}$ for $x = 1, 2, .., N$ (even) and $t = 1, 2, ..., T$. Here $0 < a_x \leq 1$ is a known attenuation factor and the matrix $\mathcal{R}$ is given by $\mathcal{R} = I_T \otimes K_\beta$ where $K_\beta : R^N \to R^N$ and K_β has the form of a discrete convolution. Letting $\mathcal{F}$ be the discrete Fourier transform, for any vector $x \in R^N$, $[\mathcal{F}K_\beta x]_\nu = |\nu|^{-\beta}[\mathcal{F}x]_\nu \equiv \widehat{x}_\nu$ for $\nu = \pm 1, \pm 2, ..., N/2$. With $\beta > 0$, the action of K_β is to smooth the vector x. If y is a realization of a Poisson with mean $\tau\gamma$, then an unbiased estimate of the underlying source distribution λ is

Table 4.3: Estimates of standard deviations for ROI **Maxima** and **CVs** of metabolic parameters in **2-D** Breast FLT studies. Note approximately 700 ROIs are considered in each case. Means and maxima of ROI maximum and CV kinetic parameters, averaged over replicates, are shown as $\bar{\mu}_\bullet$ and $\bar{\mu}_\vee$. Mean ROI standard deviation, averaged over replicates ($\bar{\sigma}_\bullet$), its standard error ($\bar{SE}_\bullet$) and the overall RMSE values, computed by ROI version of (4.12), are reported as a percentage of the maximum ($\bar{\mu}_\vee$). Estimates ($\hat{a}$ and $\hat{b}$) are based on the ROI version of (4.11).

	(a) ROI Maximum						(b) ROI CV					
Parameters	Vb	Vd	Kd	Ki	MTT	Ki/K1	Vb	Vd	Kd	Ki	MTT	Ki/K1
Mean ($\bar{\mu}_\bullet$)	0.08	0.81	0.38	0.01	5.63	0.06	0.54	0.43	0.68	0.37	0.58	0.57
Max ($\bar{\mu}_\vee$)	0.16	1.41	0.73	0.02	9.66	0.24	1.19	1.30	1.54	1.18	1.39	1.87
$\bar{\sigma}_\bullet$	16.97	9.34	12.83	5.55	6.64	8.06	14.57	9.71	14.85	7.75	17.42	9.65
$\bar{SE}_\bullet$	1.18	0.65	0.90	0.35	0.51	0.77	1.08	0.70	1.10	0.59	1.46	0.71
$\hat{a}$	1.02	1.03	1.01	1.11	1.08	0.99	1.17	1.16	1.18	1.09	1.15	1.07
$\hat{b}$	0.99	1.00	0.98	1.11	1.07	0.99	1.09	1.08	1.10	1.06	1.08	1.03
$\text{RMSE}^y_\bullet$	3.85	1.80	3.08	1.26	2.16	3.61	4.62	2.98	4.58	2.83	7.34	2.94
$\text{RMSE}^z_\bullet$	4.05	1.99	3.22	1.32	2.27	3.75	4.87	3.29	5.03	2.93	7.73	3.09

obtained by adjusting for the y-data by the attenuation factor and applying a least squares (LS) inversion procedure. This result is then smoothed to achieve consistent mean square error performance. As FBP is essentially equivalent to LS in the 2-D setting (O'Sullivan, 1995), we refer to LS as FBP in our 1-D model.

Letting S_h be a smoothing matrix with bandwidth $h > 0$ the smoothed estimate is

$$z = I_T \otimes S_h z^{(fbp)} \text{ with } z^{(fbp)} = \frac{1}{\tau} I_T \otimes [K'_\beta K_\beta]^{-1} K'_\beta (y/a) \tag{4.13}$$

where $(y/a)_{xt} = y_{xt}/a_x$.

If S_h has a discrete Fourier representation, $z^{(fbp)}$ and z are efficiently computed using the 1-D FFT. Adapting (Vardi, Shepp and Kaufman, 1985), the EM algorithm can be used to evaluate a maximum likelihood (ML) estimate, $z^{(ml)}$, and a corresponding smoothed value $z^+ = S_h z^{(ml)}$. The ML estimator is asymptotically efficient, as $\tau \to \infty$, as indeed is the FBP estimator. In estimation terms, 1-D scanning model shares some of the essential complexity of PET. In PET, K_β is replaced by the line-integral Radon transform, $\mathcal{K}$. FBP estimation is known as filtered backprojection (FBP). Similar to $K'_\beta K_\beta$, the operation $\mathcal{K}'\mathcal{K}$ is Toeplitz (Natterer, 2001). In d-dimensions, the eigenvalues of $\mathcal{K}'\mathcal{K}$ are proportional to $|\xi|^{-d/2}$; while the eigenvalues of $K'_\beta K_\beta$ are proportional to $|\nu|^{-2\beta}$. Studies reported in section 3.7.1 show that with a choice of $\beta = 1.35$, there is a good agreement between the bandwidth optimized mean square error (MSE) estimation characteristic as a function of dose for the 1-D Poisson deconvolution

model, and the corresponding MSE characteristic of 2-D PET reconstruction.

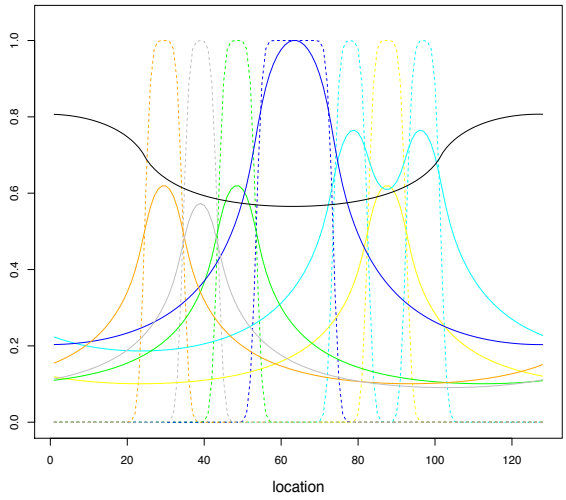


Figure 4.9: Scaled spatial patterns (α_j) for source distribution ($\lambda_{xt} = \sum_{j=1}^{6} \alpha_j(x)\mu_j(t)$) in 1-D experiments (dotted lines); projection domain patterns ($K_\beta \alpha_j$) are also shown (solid lines). Source sub-TACs (μ_j) are in Figure 4.5 A(ii). Colors of α_j's here match the colors of corresponding sub-TACs in Figure 4.5 A(ii). The solid black line is the attenuation pattern.

In the 1-D case, simulations were conducted for FLT using source distribution consisting of a mixture of six temporal components, $\lambda_{xt} = \sum_{j=1}^{6} \alpha_j(x)\mu_j(t)$. The number of voxels was set at $N = 128$. The temporal patterns are matched to those arising in the 2-D simulations. Spatial patterns are indicated in Figure 4.9, together with the transformed profiles, $K_\beta \alpha_j$'s, and the attenuation pattern. Reference dose-values τ_R were again chosen so that the qualitative variability of simulated 1-D data matched that seen at the voxel-level in the real FLT data. Five dose levels, $\tau = \tau_R/5, \tau_R/2.5, \tau_R, 2.5\tau_R, 5\tau_R$ were examined with FLT study. In the 1-D setting a more extensive bootstrapping process was used ($N_B, \tilde{N}_B = 200$ with $N_B^* = 10$) and the number of replicates was also increased ($N_S = 400$). Simulated data were reconstructed using FBP and iterative ML techniques. Raw frame-by-frame reconstructions were smoothed by convolution with a Gaussian kernel. Similar to the 2-D case, bandwidth was common across all frames, and its value was optimized according to the mean square deviation of the estimated total uptake from the true known source. Due to the implicit regularization associated with raw ML reconstruction (O'Sullivan, 1995; O'Sullivan and Roy Choudhury, 2001) bandwidths were separately optimized for the FBP and ML reconstructions. Results for the middle dose are presented in Table 4.4. Very similar results were found at other doses. Regression analysis again finds strong alignment between the bootstrap generated standard

deviations and the true values. Generally there is a tendency for the methods to underestimate the true standard deviation by on the order of 7%. The approximate image-domain bootstrap is 2-4% higher than the others. There is little or no difference between the pattern for FBP and ML reconstructed data. Raw RMSE values, computed by (4.12), are typically 16% smaller for ML reconstructed than FBP reconstructed data. However this is undoubtedly a reflection of the fact that the metabolic parameter standard deviations, summarized by $\bar{\sigma}_\bullet$ in Table 4.4, are on the order of 14% lower for data reconstructed by ML versus the FBP. In light of this, Table 4.4 reports RMSE values as a percent of the average true standard deviation. The adjusted RMSE values are very similar for FBP and ML. In the case of FLT RMSE values are 1.1% higher. In practical terms these differences are inconsequential. Results demonstrate the ability of the methodology to adapt to the characteristics of the ML data. Overall, the RMSE is 4.5% lower for the projection-domain bootstrap than the image-domain approach; the approximate method is 9.3% higher again. A similar calculation for the RMSE values reported in the 2-D simulation but expressed as a percentage of $\bar{\sigma}_\bullet$, gives values that are remarkably similar to this: The image-domain method is 2.8% higher than the projection-domain with the RMSE for the approximate method a further 6.3% higher again.

Table 4.4: Reliability of Bootstrap Estimates of **voxel** Standard Deviations for mapping Kinetics in **1-D** based on FBP and ML reconstructed data. Means and maxima of voxel kinetic estimates, averaged over replicates, are shown as $\bar{\mu}_\bullet$ and $\bar{\mu}_\vee$. Mean of voxel standard deviations, averaged over replicates ($\bar{\sigma}_\bullet$), its standard error ($\bar{SE}_\bullet$) and the overall RMSE values, see (4.12), are reported as a percentage of the maximum ($\bar{\mu}_\vee$). Estimates $(\hat{a}, \hat{b}, \hat{c})$ correspond to (4.11).

		FBP						ML					
Tracer	Parameters	Vb	Vd	Kd	Ki	MTT	Ki/K1	Vb	Vd	Kd	Ki	MTT	Ki/K1
FLT	Mean ($\bar{\mu}_\bullet$)	0.18	0.71	0.16	0.02	3.46	0.12	0.18	0.71	0.16	0.02	3.47	0.12
	Max ($\bar{\mu}_\vee$)	1.04	2.17	0.36	0.05	7.50	0.61	1.04	2.17	0.36	0.05	7.57	0.61
	$\bar{\sigma}_\bullet$	2.01	1.93	4.26	1.72	9.69	2.93	1.62	1.83	3.65	1.66	9.23	2.45
	$\bar{SE}_\bullet$	0.08	0.08	0.17	0.08	0.46	0.15	0.06	0.08	0.15	0.07	0.44	0.11
	$\hat{a}$	1.02	0.98	1.01	0.99	1.11	1.08	1.05	1.01	1.06	1.03	1.13	1.14
	$\hat{b}$	1.20	0.98	1.05	0.98	1.12	1.11	1.22	0.97	1.03	0.99	1.13	1.13
	$\hat{c}$	1.23	1.01	1.08	1.02	1.18	1.17	1.25	1.01	1.06	1.03	1.20	1.18
	$\text{RMSE}^y_\bullet$	25.4	31.6	27.2	37.8	44.4	56.0	22.2	30.6	24.9	33.7	44.2	50.2
	$\text{RMSE}^z_\bullet$	33.3	34.7	29.3	41.3	46.0	59.0	34.6	35.0	28.8	39.2	47.5	58.0
	$\text{RMSE}^{z*}_\bullet$	41.3	45.6	38.7	51.2	57.6	72.7	42.6	44.8	38.4	48.8	59.3	71.4

4.4.3 Statistical Interpretation of Simulation Data

Table 4.5 reports on a number of further analyses applied to all the simulation data generated in 2-D and 1-D experiments. These analyses are applied separately in 1-D and 2-D so the table gives the ability to see similarities across the various configurations explored and appreciate overall patterns. The focus is on two analyses, (i) the direct systematic relation between the projection-domain and image domain bootstrapping methods, and (ii), the relation between relative uncertainty in voxel-level kinetic parameters and data reconstruction error. For the first analysis we conducted regression analyses, similar to (4.11), relating the voxel-level projection-domain bootstrap standard deviation to the values from the image-domain approaches, $i.e.$

$$\sigma^y_{ip} \approx \alpha_p \sigma^z_{ip} \quad ; \quad \sigma^y_{ip} \approx \beta_p \sigma^{z^*}_{ip} \quad \text{for} \quad i = 1, 2, ..., N \tag{4.14}$$

The estimates of the α and β coefficients are in Table 4.5. Across all the simulation settings we see a very similar pattern. Apart from blood volume (V_b), whose standard deviation by the image-domain methods are consistently lower than reported by the projection-domain bootstrap, there is remarkably close alignment between the methods.

Table 4.5: Analysis of Voxel-level Error Characteristics across all Simulations. The coefficients are for the models in (4.14) and (4.15). The R^2-values only reported for (4.15). Corresponding values for (4.14), are uniformly high (in excess of 90%).

		Vb	Vd	Kd	Ki	MTT	Ki/K1
FBP (2D)	$\hat{\alpha}$	0.86	0.91	0.90	0.92	0.95	0.92
	$\hat{\beta}$	0.88	0.93	0.92	0.93	0.97	0.94
	$\hat{\gamma}_1$	0.79	0.63	0.59	0.63	0.90	0.75
	R^2	0.97	0.94	0.85	0.94	0.97	0.91
FBP (1D)	$\hat{\alpha}$	1.18	1.00	1.03	0.99	1.01	1.03
	$\hat{\beta}$	1.21	1.04	1.07	1.03	1.06	1.08
	$\hat{\gamma}_1$	0.77	0.92	0.86	0.85	1.11	0.56
	R^2	0.97	0.91	0.94	0.89	0.83	0.37
ML (1D)	$\hat{\alpha}$	1.16	0.96	0.97	0.96	1.00	0.99
	$\hat{\beta}$	1.19	1.00	1.00	1.00	1.05	1.04
	$\hat{\gamma}_1$	0.65	0.92	0.83	0.85	1.11	0.55
	R^2	0.90	0.92	0.92	0.88	0.81	0.40

The relation between voxel-level parameter standard deviation and reconstruction error was also explored. In the simulation setting, the square-root of the

weighted mean square reconstruction error can be used as an assessment of measurement error: $\sigma_i^R = \sqrt{\sum_{j=1}^T w_j^0 [z_{ij} - \lambda_{ij}]^2 / T} \approx \sigma_i$. Motivated by these theoretical considerations in (O'Sullivan et al., 2021), we examined the relation between the relative error in kinetic parameters and a scaled reconstruction error, by fitting regression models in the form

$$\log(\sigma_{ip}/\mu_{ip}) = \gamma_{0p} + \gamma_{1p} \log(\sigma_i^R/\mu_{ip}) + error \tag{4.15}$$

to each of the simulation datasets.

Table 4.5 shows estimates of γ_{1p} as well as the quality of fit of the model measured by the R^2 statistic. The model fits are remarkably good (most in excess of 80%) for all parameters. On the other hand the model variance pattern for extraction (K_i/K_1) is not very reasonable for FLT. These analyses give an understanding of the behavior of voxel-level kinetic parameter variability.

4.5 Discussion

The work has presented a novel image-domain approach to bootstrapping PET data having a dynamic component. The method is based on a novel general linear model approximation of the dynamic source distribution in which the error is described in terms of a sub-ordinate Gaussian process that is assumed independent across time-frames and stationary in the imaging space. In addition the distribution of error is allowed to adapt to the local skewness of the data. Thus there is no requirement for the method to be modified depending on whether an analytic or iterative data reconstruction process is used. This removes a number of potentially limiting assumptions used in (Huang et al., 2020). The bootstrapping scheme in (Huang et al., 2020) also made essential use of the near-replicate nature of re-binned time-frame data. But this is not required here. In essence, the generalized linear modeling of the dynamic PET data used here creates an approximate replicate residual process that provides information for data simulation. Conceptually this is similar to information provided by time-frame re-binning in (Huang et al., 2020).

Our methodology is illustrated by application to real examples involving the use of dynamic PET imaging for the purpose of mapping metabolic parameters of tissues in the field of view. The general linear modeling analysis technique enables us to create bootstrap replicate data sets for analysis. Application of the NPRM kinetic mapping technique to the bootstrap data provides

voxel-level estimates of metabolic parameters and their associated uncertainties (SEs). Numerical studies motivated by these examples compare the image-domain bootstrapping approach to the more computationally demanding but fully non-parametric projection-domain approach (Haynor and Woods, 1989). Image-domain bootstrapping is found to substantially match the RMSE performance characteristics of projection-domain bootstrapping and gives a potential to practically evaluate the uncertainties of complex biomarkers recovered from the analysis of information in an individual patient PET study (Gu, Wu and O'Sullivan, 2021).

The current analysis is implemented in R (Team et al., 2013) - an open-source statistical programming platform. An R-package is currently under development and is expected to be available on the CRAN network (`https://cran.r-project.org`) in the near future. In comparison to projection-domain bootstrapping, in which each bootstrap replicate requires reconstruction of simulated list-mode data; computation of image-domain bootstrap replicates are negligible. The computation time for a series of 3-D data sets to implement image-domain bootstrapping model is reported in Table 5.4. Based on our 2-D numerical studies, the computation of the image-domain bootstrapping model is less than what would be required for a single ML reconstruction of a list-mode time-course data set. In light of this, with iteratively reconstructed PET data - the norm in most PET scanners now - image-domain bootstrapping will always be faster than the projection-based approach; the difference between them becoming more extreme as temporal sampling or the number of bootstrap replicates required increases.

Of course as computing capabilities grow and it becomes standard to retain list-mode data for dynamic PET studies, non-parametric projection-domain bootstrapping may become practical as well. Indeed this would be an ideal circumstance because the theory underpinning the non-parametric approach is very well developed (Efron and Tibshirani, 1994). But current PET scanning technology is very far from that now. In addition, current archives of well-curated cancer clinical trial PET imaging data combined with associated patient outcomes, $e.g.$ National Cancer Institute (`https://www.cancerimagingarchive.net`), do not to our knowledge include any list-mode information. Thus the analysis of image uncertainty using data from such archives can only be based on a suitable image-domain bootstrapping approach, as we have described here.

For situations where retention of extensive bootstrap samples is prohibitive, we

have proposed a novel recycling process as an approximate image-domain bootstrapping approach. While the RMSE performance of this approximation is not as good as a full bootstrap, the results are still quite reasonable. Importantly our studies indicate that the performance of the image-domain simulation techniques are not impacted by whether or not the reconstruction methodology is analytic (FBP) or iterative (ML).

It would be interesting to use the methods here to examine multiple studies with a similar anatomy on the same scanner, in order to develop a practical scanner-specific understanding of the study-to-study stability of the image-domain model estimates. If list-mode data were available, it would also be possible to use the projection-domain bootstrap to gain some insight into this. Specifically such a bootstrap could be used to create replicate projection-domain scanning data that could be used to estimate image-domain model parameters. The collection of model parameters obtained across bootstrap replicates would then provide a direct assessment of their sampling characteristics.

There are a number of other medical imaging modalities where subject-specific assessment of uncertainty in quantitated imaging measurements are not currently available and the techniques here might be useful. For example, dynamic imaging with MR (DCE,DSC) or CT are routine in the clinical management of cancer and stroke and the structure of datasets is substantially similar to dynamic PET. This will be a focus for future work.

Chapter 5

Bootstrap Averaging Enhances the Mean Square Error of Kinetic Maps Recovered from PET Data

Abstract

Positron emission tomography (PET) is an imaging technique that is prominently used in both clinical and research settings. It has a history of methodological interest in the field of Statistics. Recent developments in the spatial and temporal resolution capabilities of PET scanners have substantially increased interest in mapping kinetic parameters from the large-scale datasets produced by dynamically acquired studies. Several schemes have been proposed for this problem. A recently developed image-domain bootstrapping technique has made assessment of the sampling distribution for imaged kinetic information feasible. The technique, which uses a somewhat sophisticated generalized linear model involving a subordinate Gaussian process, is applicable to any kinetic imaging methodology for PET. The work here summarizes the image-domain bootstrapping technique and examines its potential to improve the mean square error (MSE) performance of kinetic maps by averaging results from individual bootstrap samples. Dynamic PET case studies with fluorodeoxyglucose (FDG) and fluorothymidine (FLT) in brain and breast cancer patients are used to illustrate this proposal. A series of one and two dimensional simulations matched to both cases are used to quantitatively evaluate the approach across a range of practical noise levels. Kinetic mapping using both compartmental modeling and non-parametric residue analysis is considered.

Routinely available PET scan data arising from traditional filtered-backprojection (FBP) and iterative maximum likelihood (ML) reconstructions are examined. Root MSEs (RMSE) of raw and averaged-bootstrap (AB) kinetics are evaluated. The RMSE of AB kinetics is typically 10% to 30% lower than the RMSE of raw kinetics. The improvements are remarkably consistent across study doses and the reconstruction technique used in the PET scanner. Perhaps unsurprisingly there is some variability associated with the ground-truth kinetics and the type of kinetic mapping procedure used. The RMSE enhancements are quite similar in scale to the numerical improvements achieved when using ML instead of FBP for PET data reconstruction. These results clearly support the use of bootstrap averaging as a way to improve kinetic information extracted from dynamic PET studies. This work may stimulate further development of the image-domain bootstrapping methodology for applications to the quantitative analysis of multi-channel imaging datasets.

5.1 Introduction

Positron emission tomography (PET) imaging is an important tool in the diagnosis and therapy planning of patients with cancer or other diseases. While the standardized uptake value (SUV), is the main variable used to quantify the vast majority of routine clinical PET scans with the fluorodeoxyglucose (FDG) radiotracer (Boellaard, 2009), there is an ongoing interest in exploring the potential of using more extensive dynamic PET scanning with multiple time frames in order to recover a more complete metabolic profile of target tissue for whatever radiotracer is employed. Thus mapping the kinetics of the tracer in local tissue is an important goal of dynamic PET studies, particularly in a research setting. This has been recently emphasized in the context of long axial field-of-view (AFOV) PET systems such as the Siemens Biograph Vision Quadra (Alberts et al., 2021), the uEXPLORER (Badawi et al., 2019) and the PennPET Explorer (Pantel et al., 2020) - see (Feng et al., 2021; Gu et al., 2022; Li et al., 2021; Sari et al., 2022; Viswanath et al., 2021; Wang, Nardo, Jones, Cherry and Badawi, 2021; Wu, Gu, Wu, Zhou and Wang, 2022; O'Sullivan et al., 2022).

As information derived from kinetic mapping is integrated into clinical decisions procedures for individual patients, it may become increasingly beneficial to have techniques available for practical assessment of the reliability of the kinetic information involved in those decisions (Mankoff et al., 2002; Dunnwald et al., 2011). While traditional linear methods, see (Carson et al., 1993; Huesman, 1984; Maitra and O'Sullivan, 1998; Teymurazyan et al., 2013) for exam-

ple, can be effective for evaluation of uncertainties in some summary quantities derived from filtered-backprojection (FBP) reconstructed data, the generalization of these methods to non-linear summaries and to data reconstructed by iterative maximum likelihood (ML) methods (Vardi, Shepp and Kaufman, 1985) is not straightforward. In such situations, procedures based on the statistical bootstrap (Efron and Tibshirani, 1994; Haynor and Woods, 1989; Buvat, 2002; Dahlbom, 2001; Lartizien, Aubin and Buvat, 2010; Ibaraki et al., 2014; Kucharczak et al., 2018) are technically attractive. Previous bootstrapping methods for PET have been based on non-parametric sampling of projection-domain/ raw list-mode data. But these methods require data reconstruction for each bootstrap simulation, and have not so far proven to be practically feasible for routine use especially with dynamic ML-reconstructed data. Building on work in (Huang et al., 2020; Mou, Huang and O'Sullivan, 2017), a computationally efficient image-domain bootstrapping approach, suitable for dynamic PET data reconstructed using either FBP or ML techniques, was recently described (O'Sullivan et al., 2021). This bootstrapping method has been used to assess uncertainty in kinetic variables for voxel and potentially quite complex regional summaries of kinetic variables (O'Sullivan et al., 2021; Gu, Wu, O'Sullivan, Huang, Muzi and Mankoff, 2019; Gu, Wu and O'Sullivan, 2021). The practicality of the approach, even with long AFOV PET scanner whole body data has also been demonstrated (O'Sullivan et al., 2022).

But, since bootstrapping approximates the full sampling distribution of a parameter estimation, there may also be potential to improve the mean square error (MSE) performance by averaging the bootstrap samples (Efron and Tibshirani, 1994). Indeed the random forest (Breiman, 2001) generalization of regression tree models which is a machine learning technique in many applications, including PET (Wang, Lei, Fu, Curran, Liu, Nye and Yang, 2020; Wu et al., 2019), is of course a highly successful use of such an averaging process - see Figure 5.1.

In this chapter we explore if averaging of image-domain bootstrap-generated kinetic maps might improve mean square error performance. The methodology is described in section 5.2. Some illustrative examples from the brain and breast cancer studies are shown in section 5.3. Section 5.4 describes a series of numerical studies examining the approach in some detail. Results are presented in section 5.5. The chapter concludes with discussion.

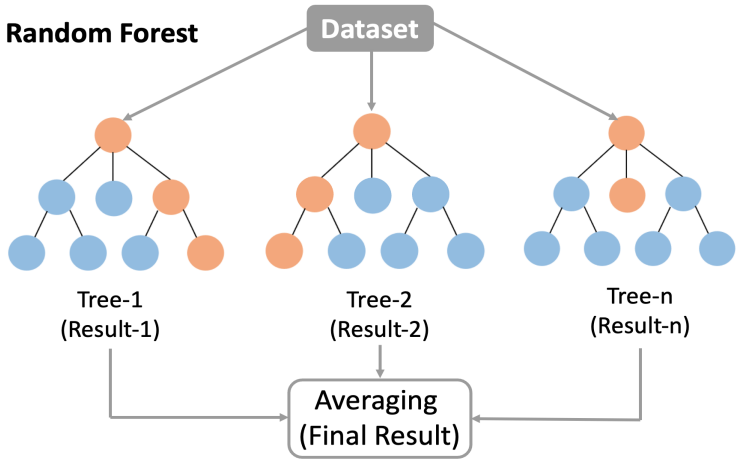


Figure 5.1: Random forests improves prediction error by averaging predictions from multiple trees trained on different bootstrap samples of data.

5.2 Methodology

5.2.1 Overview of Image-Domain Bootstrapping

Before describing the application to kinetic mapping, we first summarize the main elements of the bootstrapping methodology developed in (O'Sullivan et al., 2021) - see schematic in Figure 5.2.

The 4-D dynamic PET dataset is represented by an $N \times T$ array, $\{z_{it}; i = 1, ..., N, t = 1, ..., T\}$. N is the number of voxels and T is the number of time-frames. The data generation process (DGP) used for image-domain bootstrapping is based on a general linear model (GLM) representation for the 4-D PET data. This GLM has systematic and stochastic components. The systematic component models the mean of the voxel-level time-course as a linear combination of data-adaptive time-course shape patterns defined by segmentation of the full data volume; the stochastic component is represented in terms of an underlying or sub-ordinate stationary Gaussian process or Gaussian copula form (Csörgó and Mielniczuk, 1996; Joe, 2014). The stochastic model captures spatial and temporal non-uniformities in variance, covariance structure, and also has the ability to adapt to the dose-dependent distributional character of voxel-level PET data in a non-parametric manner. Motivated by the work in (Huang et al., 2020), the inverse coefficient of variation is used to model deviation from Gaussian

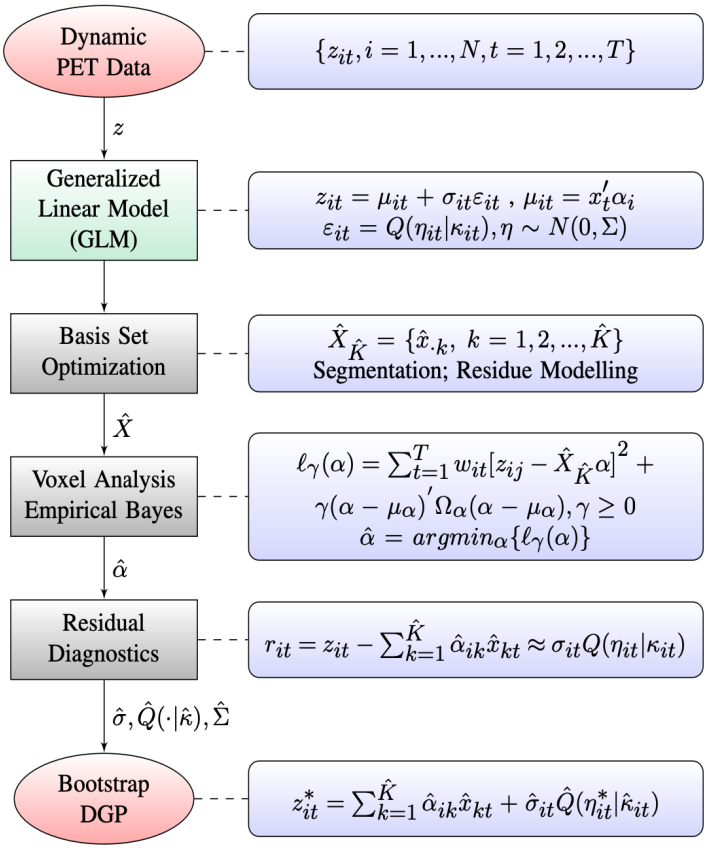


Figure 5.2: Graphical representation of the generalized linear model (GLM) used to define the data generation process (DGP) for PET image-domain bootstrapping.

behavior. The GLM is formally specified by the system of equations

$$\begin{aligned} z_{it} &= \mu_{it} + \sigma_{it}\varepsilon_{it};\ \ \varepsilon_{it} = Q(\eta_{it}|\kappa_{it}) \text{ with } \boldsymbol{\eta} \sim N(0,\Sigma) \\ \mu_{it} &= x_t'\alpha_i;\ \kappa_{it} = \mu_{it}/\sigma_{it};\ \sigma_{it} = \sigma_i\phi_t,\ \sum_{t=1}^{T}\phi_t^2 = T \\ \Sigma &= \Gamma\Lambda^2\Gamma', \Gamma = \mathcal{F}_N \otimes I_T \end{aligned} \tag{5.1}$$

The underlying Gaussian process is $\{\boldsymbol{\eta}\}$; it is assumed to be stationary. μ_{it} and σ_{it} are the true mean and standard deviation of z_{it}; μ_{it} is expressed as a linear combination of a set of flexible basis time courses (x_t is the vector corresponding to the sampled of basis time-courses at time t) and α_i is an unknown coefficient. Individual basis vectors are constrained using a non-parametric residue modeling process - see equation (5.3) below. The non-parametric residue mapping (NPRM) approach used to recover voxel-level kinetics, see section 5.2.2, makes

critical use of this. σ_{it} in equation (5.1) is a product of spatial (σ_i) and temporal (ϕ_t) factors. The quantile function, $Q(\cdot|\kappa_{it})$, is strictly monotone for each fixed value of κ - the inverse coefficient of variation. A linear quantile function implies a Gaussian distribution for z_{it}. The estimation process is based on the empirical quantile function - in simplified settings this is in line with the classical non-parametric bootstrap. $\mathcal{F}_N$ is a Fourier matrix used to map an N-vector to its 3D sine and cosine Fourier coefficients. This is implemented by the standard 3D fast Fourier transform (FFT). The Fourier structure ensures that the underlying Gaussian process is spatially stationary. I_T is a T-dimensional identity matrix and Λ is a diagonal matrix with elements, $\lambda = \{\lambda_i, i = 1, ..., N\}$. In time-series terminology, Λ corresponds to the power-spectrum of the stationary Gaussian process corresponding to the temporal components of $\{\boldsymbol{\eta}\}$.

The GLM estimation process is elaborated in (O'Sullivan et al., 2021). Basis set construction uses a cross-validation guided backwards elimination procedure. This optimizes the number and choice of individual basis elements. Voxel level analysis is based on an empirical Bayes formulation. This ensures that the regularity of voxel-level coefficients (α's) are adaptively constrained by the marginal volumetric distribution of the raw voxel coefficients and the local noise characteristics of the data. The numerical efficiency of the approach substantially derives from the critical use of both unconstrained and constrained weighted least squares techniques. Residuals from the weighted least squares fitting of voxel-coefficients, are used to determine unknown parameters, in the stochastic component of the model - $i.e.$ $\hat{\sigma}_{it}$, $\hat{Q}$ and $\hat{\Lambda}$.

The image-domain bootstrap simulates data by first generating a random sample $\{\xi^*_{it}\}$ from a standard Gaussian distribution. This sequence is first transformed to produce a realization of the underlying sub-ordinate Gaussian process $\{\eta^*_{it}\}$ and subsequently manipulated using the estimated quantile and scaling variables to produce the bootstrapped relization $\{z^*_{it}\}$. The equation is

$$z^*_{it} = \sum_{k=1}^{\hat{K}} \hat{\alpha}_{ik}\hat{x}_{kt} + \hat{\sigma}_{it}\hat{Q}(\eta^*_{it}|\hat{\kappa}_{it}) \tag{5.2}$$

where $\eta^*_{it} = \mathcal{F}^t_N(\hat{\lambda}^{1/2}\xi^*_{it})$ with $\xi^*_{it} \sim N(0, 1)$. Repeating the process N_B times gives a set of image-domain bootstrap samples, $\mathcal{B} = \{z^b, b = 1, 2, ..., N_B\}$ where z^b is the b'th realization of z^* in equation (5.2). For application to kinetic mapping, each bootstrap simulated dataset is mapped by the same process applied to the original dataset. This leads to a bootstrap $\mathcal{K}_\mathcal{B} = \{\theta^b, b = 1, 2, ..., N_B\}$, where θ^b

is the bootstrap realization of the kinetic map for the z^b.

The proposed image-domain bootstrapping technique is an example of a model-based bootstrapping scheme but with a very high dimensional model form which includes the voxel-level α and σ-coefficients as well the bivariate quantile function Q and power spectrum Λ. There is of course an extensive literature on bootstrapping dependent data (Fabjan, 2022; Politis and Romano, 1994; Lahiri and Lahiri, 2003; Horowitz, 2019; Kreiss and Lahiri, 2012; Pascual, Romo and Ruiz, 2004). Much of the associated asymptotic theory has focused on techniques for stationary data in which the localised dependence structure can be quantified by mixing conditions. There is obviously a lack of stationarity in mean and variance in PET imaging data. Complexity arising from the Gamma-like nature of PET measurements seems quite challenging, theoretically. As dose increases, reconstructed PET measurements become substantially Gaussian (Mou, Huang and O'Sullivan, 2017). This simplifies the GLM model somewhat so that a theoretical analysis of consistency of the DGP may be more accessible. We are currently investigating this.

5.2.2 Mapping Kinetics: NPRM and 2C Approaches

It is well appreciated that when a tracer's interaction with the tissue is linear and time-invariant, the tissue time course (C_T) measurable by dynamic PET can be expressed as a convolution between arterial input function (AIF or C_p) and the tissue impulse response/residue function (R):

$$C_T(t) = \int_0^t R(t-s)C_p(s)ds \equiv R \otimes C_p \tag{5.3}$$

Following Meier and Zierler (Meier and Zierler, 1954), the kinetics of the tissue such as blood or in-distribution volume (V_b,V_d), flow (K_d), flux (K_i), mean transit time (MTT) and extraction (Ext) - K_i/K_1 with $K_1 = K_d + K_i$, are model-independent quantities defined as functions of the tissue residue (O'Sullivan et al., 2014; Gu et al., 2021; O'Sullivan et al., 2021). While there is extensive reliance on 2-compartment (2C) modeling in PET, most famously in the analysis of FDG in human brain (Phelps et al., 1979), such modeling may have difficulty representing data in which the detailed assumptions related to tissue homogeneity vascular supply pattern and/or in-vivo biochemistry may be in doubt - see (Barrio et al., 2020; O'Sullivan et al., 2009). In such situations non-parametric estimation of the residue can be useful.

5.2.2.1 NPRM Mapping

The non-parametric residue mapping (NPRM) technique in (O'Sullivan et al., 2009, 2014; Gu et al., 2021) uses the linear model form in the GLM as a basis for analysis of voxel-level residues. By construction GLM basis elements, $\hat{x}_k$, are represented in terms of non-parametrically estimated residues, $\hat{R}_k$, with

$$\hat{x}_{tk} = \hat{R}_k \otimes C_p(t - \hat{\Delta}_k) \tag{5.4}$$

In NPRM the residue for a voxel x_i, denoted $\hat{R}(x_i, t)$, is given by a linear combination of basis residues as

$$\hat{R}(x_i, t) = \sum_{k=1}^{\hat{K}} \hat{\alpha}_{ik} \hat{R}_k(t) \tag{5.5}$$

Here $\hat{\alpha}$ is constrained to be non-negative. Kinetic parameters for the voxel are evaluated from the residue $\hat{R}(x_i, \cdot)$. Numerical studies with simulated dynamic PET ^{18}F-FDG data demonstrate the consistency of the NPRM technique (Gu et al., 2021). Indeed even in the case where voxel kinetics exactly follow a 2C-model, the mean square error performance of NPRM mapping was found to match, and often improve upon, the mapping kinetics by voxel-wise estimation of 2C-model - see below.

5.2.2.2 2C Mapping

This scheme is based on voxel-level fitting a 6-parameter version of the Huang-Sokoloff model for FDG in brain tissue (Phelps et al., 1979).

$$\begin{aligned} C_T(t) &= f_b C_p(t - \Delta) + A_1 \int_0^t e^{-(t-s)/\phi_1} C_p(s - \Delta) ds \\ &\quad + A_2 \int_0^t e^{-(t-s)/\phi_2} C_p(s - \Delta) ds \end{aligned} \tag{5.6}$$

The 6 unknown parameters are $(\Delta, f_b, A_1, \phi_1, A_2, \phi_2)$ The associated residue is $R_C(t) = f_b \delta_0(t) + A_1 e^{-t/\phi_1} + A_2 e^{-t/\phi_2}$, where δ_0 is a spike (Dirac delta-function) at time 0. Decomposition of this residue allows evaluation of the summary parameters describing volumes, flows and retention and mean transit time characteristics - c.f. (O'Sullivan et al., 2014; Gu et al., 2021; O'Sullivan et al., 2021). Unlike NPRM which is linear, 2C mapping requires a non-linear (weighted) least squares process with 3 intrinsically non-linear parameters (Δ, ϕ_1, ϕ_2). This requires iterative numerical computation with careful attention to ensure that

the solutions obtained are truly optimal (not just local minima). In applications of whole-body kinetics, it has been found necessary to allow a substantial range in the delay parameter in order to get reasonable model fits to time-courses in structures such as the liver (Feng et al., 2021; Wang, Nardo, Jones, Cherry and Badawi, 2021; Wu, Gu, Wu, Zhou and Wang, 2022). This impacts the computational efficiency of 2C mapping approach.

Regardless of whether voxel-level kinetics are mapped by NPRM, 2C or more complex modeling strategies, averaged-bootstrap (AB) kinetics are simply evaluated as the mean of the estimated kinetics for each bootstrap sample. Thus if $\hat{\boldsymbol{\theta}}^b$ is the mapping of kinetic parameters for the b' bootstrap sample, the AB kinetic map is

$$\hat{\boldsymbol{\theta}}^* = \frac{1}{N_B}\sum_{b=1}^{N_B}\hat{\boldsymbol{\theta}}^b \tag{5.7}$$

5.3 Illustrative Examples

Two representative studies are presented to illustrate the technique described in section 5.2. One is the brain PET scanning with ^{18}F-FDG conducted on an early generation PET scanner in University of Washington for a post-surgery glioma patient. The dynamic imaging is reconstructed by FBP with $N = 128 \times 128 \times 35$ voxels and $T = 31$ time frames. More details are reported in (Spence et al., 1998). Another one is the breast cancer study before chemotherapy with ^{18}F-FLT administration. It is from a multi-center American College of Radiology Imaging Network clinical imaging trial (ACRIN 6688) and conducted on a more recent PET scanner using ML reconstruction with $N = 168 \times 168 \times 74$ voxels and $T = 45$ time frames of acquisition over one hour. More scanning details are introduced in (Kostakoglu et al., 2015).

Raw parametric imaging is generated by NPRM procedure and 25 bootstrap replicates were implemented for the associated averaged-bootstrap (AB) mapping. Results of both studies are shown in Figure 5.3. For the brain study (Row 1&2), there is a visual difference for tumor regions on the raw and AB flux (K_i) images. Tumor can be enhanced by the bootstrap mean. The K_i image recovered from the breast cancer study (Row 3&4) by averaged bootstrap is similar to the raw one, but it appears less noisy in the tumor. Enhanced tumor region in the AB in-distribution volume and flow (V_d and K_d) images are apparent.

2C mapping of kinetics was not carried out for these illustrations. In part this

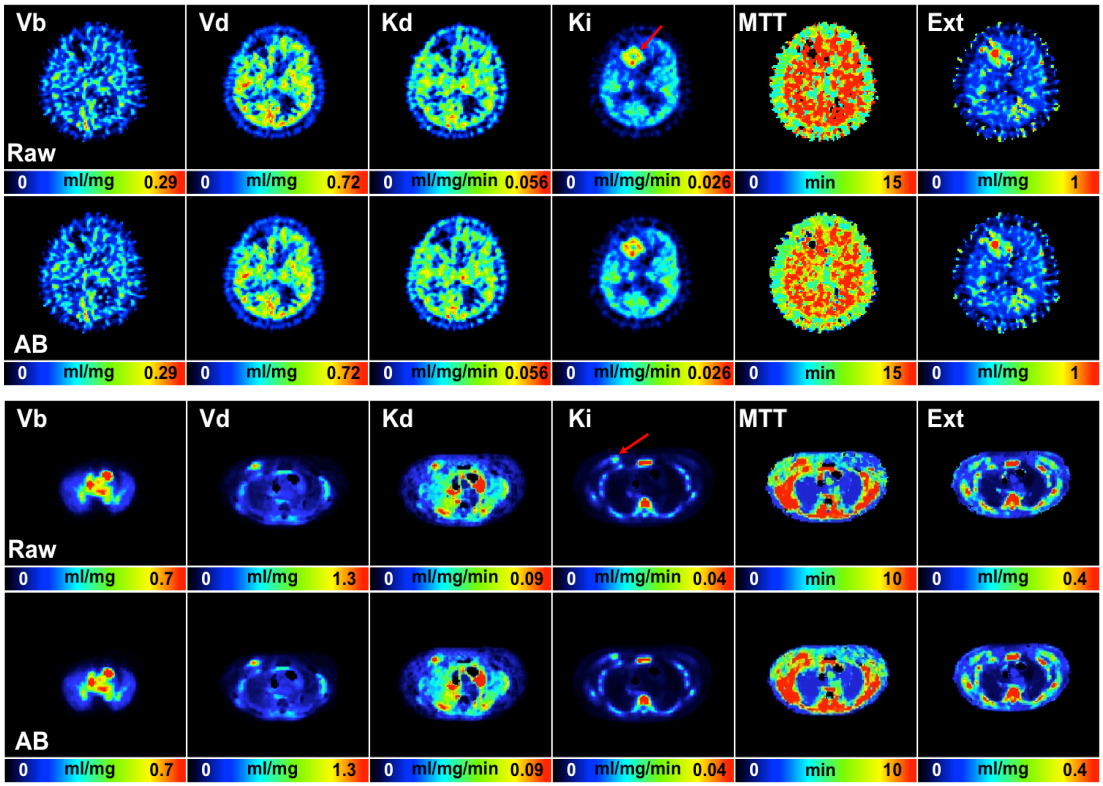


Figure 5.3: Raw and averaged-bootstrap (AB) parametric imaging: Rows 1&2 show the results from Brain tumor FDG study; 3&4 for the Breast cancer FLT study. Red arrows indicate tumors. Columns correspond to different metabolic parameters.

was because the description of representative time-course data from these studies was poorer with the 2C approach than the NPRM method. A comparison of the fitting between the non-parametric (NP) approach and 2C model for 40 segmented basis from the brain and breast studies is shown in Figure 5.4. The distribution of unexplained weighted residual sum of squares (WRSS) for the 40 time courses by NP and 2C are presented in the boxplots (A&C). The NP approach has lower percentage WRSS over 2C, particular in the breast study. In statistical terms, overall performance of NP model is found to be significantly better for a large fraction of the time-courses considered. Over a range of significance levels from 0.001 to 0.05, between 20%-30% of time-courses in the brain FDG data and 35%-40% in the breast FLT data are found to be significantly poorer with the 2C fitting approach. These results are quite consistent with the whole-body imaging results reported in (O'Sullivan et al., 2022). Of course improved data-fitting may not imply more accurate kinetic maps.

Studies reported in (Gu et al., 2021) use numerical simulations to examine the

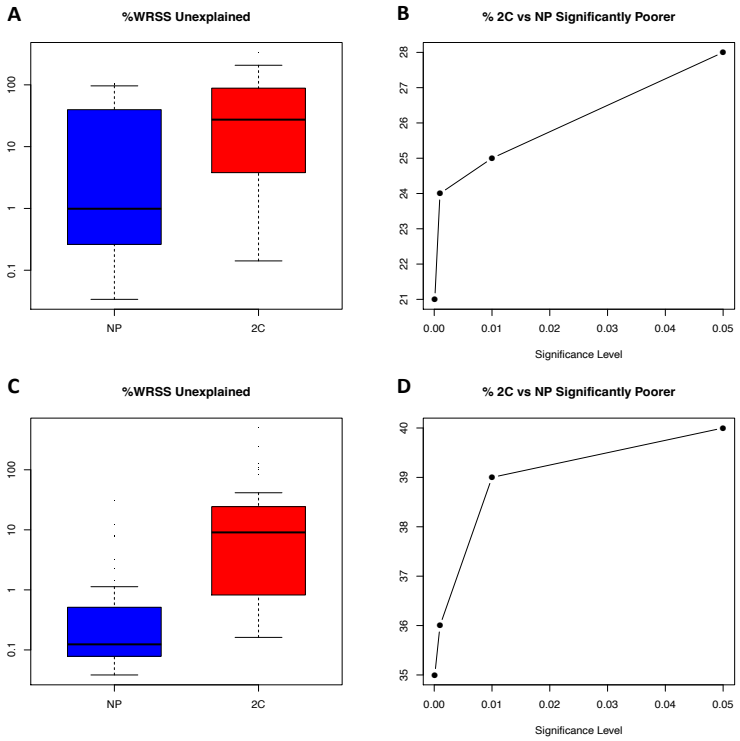


Figure 5.4: The performance of non-parametric approach (NP) and two compartmental modeling (2C). A&C - The percentage of unexplained weighted residual sum of squares (WRSS) using both methods in the brain tumor FDG and breast cancer FLT studies. B&D - The percent relative performance of 2C versus NP at different significance levels for these two studies.

accuracy of NPRM and 2C mapping under scenarios in which the underlying voxel-level truth may or may not follow a 2C compartmental model form. Results show that when the underlying truth does not follow the compartmental model form, NPRM is much preferred, which is not surprising. More interesting however, is when the ground truth does follow the compartmental form, the MSE performance of NPRM remains very much on par with 2C mapping. But of course, regardless of how NPRM and 2C compare in accuracy, it is clearly of interest to examine the benefit of the proposed bootstrap averaging process when either NPRM or 2C mapping schemes are used for kinetic mapping.

5.4 Numerical Simulations

1D and 2D numerical experiments matched to the illustrative examples - brain tumor study with FDG and breast cancer study with FLT in section 5.3 are used to examine the relative performance of averaged-bootstrap (AB) and raw kinetics with the known ground truth. The ground truth source (λ) is created

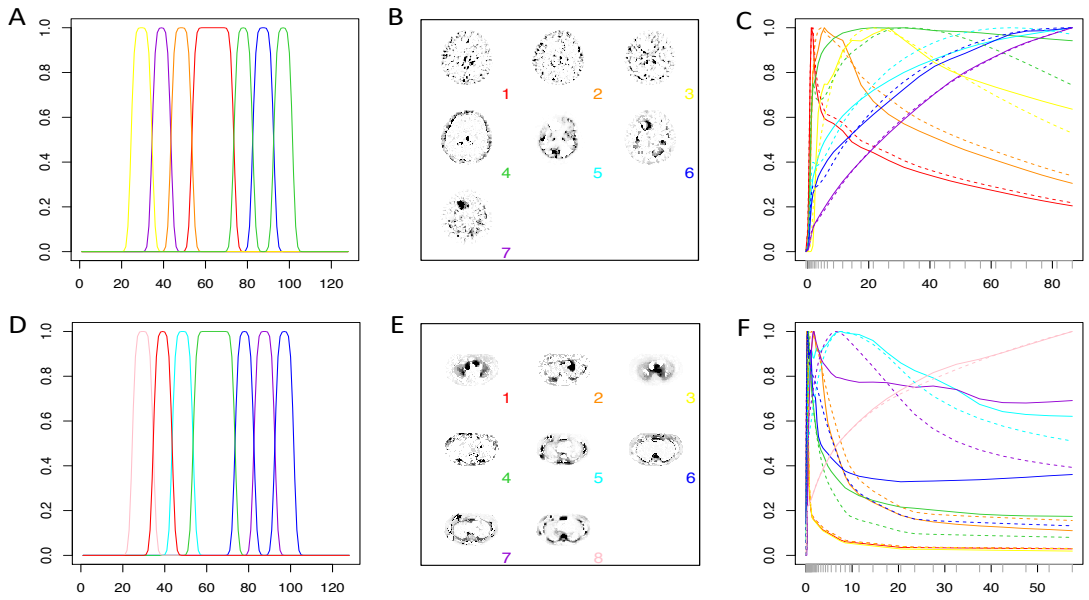


Figure 5.5: Ground truth for Brain tumor FDG (Row 1) and Breast cancer FLT (Row 2) simulation studies. True α patterns in 1D (A&D) and 2D (B&E) simulations; C&F: scaled true time courses, x-axis is in minutes with indicated temporal sampling (grey ticks). The real data basis time courses are solid lines; dashed lines are corresponding one compartmental model fits.

by a linear combination of time course basis (X)

$$\lambda_{it} = \sum_{k=1}^{K} \alpha_{ik} x_{kt}, i = 1, 2, ...N, t = 1, 2, ...T \tag{5.8}$$

- see Figure 5.5. The spatial patterns of the α coefficients correspond to a simplified phantom (Gu et al., 2021) in 1D simulation and are matched to one slice through the tumor region in the real data analyzed in section 5.3 for 2D simulation study. The true time courses and α coefficients for both brain and breast studies in 1D and 2D simulations are shown in Figure 5.5. The corresponding kinetics are $\theta = \{V_b, V_d, K_d, K_i, MTT, Ext\}$.

The simulation procedure is summarized in Figure 5.6. The dynamic images are simulated by a physical or empirical model depending on the computational complexity of data reconstruction. The physical approach generates data in the projection or sinogram domain; data are reconstruction by FBP and ML reconstruction algorithms. The details of the simulation and reconstruction process are standard and are detailed elsewhere - see for example (Gu et al., 2021; O'Sullivan et al., 2021).

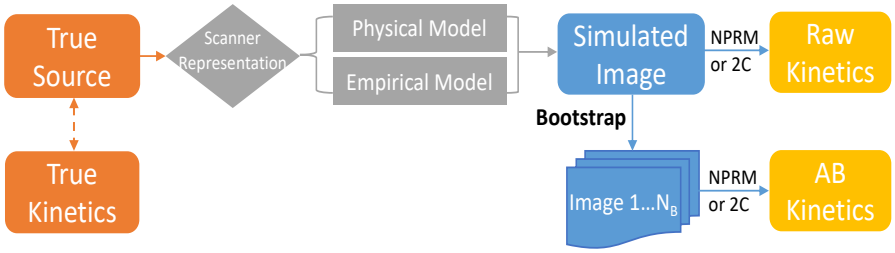


Figure 5.6: Flowchart of simulation process.

The physical model approach is used in the context of 1D simulation with both FBP and ML reconstructions and in 2D with the FBP reconstruction process. An empirical model based on an image-domain DGP, is used for simulation of 2D-ML data. Here, the scale of the noise is adjusted according to the dose (τ) - specifically in proportion to $\tau^{-\frac{1}{4}}$ - in order to achieve correspondence with the image-domain noise levels of 2D-FPB at a comparable dose. This approach is based on a combination of theoretical and numerical analysis (Gu et al., 2021; O'Sullivan, 1995; O'Sullivan et al., 2021).

The image-domain bootstrap as described in section 5.2.1 is applied to each simulated dynamic dataset. The raw and averaged-bootstrap (AB) NPRM kinetics were evaluated. 1D simulations are replicated $N_S = 80$ for both FBP and ML data. $N_B = 40$ image-domain bootstrap samples are generated for each replicate. In the 2D simulations, $N_S = 40$ replications and $N_B = 30$ bootstrap samples are generated for each replicate. Five dose levels, $\tau = (\tau_R/5, \tau_R/3, \tau_R, 3\tau_R, 5\tau_R)$ were examined with brain FDG and breast FLT studies.

A second set of simulations, in which 2C kinetic mapping is used, was also conducted. The ground truth phantom for these studies was based on a compartment model structure. Specifically the basis elements in (5.8) were replaced by the closest fitting one-compartmental model form (see dashed lines in Figure 5.5 C&F). Because the α-coefficients are quite localized, voxel-level data in these simulations effectively follow a two-compartmental model structure. A similar approach was used in (Gu et al., 2021). NPRM and 2C procedure are both applied to these data. Computational complexity of our implementation of the 2C kinetic mapping scheme meant that these simulations were only carried out in a 1-D setting. $N_S = 40$ replications with $N_B = 20$ bootstrap samples are generated.

Root mean square errors (RMSE) for each of the six kinetic parameters (p)

across $N_d = 5$ dose levels (d) and N voxels (i) are calculated as

$$\text{RMSE}_{ipd} = \sqrt{\frac{1}{N_s}\sum_{s=1}^{N_s}\left(\hat{\theta}_{ipds} - \theta_{ip}\right)^2} \quad ; \quad p = 1, 2..., 6 \tag{5.9}$$

Here $\hat{\theta}$ are the estimated kinetic parameters - either raw or AB values. Mean values of relative RMSE performance $\hat{e}_{ipd}$ across voxels and dose levels are summarized for each of the six parameters as

$$\hat{e}_p = \frac{1}{NN_d}\sum_{i,d}\hat{e}_{ipd} \quad ; \quad p = 1, 2..., 6 \tag{5.10}$$

where $\hat{e}_{ipd} = \text{RMSE}_{ipd}^{Raw}/\text{RMSE}_{ipd}^{AB}$. The estimated percent improvement achieved by the average-bootstrap is $(\hat{e}_p - 1) \times 100\%$. In addition to summarizing relative performance, the average improvements by kinetic parameter over simulation dimension and reconstruction algorithm are also calculated.

5.5 Results

Comparisons of the performance between raw and averaged bootstrap kinetics in the NPRM-based simulation are shown in Figure 5.7. The RMSEs decrease with the increased dose. The advantages of averaged kinetics are apparent (A&B) in all four cases - 1D-FBP, 1D-ML, 2D-FBP and 2D-ML.

Table 5.1: Percent Improvement, based on (5.10), with the averaged-bootstrap for the NPRM-based simulation results in Figure 5.7. Means and standard errors (SE) are shown.

Improvement		Brain-FDG						Breast-FLT					
$(\hat{e}-1)\times 100\%$		Vb	Vd	Kd	Ki	MTT	Ext	Vb	Vd	Kd	Ki	MTT	Ext
1D FBP	Mean	19.7	23.0	59.2	31.1	14.8	42.0	12.9	16.8	25.2	21.1	17.8	28.1
	SE	1.2	1.5	1.9	1.5	1.5	1.5	1.0	1.2	2.0	1.2	1.3	1.7
1D ML	Mean	33.5	16.4	69.9	27.3	12.4	40.9	19.1	12.3	25.4	16.3	14.4	22.6
	SE	1.4	1.3	2.3	1.3	1.5	1.3	1.0	1.1	2.1	1.1	1.0	1.5
2D FBP	Mean	6.4	33.4	37.6	13.9	42.3	13.3	1.2	17.0	19.4	10.7	20.1	33.1
	SE	0.1	0.2	0.2	0.1	0.3	0.2	0.1	0.1	0.1	0.1	0.2	0.2
2D ML	Mean	11.0	12.2	13.4	10.9	39.1	21.7	1.5	11.1	12.4	12.0	6.2	11.2
	SE	0.1	0.1	0.1	0.1	0.2	0.1	0.1	0.1	0.1	0.1	0.1	0.1

The distributions of voxel-level improvements - $(\hat{e}_{ipd} - 1) * 100\%$ of raw and averaged kinetic mapping at five dose levels for brain and breast studies are presented in Figure 5.7 C&D. The benefits of bootstrap-averaged kinetics appear to be unrelated to dose level, reconstruction algorithm or whether a 1-D or 2-D

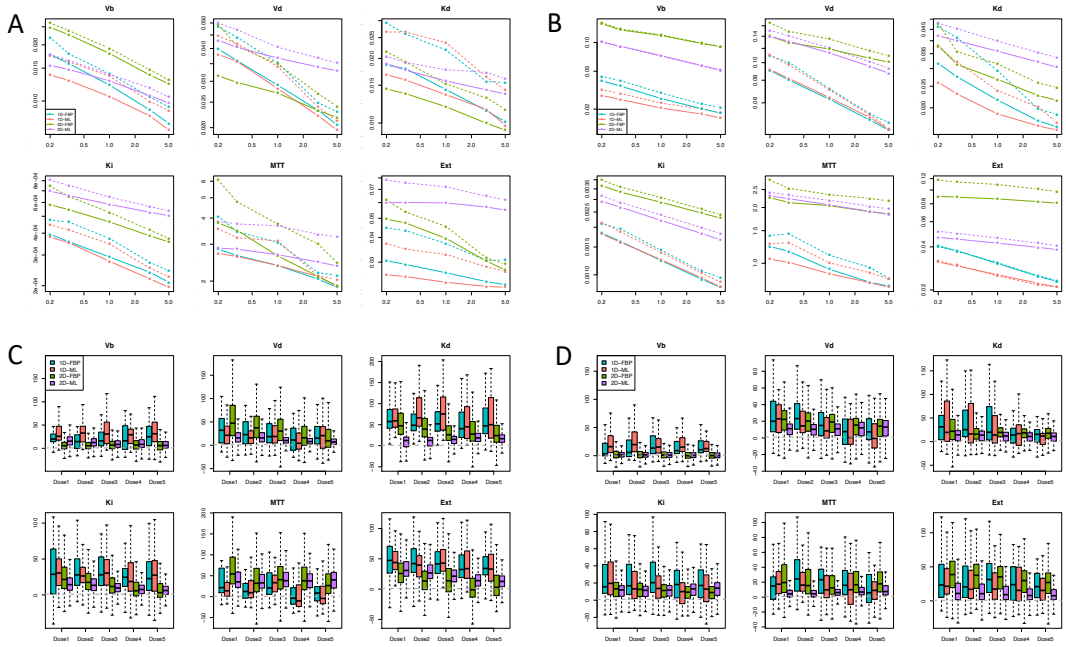


Figure 5.7: 1D and 2D simulation results with FBP and ML reconstructions in a simulation matched to FDG brain and FLT breast studies. The ground truth are (non-parametric) basis elements extracted from the real data. Kinetics are mapped by the NPRM process. Left (A&C) are for Brain; right (B&D) are for Breast. Top two rows: RMSE of raw (dashed) and averaged-bootstrap (solid) kinetic parameters as a function of dose - log-log scale. Bottom two rows: boxplots of relative performance of raw vs averaged-bootstrap kinetics by dose levels, y-axis is the percent improvement.

simulation is involved. The overall precent improvements in the RMSE values achieved by bootstrap averaging are summarized in Table 5.1. While there are some variation across different parameters, the percent improvements are generally on the order of 10% to 30% for most parameters.

Results for the 2C-based simulation are reported in Figure 5.8, with percent improvement data in Table 5.2. The general pattern in Figure 5.8 is generally similar to the NPRM-based simulation. Percent improvements with NP mapping is a little bit higher than the 2C procedure in the brain-FDG study, but this is reversed in the breast-FLT case. It is not surprising that the configuration of the ground truth would impact the nature of improvements achieved[1].

The averaged improvements over simulation dimension and reconstructions for six parameters in both simulation sets - NPRM-based Phantom I and 2C-based Phantom II are summarized in Table 5.3. The overall improvements across

[1]Qi Wu implemented the simulation experiments for 2C-based phantom (Figure 5.8 and Table 5.2).

different phantoms and parameters are generally from 10% to 30%.

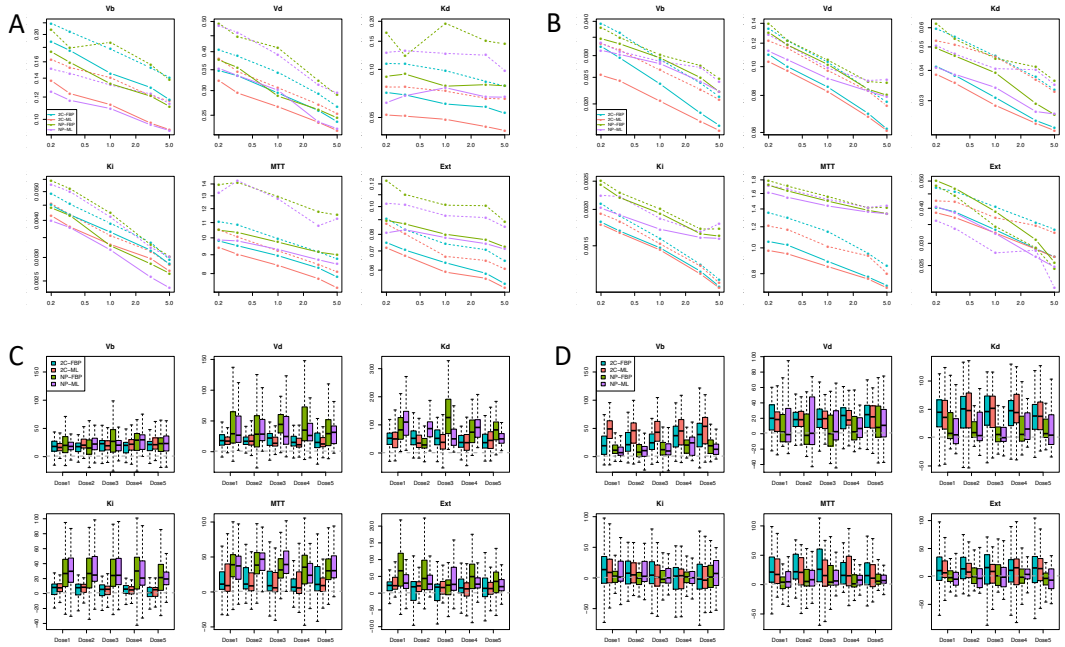


Figure 5.8: 1D results with FBP and ML reconstructions in Brain FDG and Breast FLT simulations in which ground truth follows a compartmental form. Both 2C and NP mapping of kinetics are used. A&B: root mean square error (RMSE) of raw (dashed) and averaged-bootstrap (solid) kinetic parameters as a function of dose at log-log scale for the brain FDG and breast FLT studies; C&D: boxplots of relative performance values raw and averaged-bootstrap kinetics by dose levels, y-axis is the percent improvement.

Table 5.2: Percent Improvement, based on (5.10), with the averaged-bootstrap for the 2C-based simulation results in Figure 5.8. Means and standard errors (SE) are shown.

Improvement		Brain-FDG						Breast-FLT					
$(\hat{e}-1)\times 100\%$		Vb	Vd	Kd	Ki	MTT	Ext	Vb	Vd	Kd	Ki	MTT	Ext
2C FBP	Mean	17.9	18.2	47.4	4.7	13.5	12.3	29.6	20.6	41.7	6.3	20.4	12.6
	SE	0.7	0.6	1.7	0.5	1.1	2.1	1.3	0.9	1.9	1.5	1.5	1.7
2C ML	Mean	20.3	15.5	42.6	5.4	12.8	19.5	43.5	19.0	42.5	4.4	17.6	10.4
	SE	0.7	0.6	1.9	0.4	1.1	1.5	1.5	0.8	1.9	1.3	1.4	1.5
NP FBP	Mean	23.1	39.0	80.6	27.0	34.6	45.9	14.4	7.4	12.5	0.5	7.4	0.0
	SE	1.1	1.7	3.1	1.4	1.3	2.7	0.8	1.2	1.2	0.9	1.0	0.9
NP ML	Mean	22.3	32.2	79.0	27.2	35.9	32.0	12.9	10.7	10.7	5.1	9.3	-0.8
	SE	0.8	1.3	2.4	1.2	1.2	1.7	0.8	1.5	1.5	1.1	0.8	1.0

Table 5.3: Percent improvements averaged over simulation dimension and reconstructions, with the averaged-bootstrap with NPRM in Phantom I (general ground truth) and both NPRM and 2C-mapping in Phantom II (2C ground truth) simulations. Means and standard errors (SE) are shown.

Improvement		Brain-FDG						Breast-FLT					
$(\hat{e}-1)\times 100\%$		Vb	Vd	Kd	Ki	MTT	Ext	Vb	Vd	Kd	Ki	MTT	Ext
Phantom I (general ground truth)	NP-Mean	8.9	22.9	26.2	12.7	40.3	17.8	1.7	14.1	16.1	11.5	13.5	22.5
	NP-SE	0.1	0.1	0.1	0.1	0.1	0.1	0.0	0.1	0.1	0.1	0.1	0.1
Phantom II (2C ground truth)	2C-Mean	19.1	16.9	45.0	5.1	13.2	15.8	36.5	19.8	42.1	5.3	19.0	11.5
	2C-SE	0.5	0.4	1.3	0.3	0.8	1.3	1.0	0.6	1.4	1.0	1.0	1.1
	NP-Mean	22.6	35.7	79.8	27.1	35.2	39.1	13.6	9.1	11.6	2.8	8.4	-0.4
	NP-SE	0.7	1.1	2.0	0.9	0.9	1.6	0.6	1.0	0.9	0.7	0.6	0.7

5.6 Discussion

In this work, we have explored the potential for enhancing the reliability of kinetic mapping by the use of bootstrap averaging. This approach is made possible by the availability of an efficient image-domain bootstrap procedure (O'Sullivan et al., 2021). Bootstrapping is based on a generalized linear modeling framework involving a sub-ordinate Gaussian process. The model captures the systematic and stochastic aspects of PET data in a data-adaptive and substantially non-parametric manner.

The computational demands of image-domain bootstrapping are modest. Table 5.4 presents some timing information for when a single 3.2 GHz processor is used in the computation. These results consider the brain and breast studies on the short AFOV scanners as described in section 5.3 and also report information in (O'Sullivan et al., 2022) for a larger long AFOV PET system - Siemens Biograph Vision Quadra. There are two major steps in image-domain bootstrapping: Step 1 defines the GLM - this includes the data segmentation, NPRM procedure and estimation of parameters for simulated data generation; Step 2 is the evaluation of each bootstrap replicate and associated NPRM mapped kinetics. These computational requirements have significant potential to be further reduced by suitable use of parallelization tools.

Table 5.4: Sample single 3.2 GHz processor Computation Times (in minutes) for Image-Domain Bootstrapping

Study Reference	Size (Voxels,Time-frames)	Step 1	Step 2
Brain-FDG (O'Sullivan et al., 2021)	$(128\times 128\times 35, 31)$	5	0.5
Breast-FLT (O'Sullivan et al., 2021)	$(168\times 168\times 74, 45)$	7	1
Whole body-FDG (O'Sullivan et al., 2022)	$(440\times 440\times 645, 62)$	140	80

*Step 1: GLM estimation; Step 2: Replicate simulation.

While image-domain bootstrapping uses a representation of voxel-level data as a linear combination of non-parametrically defined residues, the bootstrap simulated data can be quantified without regard to this. The study here has shown that bootstrap averaging can improve the RMSE performance of kinetic maps generated by both NPRM and 2C mapping procedures. While the benefits of bootstrap averaging are consistent across dose and data reconstruction method there do appear to be practically significant variations depending on the underlying ground truth structure and the specific kinetic parameter of interest.

Overall the results support the use of averaging based on the image-domain bootstrapping model as a way to improve kinetic information extracted from PET imaging studies. Given nature of modeling approach used, see equation (5.1), the work may also stimulate further statistical development of the image-domain bootstrapping methodology for applications to the quantitative analysis of data from other multi-channel imaging systems.

Chapter 6

Discussion, Conclusions and Future Work

6.1 Discussion

The work in this thesis is based on the analysis of dynamic PET voxel-level data and mainly focuses on improved statistical quantitation, especially in the generation of parametric imaging and assessment of the associated uncertainty. The study of this kind of data has been reported in a wide variety of literature over the years. Many different points of view have been taken. However, a series of new challenges arise with the emerging of next-generation long axial field of view PET scanners. Our work proposes the non-parametric residue mapping procedure to deal with the possible issues and its performance is examined using simulation studies. Based on this approach, we further investigate the benefits of combining data in the multiple injection PET scans. Image-domain bootstrapping provides an efficient way to simulate the dynamic PET data and derived standard errors have the potential to support clinical decisions. Also, bootstrap averaging can further enhance the mean square error of parametric imaging. These analyses are implemented in R and have been partially published in (Gu et al., 2021; Gu, O'Sullivan, Muzi and Mankoff, 2019; O'Sullivan et al., 2021; Gu, Wu, O'Sullivan, Huang, Muzi and Mankoff, 2019; Gu, Wu and O'Sullivan, 2021).

Chapter 2 reviewed the kinetic models commonly used in the quantitation of dynamic PET studies. Most of them is parametric model, which generally relies on the necessary assumptions. For example, the residue is assumed to be

a mixture of exponentials in the compartmental modeling. The unsatisfied assumptions may introduce additional bias. This would be more challenging for dynamic imaging with multiple organs on the newly developed LAFOV PET scanners such as Siemens Biograph Vision Quadra (Alberts et al., 2021), the uEXPLORER (Badawi et al., 2019) and the PennPET Explorer (Pantel et al., 2020). Currently, total-body parametric imaging is basically generated by the direct application of standard Patlak or two compartmental modeling (Zhang et al., 2020; Sari et al., 2022; Viswanath et al., 2021). The work to justify these methods for different organs is very limited (Feng et al., 2021; Wang, Nardo, Jones, Cherry and Badawi, 2021) and spectral analysis has never been applied. We assess the feasibility of standard, generalized Patlak, one and two compartmental models for dynamic imaging of multiple organs at ROI and voxel levels and propose some preliminary schemes to adapt these methods (Gu et al., 2022; Wu, Gu, Gu, Xu, Zhou and Shi, 2022; Wu, Gu, Wu, Zhou and Wang, 2022). Anyway, to handle such complex datasets, there is a long way to go. More comprehensive models need to be developed and these may be achieved by segmentation in combination with some data-driven methods (Slart et al., 2021; Wang, Rahmim and Gunn, 2020).

Outside of the traditional quantitative methods, the non-parametric technique described in section 3.2.1 is more flexible without the requirement of model assumptions, which is a refinement of (Hawe et al., 2012; O'Sullivan et al., 2014). The performance of non-parametric and compartmental modeling scenarios is assessed carefully in the real data analysis and numerical phantom studies with different ground truths, as shown in Figure 5.4 and Table 3.1. The improvement of kinetic mapping by the non-parametric approach is substantial. The established NPRM technique has the potential to further improve the kinetic quantitation for total-body PET imaging as it has some important features like the flexibility for diverse tissue environments, consideration of delays for different parts, and the ability to address issues with the bladder or injection site. Hence, the technique is illustrated using data from a LAFOV PET scanner as presented in section 6.1.1. The generalization of NPRM to the digital subtraction angiography imaging is also studied, one example is shown in section 6.1.2.

Although the single radiotracer is generally used, multiple PET tracers can be administered to the same patient to target more comprehensive pathological mechanisms. Different tracers can be injected successively or in separate hours and even days, depending on the half-life of prior tracer. Not like the tracer with short half life, e.g. ^{15}O-H_2O (2 mins), the residual radiation from previous

injection with long half-life tracer may remain if the separation time between two scans is not long enough. However, the long waiting or gap day is a burden for some patients. Hence, Utah group has developed some methodologies to separate the signals of each injection (Zhang, Morey and Kadrmas, 2016; Kadrmas and Hoffman, 2013; Kadrmas, Rust and Hoffman, 2013) and the high sensitivity of new-generation LAFOV PET scanner enables a scheme that tracers are injected at successively higher doses to swamp the spillover from prior injections (Viswanath et al., 2021). In chapter 3, we proposed a combined analysis based on NPRM technique, which is applicable to the multi-injection PET studies regardless of whether there is overlap or not between injections. This procedure is also studied in a more complex whole-body non-human study with four injections and multiple organs in the field of view, see section 6.1.3.

PET images can be used directly or after kinetic analysis to extract the physiological parameters. As such images are generally noisy, it is essential to understand their statistical properties such as variance/standard error (magnitude) and texture (correlation) (Razifar et al., 2005). There is already significant literature on variance assessment for PET images (Carson et al., 1993; Maitra and O'Sullivan, 1998; Teymurazyan et al., 2013; Mou, Huang and O'Sullivan, 2017). Procedures based on the statistical bootstrap are also reported (Haynor and Woods, 1989; Buvat, 2002; Dahlbom, 2001; Lartizien, Aubin and Buvat, 2010; Ibaraki et al., 2014; Kucharczak et al., 2018), but they usually require the sinogram or list-mode data and reconstruction, which is not feasible in the clinical setting. In 2020, Huang et.al introduced an image-domain bootstrap framework that relied on a parametric Gamma-model form to represent the marginal distributions of voxel-level data and a parametric spatial autoregressive form to represent covariance pattern (Huang et al., 2020). Motivated by this work, we develop a more flexible approach, suitable for dynamic PET data reconstructed using either FBP or ML techniques and illustrate its use to evaluate the mean and standard error of parametric imaging, as described in chapter 4 and 5. The practicality of this approach for a LAFOV PET study is demonstrated in section 6.1.1. We also give an example in section 6.1.4 to show how the treatment is improved for individual patients based on our image-domain bootstrap technique.

The efficacy and performance of all techniques and schemes proposed in this thesis have been examined using a series of numerical simulation studies. Various true sources matched to different studies following compartmental modeling or not are employed. A physical PET scanning model involving Poisson

sampling of a Radon transform of the source is used (O'Sullivan, 1995) and experiment details are justified carefully. FBP and ML reconstructions are easy to implement in 1-D mode. Some other methodologies can also be evaluated in these simulation settings, for example, the dynamic bandwidth scheme that improves reconstructed images in section 6.1.5. But the computational complexity would be increased with the higher dimensions (2-D and 3-D) in particular for the iterative reconstructions. The empirical model based on an image-domain data generation process (Figure 5.2) provides a very practical way for simulation of 2D and even 3D-ML data. This efficient approach has a potential use in the assessment of statistical characteristics associated with PET measurements.

6.1.1 Parametric imaging and associated uncertainty via the image-domain Bootstrap for a LAFOV PET FDG study[1]

The size and metabolic complexities of dynamic studies on the emerging generation of clinical scanners with LAFOV present a significant challenge for data analysis. We describe the mapping of kinetics by techniques developed in this thesis including NPRM in chapter 3, image-domain bootstrap in chapter 4 and averaging scheme in chapter 5 for a dynamic FDG study of a post-surgery breast cancer patient on a LAFOV Biograph Vision Quadra PET/CT scanner at Bern University Hospital (Sari et al., 2022; O'Sullivan et al., 2022). The observed set of volumetric scans acquired over 1 hour produced a dataset on the order of 31GB. Voxel-level bootstrap means and standard errors were evaluated and presented in Figure 6.1.

The bootstrap-averaged kinetic maps were found to be of high quality and well aligned with the vascular and metabolic FDG patterns expected for known organ structures (brain, liver, kidneys, etc). Uncertainties in kinetics varied as a function of magnitude of the kinetic variable - percent errors at higher magnitudes were typically on the order of $10 \sim 25\%$. These methodologies are shown to be highly feasible approaches to mapping kinetics and their associated uncertainties with LAFOV FDG-PET patient data. Bootstrapping provides novel uncertainty information as well as enhancing mean square error properties by averaging. The flexible nature of the approach offers particular advantages when the kinetics of the tracer's interaction with tissue might not follow the assumptions of the 2C model developed for FDG in brain tissue.

[1]Presented at 2022 Society of Nuclear Medicine & Molecular Imaging Annual Meeting.

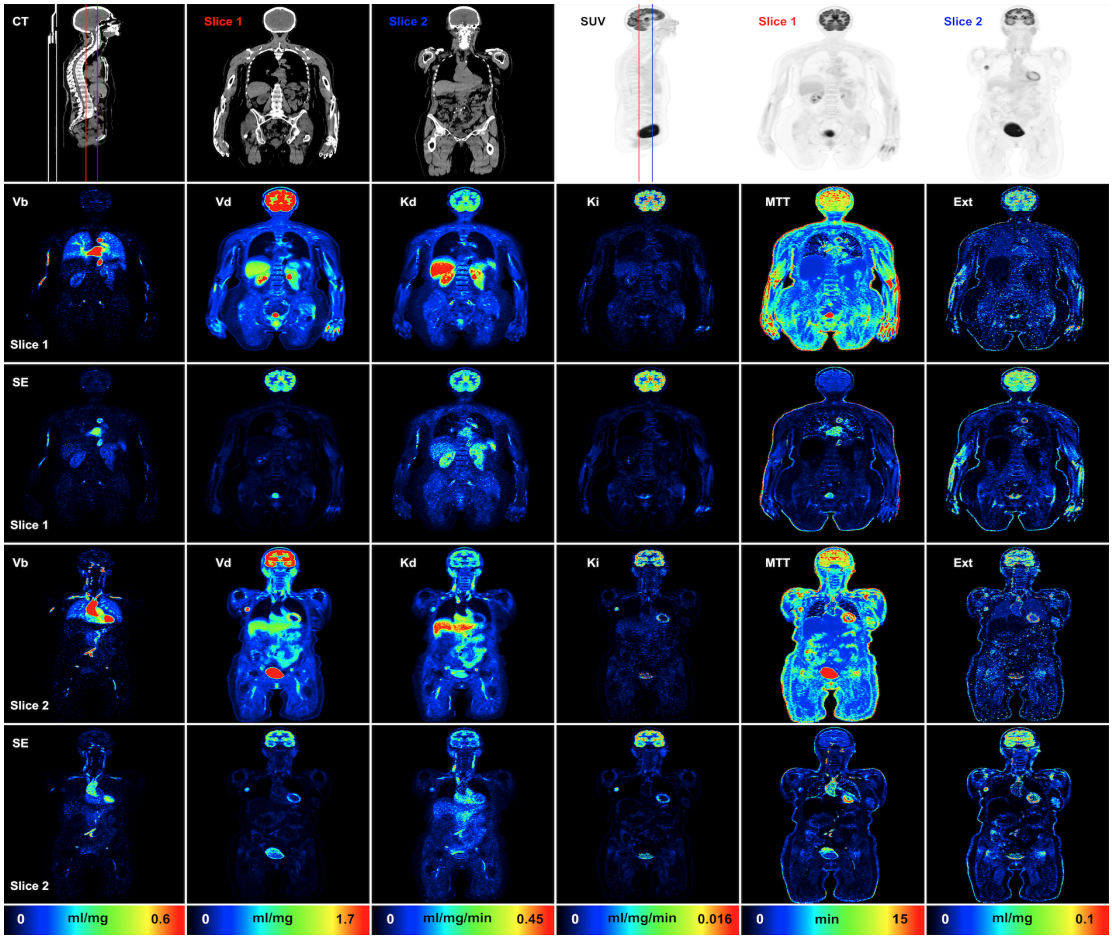


Figure 6.1: Averaged-bootstrap (AB) parametric imaging and associated standard error (SE) maps for selected slices (blue and red lines on top row). Columns correspond to different metabolic parameters.

6.1.2 Adaption of NPRM for Digital Subtraction Angiography Imaging[2]

Quantitative analysis of DSA images brings an opportunity to facilitate the diagnosis of vascular diseases and procedure assessment (Tinelli, De Nigris, Minelli, Vincenzoni and Flex, 2018). Limited literature was reported towards to this point, for example, parametric color coding (PCC) has been applied in type B chronic aortic dissection during thoracic endovascular aortic repair (TEVAR), but it does not reflect the physiologic status directly (Tinelli, Minelli, De Nigris, Vincenzoni, Filipponi, Bruno, Massetti, Flex and Iezzi, 2018; Strother et al., 2010). Also, a non-linear optimization algorithm was employed to derive blood flow from DSA images (Cheon, 2015; Hsu, Alaraj and Linninger, 2016). Cur-

[2]Presented at 39th Conference on Applied Statistics in Ireland.

rently, there is little, if any, formal quantitation applied in the interpretation of DSA data. Here we explore the potential adaptation of NPRM technique as described in section 3.2.1 for DSA. One example is shown below.

Data from the DSA study for a patient with suspected stroke is considered. This study was conducted at Einstein Medical Center, Philadelphia. A sequence of 26 time frames of 2D DSA scans data were generated. We identify three physiological parameters of particular interest - fast volume (V_F), slow flow and volume (K_S, V_S). The parametric images are given in Figure 6.2. The arterial and venous patterns are well described by fast and slow volume. But we just focus on the venous pattern: V_S and K_S, linked to the status of blood supply in the brain directly. There is no dark or red area, which means no apparent ischemic or bleeding part in the brain. The suspected patient has no stroke issue. Our technique demonstrates an ability to map key physiological parameters for DSA images.

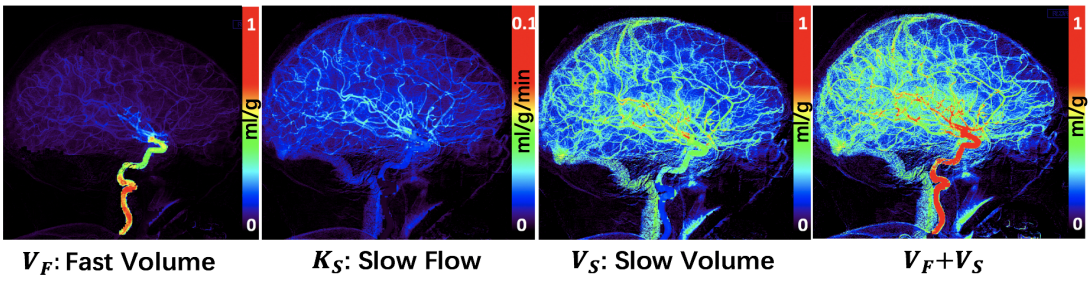


Figure 6.2: Sagittal views of parametric images of fast volume(V_F), slow flow and volume(K_S,V_S) from the suspected stroke patient study. Color bars are augmented to present the values of physiological parameters for all pixels.

6.1.3 Illustration of NPRM for the whole-body pregnant macaque PET imaging with multiple injections[3]

P-glycoprotein has a role in the removal of foreign substances out of cells. A series of studies were carried out to evaluate the ability to use positron emission tomography scanning with a C-11 labeled verapamil radiotracer, to image the P-gp status. We present a fresh analysis of data from a series of preclinical dynamic PET studies for pregnant non-human primates involving multiple injections of O-15 labeled water and C-11 labeled verapamil, before and after administration of Cyclosporine A (CsA)- an agent which has a dramatic effect on the P-gp status as shown in Figure 6.3.

[3]Presented at 2019 European Molecular Imaging Meeting.

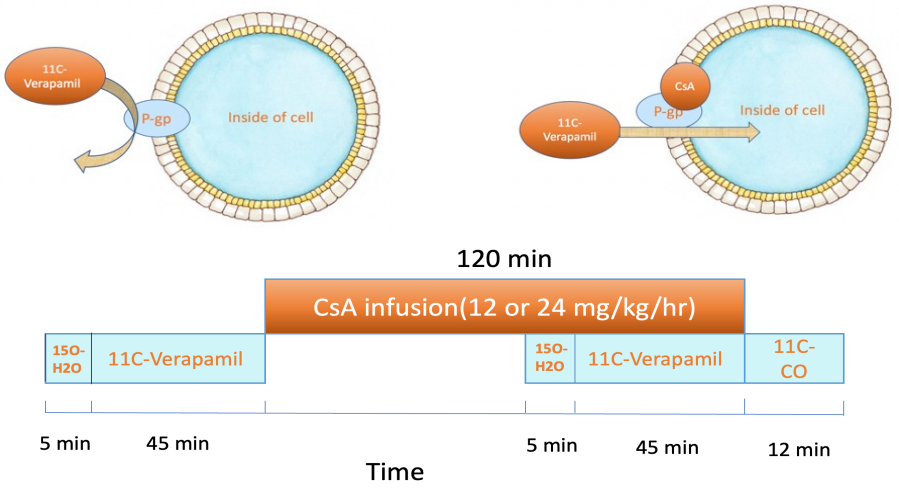


Figure 6.3: CsA inhibition of P-gp acitivity (Top Row) and PET scanning protocol (Bottom Row).

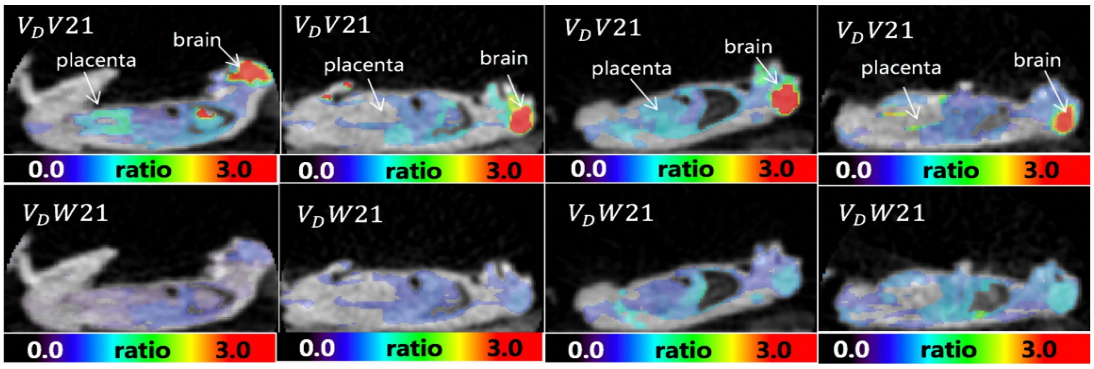


Figure 6.4: Volume of distribution ratio mapping before and after CsA infusion for water (V_DW21) and verapamil (V_DV21). Columns correspond to different pregnant non-human primates.

The previous analysis only considered a limited number of regions of interest (Chung et al., 2010; Eyal et al., 2009). The extent of time-course data (130 time frames) and its metabolic interpretation present challenges, particularly because the methodology must address the diversity of tissues in the whole body. Our work reports on a statistical analysis that is capable of producing a comprehensive voxel-level analysis of the full data set. Combined analysis of multiple-injection PET scanning based on the NPRM technique is implemented.

Parametric images of the volume of distribution (V_D) ratio values before and after CsA inhibition PET study with water and verapamil in four illustrative data sets are presented in Figure 6.4. The results show higher verapamil distribution after CsA administration in placental and brain regions, but little or no change in corresponding V_D water values. Higher verapamil ratios demon-

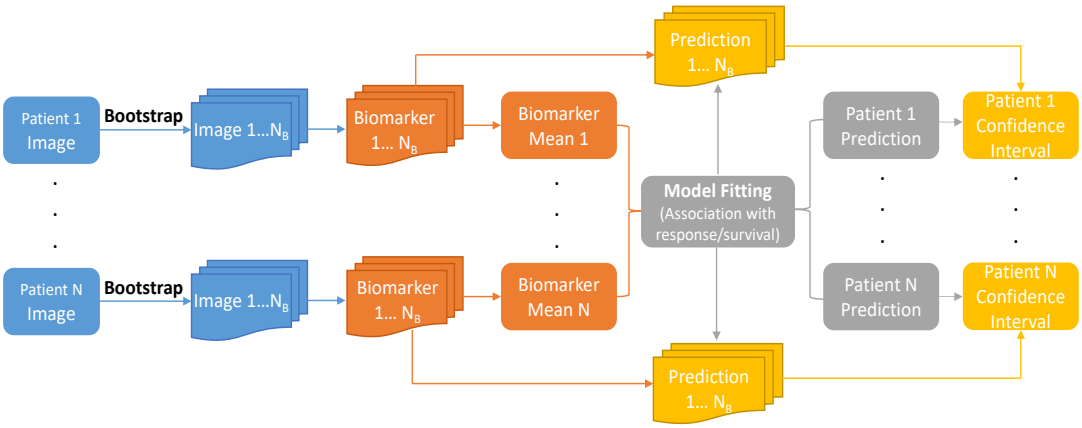


Figure 6.5: Schematic of the framework to construct the biomarker mean and confidence interval for individual patients.

strate suppression of P-gp and the greatest impact is at the blood brain barrier (BBB). This likely reflects the importance of these barriers in controlling drug entry into the brain and the fetus, respectively. This study demonstrated that comprehensive analysis of whole-body PET scanning data with multiple injections to recover complex information can be carried out with reliance on the proposed technique in chapter 3.

6.1.4 Integration of Uncertainty Information of Biomarker to Clinical Decision Making

The growth of solid tumors relies on an increasing supply of oxygen and nutrients that are delivered via vascular networks, so the tumor blood vessels usually display many structural and functional abnormalities (Fouladzadeh et al., 2021). Hence, blood volume (V_b) may be an important prognostic indicator and have an impact on treatment. Here we explore whether V_b derived from dynamic PET imaging could predict response or survival for breast cancer patients, evaluate the uncertainty of prognostic biomarkers for individual patients and show its potential to be employed in personalized medicine. The schematic of framework is presented in Figure 6.5.

Fifty three locally advanced breast cancer (LABC) patients underwent ^{18}F-FDG PET imaging at the University of Washington from January 1996 to March 2006 and only dynamic PET scans before neoadjuvant chemotherapy (NAC) are selected. ^{18}F-FDG was infused over 2 min in a 7- to 10- mL volume. Dynamic imaging was performed over one hour after the start of the ^{18}F-FDG infusion

and reconstructed into $128 \times 128 \times 35$ voxels and 25 time frames (1-min pre-injection frame, 4×20 s, 4×40 s, 4×1 min, 4×3 min, 8×5 min) by FBP algorithm. Many clinical and pathological variables including estrogen receptor (ER; positive or negative) expression, progesterone receptor (PR; positive or negative), human epidermal growth factor receptor 2 (HER2; positive or negative), the number of positive axillary lymph nodes (Node$^+$) were assessed. Pathologic response to therapy was based on examination of the surgical specimen and only 11 individuals have the pathologic complete response (pCR). Disease free survival (DFS) was calculated in years and using the patient's date of surgery and one of the following: date of known recurrence, date of death, date last known to have no evidence of disease, or date of most recent clinical follow-up (May 29, 2015) (Dunnwald et al., 2008). One woman's survival information is partially missing and 17 of 52 patients relapsed. More details are reported in (Mankoff et al., 2003, 2002; Dunnwald et al., 2008, 2011; Chitalia et al., 2021).

The NPRM technique (see section 3.2.1) is used to generate the kinetic mapping from these baseline scans. V_b of each patient is calculated for the primary tumor. The average and associated uncertainty of V_b are estimated by the efficient image-domain bootstrap approach (see section 4.2 and chapter 5). Its prediction for pCR or survival is determined by the binary logistic or Cox proportional-hazards regression. The coefficient (Coef), standard error (SE) and p value (P) of univariate and multivariate regressions for kinetic parameters (K_i and V_b) derived from pre-therapy PET imaging are presented in Table 6.1. The results show that V_b is significantly associated with response in both univariate and multivariate approaches and disease free survival only in the multivariate logistic analysis. K_i is not significant in any logistic or Cox models. The confidence interval (CI) of predicted pCR probability using V_b for each patient can also be constructed by bootstrap samples as shown in Figure 6.6. These provide more information to guide treatment and benefit individual patients.

Table 6.1: Univariate and multivariate logistic and Cox proportional hazard analyses of potential variables associated with pathological complete response and disease-free survival in the UW-FDG trial.

	Pathologic Complete Response						Disease-Free Survival					
	Univariate			Multivariate			Univariate			Multivariate		
Variable	Coef	SE	P	Coef	SE	P	Coef	SE	P	Coef	SE	P
K_i	3.66	45.85	0.94	-23.03	47.46	0.63	-14.09	37.05	0.70	-26.41	42.97	0.54
V_b	6.31	3.15	0.04*	6.99	3.45	0.04*	-3.59	2.31	0.12	-5.84	2.90	0.04*

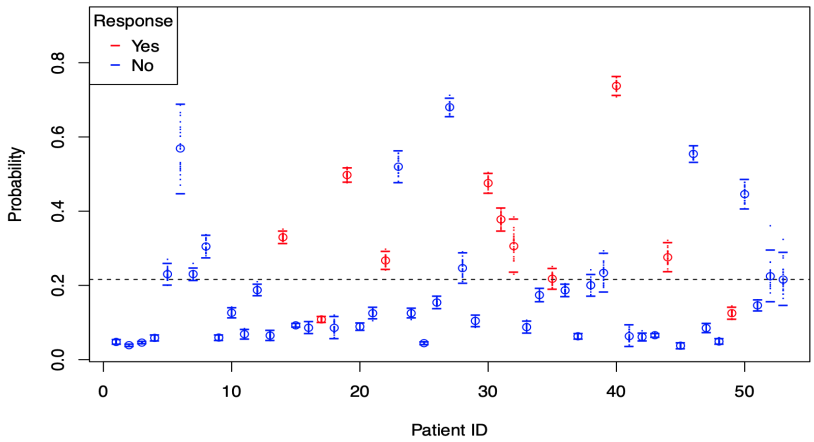


Figure 6.6: 95% confidence interval (CI) of predicted probability to have pathological complete response for individual patients in the UW-FDG cohort.

6.1.5 An Evaluation of the Benefits of Adaptive Bandwidth Scheme[4]

For dynamic PET studies, a fixed resolution filter bandwidth is typically used in the reconstruction of all time frames (O'Sullivan and O'Súilleabháin, 2013; O'Sullivan, 1995; Pawitan and O'Sullivan, 1993). This may over/under smooth some high/low counts time frames. We propose a simple procedure that adaptively modifies time-frame bandwidths in order to improve the quantitative accuracy of dynamic PET images and derived kinetic information.

The adaptive procedure assumes that an overall fixed bandwidth for the reconstruction resolution filter, suitable for the total tracer uptake, has been specified. Using established asymptotic analysis of reconstruction error as a function of dose, the fixed bandwidth is manipulated by time-frame based on the observed counts in the frame. Performance of the adaptive/dynamic and fixed bandwidth is evaluated using a series of simulation studies matched to the standard dynamic sampling scheme for ^{18}F-FLT studies. Using literature data, the field of view tissue structures corresponding to what one would typically encounter in PET breast cancer studies with these tracers are specified. A simplified scanning model, see section 3.4.1, matched to the mathematical complexity of PET is used. To facilitate accurate estimation of performance, simulations are conducted at several doses, with a large number of replicates at each dose. Voxel-level metabolic parameters are computed using both standard fixed-bandwidth dynamic data and also the dynamic data derived from the adaptive bandwidth procedure. The relationship between root mean square error characteristics

[4]Presented at 2021 Society of Nuclear Medicine & Molecular Imaging Annual Meeting.

of the image quality and local kinetic parameters for these two schemes are described. The evaluation procedure is summarized in Figure 6.7.

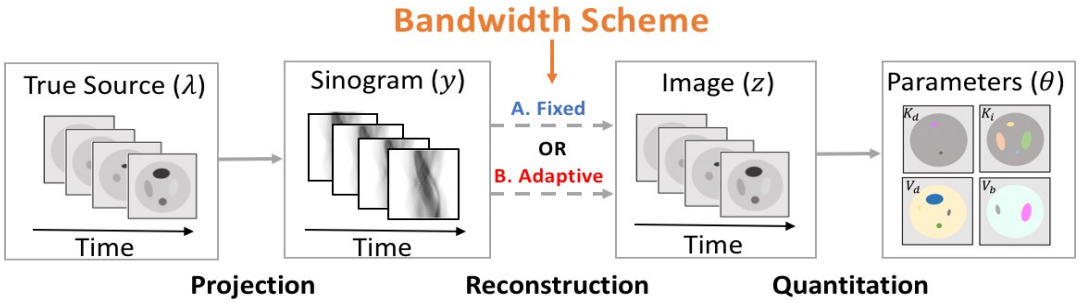


Figure 6.7: Diagram of Evaluation Procedure.

RMSE comparisons of reconstructed images and metabolic parameters across different dose levels from fixed and dynamic bandwidth approaches are presented in Figure 6.8, Table 6.2 and 6.3. These results show that the dynamic scheme substantially improves reconstructed image quality - percent improvements are on the order of 25% across a range of doses. Improvements in metabolic parameters are not as substantial but still significant - typically on the order of 10%. For flux and volume of distribution, RMSE improvements range from 7% to 15%; for flow, improvements range from 6% to 32%. The superiority of the adaptive bandwidth scheme is fully demonstrated in simulation studies. This scheme has the potential to be applied to smooth the dynamic PET images and increase the accuracy of derived kinetic information.

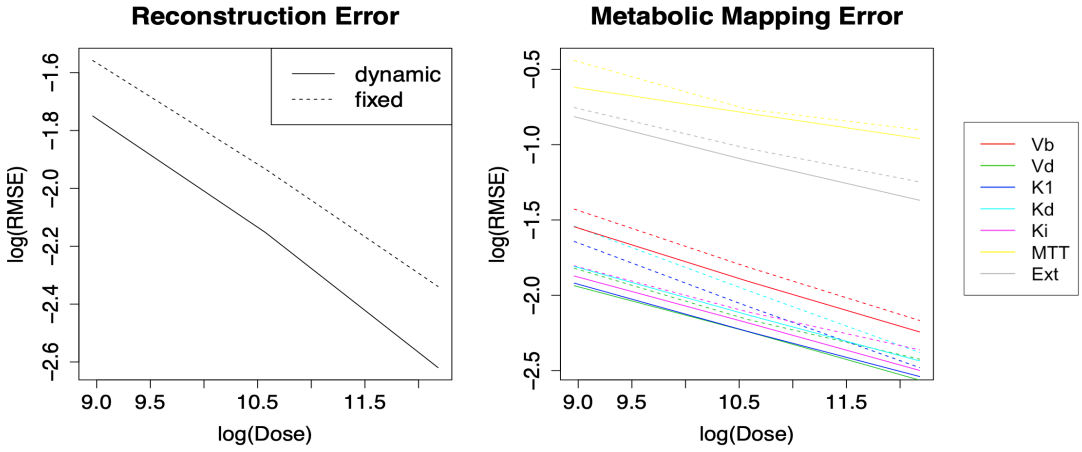


Figure 6.8: FLT simulation results at different dose levels. **Left:** root mean square error (RMSE) of reconstructed image; **Right:** RMSEs of seven metabolic parameters. V_b - volume of blood; V_d - volume of distribution; K_1 – overall flow; K_d – flow of distribution; K_i – flux; MTT – mean transit time; Ext – extraction. Dashed and solid lines represent fixed and dynamic bandwidth schemes respectively.

Table 6.2: Reconstruction RMSEs from dynamic and fixed bandwidth schemes at low, middle and high doses. Part (a) and (b) are divided by the ground truth and multiplied by 100.

	Low	Middle	High
(a) Dynamic	17.4	11.6	7.3
(b) Fixed	21.1	14.5	9.6
%Improvement	21.2	24.5	32.4

Table 6.3: Metabolic mapping RMSEs from dynamic and fixed bandwidth schemes at low, middle and high doses. First row is the true parameters, averaged over voxels. Part (a) and (b) are divided by the first row and multiplied by 100.

		Vb	Vd	K1	Kd	Ki	MTT	Ki/K1
	True	0.17	0.76	0.18	0.17	0.02	2.95	0.12
(a) Dynamic	Low	21.3	14.4	14.7	16.4	15.4	53.8	44.3
	Middle	14.9	10.7	10.7	11.9	11.3	45.4	33.1
	High	10.6	7.7	7.9	8.8	8.2	38.3	25.4
(b) Fixed	Low	24.0	16.2	19.4	21.4	16.5	64.3	47.1
	Middle	16.3	11.5	12.6	14.0	12.1	46.6	35.9
	High	11.4	8.9	8.4	9.3	9.4	40.6	28.7
% Improvement	Low	12.4	12.3	31.9	30.6	7.0	19.5	6.2
	Middle	9.8	8.4	18.2	17.6	7.5	2.7	8.4
	High	7.9	14.9	6.1	5.8	14.7	6.0	12.9

6.2 Conclusions

Overall, this thesis presents several statistical methodologies to improve and evaluate the quantitative accuracy of dynamic PET scanning. The non-parametric residue mapping procedure is flexible to represent complex kinetics in various organs and has been demonstrated to be highly feasible for both routinely used short and emerging long axial field of view PET images. Building on this approach, a pooling data framework for the multiple-injection PET study is suggested. We also develop an image-domain bootstrap model to simulate 4D PET data efficiently, which is a very practical mechanism to provide novel uncertainty information as well as enhance mean square error properties by averaging. These techniques have great potential to enhance the quantitation of dynamic total-body PET imaging and benefit clinical decisions for individual patients.

6.3 Future Work

The methodologies developed in this thesis provide a strong foundation to recover more accurate and comprehensive information from dynamic PET scans and open a few avenues for the following work. Further applications, generalizations and translations to PET and non-PET studies will be investigated. Another area of future work is to familiarize other communities, e.g. imaging, engineering and physics with these exciting techniques that may further benefit from various perspectives.

6.3.1 Enhancement of Total-Body PET Parametric Imaging

Recent development of new-generation PET scanners with ultra-high sensitivity and LAFOV stimulates valuable inspiration to map kinetics for multiple organs simultaneously (Wang, Rahmim and Gunn, 2020; Surti, Pantel and Karp, 2020). The large-scale data size and heterogeneity of diverse tissues present challenges. The non-parametric residue mapping has advantages to address these issues and the bootstrap averaging process can further reduce the MSE of generated parametric imaging. We have demonstrated, as shown in Figure 6.1, that these techniques are useful for a LAFOV (1m) PET study on Quadra (O'Sullivan et al., 2022). It is very promising to explore their application in total-body dynamic imaging on uEXPLORER. The proposed combined analysis should also be applicable to multiple-injection studies on such scanners.

The commonly used methods such as Patlak and compartmental models are still of interest to PET community. Some initial adaptions for total-body PET studies have been reported in (Gu et al., 2022; Wang, Nardo, Jones, Cherry and Badawi, 2021; Feng et al., 2021; Wu, Gu, Wu, Zhou and Wang, 2022; Wu, Gu, Gu, Xu, Zhou and Shi, 2022). The elaboration of these schemes will be considered as future work. It would also be interesting to explore the feasibility of spectral analysis (Cunningham and Jones, 1993), which was never implemented for any LAFOV PET imaging. In terms of dynamic imaging there are many other open problems including the recovery of input function without arterial sampling. Another future interest is the Markov chain model for representation of the whole body tracer kinetics (Huang and O'Sullivan, 2014).

6.3.2 Towards Personalized Medicine

Over the past decade, traditional medicine has been shifting to the concept of personalized medicine for improving individualized treatment by maximizing the therapeutic effect and minimizing toxicity, which leads to an increasing need for biomarkers such as radiomics (Katal et al., 2022; Ha, 2019). The general use of biomarkers is comparing their levels with a cut-off value. However, the prediction of outcome for patients with similar disease profiles may be different when the marker levels are close to the cut-off value (Buil-Bruna et al., 2015; Wang, Hensman, Kutkaite, Toh, Galhoz, Dry, Saez-Rodriguez, Garnett, Menden, Dondelinger et al., 2020). In such cases, the quantified uncertainty information would be very important (Tu, Chen and Wu, 2021). Hence, the potential use of image-bootstrap technique for assessing the uncertainties of radiomic features will be explored in the future.

6.3.3 Generalization to other Medical Imaging Modalities

There are a number of medical imaging modalities where dynamic scans are used such as MR (DCE or DSC) (Viallon et al., 2015) and CT (Mayer et al., 2000; Caruso et al., 2016) in the clinical management of cancer and stroke. The structure of datasets are similar to dynamic PET and the flow of contrast agent or other physiological parameters are of interest. It is natural to extend the proposed techniques including NPRM and image-domain bootstrap to these applications for quantitative analysis and assessment of uncertainty in quantitated imaging measurements. This will be a focus for future work.

6.3.4 Parallel speedup

All the analyses in this work are conducted on a Mac-mini with the single 3.2 GHz Intel Core i7 processor and 16 GB 2667 MHz DDR4 memory. Many tasks within PET like image reconstruction and time activity curve (TAC) fitting have been accelerated on the graphical processing unit (GPU) using compute unified device architecture (CUDA) (Fontaine, Luo and Carson, 2022; Przybylski et al., 2017). The data-adaptive segmentation process can be implemented block by block and image-domain bootstrap sample is also created independently. Hence, these computational requirements have significant potential to be further reduced by the suitable use of such parallelization tools.

6.3.5 Open-Source Tools

There exist many commercial and open-source softwares for PET image quantification such as PMOD (https://www.pmod.com/web/). The NMMItools website (https://nmmitools.org/) created by Dr. Nicolas A. Karakatsanis is very helpful to get an overview of these tools. The techniques proposed in this thesis are implemented in R (Team et al., 2013) - an open-source statistical programming platform. An R-package will be developed and expected to be available on the CRAN network (https://cran.r-project.org) in the near future. The user-friendly interface can also be generated by Shiny (https://shiny.rstudio.com), which is easy to build interactive web apps straight from R.

Appendix A

List of Publications and Presentations by the Author

A.1 Peer Reviewed Journals

1. F Gu, F O' Sullivan, M Muzi and D A Mankoff. "Quantitation of multiple injection dynamic PET scans: an investigation of the benefits of pooling data from separate scans when mapping kinetics". *Physics in Medicine & Biology*, 66(13), 2021. URL: https://doi.org/10.1088/1361-6560/ac0683

2. F O' Sullivan, F Gu, Q Wu and L D O'Suilleabhain. "A Generalized Linear modeling approach to bootstrapping multi-frame PET image data". *Medical Image Analysis*, 72(102132), 2021. URL: https://doi.org/10.1016/j.media.2021.102132

3. F Gu and Q Wu. "Quantitation of Dynamic Total-Body PET Imaging: Recent Developments and Future Perspectives". *European Journal of Nuclear Medicine and Molecular Imaging*, 2023. *Under Revision*.

4. F Gu, F O' Sullivan and Q Wu. "Bootstrap averaging enhances the mean square error performance of kinetic maps recovered from PET data". *Under Review*.

5. F Gu, F O' Sullivan et al. "Evaluation of Blood Volume as a Prognostic Biomarker for Breast Cancer Patients and Associated Uncertainty via Image-Domain Bootstrapping". *Manuscript*.

During the Visit in Karolinska Institute

6. T Mou, W Deng, F Gu, Y Pawitan and T Nghia Vu, "Reproducibility of methods to detect differentially expressed genes from single-cell RNA sequencing". *Frontiers in Genetics*, 10(1331), 2020. URL: https://doi.org/10.3389/fgene.2019.01331

During the Internship in United Imaging Healthcare

7. Z Huang, Y Wu, F Fu, N Meng, F Gu, Q Wu, Y Zhou, Y Yang, X Liu, H Zheng, D Liang, M Wang and Z Hu, "Parametric image generation with the uEXPLORER total-body PET/CT system through deep learning". *European Journal of Nuclear Medicine and Molecular Imaging*, 49:2482-2492, 2022. URL: https://doi.org/10.1007/s00259-022-05731-x

8. T Sun, Z Wang, Y Wu, F Gu, X Li, Y Bai, C Shen, Z Hu, D Liang, X Liu, H Zheng, Y Yang, G El Fakhri, Y Zhou, M Wang, "Identifying the individual metabolic abnormities from a systemic perspective using whole-body PET imaging". *European Journal of Nuclear Medicine and Molecular Imaging*, 49:2994–3004, 2022. URL: https://doi.org/10.1007/s00259-022-05832-7

9. Y Li, Y Ng, M D Paranjpe, Q Ge, F Gu, P Li, S Yan, J Lu, X Wang and Y Zhou, "Tracer-specific reference tissues selection improves detection of 18F-FDG, 18F-florbetapir and 18F-flortaucipir PET SUVR changes in Alzheimer's disease", *Human Brain Mapping*, 43(7):2121-2133, 2022. URL: https://doi.org/10.1002/hbm.25774

10. Z Chen, Z Cheng, Y Duan, Q Zhang, N Zhang, F Gu, Y Wang, Y Zhou, H Wang, D Liang, H Zheng and Z Hu, "Accurate total-body Ki parametric imaging with shortened dynamic 18F-FDG PET scan durations via effective data processing", *Medical Physics*, 2022. URL: https://doi.org/10.1002/mp.15893

11. Y Wu, T Feng, Y Shen, F Fu, N Meng, X Li, T Xu, T Sun, F Gu, Q Wu, Y Zhou, H Han, Y Bai and M Wang, "Total-body parametric imaging using the Patlak model: feasibility of reduced scan time". *Medical Physics*, 2022. URL: https://doi.org/10.1002/mp.15647

A.2 Conference Publications

1. F Gu, F O' Sullivan, M Muzi and D A Mankoff. "A simple evaluation of the benefit of combined kinetic analysis of multiple injection dynamic PET scans". *IEEE Nuclear Science Symposium and Medical Imaging (NSS& MIC) Records 2019*. URL: https://doi.org/10.1109/NSS/MIC42101.2019.9060073

2. F Gu, Q Wu, F O' Sullivan, J Huang, M Muzi and D A Mankoff. "An illustration of the use of model-based bootstrapping for evaluation of uncertainty in kinetic information derived from dynamic PET". *IEEE NSS& MIC Records 2019*. URL: https://doi.org/10.1109/NSS/MIC42101.2019.9059736

3. F Gu, Q Wu and F O' Sullivan. "Image-domain bootstrapping of PET time-course data for assessment of uncertainty in complex regional summaries of mapped kinetics". *IEEE NSS& MIC Records 2021*. URL: https://doi.org/10.1109/NSS/MIC44867.2021.9875531

4. F Gu and F O' Sullivan. "A simple adaptive bandwidth scheme that improves image quality and kinetic quantitation in dynamic PET scans". *Journal of Nuclear Medicine*, 62(Suppl. 1), p.1445, 2021. URL: https://jnm.snmjournals.org/content/62/supplement_1/1445

5. F O' Sullivan, Q Wu, F Gu, K Shi, L O'Suilleabhain, S Xue and A Rominger. "Mapping FDG Tracer Kinetics and their Uncertainties via the Bootstrap using data from a Long-Axial FOV PET/CT Scanner". *Journal of Nuclear Medicine*, 63(Suppl. 2), p.3220, 2022. URL: https://jnm.snmjournals.org/content/63/supplement_2/3220

During the Internship in United Imaging Healthcare

6. F Gu, Q Wu, J Wu, D Hu, S Cao, Y Zhou and H Shi. "Feasibility of standard and generalized Patlak Models for dynamic imaging of multiple organs using the uEXPLORER PET scanner". *Journal of Nuclear Medicine*, 63(Suppl. 2), p.3185, 2022. URL: https://jnm.snmjournals.org/content/63/supplement_2/3185

7. F Gu, Q Wu, Y Wu, Y Bai, Y Li, J Wang, F Fu, Y Zhou and M Wang. "Impact of fit time interval on Patlak quantitation in dynamic total-body Imaging using the uEXPLORER PET scanner". *Journal of Nuclear Medicine*, 63(Suppl. 2), p.3190, 2022. URL: https://jnm.snmjournals.org/content/63/supplement_2/3190

8. Q Wu, F Gu, Y Wu, Z Zhu, Y Bai, Q Ge, F Fu, Y Zhou and M Wang. "Assessment of Compartmental Models and delay estimation schemes for dynamic Total-body PET imaging using uEXPLORER". *Journal of Nuclear Medicine*, 63(Suppl. 2), p.3186, 2022. URL: https://jnm.snmjournals.org/content/63/supplement_2/3186

9. Q Wu, F Gu, Y Gu, Y Liu, F Shi, T Xu, Y Zhou and H Shi. "Impact of equilibration time (t*) on Patlak quantitation in dynamic total-Body imaging using the uEXPLORER PET scanner". *Journal of Nuclear Medicine*, 63(Suppl. 2), p.3184, 2022. URL: https://jnm.snmjournals.org/content/63/supplement_2/3184

10. Y Wu, Y Bai, F Gu, W Wei, Q Wu, X Yu, Y Zhou and M Wang. "Assessment of local and global input functions for total body [18F]-FDG Patlak imaging using uEXPLORER PET scanner". *Journal of Nuclear Medicine*, 63(Suppl. 2), p.3189, 2022. URL: https://jnm.snmjournals.org/content/63/supplement_2/3189

A.3 Conference Presentations

Statistical Meetings

1. F Gu, F Hernandez, L O'Suilleabhain, J Huang, E Wolsztynski and F O'Sullivan, "An Analysis of Dynamic PET Scans with a Number of Separate Radiotracer Injections", *Royal Statistical Society International Conference (RSS)*, Cardiff, UK, 3-6 Sep. 2018. [Poster Presentation]

2. F Gu, "Quantitative Analysis of Positron Emission Tomography (PET) Image Data", *Phd Seminar Series of School of Mathematical Science*, University College Cork (UCC), Cork, Ireland, 5th Jun. 2019. [Oral Presentation]

3. F Gu, F O'Sullivan, Q Wu, M Muzi and D. A. Mankoff. "A Statistical Evaluation of Alternative Techniques for Kinetic Analysis of Multiple Injection Dynamic PET Scans". *Joint Statistical Meeting (JSM)*, Virtual, Philadelphia, USA, 1 Aug-6 Aug. 2020. [Oral Presentation]

4. F Gu, "Improved Statistical Quantitation of Dynamic PET Scans", *Young Irish Statistical Association (Young-ISA) Annual Meeting*, Virtual, Ireland, 28th Jan. 2022. [Oral Presentation]

5. J Liang, F Gu, G Newman and F O' Sullivan, "Towards Quantitative Analy-

sis of Digital Subtraction Angiography Image Data". *39th Conference on Applied Statistics in Ireland (CASI)*, Dundalk, Ireland, 15-17 May. 2019. [Oral Presentation]

Molecular Imaging Meetings

6. F Gu, F Hernandez, F O'Sullivan, M Muzi, S Eyal, J Unadkat and D A Mankoff, "Whole-Body metabolic imaging of P-glycoprotein activity in pregnant macaques: illustration of the use of segmentation constrained mixture and residue analysis for comprehensive processing of data from multiple injection dynamic PET scans". *European Molecular Imaging Meeting (EMIM)*, Glasgow, UK, 19-22 Mar. 2019. [Oral Presentation]

7. F Gu, F O'Sullivan, M Muzi and D A Mankoff. "An Examination of the benefits from Combined Kinetic Analysis of Multiple Injection Dynamic PET Scans in the context of Flow-Metabolism Mismatch Studies with O-15 Water and F-18 Fluorodeoxyglucose". *World Molecular Imaging Congress (WMIC)*, Montreal, Canada, 4-7 Sep. 2019. [Poster Presentation]

8. F Gu, Q Wu, F O'Sullivan, J Huang, M Muzi and D A Mankoff. "Use of the Model-Based Bootstrap for Practical Evaluation of Uncertainty in Kinetic Information Derived from Dynamic PET Studies", *IEEE NSS& MIC*, Manchester, UK, 26 Oct-2 Nov. 2019. [Poster Presentation]

9. F Gu, F O'Sullivan, M Muzi and D A Mankoff. "A Simple Evaluation of the Benefit of Combined Kinetic Analysis of Multiple Injection Dynamic PET Scans", *IEEE NSS& MIC*, Manchester, UK, 26 Oct-2 Nov. 2019. [Poster Presentation]

10. F Gu and F O'Sullivan. "A Simple Adaptive Bandwidth Scheme that Improves Image Quality and Kinetic Quantitation in Dynamic PET Scans", *Society of Nuclear Medicine & Molecular Imaging Annual Meeting (SNMMI)*, Virtual, Washington D.C, USA, 12-15 Jun. 2021. [Poster Presentation]

11. F Gu, Q Wu and F O' Sullivan. "Image-domain bootstrapping of PET time-course data for assessment of uncertainty in complex regional summaries of mapped kinetics". *IEEE NSS& MIC*, Virtual, Yokohama, Japan, 16-23 Oct. 2021. [Oral Presentation]

12. M Muzi, T Lan, F Gu and F O'Sullivan, "1-[11C] Acetate Imaging of Membrane Biosynthesis in Glioma Patients", *European Molecular Imaging Meeting (EMIM)*, Glasgow, UK, 19-22 Mar. 2019. [Poster Presentation]

13. F O'Sullivan, Q Wu, F Gu, K Shi, L D O'Suilleabhain, S Xue and A Rominger, "Mapping FDG Tracer Kinetics and their Uncertainties via the Bootstrap using data from a Long-Axial FOV PET/CT Scanner". *Society of Nuclear Medicine & Molecular Imaging Annual Meeting (SNMMI)*, Virtual,11-14 Jun. 2022. [Poster Presentation]

Appendix B

Details of Derivations

B.1 Radon and Fourier Transform

B.1.1 Line Integral[1]

Line integral of a scalar field For a real-valued function $f(x, y)$ and a curve C in R^2, parametrized by $x = x(t)$, $y = y(t)$, $a \leq t \leq b$, the line integral of $f(x, y)$ along C with respect to arc length s is

$$\int_C f(x, y)ds = \int_a^b f(x(t), y(t))\sqrt{x'(t)^2 + y'(t)^2}dt \tag{B.1}$$

the symbol ds is the differential of the arc length function:

$$s = s(t) = \int_a^t \sqrt{x'(u)^2 + y'(u)^2}du$$

which can be recognized as the length of the curve C over the interval $[a, t]$, for all t in $[a, b]$. That is, $ds = s'(t)dt = \sqrt{x'(t)^2 + y'(t)^2}dt$

Line integral of a vector field For a vector field $f(x, y) = P(x, y)i + Q(x, y)j$ and a curve C with a smooth parameterization $x = x(t)$, $y = y(t)$, $a \leq t \leq b$, the line integral of f along C is

[1] Quoted from URL: https://math.libretexts.org/Bookshelves/Calculus/Book%3A_Vector_Calculus_(Corral)/04%3A_Line_and_Surface_Integrals/4.01%3A_Line_Integrals

$$\begin{aligned}\int_C f \cdot dr &= \int_C P(x,y)dx + \int_C Q(x,y)dy \\ &= \int_a^b f(x(t),y(t)) \cdot r^{'}(t)dt\end{aligned} \tag{B.2}$$

where $r(t) = x(t)i + y(t)j$ is the position vector for points on C.

B.1.2 Radon Transform[2]

The Radon transform is the integral transform which takes a function f defined on the plane (x, y) to a function $g(\phi, s)$ defined on the (two-dimensonal) space of lines in the plane. The value at a particular line is equal to the line integral of the function over that line (Figure B.1).

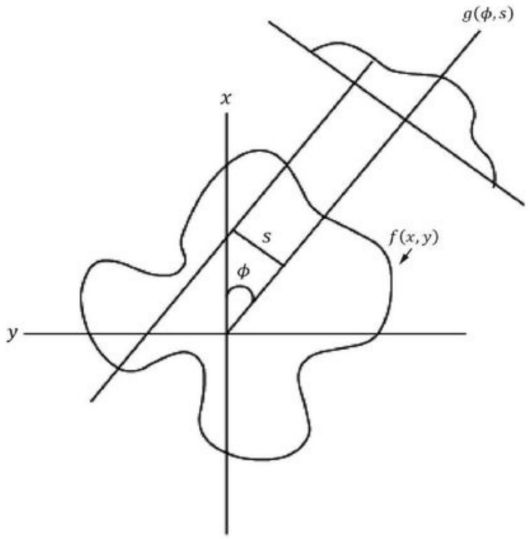


Figure B.1: Illustration of Radon transform, where x, y are axes; s is the shifting constant; ϕ is rotation angle; $f(x, y)$ is the intensity of object in (x, y); and $g(\phi, s)$ is the forward projection value after Radon transform.[2]

The function $g(\phi, s)$ is the line integral of the image intensity $f(x, y)$, along a line l that is distance s from the origin and at angle ϕ off the x-axis.

$$g(\phi, s) = \int_l f(x, y)dl \tag{B.3}$$

[2]Quoted from URL: https://slideplayer.com/slide/15255656/

All points on this line satisfy the equation:

$$xsin(\phi) - ycos(\phi) = s \tag{B.4}$$

Therefore, the forward projection function $g(\phi, s)$ can be rewritten as:

$$g(\phi, s) = \int\int f(x, y)\delta(xsin\phi - ycos\phi - s)dxdy \tag{B.5}$$

where the $\delta(n)$ is a delta function, if $n = 0$, $\delta(n) = 1$; else, $\delta(n) = 0$

If a function f represents an unknown density, then the Radon transform represents the projection data obtained as the output of a tomographic scan. Hence the inverse of the Radon transform can be used to reconstruct the original density from the projection data as shown in Figure B.2.

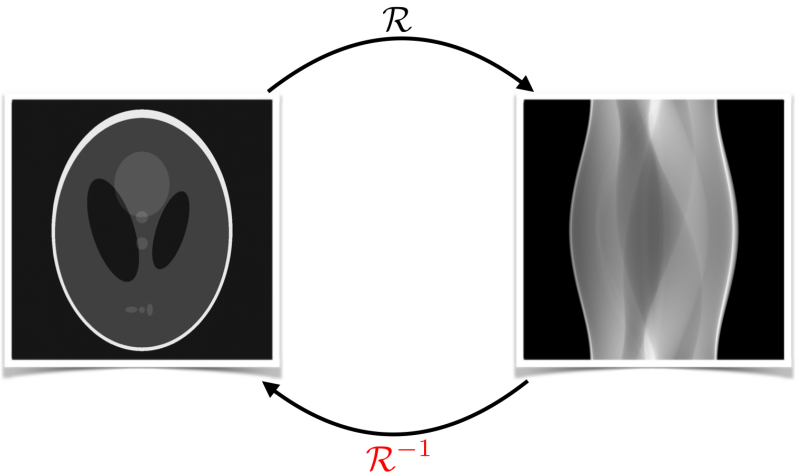


Figure B.2: Radon transform $\mathcal{R}$ and its inversion $\mathcal{R}^{-1}$ (Wieczorek, Vogel and Lasser, 2014).

B.1.3 Fourier Transform[3]

We use the notation $\mathcal{F}(\cdot)$ to denote the Fourier transform (FT) operator and $\mathcal{F}^{-1}(\cdot)$ to denote the inverse transform operator. That is:

$$\begin{cases} X(\omega) = F\{x(t)\} \\ x(t) = F^{-1}\{X(\omega)\} \end{cases} \tag{B.6}$$

Definitions of the forward and inverse FT in four cases are summarized in Figure B.3.

Fourier Series (FS)

For $x(t)$ of duration T, set $\omega_0 = \frac{2\pi}{T}$.

$$x(t): \quad 0 \le t \le T$$
$$X[k]: \quad k = \ldots, -2, -1, 0, 1, 2, \ldots$$

$$X[k] = \frac{1}{T}\int_{t=0}^{T} x(t)\, e^{-jk\omega_0 t} dt$$

$$x(t) = \sum_{k=-\infty}^{\infty} X[k]\, e^{jk\omega_0 t}$$

Fourier Transform (FT)

$$x(t): \quad -\infty < t < \infty$$
$$X(\omega): \quad -\infty < \omega < \infty$$

$$X(\omega) = \int_{t=-\infty}^{\infty} x(t)\, e^{-j\omega t} dt$$

$$x(t) = \frac{1}{2\pi}\int_{\omega=-\infty}^{\infty} X(\omega)\, e^{j\omega t} d\omega$$

Discrete Fourier Transform (DFT)

For $x[n]$ of length N, set $\omega_0 = \frac{2\pi}{N}$.

$$x[n]: \quad n = 0, 1, \ldots, N-1$$
$$X[k]: \quad k = 0, 1, \ldots, N-1$$

$$X[k] = \sum_{n=0}^{N-1} x[n]\, e^{-jk\omega_0 n}$$

$$x[n] = \frac{1}{N}\sum_{k=0}^{N-1} X[k]\, e^{jk\omega_0 n}$$

Discrete-Time Fourier Transform (DTFT)

$$x[n]: \quad n = \ldots, -2, -1, 0, 1, 2, \ldots$$
$$X(\omega): \quad -\pi \le \omega \le \pi$$

$$X(\omega) = \sum_{n=-\infty}^{\infty} x[n]\, e^{-j\omega n}$$

$$x[n] = \frac{1}{2\pi}\int_{\omega=-\pi}^{\pi} X(\omega)\, e^{j\omega n} d\omega$$

Figure B.3: Definitions of the forward and inverse Fourier transforms in four cases.[3]

FT of the delta function:

$$F\{\delta(t)\} = \int_{-\infty}^{\infty} \delta(t) e^{-j\omega t} dt = 1 \tag{B.7}$$

[3]Quoted from URL: https://www.princeton.edu/~cuff/ele201/kulkarni_text/frequency.pdf

B.1.4 Radon Transform with Fourier Transform[4]

The 1D Fourier Transform of g is given by:

$$G(\phi, \omega) = \int e^{-j\omega s} g(\phi, s) ds \tag{B.8}$$

Substitute the expression for $g(\phi, s)$ into the Radon transform (B.5) to get:

$$G(\phi, \omega) = \int \int \int f(x, y) e^{-j\omega s} \delta(xsin\phi - ycos\phi - s) dxdyds \tag{B.9}$$

Use the sifting property of the Dirac delta function to simplify, we get:

$$G(\phi, \omega) = \int \int f(x, y) e^{-j\omega(xsin\phi - ycos\phi - s)} dxdy \tag{B.10}$$

The definition of the 2D Fourier transform of f:

$$F(u, v) = \int \int f(x, y) e^{-j(ux+vy)} dxdy \tag{B.11}$$

It shows that Radon transform with Fourier slice transform is $F(u, v)$ evaluated at $u = \omega * sin(\phi)$ and $v = -\omega * cos(\phi)$. Therefore, we can apply some image operation in Fourier domain instead of spatial domain.

B.2 Derivation of Equation (2.14)

$$\begin{aligned} y[n] &= H[x[n]] \\ &= H[\sum_{i=-\infty}^{\infty} x[i]\delta[n-i]] \\ &= \sum_{i=-\infty}^{\infty} x[i]H[\delta[n-i]] \\ &= \sum_{i=-\infty}^{\infty} x[i]h[n-i] \end{aligned}$$

[4]Quoted from URL: https://slideplayer.com/slide/15255656/

B.3 Solution of One Compartmental Model Ordinary Differential Equation (2.18)

$$\begin{aligned}
\frac{dC_1(t)}{dt} = K_1C_p(t) - k_2C_1(t) \quad &\Rightarrow \quad \frac{dC_1(t)}{dt} + k_2C_1(t) = K_1C_p(t) \\
&\Rightarrow \quad e^{k_2t}\frac{dC_1(t)}{dt} + e^{k_2t}k_2C_1(t) = K_1e^{k_2t}C_p(t) \\
&\Rightarrow \quad \frac{d}{dt}(e^{k_2t}C_1(t)) = K_1e^{k_2t}C_p(t) \\
&\Rightarrow \quad e^{k_2t}C_1(t) = \int_0^t K_1e^{k_2s}C_p(s)ds \\
&\Rightarrow \quad C_1(t) = \int_0^t K_1e^{-k_2(t-s)}C_p(s)ds
\end{aligned}$$

B.4 Laplace's Transformation[5]

B.4.1 Introduction to the Laplace Transform

Recall the definition of an *improper* integral. If g is integrable over the interval $[a, T]$ for every $T > a$, then the improper integral of g over $[a, \infty]$ is defined as:

$$\int_0^\infty g(t)dt = \lim_{T\to\infty}\int_a^T g(t)dt \tag{B.12}$$

We say that the improper integral *converges* if the limit in (B.12) exists; otherwise, the improper integral *diverges* or does not exist.

Laplace Transform: Let f be defined for $t \geq 0$ and let s be a real number. Then the Laplace transform of f is the function F defined by

$$F(s) = \int_0^\infty e^{-st}f(t)dt \tag{B.13}$$

for those values of s for which the improper integral converges.

It is important to keep in mind that the variable of integration in (B.13) is t, which s is a parameter independent of t. We use t as the independent variable for f because in applications the Laplace transform is usually applied to functions of time.

The Laplace transform can be viewed as an operator L that transforms the

[5] Quoted from (Trench, 2013).

function $f = f(t)$ into the function $F = F(s)$. Thus, (B.13) can be expressed as: $F = L(f)$. The function f and F form a $transform\ pair$, which we will sometimes denote by $f(t) \leftrightarrow F(s)$. It can be shown that if $F(s)$ is defined for $s = s_0$ then it's defined for all $s > s_0$.

Linearity of Laplace Transform: Suppose $L(f_i)$ is defined for $s > s_i$, $(1 \leq i \leq n)$. Let s_0 be the largest of numbers $s_1, s_2, ...s_n$ and let $c_1, c_2, ...c_n$ be constants. Then

$$L(c_1 f_1 + c_2 f_2 + ... + c_n f_n) = c_1 L(f_1) + c_2 L(f_2) + ... + c_n L(f_n), \quad for \quad s > s_0$$

First shifting theorem: If $F(s) = \int_0^\infty e^{-st} f(t)dt$ is the Laplace transform of $f(t)$ for $s > s_0$, then $F(s-a)$ is the Laplace transform of $e^{at} f(t)$ for $s > s_0 + a$. Hence, $F(s-a) = \int_0^\infty e^{-st}(e^{at} f(t))dt$.

B.4.2 The Inverse Laplace Transform

We defined the Laplace transform of f by $F(s) = L(f) = \int_0^\infty e^{-st} f(t)dt$, we will say that f is an inverse Laplace Transform of F, and write: $f = L^{-1}(F)$.

Linearity Property: If F_1, F_2,...F_n are Laplace transforms and c_1, c_2, ...c_n are constants, then

$$L^{-1}(c_1 f_1 + c_2 f_2 + ... + c_n f_n) = c_1 L^{-1}(f_1) + c_2 L^{-1}(f_2) + ... + c_n L^{-1}(f_n)$$

Inverse Laplace Transforms of Rational Functions: Using the Laplace transform to solve differential equations often requires finding the inverse transform of a rational function: $F(s) = P(s)/Q(s)$, where P and Q are polynomials s with no common factor. Since it can be shown that $\lim_{s\to\infty} F(s) = 0$ if F is a Laplace transform, we need only consider the case where degree(P)<degree(Q). To obtain $L^{-1}(F)$, we find the partial fraction expansion of F, obtain inverse transforms of the individual terms in the expansion from the table of Laplace transforms, and use the linearity property of the inverse transform.

Theorem B.4.1. *Suppose*

$$F(s) = \frac{P(s)}{(s-s_1)(s-s_2)...(s-s_n)}$$

Table B.1: A brief table of Laplace transforms

$f(t)$	$F(s)$	
1	$\frac{1}{s}$	$s>0$
t^n (n=integer>0)	$\frac{n!}{s^{n+1}}$	$s>0$
$t^p, p>-1$	$\frac{\Gamma(p+1)}{s^{(p+1)}}$	$s>0$
e^{at}	$\frac{1}{s-a}$	$s>a$
$t^n e^{at}$ (n=integer>0)	$\frac{n!}{(s-a)^{n+1}}$	$s>0$
$cos\omega t$	$\frac{s}{s^2+\omega^2}$	$s>0$
$sin\omega t$	$\frac{\omega}{s^2+\omega^2}$	$s>0$
$e^{\lambda t}cos\omega t$	$\frac{s-\lambda}{(s-\lambda)^2+\omega^2}$	$s>\lambda$
$e^{\lambda t}sin\omega t$	$\frac{\omega}{(s-\lambda)^2+\omega^2}$	$s>\lambda$
$coshbt$	$\frac{s}{s^2-b^2}$	$s>\lvert b\rvert$
$sinhbt$	$\frac{b}{s^2-b^2}$	$s>\lvert b\rvert$
$tcos\omega t$	$\frac{s^2-\omega^2}{(s^2+\omega^2)^2}$	$s>0$
$tsin\omega t$	$\frac{2\omega s}{(s^2+\omega^2)^2}$	$s>0$
$sin\omega t-\omega tcos\omega t$	$\frac{2\omega^3}{(s^2+\omega^2)^2}$	$s>0$
$\omega t-sin\omega t$	$\frac{\omega^3}{s^2(s^2+\omega^2)^2}$	$s>0$
$\frac{1}{t}sin\omega t$	$arctan(\frac{\omega}{s})$	$s>0$
$e^{at}f(t)$	$F(s-a)$	
$t^k f(t)$	$(-1)^k F^{(k)}(s)$	
$f(\omega t)$	$\frac{1}{\omega}F(\frac{s}{\omega})$	
$u(t-\tau)$	$\frac{e^{-\tau s}}{s}$	$s>0$
$u(t-\tau)(t-\tau)(\tau>0)$	$e^{-\tau s}F(s)$	
$\int_0^t f(\tau)g(t-\tau)d\tau$	$F(s)\cdot G(s)$	
$\delta(t-a)$	e^{-as}	$s>0$

where $s_1, s_2, ...s_n$ are distinct and P is a polynomial of degree less than n. Then

$$F(s)=\frac{A_1}{s-s_1}+\frac{A_2}{s-s_2}+....+\frac{A_n}{s-s_n}$$

where A_i can be computed by ignoring the factor $s-s_i$ and setting $s=s_i$ elsewhere.

B.4.3 Solution of Initial Value Problems

Theorem B.4.2. *Suppose f is continuous on $[0,\infty]$ and of exponential order s_0, and f' is piecewise continuous on $[0,\infty]$. Then f and f' have Laplace transforms for $s>s_0$, and*

$$L(f')=sL(f)-f(0) \tag{B.14}$$

Proof: Integration by parts yields:

$$\begin{aligned}\int_0^T e^{-st} f^{'}(t)dt &= e^{-st} f(t) \mid_0^T + s\int_0^T e^{-st} f(t)dt \\ &= e^{-sT} f(T) - f(0) + s\int_0^T e^{-st} f(t)dt\end{aligned}$$

For any $T > 0$. Sin f is of exponential order s_0, $\lim_{T\to\infty} e^{-sT} f(T) = 0$ and the last integral converges as $T \to \infty$ if $s > s_0$. Therefore

$$\int_0^T e^{-st} f^{'}(t)dt = -f(0) + s\int_0^\infty e^{-st} f(t)dt = -f(0) + sL(f)$$

Theorem B.4.3. *Suppose f and $f^{'}$ are continuous on $[0,\infty]$ and of exponential order s_0, and that $f^{''}$ is piecewise continuous on $[0,\infty]$. Then f, $f^{'}$, and $f^{''}$ have Laplace transforms for $s > s_0$,*

$$\begin{cases} L(f^{'}) = sL(f) - f(0) \\ L(f^{''}) = s^2 L(f) - f^{'}(0) - sf(0) \end{cases} \tag{B.15}$$

B.5 Solution of Two Compartmental Model Ordinary Differential Equation (2.20)

$$\begin{cases} \frac{dC_1}{dt} = K_1 C_p(t) - (k_2 + k_3)C_1(t) + k_4 C_2(t) \\ \\ \frac{dC_2}{dt} = k_3 C_1(t) - k_4 C_2(t) \end{cases} \tag{B.16}$$

As described in (B.14), by taking the Laplace transform of (B.16), which becomes

$$\begin{cases} SC_1(S) = K_1 C_p(S) - (k_2 + k_3)C_1(S) + k_4 C_2(S) \\ \\ SC_2(S) = k_3 C_1(S) - k_4 C_2(S) \end{cases} \tag{B.17}$$

where initial conditions are assumed to be zero, and $C_1(S)$, $C_2(S)$, and $C_p(S)$ are the Laplace transforms of $C_1(t)$, $C_2(t)$, and $C_p(t)$. From (B.17), $C_1(S)$ and $C_2(S)$ can be expressed in terms of $C_p(S)$ as

$$\begin{cases} C_1(S) = \frac{K_1}{\theta_2 - \theta_1}\left(\frac{k_4 - \theta_1}{S + \theta_1} + \frac{\theta_2 - k_4}{S + \theta_2}\right) C_p(S) \\ C_2(S) = \frac{K_1 k_3}{\theta_2 - \theta_1}\left(\frac{1}{S + \theta_1} - \frac{1}{S + \theta_2}\right) C_p(S) \end{cases} \tag{B.18}$$

where $\theta_1 = \frac{k_2+k_3+k_4-\sqrt{(k_2+k_3+k_4)^2-4k_2k_4}}{2}$ and $\theta_2 = \frac{k_2+k_3+k_4+\sqrt{(k_2+k_3+k_4)^2-4k_2k_4}}{2}$

$(\theta_1\theta_2 = k_2k_4, \theta_1+\theta_2 = k_2+k_3+k_4)$

Derivation details are below:

$$
\begin{aligned}
SC_2(S) &= k_3C_1(S) - k_4C_2(S) \Rightarrow C_2(S) = \frac{k_3C_1(S)}{S+k_4} \\
SC_1(S) &= K_1C_p(S) - (k_2+k_3)C_1(S) + k_4C_2(S) \\
&= K_1C_p(S) - (k_2+k_3)C_1(S) + k_4\frac{k_3C_1(S)}{S+k_4} \\
&\Rightarrow (S+k_2+k_3-\frac{k_3k_4}{S+k_4})C_1(S) = K_1C_p(S) \\
C_1(S) &= \frac{K_1(S+k_4)}{(S+k_2+k_3)(S+k_4)-k_3k_4}C_p(S) \\
&= \frac{K_1(S+k_4)}{S^2+(k_2+k_3+k_4)S+k_2k_4}C_p(S) \\
&= \frac{K_1(S+k_4)}{S^2+(\theta_1+\theta_2)S+\theta_1\theta_2}C_p(S) \\
&= \frac{K_1(S+k_4)}{(S+\theta_1)(S+\theta_2)}C_p(S) \equiv \frac{K_1}{\theta_2-\theta_1}\left(\frac{k_4-\theta_1}{S+\theta_1}+\frac{\theta_2-k_4}{S+\theta_2}\right)C_p(S) \\
C_2(S) &= \frac{k_3C_1(S)}{S+k_4} \\
&= \frac{K_1k_3}{(S+\theta_1)(S+\theta_2)}C_p(S) \equiv \frac{K_1k_3}{\theta_2-\theta_1}\left(\frac{1}{S+\theta_1}-\frac{1}{S+\theta_2}\right)C_p(S)
\end{aligned}
$$

Inverse Laplace transform (see Table B.1) of (B.18) gives:

$$
\begin{cases}
C_1(t) = \frac{K_1}{\theta_2-\theta_1}\left((k_4-\theta_1)e^{-\theta_1t}+(\theta_2-k_4)e^{-\theta_2t}\right)\otimes C_p(t) \\
C_2(t) = \frac{K_1k_3}{\theta_2-\theta_1}\left(e^{-\theta_1t}-e^{-\theta_2t}\right)\otimes C_p(t)
\end{cases} \tag{B.19}
$$

Hence:

$$
C_T(t) = C_1(t)+C_2(t) = K_1(\pi_1e^{-\theta_1t}+\pi_2e^{-\theta_2t})\otimes C_p(t) \tag{B.20}
$$

where $\pi_1 = \frac{k_4-\theta_1+k_3}{\theta_2-\theta_1}, \pi_2 = \frac{\theta_2-k_4-k_3}{\theta_2-\theta_1}; \pi_1+\pi_2 = 1.$

Nomenclature

Δ	Delay
^{11}C	Carbon-11
^{13}N	Nitrogen-13
^{15}O	Oxygen-15
^{18}F	Fluorine-18
C_p	Arterial Input Function
C_T	Tissue Activity
iid	Independent Identically Distributed
K_1	Overall Flow
K_B	Blood Flow
K_D	In-Distribution Flow
K_i	Flux
K_{trans}	Transfer Constant
R	Residue Function
V_B or V_b	Blood Volume
V_D	In-Distribution Volume
V_p	Fractional Plasma Volume
1C	One Compartmental Model/Modeling
1D	One Dimension/Dimensional
2C	Two Compartmental Model/Modeling

2Ci Two Irreversible Compartmental Model/Modeling

2Cr Two Reversible Compartmental Model/Modeling

2D Two Dimension/Dimensional

3D Three Dimension/Dimensional

4D Four Dimension/Dimensional

AB Averaged-Bootstrap

ACF Auto-correlation Function

ACRIN American College of Radiology Imaging Network

AIF Arterial Input Function

BBB Blood Brain Barrier

BGO Bismuth Germanium Oxide

CI Confidence Interval

COV or CV Coefficient of Variation

CsA Cyclosporine A

CT Computed Tomography

CTN Clinical Trials Network

CUDA Compute Unified Device Architecture

DCE Dynamic Contrast Enhanced

DFS Disease Free Survival

DGP Data Generation Process

DSA Digital Subtraction Angiography

DSC Dynamic Susceptibility Contrast

DWB Dynamic Whole-Body

ECAT Emission Computed Axial Tomography

EM Expectation Maximization

FA Factor Analysis

FBP Filtered Backprojection

FDG Fluorodeoxyglucose

FFT Fast Fourier Transform

FLT Fluorothymidine

fMRI Functional Magnetic Resonance Imaging

FOV Field of View

FT Fourier Transform

FWHM Full Width at Half Maximum

GE General Electric

GLM Generalized Linear Model/Modeling

GLUT Glucose Transporter

GPU Graphical Processing Unit

IDIF Image-Derived Input Function

IRLS Iteratively Re-Weighted Least Square

LABC Locally Advanced Breast Cancer

LAFOV Long Axial Field of View

LOR Line of Response

LSO Lutetium Oxyorthosilicate

LTI Linear Time-Invariant

LYSO Lutetium-Yttrium Oxyorthosilicate

MBIF Model-Based Input Function

ML Maximum Likelihood

MLE Maximum Likelihood Estimate

MR Magnetic Resonance

MRI Magnetic Resonance Imaging

MSE Mean Square Error

MTT Mean Transit Time

NAC Neoadjuvant Chemotherapy

NCI National Cancer Institute

NECR Noise-Equivalent Count Rate

NEMA National Electrical Manufactures Association

NLLS Non-Linear Least Square

NPRM Non-Parametric Residue Mapping

OLS Ordinary Least Square

OSEM Ordered Subset Expectation Maximization

P-gp P-glycoprotein

PAT Phantom Analysis Toolkit

PBIF Population-Based Input Function

PBPM Population-Based Projection Model

PCA Principal Component Analysis

PCC Parametric Color Coding

pCR Pathologic Complete Response

PET Positron Emission Tomography

PETT Positron Emission Transaxial Tomography

PSF Point-Spread Function

PSMA Prostate-specific Membrane Antigen

QP Quadratic Programming

RF Radio Frequency

RMSE Root Mean Square Error

ROI Region of Interest

RSS Residual Sum of Squares

RSSA Rank-Shaping Spectral Analysis

SA Spectral Analysis

SAFOV Short Axial Field of View

SAIF Spectral Analysis with Iterative Filter

SAR Spatial Autoregressive

SD Standard Deviation

SE Standard Error

SNMMI Society of Nuclear Medicine and Molecular Imaging

SNR Signal-to-noise Ratio

SUV Standardized Uptake Value

SVD Singular Value Decomposition

T1 Longitudinal Relaxation Time

T2 Transverse Relaxation Time

TAC Time Activity Curve

TEVAR Thoracic Endovascular Aortic Repair

TOF Time of Flight

UCC University College Cork

UCLA University of California, Los Angeles

UIH United Imaging Healthcare

VOI Volume of Interest

VSK Vardi-Shepp-Kaufman

WLS Weighted Least Square

WRSS Weighted Residual Sum of Squares

Bibliography

Ahn, JY, K Seo, JS Lee and DS Lee. 2000. Factor analysis for the quantification of renal cortical blood flow using O-15 water dynamic PET. In *2000 IEEE Nuclear Science Symposium. Conference Record (Cat. No. 00CH37149)*. Vol. 3 IEEE pp. 18–153.

Alberts, Ian, Jan-Niklas Hünermund, George Prenosil, Clemens Mingels, Karl Peter Bohn, Marco Viscione, Hasan Sari, Bernd Vollnberg, Kuangyu Shi, Ali Afshar-Oromieh et al. 2021. "Clinical performance of long axial field of view PET/CT: a head-to-head intra-individual comparison of the Biograph Vision Quadra with the Biograph Vision PET/CT." *European Journal of Nuclear Medicine and Molecular Imaging* pp. 1–10.

Alpert, NM, DA Chesler, JA Correia, RH Ackerman, JY Chang, S Finklestein, SM Davis, GL Brownell and JM Taveras. 1982. "Estimation of the local statistical noise in emission computed tomography." *IEEE transactions on medical imaging* 1(2):142–146.

Arabi, Hossein and Habib Zaidi. 2021. "Non-local mean denoising using multiple PET reconstructions." *Annals of nuclear medicine* 35(2):176–186.

Badawi, Ramsey D, Hongcheng Shi, Pengcheng Hu, Shuguang Chen, Tianyi Xu, Patricia M Price, Yu Ding, Benjamin A Spencer, Lorenzo Nardo, Weiping Liu et al. 2019. "First Human Imaging Studies with the EXPLORER Total-Body PET Scanner." *Journal of Nuclear Medicine* 60(3):299–303.

Barrett, Harrison H, Donald W Wilson and Benjamin MW Tsui. 1994. "Noise properties of the EM algorithm. I. Theory." *Physics in medicine and biology* 39(5):833–846.

Barrett, Harrison H and Kyle J Myers. 2013. *Foundations of image science*. John Wiley & Sons.

Barrio, Jorge R, Sung-Cheng Huang, Nagichettiar Satyamurthy, Claudio S

Scafoglio, S Yu Amy, Abass Alavi and Kenneth A Krohn. 2020. "Does 2-FDG PET accurately reflect quantitative in vivo glucose utilization?" *Journal of Nuclear Medicine* 61(6):931–937.

Beason-Held, Lori L, Richard E Desmond, Peter Herscovitch and Richard E Carson. 1999. "Bolus injection versus slow infusion of [15O] water for positron emission tomography activation studies." *Journal of Cerebral Blood Flow and Metabolism* 19(8):843–852.

Berger, Abi. 2002. "How does it work?: Magnetic resonance imaging." *BMJ: British Medical Journal* 324(7328):35.

Bertoldo, Alessandra, Gaia Rizzo and Mattia Veronese. 2014. "Deriving physiological information from PET images: from SUV to compartmental modelling." *Clinical and Translational Imaging* 2(3):239–251.

Black, Noel F., Scott McJames and Dan J. Kadrmas. 2009. "Rapid Multi-Tracer PET Tumor Imaging With ^{18}F-FDG and Secondary Shorter-Lived Tracers." *IEEE Transactions on Nuclear Science* 56(5):2750–2758.

Bloch, Felix. 1946. "Nuclear induction." *Physical review* 70(7-8):460.

Boellaard, Ronald. 2009. "Standards for PET image acquisition and quantitative data analysis." *Journal of nuclear medicine* 50(Suppl 1):11S–20S.

Bollmann, Saskia and Markus Barth. 2021. "New acquisition techniques and their prospects for the achievable resolution of fMRI." *Progress in neurobiology* 207:101936.

Box, George E. 1976. "Science and statistics." *Journal of the American Statistical Association* 71(356):791–799.

Breiman, Leo. 2001. "Random forests." *Machine learning* 45(1):5–32.

Brenner, David J and Eric J Hall. 2007. "Computed tomography—an increasing source of radiation exposure." *New England journal of medicine* 357(22):2277–2284.

Brockwell, Peter J and Richard A Davis. 1991. *Time Series: Theory and Methods*. New York, NY, USA: Springer.

Buil-Bruna, Núria, Tarjinder Sahota, José-María López-Picazo, Marta Moreno-Jiménez, Salvador Martín-Algarra, Benjamin Ribba and Iñaki F Trocóniz. 2015. "Early Prediction of Disease Progression in Small Cell Lung Cancer: To-

ward Model-Based Personalized Medicine in OncologyModel-Based Personalized Disease Monitoring." *Cancer research* 75(12):2416–2425.

Busemann Sokole, Ellinor, Anna Płachcínska, Alan Britten, Maria Lyra Georgosopoulou, Wendy Tindale and Rigobert Klett. 2010. "Routine quality control recommendations for nuclear medicine instrumentation." *European journal of nuclear medicine and molecular imaging* 37(3):662–671.

Buvat, Irene. 2002. "A non-parametric bootstrap approach for analysing the statistical properties of SPECT and PET images." *Physics in Medicine & Biology* 47(10):1761.

Buvat, Irene and Delphine Lazaro. 2006. "Monte Carlo simulations in emission tomography and GATE: An overview." *Nuclear Instruments and Methods in Physics Research Section A: Accelerators, Spectrometers, Detectors and Associated Equipment* 569(2):323–329.

Carson, Richard E, Yuchen Yan, Margaret E Daube-Witherspoon, Nanette Freedman, Stephen L Bacharach and Peter Herscovitch. 1993. "An approximation formula for the variance of PET region-of-interest values." *IEEE transactions on medical imaging* 12(2):240–250.

Caruso, Damiano, Marwen Eid, U Joseph Schoepf, Kwang Nam Jin, Akos Varga-Szemes, Christian Tesche, Stefanie Mangold, Adam Spandorfer, Andrea Laghi and Carlo N De Cecco. 2016. "Dynamic CT myocardial perfusion imaging." *European journal of radiology* 85(10):1893–1899.

Casey, ME and R Nutt. 1986. "A multicrystal two dimensional BGO detector system for positron emission tomography." *Ieee transactions on nuclear science* 33(1):460–463.

Cavalcanti, Yanna Cruz, Thomas Oberlin, Nicolas Dobigeon, Cédric Févotte, Simon Stute, Maria-Joao Ribeiro and Clovis Tauber. 2019. "Factor analysis of dynamic PET images: beyond Gaussian noise." *IEEE transactions on medical imaging* 38(9):2231–2241.

Chen, Yakuan, Jeff Goldsmith and R Todd Ogden. 2019. "Functional data analysis of dynamic PET data." *Journal of the American Statistical Association* 114(526):595–609.

Cheon, Jung-Eun. 2015. "Quantitative digital subtraction angiography in pediatric moyamoya disease." *Journal of Korean Neurosurgical Society* 57(6):432.

Chernick, M. R. 2011. "Bootstrap Methods: A guide for Parctitioners and Researchers, ser. Probability and Statistics." *John Wiley and Sons* .

Cherry, Simon R and Magnus Dahlbom. 2006. PET: physics, instrumentation, and scanners. In *PET*. Springer pp. 1–117.

Cherry, Simon R, Y Shao, RW Silverman, K Meadors, S Siegel, A Chatziioannou, JW Young, W Jones, JC Moyers, D Newport et al. 1997. "MicroPET: a high resolution PET scanner for imaging small animals." *Ieee transactions on nuclear science* 44(3):1161–1166.

Chesler, DA. 1971. 3-Dimensional activity distribution from multiple positron scintigraphs. In *Journal of Nuclear Medicine*. Vol. 12 SOC NUCLEAR MEDICINE INC 1850 SAMUEL MORSE DR, RESTON, VA 20190-5316 p. 347.

Chesler, DA. 1973. "Positron tomography and three-dimensional reconstruction technique." *Tomographic imaging in nuclear medicine* pp. 176–183.

Chesler, DA, B Hoop and GL Brownell. 1973. TRANSVERSE SECTION IMAGING OF MYOCARDIUM WITH N-13H4. In *Journal of Nuclear Medicine*. Vol. 14 SOC NUCLEAR MEDICINE INC 1850 SAMUEL MORSE DR, RESTON, VA 20190-5316 pp. 623–623.

Chitalia, Rhea, Varsha Viswanath, Austin R Pantel, Lanell M Peterson, Aimilia Gastounioti, Eric A Cohen, Mark Muzi, Joel Karp, David A Mankoff and Despina Kontos. 2021. "Functional 4-D clustering for characterizing intratumor heterogeneity in dynamic imaging: evaluation in FDG PET as a prognostic biomarker for breast cancer." *European Journal of Nuclear Medicine and Molecular Imaging* pp. 1–12.

Cho, ZH, JK Chan and L Eriksson. 1976. "Circular ring transverse axial positron camera for 3-dimensional reconstruction of radionuclides distribution." *IEEE Transactions on Nuclear Science* 23(1):613–622.

Cho, ZH and MR Farukhi. 1977. "Bismuth germanate as a potential scintillation detector in positron cameras." *Journal of nuclear medicine* 18(8):840–844.

Choi, Yong, Randall A Hawkins, Sung-Cheng Huang, Sanjiv S Gambhir, Richard C Brunken, Michael E Phelps and Heinrich R Schelbert. 1991. "Parametric images of myocardial metabolic rate of glucose generated from dynamic cardiac PET and 2-[18F] fluoro-2-deoxy-d-glucose studies." *Journal of nuclear medicine: official publication, Society of Nuclear Medicine* 32(4):733–738.

Chung, FS, S Eyal, M Muzi, JM Link, DA Mankoff, A Kaddoumi, F O'sullivan, P Hsiao and Jashvant D Unadkat. 2010. "Positron emission tomography imaging of tissue P-glycoprotein activity during pregnancy in the non-human primate." *British journal of pharmacology* 159(2):394–404.

Cormack, Allan M. 1980. "Early two-dimensional reconstruction (CT scanning) and recent topics stemming from it." *Journal of Computer Assisted Tomography* 4(5):658–664.

Csörgó, Sándor and Jan Mielniczuk. 1996. "The empirical process of a short-range dependent stationary sequence under Gaussian subordination." *Probability Theory and Related Fields* 104(1):15–25.

Cunningham, Vincent J and Terry Jones. 1993. "Spectral analysis of dynamic PET studies." *Journal of Cerebral Blood Flow & Metabolism* 13(1):15–23.

Dahlbom, M, EJ Hoffman, CK Hoh, C Schiepers, G Rosenqvist, RA Hawkins and ME Phelps. 1992. "Evaluation of a positron emission tomography (PET) scanner for whole body imaging." *J Nucl Med* 33:1191–1199.

Dahlbom, Magnus. 2001. Estimation of image noise in PET using the bootstrap method. In *2001 IEEE Nuclear Science Symposium Conference Record (Cat. No. 01CH37310)*. Vol. 4 IEEE pp. 2075–2079.

Davis, Kenneth R, JUAN M Taveras, GLENN H Roberson and ROBERT H Ackerman. 1976. "Some limitations of computed tomography in the diagnosis of neurological diseases." *American journal of Roentgenology* 127(1):111–123.

Dempster, Arthur P, Nan M Laird and Donald B Rubin. 1977. "Maximum likelihood from incomplete data via the EM algorithm." *Journal of the Royal Statistical Society: Series B (Methodological)* 39(1):1–22.

Deo, Anand K, Soo Borson, Jeanne M Link, Karen Domino, Janet F Eary, Ban Ke, Todd L Richards, David A Mankoff, Satoshi Minoshima, Finbarr O'Sullivan et al. 2014. "Activity of P-glycoprotein, a β-amyloid transporter at the blood–brain barrier, is compromised in patients with mild Alzheimer disease." *Journal of Nuclear Medicine* 55(7):1106–1111.

Dias, André H, Anne M Smith, Vijay Shah, David Pigg, Lars C Gormsen and Ole L Munk. 2022. "Clinical validation of a population-based input function for 20-min dynamic whole-body 18F-FDG multiparametric PET imaging." *EJNMMI physics* 9(1):1–18.

Dilsizian, V, SL Bacharach, RS Beanlands, SR Bergmann, D Delbeke, RJ Gropler, J Knuuti, HR Schelbert and M Travin. 2013. "PET myocardial perfusion and metabolism clinical imaging. 2008.".

Dunnwald, Lisa K, Julie R Gralow, Georgiana K Ellis, Robert B Livingston, Hannah M Linden, Jennifer M Specht, Robert K Doot, Thomas J Lawton, William E Barlow, Brenda F Kurland et al. 2008. "Tumor metabolism and blood flow changes by positron emission tomography: relation to survival in patients treated with neoadjuvant chemotherapy for locally advanced breast cancer." *Journal of Clinical Oncology* 26(27):4449.

Dunnwald, Lisa K, Robert K Doot, Jennifer M Specht, Julie R Gralow, Georgiana K Ellis, Robert B Livingston, Hannah M Linden, Vijayakrishna K Gadi, Brenda F Kurland, Erin K Schubert et al. 2011. "PET tumor metabolism in locally advanced breast cancer patients undergoing neoadjuvant chemotherapy: value of static versus kinetic measures of fluorodeoxyglucose uptake." *Clinical Cancer Research* 17(8):2400–2409.

Dutta, Joyita, Richard M Leahy and Quanzheng Li. 2013. "Non-local means denoising of dynamic PET images." *PloS one* 8(12):e81390.

Eary, Janet F, Jeanne M Link, Mark Muzi, Ernest U Conrad, David A Mankoff, Jedediah K White and Kenneth A Krohn. 2011. "Multiagent PET for risk characterization in sarcoma." *Journal of Nuclear Medicine* 52(4):541–546.

Efron, Bradley. 1979. "Bootstrap Methods: Another Look at the Jackknife." *Annals of Statistics* 7(1):1–26.

Efron, Bradley. 1981*a*. "Nonparametric estimates of standard error: the jackknife, the bootstrap and other methods." *Biometrika* 68(3):589–599.

Efron, Bradley. 1981*b*. "Nonparametric standard errors and confidence intervals." *canadian Journal of Statistics* 9(2):139–158.

Efron, Bradley. 1982. *The jackknife, the bootstrap and other resampling plans*. SIAM.

Efron, Bradley and Robert J Tibshirani. 1994. *An introduction to the bootstrap*. CRC press.

Efron, Bradley and Robert Tibshirani. 1986. "Bootstrap methods for standard errors, confidence intervals, and other measures of statistical accuracy." *Statistical science* pp. 54–75.

Ehrhardt, Matthias J, Kris Thielemans, Luis Pizarro, David Atkinson, Sébastien Ourselin, Brian F Hutton and Simon R Arridge. 2014. "Joint reconstruction of PET-MRI by exploiting structural similarity." *Inverse Problems* 31(1):015001.

El Fakhri, Georges, Cathryn M Trott, Arkadiusz Sitek, Ali Bonab and Nathaniel M Alpert. 2013. "Dual-tracer PET using generalized factor analysis of dynamic sequences." *Molecular Imaging and Biology* 15(6):666–674.

Erlandsson, Kjell, Irene Buvat, P Hendrik Pretorius, Benjamin A Thomas and Brian F Hutton. 2012. "A review of partial volume correction techniques for emission tomography and their applications in neurology, cardiology and oncology." *Physics in Medicine & Biology* 57(21):R119.

Eyal, Sara, Francisco S Chung, Mark Muzi, Jeanne M Link, David A Mankoff, Amal Kaddoumi, Finbarr O'Sullivan, Mary F Hebert and Jashvant D Unadkat. 2009. "Simultaneous PET imaging of P-glycoprotein inhibition in multiple tissues in the pregnant nonhuman primate." *Journal of Nuclear Medicine* 50(5):798–806.

Fabjan, Gregor. 2022. "Stationary Bootstrap." https://github.com/qnity/stationary_bootstrap_matlab.

Fahey, Frederic H. 2002. "Data acquisition in PET imaging." *Journal of nuclear medicine technology* 30(2):39–49.

Feng, Dagan, Sung-Cheng Huang and Xinmin Wang. 1993. "Models for computer simulation studies of input functions for tracer kinetic modeling with positron emission tomography." *International journal of bio-medical computing* 32(2):95–110.

Feng, David Dagan, Kewei Chen and Lingfeng Wen. 2020. "Noninvasive input function acquisition and simultaneous estimations with physiological parameters for PET quantification: a brief review." *IEEE Transactions on Radiation and Plasma Medical Sciences* 4(6):676–683.

Feng, Tao, Yizhang Zhao, Hongcheng Shi, Hongdi Li, Xuezhu Zhang, Guobao Wang, Patricia M Price, Ramsey D Badawi, Simon R Cherry and Terry Jones. 2021. "Total-body quantitative parametric imaging of early kinetics of 18F-FDG." *Journal of Nuclear Medicine* 62(5):738–744.

Feng, Tao, Yizhang Zhao, Hongcheng Shi, Hongdi Li, Xuezhu Zhang, Guobao Wang, Ramsey D Badawi, Patricia M Price, Terry Jones and Simon R Cherry. 2019. The Effects of Delay on the Input Function for Early Dynamics in

Total Body Parametric Imaging. In *2019 IEEE Nuclear Science Symposium and Medical Imaging Conference (NSS/MIC)*. IEEE pp. 1–6.

Fontaine, Kathryn, Ping Luo and Richard Carson. 2022. Accelerating PET Image Reconstruction with CUDA. In *Practice and Experience in Advanced Research Computing*. pp. 1–2.

Fouladzadeh, Anahita, Mohsen Dorraki, Kay Khine Myo Min, Michaelia P Cockshell, Emma J Thompson, Johan W Verjans, Andrew Allison, Claudine S Bonder and Derek Abbott. 2021. "The development of tumour vascular networks." *Communications biology* 4(1):1–10.

Fowler, Amy M, Amy S Clark, John A Katzenellenbogen, Hannah M Linden and Farrokh Dehdashti. 2016. "Imaging diagnostic and therapeutic targets: steroid receptors in breast cancer." *Journal of Nuclear Medicine* 57(Supplement 1):75S–80S.

Fred, Herbert L. 2004. "Drawbacks and limitations of computed tomography: views from a medical educator." *Texas Heart Institute Journal* 31(4):345.

Gordon, Yaron, Sasan Partovi, Matthias Müller-Eschner, Erick Amarteifio, Tobias Bäuerle, Marc-André Weber, Hans-Ulrich Kauczor and Fabian Rengier. 2014. "Dynamic contrast-enhanced magnetic resonance imaging: fundamentals and application to the evaluation of the peripheral perfusion." *Cardiovascular diagnosis and therapy* 4(2):147.

Graham, Michael M and Barbara L Lewellen. 1993. "High-speed automated discrete blood sampling for positron emission tomography." *Journal of Nuclear Medicine* 34(8):1357–1360.

Gu, Fengyun and Finbarr O'Sullivan. 2021. "A Simple Adaptive Bandwidth Scheme that Improves Image Quality and Kinetic Quantitation in Dynamic PET Scans." *Journal of Nuclear Medicine* 62(Supplement 1):1445–1445.

Gu, Fengyun, Finbarr O'Sullivan, Mark Muzi and David A Mankoff. 2019. A Simple Evaluation of the Benefit of Combined Kinetic Analysis of Multiple Injection Dynamic PET Scans. In *2019 IEEE Nuclear Science Symposium and Medical Imaging Conference (NSS/MIC)*. IEEE pp. 1–3.

Gu, Fengyun, Finbarr O'Sullivan, Mark Muzi and David A Mankoff. 2021. "Quantitation of multiple injection dynamic PET scans: an investigation of the benefits of pooling data from separate scans when mapping kinetics." *Physics in Medicine & Biology* 66(13):135010.

Gu, Fengyun, Qi Wu and Finbarr O'Sullivan. 2021. Image-Domain Bootstrapping of PET Time-Course Data for Assessment of Uncertainty in Complex Regional Summaries of Mapped Kinetics. In *2021 IEEE Nuclear Science Symposium and Medical Imaging Conference (NSS/MIC)*. IEEE pp. 1–3.

Gu, Fengyun, Qi Wu, Finbarr O'Sullivan, Jian Huang, Mark Muzi and David A Mankoff. 2019. An illustration of the use of model-based bootstrapping for evaluation of uncertainty in kinetic information derived from dynamic pet. In *2019 IEEE Nuclear Science Symposium and Medical Imaging Conference (NSS/MIC)*. IEEE pp. 1–3.

Gu, Fengyun, Qi Wu, Jianmao Wu, Debin Hu, Tianyi Xu, Shuangliang Cao, Yun Zhou and Hongcheng Shi. 2022. "Feasibility of standard and generalized Patlak Models for dynamic imaging of multiple organs using the uEXPLORER PET scanner." *Journal of Nuclear Medicine* 63(Supplement 2):3185–3185.

Gunn, Roger N, Steve R Gunn and Vincent J Cunningham. 2001. "Positron emission tomography compartmental models." *Journal of Cerebral Blood Flow & Metabolism* 21(6):635–652.

Ha, Seunggyun. 2019. "Perspectives in radiomics for personalized medicine and theranostics." *Nuclear Medicine and Molecular Imaging* 53(3):164–166.

Haidekker, Mark A. 2013. "Medical imaging technology.".

Hamilton, WF, John Walker Moore, JM Kinsman and RG Spurling. 1932. "Studies on the circulation: IV. Further analysis of the injection method, and of changes in hemodynamics under physiological and pathological conditions." *American Journal of Physiology-Legacy Content* 99(3):534–551.

Hawe, David. 2016. Statistical considerations in the kinetic analysis of PET-FDG brain tumour studies PhD thesis University College Cork.

Hawe, David, Francisco R Hernández Fernández, Liam O'Suilleabháin, Jian Huang, Eric Wolsztynski and Finbarr O'Sullivan. 2012. "Kinetic analysis of dynamic positron emission tomography data using open-source image processing and statistical inference tools." *Wiley Interdisciplinary Reviews: Computational Statistics* 4(3):316–322.

Haynor, DAVID R and STEVEN D Woods. 1989. "Resampling estimates of precision in emission tomography." *IEEE Transactions on Medical Imaging* 8(4):337–343.

Herscovitch, P, Joanne Markham and ME Raichle. 1983. "Brain blood flow measured with intravenous H215O. I. Theory and error analysis." *Journal of Nuclear Medicine* 24(9):782–789.

Hickeson, Marc, Mijin Yun, Alexander Matthies, Hongming Zhuang, Lars-Eric Adam, Lester Lacorte and Abass Alavi. 2002. "Use of a corrected standardized uptake value based on the lesion size on CT permits accurate characterization of lung nodules on FDG-PET." *European journal of nuclear medicine and molecular imaging* 29(12):1639–1647.

Hoffman, Edward J, Michael E Phelps, Nizar A Mullani, Carol S Higgins and Michel M Ter-Pogossian. 1976. "Design and performance characteristics of a whole-body positron transaxial tomograph." *Journal of Nuclear Medicine* 17(6):493–502.

Hoh, Carl K. 2007. "Clinical use of FDG PET." *Nuclear medicine and biology* 34(7):737–742.

Horowitz, Joel L. 2019. "Bootstrap methods in econometrics." *Annual Review of Economics* 11:193–224.

Hounsfield, Godfrey N. 1973. "Computerized transverse axial scanning (tomography): Part 1. Description of system." *The British journal of radiology* 46(552):1016–1022.

Hsu, CY, A Alaraj and AA Linninger. 2016. "Cere-bral blood flow assessment by digital subtraction angiography." *Radiol Open J* 1(1):21–30.

Huang, Jian and Finbarr O'Sullivan. 2014. "An analysis of whole body tracer kinetics in dynamic PET studies with application to image-based blood input function extraction." *IEEE transactions on medical imaging* 33(5):1093–1108.

Huang, Jian, Tian Mou, Kevin O'Regan and Finbarr O'Sullivan. 2020. "Spatial Auto-regressive Analysis of Correlation in 3-D PET with Application to Model-Based Simulation of Data." *IEEE Transactions on Medical Imaging* 39(4):964–974.

Huang, S. C., R. E. Carson, E. J. Hoffman, D. E. Kuhl and M. E. Phelps. 1982. "An investigation of a double-tracer technique for positron computerized tomography." *The Journal of Nuclear Medicine* 23(9):816–822.

Huang, Sheng-Cheng, Liang-Chih Wu, Wen-Chen Lin, Kang-Ping Lin and Ren-Shyan Liu. 2018. "Adaptive weighted nonlinear least squares method for

fluorodeoxyglucose positron emission tomography quantification." *Journal of Medical and Biological Engineering* 38(1):63–75.

Huang, Sung-Cheng, Michael E Phelps, Edward J Hoffman, Klear Sideris, Carl J Selin and David E Kuhl. 1980. "Noninvasive determination of local cerebral metabolic rate of glucose in man." *American Journal of Physiology-Endocrinology And Metabolism* 238(1):E69–E82.

Huang, Zhenxing, Yaping Wu, Fangfang Fu, Nan Meng, Fengyun Gu, Qi Wu, Yun Zhou, Yongfeng Yang, Xin Liu, Hairong Zheng et al. 2022. "Parametric image generation with the uEXPLORER total-body PET/CT system through deep learning." *European Journal of Nuclear Medicine and Molecular Imaging* pp. 1–11.

Hudson, H Malcolm and Richard S Larkin. 1994. "Accelerated image reconstruction using ordered subsets of projection data." *IEEE transactions on medical imaging* 13(4):601–609.

Hudson, Malcolm. 1995. Statistical models & algorithms for tomography. In *Asian Conference on Computer Vision*. Springer pp. 287–295.

Huesman, RH. 1977. "The effects of a finite number of projection angles and finite lateral sampling of projections on the propagation of statistical errors in transverse section reconstruction." *Physics in Medicine and Biology* 22(3):511–521.

Huesman, Ronald H. 1984. "A new fast algorithm for the evaluation of regions of interest and statistical uncertainty in computed tomography." *Physics in Medicine & Biology* 29(5):543.

Huettel, Scott A, Allen W Song, Gregory McCarthy et al. 2004. *Functional magnetic resonance imaging*. Vol. 1 Sinauer Associates Sunderland.

Ibaraki, Masanobu, Keisuke Matsubara, Kazuhiro Nakamura, Hiroshi Yamaguchi and Toshibumi Kinoshita. 2014. "Bootstrap methods for estimating PET image noise: experimental validation and an application to evaluation of image reconstruction algorithms." *Annals of nuclear medicine* 28(2):172–182.

Ido, T, C-N Wan, Va Casella, JS Fowler, AP Wolf, M Reivich and DE Kuhl. 1978. "Labeled 2-deoxy-D-glucose analogs. 18F-labeled 2-deoxy-2-fluoro-D-glucose, 2-deoxy-2-fluoro-D-mannose and 14C-2-deoxy-2-fluoro-D-glucose." *Journal of Labelled Compounds and Radiopharmaceuticals* 14(2):175–183.

Iriarte, Ana, Roberto Marabini, Samuel Matej, Carlos Oscar Sánchez Sorzano and Robert M Lewitt. 2016. "System models for PET statistical iterative reconstruction: A review." *Computerized Medical Imaging and Graphics* 48:30–48.

Jahng, Geon-Ho, Ka-Loh Li, Leif Ostergaard and Fernando Calamante. 2014. "Perfusion magnetic resonance imaging: a comprehensive update on principles and techniques." *Korean journal of radiology* 15(5):554–577.

Jan, Sébastien, G Santin, D Strul, Steven Staelens, K Assié, D Autret, S Avner, R Barbier, M Bardies, PM Bloomfield et al. 2004. "GATE: a simulation toolkit for PET and SPECT." *Physics in Medicine & Biology* 49(19):4543.

Jiang, Wei, Yamn Chalich and M Jamal Deen. 2019. "Sensors for positron emission tomography applications." *Sensors* 19(22):5019.

Joe, Harry. 2014. *Dependence modeling with copulas*. CRC press.

Jones, Terry and David W Townsend. 2017. "History and future technical innovation in positron emission tomography." *Journal of Medical Imaging* 4(1):011013.

Kadrmas, Dan J and John M Hoffman. 2013. "Methodology for quantitative rapid multi-tracer PET tumor characterizations." *Theranostics* 3(10):757.

Kadrmas, Dan J, Thomas C Rust and John M Hoffman. 2013. "Single-scan dual-tracer FLT+ FDG PET tumor characterization." *Physics in Medicine and Biology* 58(3):429.

Kak, Avinash C, Malcolm Slaney and Ge Wang. 2002. "Principles of computerized tomographic imaging.".

Kalra, Mannudeep K, Aaron D Sodickson and William W Mayo-Smith. 2015. "CT radiation: key concepts for gentle and wise use." *Radiographics* 35(6):1706–1721.

Karakatsanis, Nicolas A, Martin A Lodge, Abdel K Tahari, Y Zhou, Richard L Wahl and Arman Rahmim. 2013. "Dynamic whole-body PET parametric imaging: I. Concept, acquisition protocol optimization and clinical application." *Physics in Medicine & Biology* 58(20):7391.

Karakatsanis, Nicolas A, Yun Zhou, Martin A Lodge, Michael E Casey, Richard L Wahl, Habib Zaidi and Arman Rahmim. 2015. "Generalized whole-body Pat-

lak parametric imaging for enhanced quantification in clinical PET." *Physics in Medicine & Biology* 60(22):8643.

Karp, Joel S, Varsha Viswanath, Michael J Geagan, Gerd Muehllehner, Austin R Pantel, Michael J Parma, Amy E Perkins, Jeffrey P Schmall, Matthew E Werner and Margaret E Daube-Witherspoon. 2020. "PennPET Explorer: design and preliminary performance of a whole-body imager." *Journal of Nuclear Medicine* 61(1):136–143.

Katal, Sanaz, Liesl S Eibschutz, Babak Saboury, Ali Gholamrezanezhad and Abass Alavi. 2022. "Advantages and applications of total-body PET scanning." *Diagnostics* 12(2):426.

Keramida, Georgia, Jonathan Potts, Jan Bush, Sumita Verma, Sabina Dizdarevic and Adrien M Peters. 2014. "Accumulation of 18F-FDG in the liver in hepatic steatosis." *American Journal of Roentgenology* 203(3):643–648.

Kety, Seymour S and Carl F Schmidt. 1948. "The nitrous oxide method for the quantitative determination of cerebral blood flow in man: theory, procedure and normal values." *The Journal of Clinical Investigation* 27(4):476–483.

Kim, Chun K, Naresh C Gupta, B Chandramouli and Abass Alavi. 1994. "Standardized uptake values of FDG: body surface area correction is preferable to body weight correction." *Journal of Nuclear Medicine* 35(1):164–167.

Kobayashi, Katsuhiro, Peeyush Bhargava, Shanker Raja, Farbod Nasseri, Hassan A Al-Balas, Darryl D Smith, Sharad P George and Meena S Vij. 2012. "Image-guided biopsy: what the interventional radiologist needs to know about PET/CT." *Radiographics* 32(5):1483–1501.

Koeppe, RA, EP Ficaro, DM Raffel, S Minoshima and MR Kilbourn. 1998. Temporally overlapping dual-tracer PET studies. In *Quantitative Functional Brain Imaging with Positron Emission Tomography*. Elsevier pp. 359–366.

Koeppe, Robert A, David M Raffel, Scott E Snyder, Edward P Ficaro, Michael R Kilbourn and David E Kuhl. 2001. "Dual-[11C] tracer single-acquisition positron emission tomography studies." *Journal of Cerebral Blood Flow and Metabolism* 21(12):1480–1492.

Konstas, AA, GV Goldmakher, T-Y Lee and MH Lev. 2009. "Theoretic basis and technical implementations of CT perfusion in acute ischemic stroke, part 1: theoretic basis." *American Journal of Neuroradiology* 30(4):662–668.

Kostakoglu, Lale, Fenghai Duan, Michael O Idowu, Paul R Jolles, Harry D Bear, Mark Muzi, Jean Cormack, John P Muzi, Daniel A Pryma, Jennifer M Specht et al. 2015. "A phase II study of 3-deoxy-3-18F-fluorothymidine PET in the assessment of early response of breast cancer to neoadjuvant chemotherapy: results from ACRIN 6688." *Journal of Nuclear Medicine* 56(11):1681–1689.

Kreiss, Jens-Peter and Soumendra Nath Lahiri. 2012. Bootstrap methods for time series. In *Handbook of statistics*. Vol. 30 Elsevier pp. 3–26.

Krohn, Kenneth A, Finbarr O'Sullivan, John Crowley, Janet F Eary, Hannah M Linden, Jeanne M Link, David A Mankoff, Mark Muzi, Joseph G Rajendran, Alexander M Spence et al. 2007. "Challenges in clinical studies with multiple imaging probes." *Nuclear medicine and biology* 34(7):879–885.

Kubota, Kazuo, Taiju Matsuzawa, Masatoshi Ito, Kengo Ito, Takehiko Fujiwara, Yoshinao Abe, Seiro Yoshioka, Hiroshi Fukuda, Jun Hatazawa, Ren Iwata et al. 1985. "Lung tumor imaging by positron emission tomography using C-11 L-methionine." *Journal of nuclear medicine* 26(1):37–42.

Kucharczak, Florentin, Kevin Loquin, Irène Buvat, Olivier Strauss and Denis Mariano-Goulart. 2018. "Interval-based reconstruction for uncertainty quantification in PET." *Physics in Medicine & Biology* 63(3):035014.

Kuhl, David E and Roy Q Edwards. 1963. "Image separation radioisotope scanning." *Radiology* 80(4):653–662.

Kutner, MH., CJ. Nachtsheim, J. Neter and W. Li. 2013. *Applied linear statistical models*. McGraw-Hill.

Lahiri, SK and SN Lahiri. 2003. *Resampling methods for dependent data*. Springer Science & Business Media.

Lammertsma, Adriaan A. 2019. "Quantification of PET Studies.".

Lan, Tao, Mark Muzi and Finbarr O'Sullivan. 2019. Semi-Parametric Residue Analysis of Dual-Injection PET Studies Illustrated by Brain Tumor Imaging with [11C]- labeled CO2 and Acetate [Poster Presentation]. IEEE Nuclear Science Symposium and Medical Imaging Conference.

Lange, Kenneth, Richard Carson et al. 1984. "EM reconstruction algorithms for emission and transmission tomography." *J. Comput. Assist. Tomogr* 8(2):306–316.

Lartizien, Carole, J-B Aubin and Irène Buvat. 2010. "Comparison of bootstrap

resampling methods for 3-D PET imaging." *IEEE transactions on medical imaging* 29(7):1442–1454.

Lau, Joseph, Etienne Rousseau, Daniel Kwon, Kuo-Shyan Lin, François Bénard and Xiaoyuan Chen. 2020. "Insight into the Development of PET Radiopharmaceuticals for Oncology." *Cancers* 12(5):1312.

Lauterbur, Paul C. 1973. "Image formation by induced local interactions: examples employing nuclear magnetic resonance." *nature* 242(5394):190–191.

Laws, Edward R, Ian F Parney, Wei Huang, Fred Anderson, Angel M Morris, Anthony Asher, Kevin O Lillehei, Mark Bernstein, Henry Brem, Andrew Sloan et al. 2003. "Survival following surgery and prognostic factors for recently diagnosed malignant glioma: data from the Glioma Outcomes Project." *Journal of neurosurgery* 99(3):467–473.

Leahy, Richard M and Jinyi Qi. 2000. "Statistical approaches in quantitative positron emission tomography." *Statistics and Computing* 10(2):147–165.

Lecoq, P and S Gundacker. 2021. "SiPM applications in positron emission tomography: toward ultimate PET time-of-flight resolution." *The European Physical Journal Plus* 136(3):292.

Lennon, H. and J. Yuan. 2019. "Estimation of a digitised Gaussian ARMA model by Monte Carlo Expectation Maximisation." *Computational Statistics and Data Analysis* 133:277–284.

Li, Elizabeth, Benjamin A Spencer, Jeffrey P Schmall, Yasser Abdelhafez, Ramsey D Badawi, Guobao Wang and Simon R Cherry. 2021. "Efficient delay correction for total-body PET kinetic modeling using pulse timing methods." *Journal of Nuclear Medicine* .

Li, Yusheng. 2011. "Noise propagation for iterative penalized-likelihood image reconstruction based on Fisher information." *Physics in Medicine & Biology* 56(4):1083.

Li, Zheng, Tada Yipintsoi and James B Bassingthwaighte. 1997. "Nonlinear model for capillary-tissue oxygen transport and metabolism." *Annals of biomedical engineering* 25(4):604–619.

Liang, J., F. Gu, G. Newman and F. O'Sullivan. 2019. Towards Quantitative Analysis of Digital Subtraction Angiography Imaging Data. In *39th Conference on Applied Statistics in Ireland*.

Liu, Guobing, Hongrong Xu, Pengcheng Hu, Hui Tan, Yiqiu Zhang, Haojun Yu, Xuening Li and Hongcheng Shi. 2021. "Kinetic metrics of 18F-FDG in normal human organs identified by systematic dynamic total-body positron emission tomography." *European Journal of Nuclear Medicine and Molecular Imaging* 48(8):2363–2372.

Logan, Jean, Joanna S Fowler, Nora D Volkow, Alfred P Wolf, Stephen L Dewey, David J Schlyer, Robert R MacGregor, Robert Hitzemann, Bernard Bendriem, S John Gatley et al. 1990. "Graphical analysis of reversible radioligand binding from time—activity measurements applied to [N-11C-methyl]-(-)-cocaine PET studies in human subjects." *Journal of Cerebral Blood Flow & Metabolism* 10(5):740–747.

Maitra, Ranjan and Finbarr O'Sullivan. 1997. Variability Assessment in PET and Related Generalized Deconvolution Models. In *Journal of the American Statistical Association*. Citeseer.

Maitra, Ranjan and Finbarr O'Sullivan. 1998. "Variability Assessment in Positron Emission Tomography and Related Generalized Deconvolution Models." *Journal of the American Statistical Association* 93(444):1340–1355.
URL: *http://www.jstor.org/stable/2670050*

Makvandi, Mehran, Austin Pantel, Lauren Schwartz, Erin Schubert, Kuiying Xu, Chia-Ju Hsieh, Catherine Hou, Hyoung Kim, Chi-Chang Weng, Harrison Winters et al. 2018. "A PET imaging agent for evaluating PARP-1 expression in ovarian cancer." *The Journal of clinical investigation* 128(5):2116–2126.

Mankoff, David A, Austin R Pantel, Varsha Viswanath and Joel S Karp. 2019. "Advances in PET diagnostics for guiding targeted cancer therapy and studying in vivo cancer biology." *Current Pathobiology Reports* 7(3):97–108.

Mankoff, David A, Lisa K Dunnwald, Julie R Gralow, Georgiana K Ellis, Aaron Charlop, Thomas J Lawton, Erin K Schubert, Jeffrey Tseng and Robert B Livingston. 2002. "Blood flow and metabolism in locally advanced breast cancer: relationship to response to therapy." *Journal of Nuclear Medicine* 43(4):500–509.

Mankoff, David A, Lisa K Dunnwald, Julie R Gralow, Georgiana K Ellis, Erin K Schubert, Jeffrey Tseng, Thomas J Lawton, Hannah M Linden and Robert B Livingston. 2003. "Changes in blood flow and metabolism in locally advanced

breast cancer treated with neoadjuvant chemotherapy." *Journal of Nuclear Medicine* 44(11):1806–1814.

Mayer, Thomas E, Gerhard F Hamann, Jan Baranczyk, Bernhard Rosengarten, Erich Klotz, Martin Wiesmann, Ulrich Missler, Gernot Schulte-Altedorneburg and Hartmuth J Brueckmann. 2000. "Dynamic CT perfusion imaging of acute stroke." *American journal of neuroradiology* 21(8):1441–1449.

Mehrotra, Pallavi. 2016. "Applied surgical radiology." *Oxford Textbook of Fundamentals of Surgery* p. 195.

Meier, Paul and Kenneth L Zierler. 1954. "On the theory of the indicator-dilution method for measurement of blood flow and volume." *Journal of applied physiology* 6(12):731–744.

Meikle, Steven R, Vesna Sossi, Emilie Roncali, Simon R Cherry, Richard Banati, David Mankoff, Terry Jones, Michelle James, Julie Sutcliffe, Jinsong Ouyang et al. 2021. "Quantitative PET in the 2020s: a roadmap." *Physics in Medicine & Biology* 66(6):06RM01.

Melcher, CL and JS Schweitzer. 1992. "Cerium-doped lutetium oxyorthosilicate: a fast, efficient new scintillator." *IEEE Transactions on Nuclear Science* 39(4):502–505.

Miller, Philip W, Nicholas J Long, Ramon Vilar and Antony D Gee. 2008. "Synthesis of 11C, 18F, 15O, and 13N radiolabels for positron emission tomography." *Angewandte Chemie International Edition* 47(47):8998–9033.

Mintun, Mark A, Marcus E Raichle, Michael R Kilbourn, G Frederick Wooten and Michael J Welch. 1984. "A quantitative model for the in vivo assessment of drug binding sites with positron emission tomography." *Annals of Neurology: Official Journal of the American Neurological Association and the Child Neurology Society* 15(3):217–227.

Morgan, Thomas L. 2012. "Quality assurance for PET and PET/CT systems.".

Mou, Tian. 2018. Statistical analysis of positron emission tomography data PhD thesis University College Cork.

Mou, Tian, Jian Huang and Finbarr O'Sullivan. 2017. "The Gamma characteristic of reconstructed PET images: Implications for ROI analysis." *IEEE transactions on medical imaging* 37(5):1092–1102.

Muzi, Mark, Finbarr O'Sullivan, David A Mankoff, Robert K Doot, Larry A Pierce,

Brenda F Kurland, Hannah M Linden and Paul E Kinahan. 2012. "Quantitative assessment of dynamic PET imaging data in cancer imaging." *Magnetic resonance imaging* 30(9):1203–1215.

Nadig, Vanessa, Ken Herrmann, Felix M Mottaghy and Volkmar Schulz. 2021. "Hybrid total-body pet scanners—Current status and future perspectives." *European journal of nuclear medicine and molecular imaging* pp. 1–15.

Natterer, Frank. 2001. *The Mathematics of Computerized Tomography*. SIAM.

Neumayer, Bernhard, Matthias Schloegl, Christian Payer, Thomas Widek, Sebastian Tschauner, Thomas Ehammer, Rudolf Stollberger and Martin Urschler. 2018. "Reducing acquisition time for MRI-based forensic age estimation." *Scientific reports* 8(1):1–9.

Nutt, Ronald. 2002. "The history of positron emission tomography." *Molecular Imaging & Biology* 4(1):11–26.

Ogawa, Seiji, Tso-Ming Lee, Asha S Nayak and Paul Glynn. 1990. "Oxygenation-sensitive contrast in magnetic resonance image of rodent brain at high magnetic fields." *Magnetic resonance in medicine* 14(1):68–78.

Oldendorf, William. 1988. Advantages and Disadvantages of MRI. In *Basics of Magnetic Resonance Imaging*. Springer pp. 125–138.

Østergaard, Leif, Robert M Weisskoff, David A Chesler, Carsten Gyldensted and Bruce R Rosen. 1996. "High resolution measurement of cerebral blood flow using intravascular tracer bolus passages. Part I: Mathematical approach and statistical analysis." *Magnetic resonance in medicine* 36(5):715–725.

O'Sullivan, Finbarr. 1993. "Imaging radiotracer model parameters in PET: a mixture analysis approach." *IEEE Transactions on Medical Imaging* 12(3):399–412.

O'Sullivan, Finbarr. 1995. "A study of least squares and maximum likelihood for image reconstruction in positron emission tomography." *The Annals of Statistics* 23(4):1267–1300.

O'Sullivan, Finbarr, Fengyun Gu, Qi Wu and Liam D O'Suilleabhain. 2021. "A Generalized Linear Modeling Approach to Bootstrapping Multi-frame PET Image Data." *Medical Image Analysis* p. 102132.

O'Sullivan, Finbarr, Janet N O'Sullivan, Jian Huang, Robert Doot, Mark Muzi, Erin Schubert, Lanell Peterson, Lisa K Dunnwald and David M Mankoff. 2017.

"Assessment of a statistical AIF extraction method for dynamic PET studies with 15 O water and 18 F fluorodeoxyglucose in locally advanced breast cancer patients." *Journal of Medical Imaging* 5(1):011010.

O'Sullivan, Finbarr and Kingshuk Roy Choudhury. 2001. "An analysis of the role of positivity and mixture model constraints in Poisson deconvolution problems." *Journal of Computational and Graphical Statistics* 10(4):673–696.

O'Sullivan, Finbarr and Liam O'Súilleabháin. 2013. A multi-grid approach to ML reconstruction in PET: A fast alternative to EM-based techniques. In *2013 IEEE Nuclear Science Symposium and Medical Imaging Conference (2013 NSS/MIC)*. IEEE pp. 1–5.

O'Sullivan, Finbarr, Mark Muzi, Alexander M Spence, David M Mankoff, Janet N O'sullivan, Niall Fitzgerald, George C Newman and Kenneth A Krohn. 2009. "Nonparametric residue analysis of dynamic PET data with application to cerebral FDG studies in normals." *Journal of the American Statistical Association* 104(486):556–571.

O'Sullivan, Finbarr, Mark Muzi, David A Mankoff, Janet F Eary, Alexander M Spence and Kenneth A Krohn. 2014. "Voxel-level mapping of tracer kinetics in PET studies: a statistical approach emphasizing tissue life tables." *The annals of applied statistics* 8(2):1065.

O'Sullivan, Finbarr, Qi Wu, Fengyun Gu, Kuangyu Shi, Liam O'Suilleabhain, Song Xue and Axel Rominger. 2022. "Mapping FDG Tracer Kinetics and their Uncertainties via the Bootstrap using data from a Long-Axial FOV PET/CT Scanner." *Journal of Nuclear Medicine* 63(Supplement 2):3220–3220.

O'Sullivan, Finbarr, Yudianto Pawitan and David Haynor. 1993. "Reducing negativity artifacts in emission tomography: post-processing filtered backprojection solutions." *IEEE transactions on medical imaging* 12(4):653–663.

Ou, Xiangyu, Xue Chen, Xianning Xu, Lili Xie, Xiaofeng Chen, Zhongzhu Hong, Hua Bai, Xiaowang Liu, Qiushui Chen, Lin Li et al. 2021. "Recent Development in X-Ray Imaging Technology: Future and Challenges." *Research* 2021.

Pajevic, Sinisa, Margaret E Daube-Witherspoon, Stephen L Bacharach and Richard E Carson. 1998. "Noise characteristics of 3-D and 2-D PET images." *IEEE transactions on medical imaging* 17(1):9–23.

Pantel, Austin R, David A Mankoff and Joel S Karp. 2022. "Total-Body PET: Will It Change Science and Practice?" *Journal of Nuclear Medicine* 63(5):646–648.

Pantel, Austin R, Varsha Viswanath, Margaret E Daube-Witherspoon, Jacob G Dubroff, Gerd Muehllehner, Michael J Parma, Daniel A Pryma, Erin K Schubert, David A Mankoff and Joel S Karp. 2020. "PennPET Explorer: human imaging on a whole-body imager." *Journal of Nuclear Medicine* 61(1):144–151.

Pantel, Austin R, Varsha Viswanath, Mark Muzi, Robert K Doot and David A Mankoff. 2022. "Principles of tracer kinetic analysis in oncology, part I: principles and overview of methodology." *Journal of Nuclear Medicine* 63(3):342–352.

Paquette, Michel, Serge Phoenix, Christine Lawson, Brigitte Guérin, Roger Lecomte, Lee-Hwa Tai, Éric E Turcotte and Jeffrey V Leyton. 2020. "A preclinical PET dual-tracer imaging protocol for ER and HER2 phenotyping in breast cancer xenografts." *EJNMMI research* 10(1):1–13.

Parsey, Ramin V, Mark Slifstein, Dah-Ren Hwang, Anissa Abi-Dargham, Norman Simpson, Osama Mawlawi, Ning-Ning Guo, Ronald Van Heertum, J John Mann and Marc Laruelle. 2000. "Validation and reproducibility of measurement of 5-HT1A receptor parameters with [carbonyl-11C] WAY-100635 in humans: comparison of arterial and reference tissue input functions." *Journal of Cerebral Blood Flow & Metabolism* 20(7):1111–1133.

Pascual, Lorenzo, Juan Romo and Esther Ruiz. 2004. "Bootstrap predictive inference for ARIMA processes." *Journal of Time Series Analysis* 25(4):449–465.

Patlak, Clifford S and Ronald G Blasberg. 1985. "Graphical evaluation of blood-to-brain transfer constants from multiple-time uptake data. Generalizations." *Journal of Cerebral Blood Flow & Metabolism* 5(4):584–590.

Patlak, Clifford S, Ronald G Blasberg and Joseph D Fenstermacher. 1983. "Graphical evaluation of blood-to-brain transfer constants from multiple-time uptake data." *Journal of Cerebral Blood Flow & Metabolism* 3(1):1–7.

Pawitan, Yudi and Finbarr O'Sullivan. 1993. "Data-dependent bandwidth selection for emission computed tomography reconstruction." *IEEE transactions on medical imaging* 12(2):167–172.

Pedersen, Finn, M Bergström, Ewert Bengtsson and B Långström. 1994. "Principal component analysis of dynamic positron emission tomography images." *European journal of nuclear medicine* 21(12):1285–1292.

Phelps, ME, SC Huang, EJ Hoffman, C Selin, L Sokoloff and DE Kuhl. 1979. "Tomographic measurement of local cerebral glucose metabolic rate in humans with (F-18) 2-fluoro-2-deoxy-D-glucose: validation of method." *Annals of Neurology: Official Journal of the American Neurological Association and the Child Neurology Society* 6(5):371–388.

Phelps, Michael E, Edward J Hoffman, Nizar A Mullani, Carol S Higgins and Michael M Ter Pogossian. 1976. Design considerations for a positron emission transaxial tomograph (PETT III). Technical report Univ. of Pennsylvania, Philadelphia.

Phelps, Michael E, Edward J Hoffman, Nizar A Mullani and Michel M Ter-Pogossian. 1975. "Application of annihilation coincidence detection to transaxial reconstruction tomography." *Journal of nuclear medicine* 16(3):210–224.

Politis, Dimitris N and Joseph P Romano. 1994. "The stationary bootstrap." *Journal of the American Statistical association* 89(428):1303–1313.

Prenosil, George A, Hasan Sari, Markus Fürstner, Ali Afshar-Oromieh, Kuangyu Shi, Axel Rominger and Michael Hentschel. 2022. "Performance Characteristics of the Biograph Vision Quadra PET/CT System with a Long Axial Field of View Using the NEMA NU 2-2018 Standard." *Journal of nuclear medicine* 63(3):476–484.

Przybylski, Adrian, Björn Thiel, Jan Keller-Findeisen, Bernd Stock and Mark Bates. 2017. "Gpufit: An open-source toolkit for GPU-accelerated curve fitting." *Scientific reports* 7(1):1–9.

Purcell, Edward M, Henry Cutler Torrey and Robert V Pound. 1946. "Resonance absorption by nuclear magnetic moments in a solid." *Physical review* 69(1-2):37.

Qi, Jinyi and Richard M Leahy. 2000. "Resolution and noise properties of MAP reconstruction for fully 3-D PET." *IEEE transactions on medical imaging* 19(5):493–506.

Rahmim, Arman, Martin A Lodge, Nicolas A Karakatsanis, Vladimir Y Panin, Yun Zhou, Alan McMillan, Steve Cho, Habib Zaidi, Michael E Casey and Richard L Wahl. 2019. "Dynamic whole-body PET imaging: principles, potentials and applications." *European journal of nuclear medicine and molecular imaging* 46(2):501–518.

Rao, Calyampudi Radhakrishna. 1973. *Linear statistical inference and its applications*. New York, NY, USA: John Wiley & Sons.

Razifar, Pasha. 2005. Novel approaches for application of principal component analysis on dynamic PET images for improvement of image quality and clinical diagnosis PhD thesis Acta Universitatis Upsaliensis.

Razifar, Pasha, Mark Lubberink, Harald Schneider, Bengt Långström, Ewert Bengtsson and Mats Bergström. 2005. "Non-isotropic noise correlation in PET data reconstructed by FBP but not by OSEM demonstrated using autocorrelation function." *BMC medical imaging* 5(1):1–18.

Reivich, Martin, D Kuhl, A Wolf, J Greenberg, Met al Phelps, T Ido, V Casella, J Fowler, E Hoffman, A Alavi et al. 1979. "The [18F] fluorodeoxyglucose method for the measurement of local cerebral glucose utilization in man." *Circulation research* 44(1):127–137.

Rich, Dayton A. 1997. "A brief history of positron emission tomography." *Journal of Nuclear Medicine Technology* 25(1):4–11.

Rizzo, Maria L. 2019. *Statistical computing with R*. Chapman and Hall/CRC.

Rockall, Andrea G, Norbert Avril, Raymond Lam, Robert Iannone, P David Mozley, Christine Parkinson, Donald Bergstrom, Evis Sala, Shah-Jalal Sarker, Iain A McNeish et al. 2014. "Repeatability of quantitative FDG-PET/CT and contrast-enhanced CT in recurrent ovarian carcinoma: test–retest measurements for tumor FDG uptake, diameter, and volume." *Clinical Cancer Research* 20(10):2751–2760.

Rockmore, Anthony Joseph and Albert Macovski. 1976. "A maximum likelihood approach to emission image reconstruction from projections." *IEEE transactions on nuclear science* 23(4):1428–1432.

Röntgen, WC. 1899. "Further Observations on the Properties of X Rays.".

Rowe, R Wanda and Shubo Dai. 1992. "A pseudo-Poisson noise model for simulation of positron emission tomographic projection data." *Medical physics* 19(4):1113–1119.

Rudd, James HF, Jagat Narula, H William Strauss, Renu Virmani, Josef Machac, Mike Klimas, Nobuhiro Tahara, Valentin Fuster, Elizabeth A Warburton, Zahi A Fayad et al. 2010. "Imaging atherosclerotic plaque inflammation

by fluorodeoxyglucose with positron emission tomography: ready for prime time?" *Journal of the American College of Cardiology* 55(23):2527–2535.

Rust, TC and DJ Kadrmas. 2005. "Rapid dual-tracer PTSM+ ATSM PET imaging of tumour blood flow and hypoxia: a simulation study." *Physics in Medicine and Biology* 51(1):61.

Saha, Gopal B. 2015. *Basics of PET imaging: Physics, Chemistry, and Regulations*. Springer.

Samei, Ehsan and Donald J Peck. 2019. *Hendee's physics of medical imaging*. John Wiley & Sons.

Sari, Hasan, Clemens Mingels, Ian Alberts, Jicun Hu, Dorothee Buesser, Vijay Shah, Robin Schepers, Patrik Caluori, Vladimir Panin, Maurizio Conti et al. 2022. "First results on kinetic modelling and parametric imaging of dynamic 18F-FDG datasets from a long axial FOV PET scanner in oncological patients." *European journal of nuclear medicine and molecular imaging* pp. 1–13.

Sarrut, David, Mateusz Bała, Manuel Bardiès, Julien Bert, Maxime Chauvin, Konstantinos Chatzipapas, Mathieu Dupont, Ane Etxebeste, Louise M Fanchon, Sébastien Jan et al. 2021. "Advanced Monte Carlo simulations of emission tomography imaging systems with GATE." *Physics in Medicine & Biology* 66(10):10TR03.

Scheuermann, Joshua, Adam Opanowski, Joseph Maffei, Deborah Harbison Thibeault, Joel Karp, Barry Siegel, Mark Rosen and Paul Kinahan. 2013. "Qualification of NCI-designated comprehensive cancer centers for quantitative PET/CT imaging in clinical trials." *Journal of Nuclear Medicine* 54(supplement 2):334–334.

Schmitz, Ruth E, Adam M Alessio, Paul E Kinahan, Neale S Mason and Eugene C Lin. 2005. "The physics of PET/Ct scanners." *Lin EG, Alavi A. PET and PET/CT: A clinical guide. Thieme: New York, NY* pp. 3–14.

Seber, G.A.F. 2009. *Multivariate Observations*. Wiley Series in Probability and Statistics Wiley.
URL: *https://books.google.co.jp/books?id=UWk6YmtkhLgC*

Seber, George A.F. 2015. *The Linear Model and Hypothesis: A General Unifying Theory*. Springer International Publishing.

Seeram, Euclid. 2015. *Computed Tomography-E-Book: Physical Principles, Clinical Applications, and Quality Control*. Elsevier Health Sciences.

Shepp, Lawrence A and Yehuda Vardi. 1982. "Maximum likelihood reconstruction for emission tomography." *IEEE transactions on medical imaging* 1(2):113–122.

Sitek, Arkadiusz and Anna M Celler. 2015. "Limitations of Poisson statistics in describing radioactive decay." *Physica Medica* 31(8):1105–1107.

Slart, Riemer HJA, Charalampos Tsoumpas, Andor WJM Glaudemans, Walter Noordzij, Antoon Willemsen, Ronald JH Borra, Rudi AJO Dierckx and Adriaan A Lammertsma. 2021. "Long axial field of view PET scanners: a road map to implementation and new possibilities." *European journal of nuclear medicine and molecular imaging* 48(13):4236–4245.

Smith, Steven W et al. 1997. "The scientist and engineer's guide to digital signal processing.".

Sokoloff, Louis, M Reivich, C Kennedy, MH Des Rosiers, CS Patlak, KD et al Pettigrew, Oi Sakurada and M Shinohara. 1977. "The [14C] deoxyglucose method for the measurement of local cerebral glucose utilization: theory, procedure, and normal values in the conscious and anesthetized albino rat 1." *Journal of neurochemistry* 28(5):897–916.

Spence, Alexander M, Mark Muzi, Michael M Graham, Finbarr O'Sullivan, Kenneth A Krohn, Jeanne M Link, Thomas K Lewellen, Barbara Lewellen, Scott D Freeman, Mitchel S Berger et al. 1998. "Glucose Metabolism in Human Malignant Gliomas Measured Quantitatively with PET, l-[C-ll] Glucose and FDG: Analysis of the FDG Lumped Constant." *Journal of Nuclear Medicine* 39(3):440–448.

Stewart, George Neil. 1897. "Researches on the circulation time and on the influences which affect it." *The Journal of physiology* 22(3):159.

Stewart, George Neil. 1921. "The pulmonary circulation time, the quantity of blood in the lungs and the output of the heart." *American Journal of Physiology-Legacy Content* 58(1):20–44.

Stiller, Wolfram. 2018. "Basics of iterative reconstruction methods in computed tomography: a vendor-independent overview." *European journal of radiology* 109:147–154.

Strother, CM, F Bender, Y Deuerling-Zheng, K Royalty, KA Pulfer, J Baumgart, M Zellerhoff, B Aagaard-Kienitz, DB Niemann and ML Lindstrom. 2010. "Parametric color coding of digital subtraction angiography." *American Journal of Neuroradiology* 31(5):919–924.

Surti, Suleman, Austin R Pantel and Joel S Karp. 2020. "Total Body PET: Why, How, What for?" *IEEE Transactions on Radiation and Plasma Medical Sciences* 4(3):283–292.

Sweet, WG. 1953. "Localization of brain tumors with positron emitters." *Nucleonics* 11:40–45.

Sweet, William H. 1951. "The uses of nuclear disintegration in the diagnosis and treatment of brain tumor." *New England Journal of Medicine* 245(23):875–878.

Takikawa, Shugo, V Dhawan, P Spetsieris, W Robeson, T Chaly, R Dahl, D Margouleff and D Eidelberg. 1993. "Noninvasive quantitative fluorodeoxyglucose PET studies with an estimated input function derived from a population-based arterial blood curve." *Radiology* 188(1):131–136.

Tanaka, Eiichi and Hideo Murayama. 1982. Properties of statistical noise in positron emission tomography. In *International Workshop on Physics and Engineering in Medical Imaging*. International Society for Optics and Photonics pp. 158–164.

Team, R Core et al. 2013. "R: A language and environment for statistical computing.".

Ter-Pogossian, Michel M, Michael E Phelps, Edward J Hoffman and Nizar A Mullani. 1975. "A positron-emission transaxial tomograph for nuclear imaging (PETT)." *Radiology* 114(1):89–98.

Teymurazyan, A, Terence Riauka, H-S Jans and D Robinson. 2013. "Properties of noise in positron emission tomography images reconstructed with filtered-backprojection and row-action maximum likelihood algorithm." *Journal of digital imaging* 26(3):447–456.

Thiele, Frank and Ralph Buchert. 2008. "Evaluation of non-uniform weighting in non-linear regression for pharmacokinetic neuroreceptor modelling." *Nuclear medicine communications* 29(2):179–188.

Tinelli, G, F Minelli, F De Nigris, C Vincenzoni, M Filipponi, P Bruno, M Mas-

setti, A Flex and R Iezzi. 2018. "The potential role of quantitative digital subtraction angiography in evaluating type B chronic aortic dissection during TEVAR: preliminary results." *European review for medical and pharmacological sciences* 22(2):516–522.

Tinelli, Giovanni, Francesca De Nigris, Fabrizio Minelli, Claudio Vincenzoni and Andrea Flex. 2018. "Quantitative digital subtraction angiography during type B chronic aortic dissection endovascular repair." *Vascular Medicine (United Kingdom)* 23(2):181–182.

Tomasi, Giampaolo, Federico Turkheimer and Eric Aboagye. 2012. "Importance of quantification for the analysis of PET data in oncology: review of current methods and trends for the future." *Molecular Imaging and Biology* 14:131–146.

Tong, Shan, Adam M Alessio and Paul E Kinahan. 2010. "Image reconstruction for PET/CT scanners: past achievements and future challenges." *Imaging in medicine* 2(5):529.

Tonietto, Matteo, Gaia Rizzo, Mattia Veronese and Alessandra Bertoldo. 2015. Modelling arterial input functions in positron emission tomography dynamic studies. In *2015 37th annual international conference of the IEEE Engineering in Medicine and Biology Society (EMBC)*. IEEE pp. 2247–2250.

Trench, William F. 2013. "Elementary differential equations with boundary value problems.".

Trinder, RR, Tz Kokalova, DJ Parker, Carl Wheldon, Ben Phoenix, Peter Ivanov, Ben Russel, Ben Webster, Patrick Regan, Andrew Robinson et al. 2020. Theragnostics-Alternative production of terbium isotopes at the University of Birmingham using an MC40 cyclotron. In *Journal of Physics: Conference Series*. Vol. 1643 IOP Publishing p. 012209.

Tu, Shu-Ju, Wei-Yuan Chen and Chen-Te Wu. 2021. "Uncertainty measurement of radiomics features against inherent quantum noise in computed tomography imaging." *European Radiology* 31(10):7865–7875.

Turkheimer, Federico E, Rainer Hinz, Roger N Gunn, John AD Aston, Steve R Gunn and Vincent J Cunningham. 2003. "Rank-shaping regularization of exponential spectral analysis for application to functional parametric mapping." *Physics in Medicine & Biology* 48(23):3819.

Ulaner, Gary A, Anne Eaton, Patrick G Morris, Joshua Lilienstein, Komal Jhaveri,

Sujata Patil, Maurizio Fazio, Steven Larson, Clifford A Hudis and Maxine S Jochelson. 2013. "Prognostic value of quantitative fluorodeoxyglucose measurements in newly diagnosed metastatic breast cancer." *Cancer medicine* 2(5):725–733.

Ulrich, Ethan J, John J Sunderland, Brian J Smith, Imran Mohiuddin, Jessica Parkhurst, Kristin A Plichta, John M Buatti and Reinhard R Beichel. 2018. "Automated model-based quantitative analysis of phantoms with spherical inserts in FDG PET scans." *Medical physics* 45(1):258–276.

Van der Vaart, Aad W. 2000. *Asymptotic statistics*. Vol. 3 Cambridge university press.

Vandenberghe, Stefaan, Ekaterina Mikhaylova, Ester D'Hoe, Pieter Mollet and Joel S Karp. 2016. "Recent developments in time-of-flight PET." *EJNMMI physics* 3(1):1–30.

Vandenberghe, Stefaan, Pawel Moskal and Joel S Karp. 2020. "State of the art in total body PET." *EJNMMI physics* 7(1):1–33.

Vardi, Yehuda, Larry A Shepp and Linda Kaufman. 1985. "A statistical model for positron emission tomography." *Journal of the American statistical Association* 80(389):8–20.

Veronese, Mattia, Alessandra Bertoldo, Shrinivas Bishu, Aaron Unterman, Giampaolo Tomasi, Carolyn Beebe Smith and Kathleen C Schmidt. 2010. "A spectral analysis approach for determination of regional rates of cerebral protein synthesis with the L-[1-11C] leucine PET method." *Journal of Cerebral Blood Flow & Metabolism* 30(8):1460–1476.

Veronese, Mattia, Gaia Rizzo, Alessandra Bertoldo and Federico E Turkheimer. 2016. "Spectral analysis of dynamic PET studies: a review of 20 years of method developments and applications." *Computational and mathematical methods in medicine* 2016.

Viallon, Magalie, Victor Cuvinciuc, Benedicte Delattre, Laura Merlini, Isabelle Barnaure-Nachbar, Seema Toso-Patel, Minerva Becker, Karl-Olof Lovblad and Sven Haller. 2015. "State-of-the-art MRI techniques in neuroradiology: principles, pitfalls, and clinical applications." *Neuroradiology* 57(5):441–467.

Viswanath, Varsha. 2020. Studying the Clinical and Research Applications of the PennPet Explorer, a Long Axial Field-Of-View Pet Scanner PhD thesis University of Pennsylvania.

Viswanath, Varsha, Rhea Chitalia, Austin R Pantel, Joel S Karp and David A Mankoff. 2021. "Analysis of Four-Dimensional Data for Total Body PET Imaging." *PET clinics* 16(1):55–64.

Vriens, Dennis, Lioe-Fee de Geus-Oei, Wim JG Oyen and Eric P Visser. 2009. "A curve-fitting approach to estimate the arterial plasma input function for the assessment of glucose metabolic rate and response to treatment." *Journal of Nuclear Medicine* 50(12):1933–1939.

Wacholtz, Elaine H. 2011. "History and Development of PET." *ECEI, CEwebsources. http://www. cewebsource. com/coursePDFs/historyofPET. pdf (page consultée le 22 Février 2012)* .

Wang, Dennis, James Hensman, Ginte Kutkaite, Tzen S Toh, Ana Galhoz, Jonathan R Dry, Julio Saez-Rodriguez, Mathew J Garnett, Michael P Menden, Frank Dondelinger et al. 2020. "A statistical framework for assessing pharmacological responses and biomarkers using uncertainty estimates." *Elife* 9:e60352.

Wang, Guobao, Arman Rahmim and Roger N Gunn. 2020. "PET Parametric Imaging: Past, Present, and Future." *IEEE Transactions on Radiation and Plasma Medical Sciences* 4(6):663–675.

Wang, Guobao, Lorenzo Nardo, Terry Jones, Simon R Cherry and Ramsey D Badawi. 2021. "Total-Body PET Multiparametric Imaging of Cancer Using a Voxel-wise Strategy of Compartmental Modeling." *Journal of Nuclear Medicine* .

Wang, Tonghe, Yang Lei, Yabo Fu, Walter J Curran, Tian Liu, Jonathon A Nye and Xiaofeng Yang. 2020. "Machine learning in quantitative PET: A review of attenuation correction and low-count image reconstruction methods." *Physica Medica* 76:294–306.

Wang, Wenli and Gene Gindi. 1997. "Noise analysis of MAP-EM algorithms for emission tomography." *Physics in Medicine and Biology* 42(11):2215–2232.

Wang, Yiran, Elizabeth Li, Simon R Cherry and Guobao Wang. 2021. "Total-body PET kinetic modeling and potential opportunities using deep learning." *PET clinics* 16(4):613–625.

Wernick, Miles N and John N Aarsvold. 2004. *Emission tomography: the fundamentals of PET and SPECT*. Elsevier.

Wieczorek, Matthias, Jakob Vogel and Tobias Lasser. 2014. "CampRecon—a software framework for linear inverse problems." *Tech. Rep.* .

Willemink, Martin J, Mats Persson, Amir Pourmorteza, Norbert J Pelc and Dominik Fleischmann. 2018. "Photon-counting CT: technical principles and clinical prospects." *Radiology* 289(2):293–312.

Wong, Koon-Pong, Dagan Feng, Steven R Meikle and Michael J Fulham. 2002. "Segmentation of dynamic PET images using cluster analysis." *IEEE Transactions on nuclear science* 49(1):200–207.

Wrenn Jr, Frank R, Myron L Good and Philip Handler. 1951. "The use of positron-emitting radioisotopes for the localization of brain tumors." *Science* 113(2940):525–527.

Wu, Qi, Fengyun Gu, Yaping Wu, Yun Zhou and Meiyun Wang. 2022. "Assessment of Compartmental models and delay estimation schemes for dynamic Total-body PET imaging using uEXPLORER." *Journal of Nuclear Medicine* 63(Supplement 2):3186–3186.

Wu, Qi, Fengyun Gu, Yushen Gu, Tianyi Xu, Yun Zhou and Hongcheng Shi. 2022. "Impact of Equilibration Time (t*) on Patlak Quantitation in Dynamic Total-Body Imaging using the uEXPLORER PET Scanner." 63(Supplement 2):3184–3184.

Wu, Qi, Finbarr O'Sullivan, Mark Muzi and David A Mankoff. 2019. An exploration of the prognostic utility of shortened dynamic imaging protocols for PET-FDG scans. In *2019 IEEE Nuclear Science Symposium and Medical Imaging Conference (NSS/MIC)*. IEEE pp. 1–3.

Wu, Yaping, Tao Feng, Yizhang Zhao, Tianyi Xu, Fangfang Fu, Zhun Huang, Nan Meng, Hongdi Li, Fengmin Shao and Meiyun Wang. 2022. "Whole-Body Parametric Imaging of 18F-FDG PET Using uEXPLORER with Reduced Scanning Time." *Journal of Nuclear Medicine* 63(4):622–628.

Xiu, Zhaoyan, Mark Muzi, Jian Huang and Eric Wolsztynski. 2022. "Patient-adaptive Population-based Modeling of Arterial Input Functions." *IEEE Transactions on Medical Imaging* .

Yamagishi, Hiroyuki, Kaname Akioka, Kumiko Hirata, Yuji Sakanoue, Kazuhide Takeuchi, Junichi Yoshikawa and Hironobu Ochi. 1999. "A reverse flow-metabolism mismatch pattern on PET is related to multivessel disease in

patients with acute myocardial infarction." *Journal of Nuclear Medicine* 40(9):1492–1498.

Yao, Shulin, Tao Feng, Yizhang Zhao, Runze Wu, Ruimin Wang, Shina Wu, Can Li and Baixuan Xu. 2021. "Simplified protocol for whole-body Patlak parametric imaging with 18F-FDG PET/CT: Feasibility and error analysis." *Medical physics* 48(5):2160–2169.

Yaqub, Maqsood, Ronald Boellaard, Marc A Kropholler and Adriaan A Lammertsma. 2006. "Optimization algorithms and weighting factors for analysis of dynamic PET studies." *Physics in Medicine & Biology* 51(17):4217.

Zaidi, Habib. 2006. *Quantitative analysis in nuclear medicine imaging*. Springer.

Zaidi, Habib and Nicolas Karakatsanis. 2017. "Towards enhanced PET quantification in clinical oncology." *The British Journal of Radiology* 91(1081):20170508.

Zanderigo, Francesca, Ramin V Parsey and R Todd Ogden. 2015. "Model-free quantification of dynamic PET data using nonparametric deconvolution." *Journal of Cerebral Blood Flow & Metabolism* 35(8):1368–1379.

Zanotti-Fregonara, Paolo, Christina S Hines, Sami S Zoghbi, Jeih-San Liow, Yi Zhang, Victor W Pike, Wayne C Drevets, Alan G Mallinger, Carlos A Zarate Jr, Masahiro Fujita et al. 2012. "Population-based input function and image-derived input function for [11C](R)-rolipram PET imaging: Methodology, validation and application to the study of major depressive disorder." *Neuroimage* 63(3):1532–1541.

Zhang, Jeff L, A Michael Morey and Dan J Kadrmas. 2016. "Application of separable parameter space techniques to multi-tracer PET compartment modeling." *Physics in Medicine and Biology* 61(3):1238.

Zhang, Xuezhu, Zhaoheng Xie, Eric Berg, Martin S Judenhofer, Weiping Liu, Tianyi Xu, Yu Ding, Yang Lv, Yun Dong, Zilin Deng et al. 2020. "Total-body dynamic reconstruction and parametric imaging on the uEXPLORER." *Journal of Nuclear Medicine* 61(2):285–291.

Zhou, Rong, Austin R Pantel, Shihong Li, Brian P Lieberman, Karl Ploessl, Hoon Choi, Eric Blankemeyer, Hsiaoju Lee, Hank F Kung, Robert H Mach et al. 2017. "[18F](2S, 4R) 4-fluoroglutamine PET detects glutamine pool size changes in triple-negative breast cancer in response to glutaminase inhibition." *Cancer research* 77(6):1476–1484.

Zondervan, Robert L, Peter F Hahn, Cheryl A Sadow, Bob Liu and Susanna I Lee. 2013. "Body CT scanning in young adults: examination indications, patient outcomes, and risk of radiation-induced cancer." *Radiology* 267(2):460–469.